

Event-by-event Hydrodynamic Simulations for Relativistic Heavy-ion Collisions

Dissertation

Presented in Partial Fulfillment of the Requirements for the Degree Doctor of
Philosophy in the Graduate School of The Ohio State University

By

Zhi Qiu, B.S., Ph.D.

Graduate Program in Physics

The Ohio State University

2021

Dissertation Committee:

Professor Ulrich W. Heinz, Advisor

Professor Yuri Kovchegov

Professor Eric Braaten

Professor Chris Hammel

© Copyright by
Zhi Qiu
2021

Abstract

In this thesis, I show my Ph.D. work on event-by-event hydrodynamic simulations for relativistic heavy-ion collision. I show that event-by-event hydrodynamic simulations have become an indispensable tool for studying relativistic heavy-ion collisions and how it can be used to explain many phenomena.

In Chap. 2, I compare the previously dominating single-shot hydrodynamics with event-by-event hydrodynamic simulations which are now becoming mainstream. The event-by-event simulations are more realistic, but they are also very time consuming; the single-shot simulations are economical, but then the question arises as to whether they can be used as a sufficiently precise replacement for event-by-event simulations. I will compare these two simulation types for two popular initial condition models.

I show that for the event averages of the multiplicity and elliptic and triangular flows, the time consuming event-by-event hydrodynamic simulations can, to a good approximation, be replaced by single-shot ones, when using properly constructed initial conditions. For higher-order flows such as $v_{4,5}$ the single-shot simulations are shown to be incapable of reproducing those from event-by-event simulations.

In Chap. 3, we show that the elliptic and triangular flow data measured by the ALICE collaboration at the LHC prefer a small specific shear viscosity close to $\eta/s = 0.08$, when considering the MC-Glauber and MC-KLN models. In order to allow for a much larger η/s value, the initial condition model must feature triangularity values $\sim 50\%$ larger than the ones provided by the MC-Glauber and MC-KLN models.

Chap. 4 focuses on correlations between event-plane angles. We show that the event-plane angle correlation measurements by the ATLAS collaboration can be explained by hydrodynamic simulations. The same correlation patterns cannot be explained directly from the initial conditions.

In Chap. 5, we show that including only ~ 20 out of 319 carefully chosen resonances can already yield spectra and flow results within 1% relative error. Such a treatment can be used to shorten the currently lengthy (~ 3 hours) resonance decay calculations by a factor of ten.

Chap. 6 focuses on various ways of calculating and measuring anisotropic flows, and their comparisons. We point out that the event planes angle Ψ_n fluctuates from event to event, and that the differential event-plane angle $\Psi_n(p_T) - \Psi_n$ also fluctuates from event to event. We show that traces of such angular fluctuations can be measured experimentally, and explain how such measurements allow the study of the fluctuation of the flow orientations in addition to the fluctuation of the flow magnitudes.

In Chap. 7 we give a thorough description of the general sampling methodology, and show that it can be applied in an efficient way to sample particles whose emission is determined by the Cooper-Frye formula, using the simplification of longitudinal boost invariance.

Dedicated to my family

Acknowledgments

First, I want to sincerely thank my advisor, Prof. Ulrich W. Heinz, for all his selfless teaching and support during my Ph.D. period. Not only did I learn a great amount of knowledge from him, but I also acquired the ability to learn, to think, and to question by myself, to talk and to communicate with people in a professional and concise way, to be strict and cautious in research but respectful to people's work at the same time, and last but not least, the attitude that "one should either not do something or give it his best". His wisdom, sense of humor, strictness to his students but also constant support at the same time, all make an invaluable mix from which I, as his student, benefited a lot. I feel so lucky to have him as my advisor.

Next I want to thank all other professors in the Physics Department at OSU, especially those from whom I took courses and those on my Ph.D. committee, for providing such a friendly, active, and supportive environment to all students. I enjoyed very much taking classes from various professors, questioning them or being questioned by them, sharing their visions on the current status and the future of physics. Their energy and friendliness formed another unforgettable experience.

I also want to thank all my friends, especially Chun Shen; our constant discussions and collaborations were a great help to my work.

Finally I want to thank my family. Their consideration for my situation and their unceasing support is what made my work possible.

Vita

Sep.2000-Sep.2004	Bachelor in Mathematics University of Science and Technology of China
Sep.2004-Sep.2009	Ph.D. in Mathematics Research and Teaching Assistant Art and Science College The Ohio State University
Sep.2009-Aug.2013	Research and Teaching Assistant Art and Science College The Ohio State University

Publications

- Zhi Qiu, Ulrich W. Heinz *Event-by-event shape and flow fluctuations of relativistic heavy-ion collision fireballs* Physics Review C84 (2011) 024911
- Zhi Qiu, Chun Shen, Ulrich Heinz *Hydrodynamic elliptic and triangular flow in Pb-Pb collisions at $\sqrt{s}=2.76$ ATeV* Physics Letter B707 (2012) 151-155
- Chun Shen, Steffen A. Bass, Tetsufumi Hirano, Pasi Huovinen, Zhi Qiu, Huichao Song, Ulrich Heinz *The QGP shear viscosity: Elusive goal or just around the corner?* Journal of Physics, G38 (2011) 124045
- Zhi Qiu, Ulrich Heinz *Hydrodynamic event-plane correlations in Pb+Pb collisions at $\sqrt{s}=2.76$ ATeV* Physics Letter B717 (2012) 261-265
- Zhi Qiu, Ulrich Heinz *Event-by-event hydrodynamics for heavy-ion collisions* AIP Conference Proceeding, 1441 (2012) 774-776
- J.Scott Moreland, Zhi Qiu, Ulrich W. Heinz *Imprinting quantum fluctuations on hydrodynamic initial conditions* e-Print: arXiv:1210.5508
- Zhi Qiu, Chun Shen, Ulrich W. Heinz *Resonance decay contributions to higher-order anisotropic flow coefficients* Phys.Rev. C86 (2012) 064906
- Ovidiu Costin, Min Huang, Zhi Qiu *Ionization in damped time-harmonic fields* Journal of Physics. A42 (2009) 325202

Fields of Study

Major Field: Physics

Table of Contents

	Page
Abstract	ii
Dedication	iii
Acknowledgments	iv
Vita	v
1. Introduction	1
1.1 Disclaimer	1
1.2 Relativistic heavy-ion collision experiments	1
1.3 Relativistic hydrodynamic simulations	2
1.4 Observables	5
2. Comparison between event-by-event and single-shot hydrodynamic simulations	9
2.1 Definitions	9
2.1.1 Ellipticity	9
2.1.2 Higher order eccentricity coefficients	12
2.1.3 Harmonic flow coefficients	13
2.1.4 Initial-state models	13
2.1.5 Averaging procedures for the initial profiles	14
2.2 Eccentricities	14
2.2.1 Centrality dependence of different ellipticities	14
2.2.2 Ellipticities with different weight functions	18
2.2.3 Higher order harmonics	19
2.2.4 Eccentricity correlations	20
2.3 Event-by-event hydrodynamics and flow fluctuations	21
2.3.1 Correlations between participant plane, event plane, and reaction plane	21
2.3.2 Centrality dependence of event and participant plane correlations	22
2.3.3 Harmonic flows and their corresponding initial eccentricities: nonlinear hydrodynamic response	24
2.4 Single-shot versus event-by-event hydrodynamics	26
2.4.1 Transverse momentum spectra	27
2.4.2 Elliptic and triangular flow	29
2.4.3 Elliptic flow fluctuations	33
2.5 Chapter summary	36

3.	Using simultaneously measured elliptic and triangular flow to resolve initial condition ambiguities	38
3.1	Introduction	38
3.2	Justification for using single-shot simulations	38
3.3	Setup for the simulations	40
3.4	Transverse momentum spectra	41
3.5	p_T -integrated elliptic and triangular flow	42
3.6	p_T -differential elliptic and triangular flow	43
3.7	Chapter summary	44
4.	Hydrodynamic event-plane correlations in Pb+Pb collisions	46
4.1	Introduction	46
4.2	Methodology	47
4.3	Results	47
5.	Resonance decay contributions to higher-order anisotropic flow coefficients	55
5.1	Chapter introduction	55
5.2	Resonance ordering	56
5.3	Results and discussion	58
5.4	Chapter conclusions	61
6.	Fluctuating flow angles and anisotropic flow measurements	63
6.1	Chapter introduction	63
6.2	Differential flows from the event-plane method and from two-particle correlations	65
6.3	The effect of flow fluctuations on differential v_n measures	69
6.4	Non-factorization of flow-induced two-particle correlations	74
6.5	Chapter summary	76
7.	Sampling particles from the Cooper-Frye distribution	78
7.1	iS and iSS overview	78
7.2	Random variables and sampling methods	79
7.2.1	Random variable, PDF and CDF	79
7.2.2	Sampling 1d random variables according to the inverse CDF	79
7.2.3	Direct sampling of 1d random variables according to their PDF: special accept-reject method	79
7.2.4	Sampling a 1d random variable using envelope distribution: general accept-reject method	80
7.2.5	Sampling 1d random variable using grouping	80
7.2.6	Sampling efficiency	80
7.2.7	Automatically generated stair function envelope distribution	83
7.2.8	Generating genuine continuous samples	84
7.2.9	Sampling multi-dimensional random variables	84
7.2.10	Possible issues	85
7.3	Sampling the particle momentum distribution	86
7.3.1	Emission function and Cooper-Frye formula	86
7.3.2	Spectra and flow calculations	86
7.4	Sampling the emission function	87
7.4.1	The purely numerical approach	88
7.4.2	Semi-analytic approach	89
7.4.3	Comparison between the approaches	92
7.4.4	Other optimizations and implemented models	94
7.5	Code verification	95

8.	Miscellaneous topics	101
8.1	Comparison between eccentricities defined with r^2 and r^n weights	101
8.2	Robust viscous hydrodynamics	101
8.3	Time evolution of the event plane orientations	104
8.4	Best estimator for flows using eccentricities	104
9.	Summary	107
Appendices		109
A.	Choice of parameters used in the simulations	109
B.	Table of parameters for cutting centralities	110
C.	Feed down contribution tables for π , K , p , Λ , Σ^+ , and Ξ^- [100]	117
D.	Compiling, running, and tuning iSS	130
D.1	Compiling	130
D.2	Running	130
D.3	Input and output files	130
D.4	Parameter file	131
D.5	Tables	132
E.	Introduction to iSS support classes	133
E.1	Table class and table-function classes	133
E.2	Classes related to random variables	133
E.3	Parameter reader class	134
F.	The iEBE package	135
F.1	How to use the package to perform multi-job calculations	135
F.2	How to analyze generated data	136
F.3	How to tune parameters	136
Bibliography		137

Chapter 1: Introduction

1.1 Disclaimer

I would like to start with a quote from the book [1]:

“The aim of classical mechanics and theoretical physics is to provide and develop a self-consistent mathematical structure which runs so closely parallel to the development of physical phenomena that, starting from a minimum number of hypotheses, it may be used to accurately describe and even predict the results of all carefully controlled experiments.”

I quote it here to as a reminder that the development of theoretical physics is the process of improving the *mathematical model* behind the material world; thus, however successful the current achievement in theoretical physics becomes, whether it can be categorized as “the truth” depends on how well it stands the test of time. In this thesis, I use the words “truth”, “nature”, etc., to mean the current state-of-art understanding of theoretical physics.

1.2 Relativistic heavy-ion collision experiments

“Heavy ions” are the atomic nuclei of atoms with mass number $A \geq 4$. The relativistic heavy-ion collision program was initiated partially in the hope to study a new type of matter, the quark-gluon plasma, which otherwise can only be found shortly after the big bang or (possibly) in the core of neutron stars. In this section a brief introduction is given to make the thesis self-contained; for a more thorough motivation and background of heavy-ion collision experiments, see for example [2], [3], and [4].

Relativistic heavy-ion collision experiments are mainly performed at the Relativistic Heavy-Ion Collider (RHIC) at Brookhaven National Lab (BNL) near New York and at the Large Hadron Collider (LHC) operated by European Organization for Nuclear Research (CERN) near Geneva. In relativistic heavy-ion collision experiments, one generates beams of bare heavy nuclei (“heavy ions”) and accelerates them to close to the speed of light: RHIC: $v > 99\%c$; LHC: $v > 99.9\%c$.

The two beams moving around the accelerator ring anti-parallel to each other are brought to collision in the so-called interaction regions. Those interaction regions are instrumented with detectors. Both RHIC and LHC have multiple detectors. Each detector is a complicated engineering piece of art that is a product of, and operated and maintained by a large collaboration of physicists and engineers (ranging from ~ 500 to ~ 3500 members each).

The collision systems that have been run at RHIC include proton-proton (p+p), deuterium-gold (d+Au), copper-copper (Cu+Cu), gold-gold (Au+Au), uranium-uranium (U+U), and most recently copper-gold (Cu+Au) collisions. At the LHC, so far only proton-proton (p+p), lead-lead (Pb+Pb), and proton-lead (p-Pb) have been studied. Among these nuclei, Cu, Au, Pb, and U are heavy nuclei, and others are light ones. The light nuclei collisions such as p+p and mixed-type collision like d+Au are often used to “calibrate” the heavy-ion collisions. It is worth mentioning that Cu, Au, and Pb nuclei are almost perfectly spherical while U nuclei have an ellipsoidal shape in their ground states.

The detectors can be used to identify the species of particles, and measure their energy and momentum. What we do not know about the particles are their creation times and their emission

locations — the resolution of the measurement is much coarser than the actual scale of the collision zone; each collision is, from the detector’s point of view, point-like and instantaneous.

When the two heavy nuclei collide, their nucleons are shattered. Their constituents, the quarks and gluons, are spilled out for a brief amount of time and form a new type of matter: the quark gluon matter. This matter can exist for only very short amount of time ($\sim 10^{-23}$ second) before it “evaporates”: the quarks and gluons quickly recombine into hadrons and fly into the detectors.

It is not only heavy-ion collision that can shatter nucleons into quarks and gluons; proton-proton collisions collisions can also break the proton cage to free the quarks and gluons at high enough energy: in all such collisions the quark-gluon matter is created. However one peculiar property of the quark-gluon matter created by heavy-ion collision is that the created matter can actually equilibrate, meaning that the quarks and gluons in the matter can almost reach local equilibrium, which is another way to say that the particle number probability density of finding quarks and gluons with given energy satisfy their corresponding Boltzmann distributions. This thermalized medium is the quark-gluon plasma (QGP).

The information on the out-going particles can be analyzed to form observables, which will be compared with various theoretical results in order to learn about the properties of the QGP.

Another concept that needs to be introduced is “centrality”. A collision where the two nuclei hit head-on is very different from another collision where the two nuclei only graze each other; for this reason, collisions are usually sub-divided into “centrality classes”, where each class contains collisions under similar conditions. The conventional quantity that can be used theoretically to perform such a division is the impact parameter, which is defined as the closest distance between the tracks of the centers of the two nuclei. However, as mentioned above, in heavy-ion collisions no detailed information including impact parameter can be directly obtained, therefore in measurements another quantity is used to define the “centrality” of the collision. Let us explain the idea: it is plausible, at least statistically, that the more central a collision is, the more particles it will produce. Based on this observation, the number of produced particles can be used to indicate how central a collision is. Operationally, all collisions are ordered by the number of charged hadrons they produce, and the rank of a collision is its “centrality”. For example, the top 5% of all the events in this ordered list form the 0-5% centrality class (or centrality bin). The smaller the centrality class, the more central the collisions it contains¹.

1.3 Relativistic hydrodynamic simulations

The evolution of the quark-gluon plasma is simulated using relativistic hydrodynamics. There are several stages involved in this process. For an illustration, a typical simulation is visualized in Fig. 1.1.

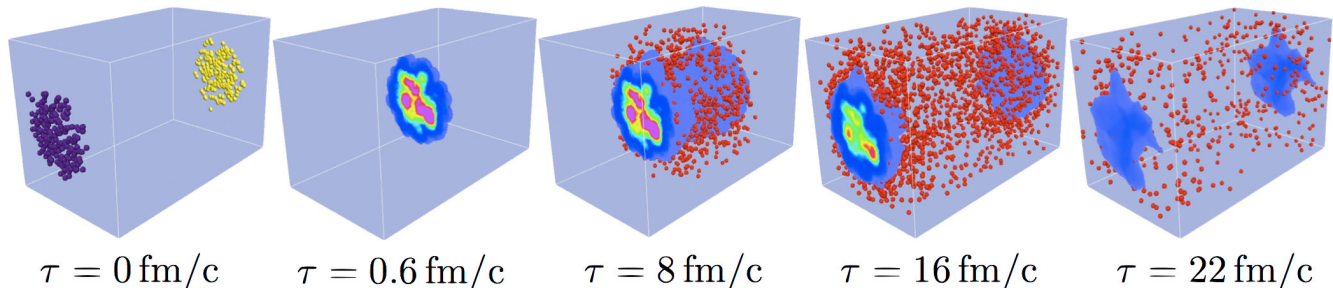


Figure 1.1: Snapshots of a simulated event at indicated time. The two groups of colored balls are the colliding nuclei, the color patches are the quark-gluon plasma, and the red balls are the final hadrons emitted from the quark-gluon plasma.

¹This procedure does not work for p-p collisions, due to multiplicity fluctuations. It only works for nuclear collisions where the monotonic increase of multiplicity with the number of nucleons participating in the collision overwhelms the fluctuations in individual nucleon-nucleon collisions.

The first stage is to generate the initial state for the quark-gluon plasma, which is usually represented as an energy density profile. In principle, there is a pre-equilibrium stage between the time of collision and the starting time of the quark-gluon plasma, during which the quark matter quickly evolves towards local equilibrium. As a result of this pre-equilibrium evolution, the initial hydrodynamic energy density profile is not the same profile as *just* after the collision. Relatively little is known about this pre-equilibrium stage and its study is new and still on-going. However, the pre-equilibrium stage is believed to last only for a very brief amount of time (~ 1 fm/c) and to contribute at most minor changes to observables I studied. Therefore, in all of my simulations, this stage is assumed to be absent, and energy density profiles produced by models which strictly speaking should only be applied at the beginning of the pre-equilibrium stage are used as the final state of the pre-equilibrium stage — that is, as the initial state of the hydrodynamic simulation. Because of the pre-equilibrium stage, there could be collective particle motion already before the system equilibrates; in my simulations such initial flow is ignored.

The initial condition models used in my simulations are the Glauber model [5, 6] and the fKLN model [6–9]. Both models start with generating the three dimensional nucleon position configurations assuming independent draws from the Woods-Saxon density distributions for the colliding nuclei. Next, the density distributions of these nucleons are projected onto the plane perpendicular to the beam direction (the transverse plane). Fig. 1.2 is an illustration for such a projection. The big dashed circles indicate the boundaries of the two colliding nuclei, and the smaller disks are the nucleons inside each nucleus, identified by their color.

The Glauber model first simulates how the nucleons from one nucleus overlap in the transverse plane with nucleons from the other nucleus. Each overlap of a pair of nucleons gives one binary collision, producing two wounded (participant) nucleons. If a wounded nucleon scatters again with another nucleon from the other nucleus, it remains wounded, wounds the other nucleon (if not already wounded), and contributes one to the binary collision count. In Fig. 1.2, the solid colored small disks are the wounded nucleons. The Glauber model then assumes that the initially produced entropy density at a given location in the transverse plane is proportional to a linear combination of the wounded nucleon and the binary collision densities (“two-component” model). Both the proportionality factor and the mixing factor are fitted later by comparing simulated observables to experimental data.

The KLN model uses the nuclear density functions from the nucleon profiles of the two colliding nuclei to determine their local saturation scale Q_s , which is then used to determine the unintegrated nuclear gluon density distribution; the unintegrated gluon distributions from the two colliding nuclei can then be used to generate the density of the gluons produced in the collision [6–9]. This produced gluon density is then assumed to be proportional to the initial entropy density, and the proportionality factor, as well as a model parameter λ used in determining Q_s from nucleon density functions, are fitted to experimental data.

For both models, the initial entropy density profiles are translated into energy density profiles using the s95p-PCE equation of state (EOS) [11, 12]. Our group uses the superMC code (modified from the rcBk model [13] and the MC-KLN code [6, 8]²) to generate both types of initial conditions. The actual choice of parameters varies between different simulations and will be reported in the corresponding chapters and in Table B.1 in the Appendix.

The second stage is to evolve the initial energy density profile hydrodynamically by numerically solving the relativistic hydrodynamic evolution differential equations. Our group solves the Israel-Stewart second-order hydrodynamic equations [14] under the assumption of longitudinal boost-invariance³, using the VISH2+1 code [15]. There are several tunable parameters that describe the properties of the quark-gluon plasma, among which the most famous one is the specific shear

²<http://www.aiu.ac.jp/~ynara/>.

³The longitudinal boost-invariant assumption assumes that the system is invariant under a boost in the longitudinal (beam) direction. The experimentally measured rapidity region where this assumption approximately holds is known as the “plateau”; it covers roughly ± 0.5 units of rapidity at RHIC energy and ± 2.5 units of rapidity at LHC energy, and these regions are the validity regions of our simulations. In particular, our simulations can be applied to the important “mid-rapidity” region (around zero rapidity) where most experiments have the best sensitivities.

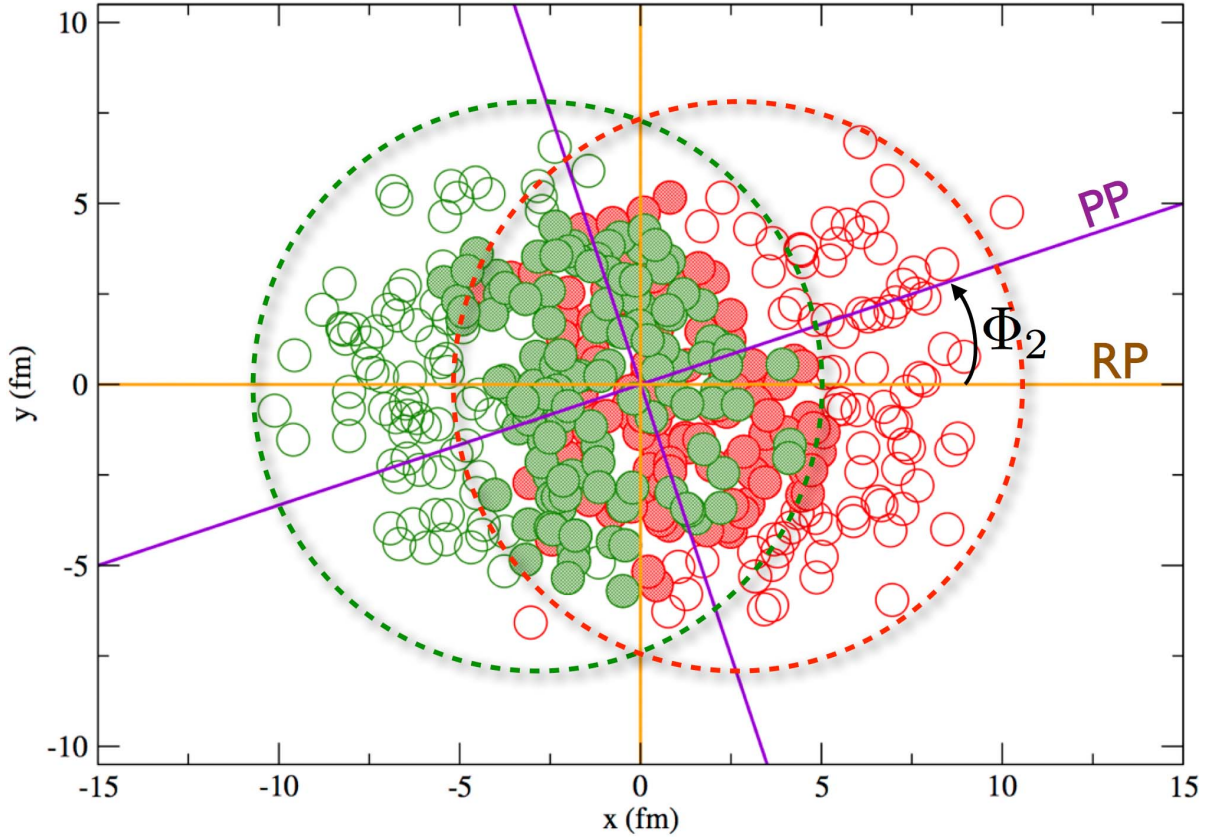


Figure 1.2: (From [10]) Sample nucleon profiles of two colliding nuclei in the transverse plane. The dashed circle indicates the location and the boundary of the two colliding nuclei. The small disks represent nucleons, and solid colored small disks are the wounded ones. Here the frame is the reaction plane frame where the x direction is the direction of the impact parameter, and the y direction is its perpendicular direction in the transverse plane. The plane formed by the x direction and the beam direction is the reaction plane (RP). The direction that maximizes the second order deformation has angle Φ_2 relative to the x direction, and the plane formed by this direction and the beam direction is the (second-order) participant plane (PP).

viscosity η/s , the ratio of shear viscosity η to entropy density s . These parameters are not well-known theoretically and will be adjusted to experimental data. As we will see, different initial conditions require different η/s values to describe the same data. This will be discussed later in this thesis. Fig. 1.3 is an illustration of the evolution of the energy density profile from one simulation.

The VISH2+1 code simulates the evolution of the energy density distribution, and outputs information like flow velocity, energy density, etc. along a constant temperature (isothermal) freeze-out surface, whose functionality depends on the type of simulations:

1. In a purely hydrodynamic simulation, both the quark-gluon plasma and the re-scattering of the emitted hadrons are simulated using hydrodynamics. In such an approach, the freeze-out surface is defined as the surface outside which hadrons cease to interact and reach the detectors by streaming freely.
2. In a hybrid hydrodynamic simulation, only the quark-gluon plasma is simulated hydrodynamically, and the scattering of the hadrons, after they materialize from the quark-gluon plasma, is simulated using a hadron re-scattering simulator based on a transport approach. In such an approach, the freeze-out surface (or better “switching surface”) is the surface that separates the quark-gluon plasma phase from the hadronic phase.

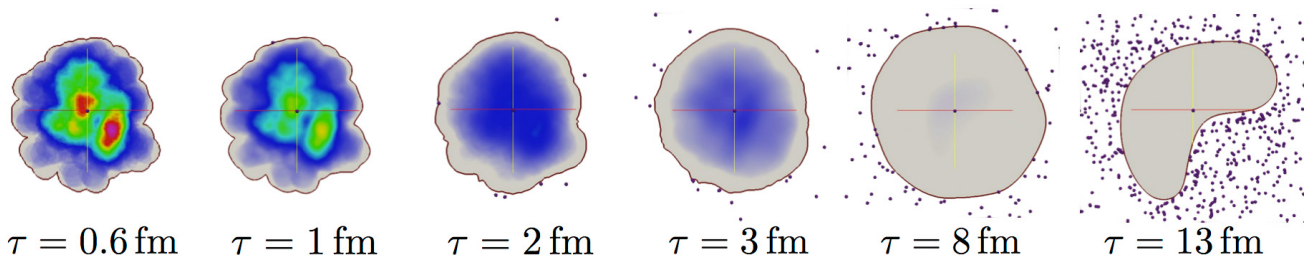


Figure 1.3: The evolution of energy density in the transverse plane from a simulated event, at time τ as indicated. Red indicates high and grey indicates low energy density. The QGP is assumed to convert to hadrons at $e_{\text{hadron}} = 0.508 \text{ GeV}/\text{fm}^3$ (indicated by the thin purple line at the edge of the grey region).

In both types of simulation, the temperature of the freeze-out surface is a tunable parameter, although for the hybrid simulations people choose it according to the results from lattice QCD calculations [16, 17].

The next stage of the simulation is to generate the momentum distributions of particles from the freeze-out surface. The Cooper-Frye formula (see Sec. 7.3 for details) is used to calculate the momentum distribution of the emitted particles from the surface.

For purely hydrodynamic simulations, knowing these distributions as continuous functions enables one to calculate many observables. However, in real experiments, each collision only emits a limited number of particles and calculations done using the continuous distribution function do not allow one to study the fluctuations caused by finite statistics. To study finite-statistics fluctuations, one can also simulate a finite number of particles emitted from the freeze-out surface by Monte-Carlo sampling the continuous Cooper-Frye distribution.

For hybrid simulations one must in any case simulate the emission of finite numbers of particles, which is required by the hadron re-scattering simulator.

There is one more subtlety: even for purely hydrodynamic simulations, although the emitted particles are assumed to stop interacting, unstable particles continue to decay into lighter ones before they reach the detectors, and this process changes the momentum distributions of the light particles. This process is called resonance decay and it needs to be additionally computed. For hybrid simulations, the decay of unstable particles is usually included in the hadronic re-scattering simulator and it does not need to be computed separately.

Our group uses the iS code to calculate the continuous distributions of emitted particles and their resonance decays, and the iSS code to simulate the emission of a finite discrete number of particles. The methodology used for sampling in the iSS code will be explained in chapter Chap. 7.

For purely hydrodynamic simulations, this is the end of the simulation process. All of my publications are based on purely hydrodynamic simulations, but since part of the work I have contributed is a package for hybrid calculations, I will explain it briefly.

Once the emissions of hadrons has been successfully simulated, they can then be passed to the hadronic re-scattering simulator, from which the final-state momenta of the particles are produced, which can be analyzed to generate simulated observables. Our group uses the UrQMD code [18] to simulate the hadronic re-scattering. The particle information generated from UrQMD is huge and to efficiently compute simulated observables from it, a code binUtilities has been developed.

The stages involved in hydrodynamic simulations, and the corresponding codes used by our group used are schematically summarized in Fig. 1.4.

1.4 Observables

There are many interesting observables that can be studied using hydrodynamic simulations. One type of observables that are particularly important are the anisotropic flows v_n , which are the harmonic Fourier coefficients that describe the anisotropy of the particle emission distribution in

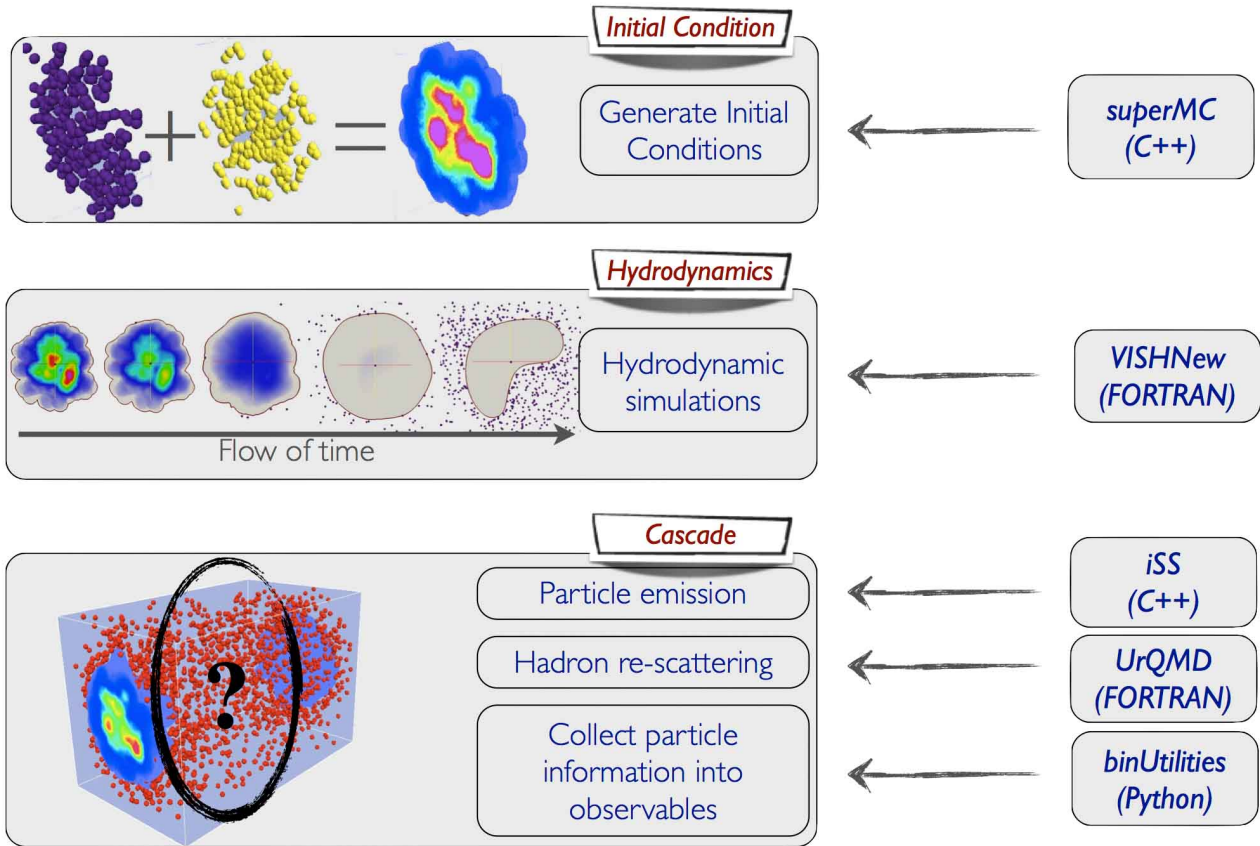


Figure 1.4: The three-step process for a hydrodynamics simulation (see text for details).

the transverse direction. Another set of theoretically interesting quantities are the initial eccentricities ε_n , which describe in the form of Fourier coefficients the anisotropies of the initial density distributions. Fig. 1.5 is a schematic illustration of the decomposition of one initial condition into its first 4 harmonic deformations.

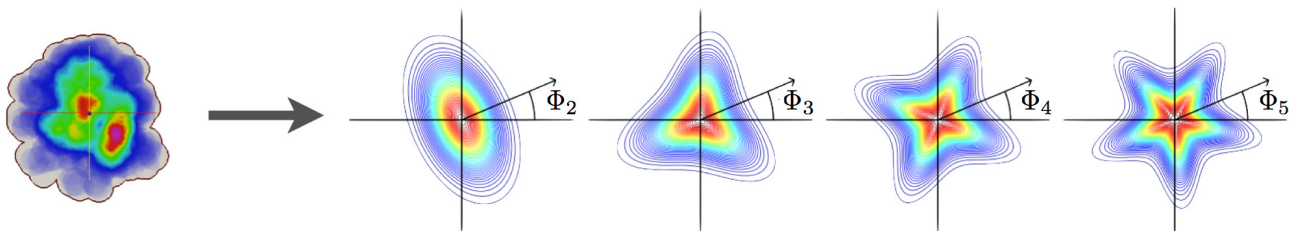


Figure 1.5: Decomposition of one initial condition into its first 4 harmonic deformations. The Φ_n are the participant plane angles for each deformation relative to the impact-parameter direction.

It is important to point out, that “anisotropy” is a vector, not a scalar, because it carries the information for the orientation of the deformation as well as its magnitude. Because of this, when people report a single scalar as the “anisotropy coefficient”, they are implicitly projecting the vector to a referencing direction and only report its component along that direction. The choice of the referencing direction is not unique, and we will be explicit on our choice of references when used. For each given harmonic order, there is no ambiguity about the direction of the deformation or the direction that “maximizes the anisotropy”; these directions can be used to define important

planes. The plane spanned by the direction Ψ_n of the anisotropic flow v_n and the beam direction is the n -th order *event plane* (EP). The plane spanned by the direction Φ_n of the complex eccentricity vector \mathcal{E}_n (see eq. (2.17) for formal definition) and the beam direction is the *participant plane* (PP). As a quick illustration in Fig. 1.5, the participant plane angles are marked on the figures for each decomposed deformation. Fig. 1.2 has an illustration of the 2nd-order participant plane angle. Precise formal definitions will be given in each chapter when needed.

Another classification separates hydrodynamic simulations into single-shot simulations and event-by-event simulations. The two procedures and their differences are summarized in Fig. 1.6.

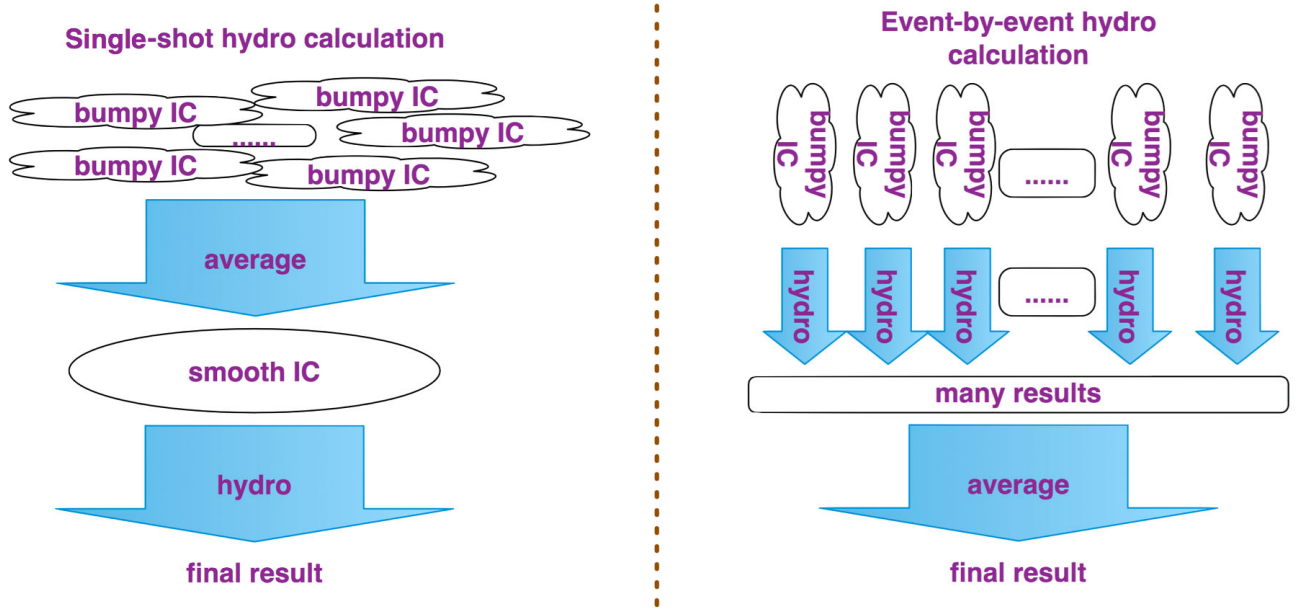


Figure 1.6: Single-shot hydrodynamic simulations versus event-by-event hydrodynamic simulations.

Event-by-event simulation is de facto the standard simulation type for heavy-ion collisions today, whose goal is to simulate each individual collision, then statistically construct simulated observables using all the simulated events in the same way as the experimentalists do with measured events. In this type of simulations, the initial energy density profile for each simulated collision is Monte-Carlo generated and propagated through hydrodynamic simulations, and the results are analyzed from a collection of particles summed over all simulated events. However such simulations are extremely resource demanding, and they have only been extensively applied in the last few years.

The single-shot simulation was dominantly used half a decade ago, when due to technological limitations people tried to study results from multiple collisions using only a single hydrodynamic simulation. The underlying logic is the following: since event-by-event evolution of many fluctuating initial conditions is expensive but most observables are anyhow measured by summing over many events, we might as well average over the fluctuations in the initial state and evolve only a single, averaged and smooth initial profile, computing the observables from the single final state.

This, unfortunately, ignores the nonlinearities in the hydrodynamic evolution, which leads to characteristic differences between the initial and final fluctuation distributions. I found in my work specific limitations of the single-shot approach and thereby established the need for event-by-event hydrodynamics unambiguously.

It is obvious that the applicability of the single-shot approach depends on the type of observables, since by definition only observables that are direct averages have a chance to be amenable to single-shot hydrodynamics.

There are many ways to generate initial conditions for single-shot calculations. The most common choice of averaging initial conditions is to rotate the initial conditions to align their orientations Φ_n before averaging. This operation can be done for anisotropies of any given harmonic order n , and the resulting averaged profiles are different for different n . For example, aligning the second-order harmonic deformation will result in an ellipse-shaped averaged profile while aligning the third-order harmonics will result in a triangular-shaped averaged profile. More details will be given explicitly in related chapters.

The classification of hydrodynamic simulations into single-shot and event-by-event ones is independent of their classification into pure hydrodynamic and hybrid simulations: single-shot pure hydrodynamic simulations dominated half a decade ago, event-by-event pure hydrodynamic simulations are the basis of this thesis, but single-shot hybrid simulations with a hybrid code (e.g. VISHNU [19]) and event-by-event hybrid simulations will be the mainstream in the future.

The event-by-event simulations and the data collection and management processes are tedious to perform manually. To automate these processes, we have collaborated with the QCD group at Duke University to develop the iEBE package⁴ which allows one to easily set up and perform event-by-event simulations locally or on a cluster; simulated observables can be calculated from the final results using a simple one-line-command interface. The details of this package will be explained in the Appendix Sec. F.

⁴<https://bitbucket.org/qiu.24/iebe>.

Chapter 2: Comparison between event-by-event and single-shot hydrodynamic simulations

This chapter focuses on the comparison of event-by-event hydrodynamic simulations and the single-shot ones. The material is largely based on previous work reported in [20], but is supplemented by calculations for nonzero shear viscosities. (The work in [20] was based on ideal fluid dynamics.)

2.1 Definitions

In this section, we formally define the harmonic flow and eccentricity coefficients and briefly describe the models used in computing the initial entropy and energy density profiles.

2.1.1 Ellipticity

The “ellipticity” $\varepsilon \equiv \varepsilon_2$ of a given matter distribution in the transverse (x, y) plane is defined in terms of its r^2 -weighted second azimuthal moment [21, 22],

$$\mathcal{E}_2 := \varepsilon_2 e^{i2\Phi_2} = -\frac{\int dx dy r^2 e^{i2\phi} e(x, y)}{\int dx dy r^2 e(x, y)}, \quad (2.1)$$

where $x = r \cos \phi$, $y = r \sin \phi$, and \mathcal{E}_2 is the complex ellipticity. This formula assumes that the origin is the center of the distribution $e(x, y)$. In a Monte Carlo approach for generating the initial distribution $e(x, y)$ (see Sec. 2.1.4), this must be ensured by recentering each event before using Eq. (2.1). By default, we characterize in Eq. (2.1) the matter distribution by its energy density $e(x, y)$ [23]. In Sec. 2.2.2, we compare energy- and entropy-weighted ellipticities.

In Eq. (2.1), x and y are “reaction plane” (RP) coordinates: the reaction plane is the (x, z) plane, with z pointing along the beam and x pointing along the direction of the impact parameter \mathbf{b} between the colliding nuclei, while y is perpendicular to the reaction plane. Because of the minus sign on the right hand side of Eq. (2.1), the angle Φ_2 on the left hand side of Eq. (2.1) points in the direction of the minor axis of the corresponding ellipse. For an elliptically deformed Gaussian density distribution, this is the direction of the largest density gradient and thus of the largest hydrodynamic acceleration and also of the finally observed elliptic flow. The direction of this minor axis together with the beam direction z defines the participant plane (PP). It is tilted relative to the reaction plane by Φ_2 . The label “participant” is motivated by the fact that the initial energy and entropy density distributions of the collision fireball reflect (more or less directly, depending on the model for secondary particle creation) the transverse distribution of the nucleons participating in the particle production process. The ellipticity ε_2 in Eq. (2.1) is correspondingly

called “*participant eccentricity*” and also denoted as $\varepsilon_{\text{part}}$.⁵ It can be written as

$$\begin{aligned}\varepsilon_{\text{part}} &\equiv \varepsilon_2 = |\varepsilon_2 e^{i2\Phi_2}| \\ &= \frac{\sqrt{\{r^2 \cos(2\phi)\} + \{r^2 \sin(2\phi)\}}}{\{r^2\}} \\ &= \frac{\sqrt{\{y^2 - x^2\}^2 + 4\{xy\}^2}}{\{y^2 + x^2\}}.\end{aligned}\tag{2.2}$$

Here $\{\dots\} = \int dx dy (\dots) e(x, y) = \int r dr d\phi (\dots) e(r, \phi)$ defines the “event average” over the matter distribution $e(x, y)$ in a single collision event [24]. Equivalently, the participant eccentricity can be written as

$$\varepsilon_{\text{part}} = \frac{\{y^2 - x^2\}'}{\{y^2 + x^2\}'}\tag{2.3}$$

where $\{\dots\}' = \int dx dy (\dots) e'(x, y)$ indicates the average over a rotated event with energy density $e'(x, y) = e(x \cos \Phi_2 - y \sin \Phi_2, x \sin \Phi_2 + y \cos \Phi_2)$ whose minor and major axes now align with x and y .

The event-average $\{\dots\}$ is to be distinguished from the “ensemble average” $\langle \dots \rangle = \frac{1}{N} \sum_{n=1}^N \{\dots\}_n$ where N is the total number of events and $\{\dots\}_n$ is the event-average over the energy density $e_n(x, y)$ in event number n . The *average participant eccentricity* is thus defined as

$$\langle \varepsilon_{\text{part}} \rangle = \frac{1}{N} \sum_{n=1}^N (\varepsilon_{\text{part}})_n.\tag{2.4}$$

This differs from the *mean eccentricity* $\bar{\varepsilon}_{\text{part}}$ of the average (recentered and rotated by Φ_2) energy density $\bar{e}'(x, y) = \frac{1}{N} \sum_{n=1}^N e'_n(x, y)$ which can be written in the following equivalent ways:

$$\bar{\varepsilon}_{\text{part}} = \frac{\sqrt{\langle \{y^2 - x^2\} \rangle^2 + 4\langle \{xy\} \rangle^2}}{\langle \{y^2 + x^2\} \rangle} = \frac{\langle \{y^2 - x^2\}' \rangle}{\langle \{y^2 + x^2\}' \rangle}.\tag{2.5}$$

In contrast to (2.4), one here ensemble-averages over numerator and denominator separately before forming the ratio.

In event-by-event simulations, the hydrodynamic forces generate in each event an elliptic component v_2 of the anisotropic flow, which is causally related to the specific initial ellipticity $\varepsilon_{\text{part}}$ in that event. In single-shot simulations, fluctuating initial conditions are averaged into a single smooth initial distribution $\bar{e}(x, y)$, which is then evolved hydrodynamically and from which the *mean elliptic flow* \bar{v}_2 is extracted, corresponding to the *mean eccentricity* $\bar{\varepsilon}_{\text{part}}$ of that averaged source distribution. Obviously, \bar{v}_2 is a deterministic consequence of $\bar{\varepsilon}_{\text{part}}$ and does not fluctuate at all; it can not be measured experimentally. What could be measured experimentally [25, 26] is the *average elliptic flow* $\langle v_2 \rangle$ of a large ensemble of collision events. This observable is conceptually more closely related to $\langle \varepsilon_{\text{part}} \rangle$ than to $\bar{\varepsilon}_{\text{part}}$; for an exactly linear hydrodynamic response $v_2 \sim \varepsilon_{\text{part}}$, one has $\langle v_2 \rangle / \langle \varepsilon_{\text{part}} \rangle = \bar{v}_2 / \bar{\varepsilon}_{\text{part}}$ [27]. We will explore the differences between $\bar{\varepsilon}_{\text{part}}$ and $\langle \varepsilon_{\text{part}} \rangle$ and discuss consequences for the theoretically computed \bar{v}_2 as opposed to the measured $\langle v_2 \rangle$ in Secs. 2.2.1 and 2.4.

⁵Traditionally $\varepsilon_{\text{part}}$ is defined in terms of the transverse density of wounded nucleons, but since what matters for the subsequent hydrodynamic evolution is not the distribution of wounded nucleons themselves but of the matter generated by the wounded nucleons, we use the name $\varepsilon_{\text{part}}$ for the ellipticity characterizing the thermalized matter.

In addition to these “participant eccentricities”, one can also define “reaction plane eccentricities”. For a single event, the *reaction plane eccentricity* ε_{RP} is defined by

$$\varepsilon_{\text{RP}} = \frac{\{y^2 - x^2\}}{\{y^2 + x^2\}} \quad (2.6)$$

in terms of an event average over the (properly centered) energy density $e(x, y)$. The so-called *standard eccentricity* is defined as the analogous ratio of expectation values taken with a smooth average energy density $\bar{e}(x, y) = \frac{1}{N} \sum_{n=1}^N e_n(x, y)$ obtained by superimposing many events *without* rotating them from the participant to the reaction plane:

$$\varepsilon_s \equiv \bar{\varepsilon}_{\text{RP}} = \frac{\langle \{y^2 - x^2\} \rangle}{\langle \{y^2 + x^2\} \rangle}. \quad (2.7)$$

In other words, the standard eccentricity is the *mean reaction-plane eccentricity*. In contrast, the *average reaction-plane eccentricity* is defined by

$$\langle \varepsilon_{\text{RP}} \rangle = \left\langle \frac{\{y^2 - x^2\}}{\{y^2 + x^2\}} \right\rangle. \quad (2.8)$$

In real experiments, the actual measured quantities are $v_2\{\text{EP}\}$, $v_2\{2\}$, and $v_2\{4\}$ (defined below) that, even if non-flow contributions could be completely ignored, are affected by event-by-event v_2 -fluctuations and thus differ from $\langle v_2 \rangle$. $\langle v_2 \rangle$ can be reconstructed from the experimental measurements with some additional assumptions [25], which on the surface look harmless but should be further tested, and we will come back to this point in Chap. 6. Motivated by the hypothesis of linear hydrodynamic response, $v_2 \sim \varepsilon_{\text{part}}$, these v_2 measures motivate the definition of corresponding ellipticity measures [27], the 2nd and 4th order cumulants:

$$\varepsilon\{2\} = \sqrt{\langle \varepsilon_{\text{part}}^2 \rangle} \quad (2.9)$$

and

$$\varepsilon\{4\} = \left(\langle \varepsilon_{\text{part}}^2 \rangle^2 - (\langle \varepsilon_{\text{part}}^4 \rangle - \langle \varepsilon_{\text{part}}^2 \rangle^2) \right)^{1/4}. \quad (2.10)$$

Note that the last expression involves the difference of two positive-definite quantities, which itself does not need to be positive definite. If fluctuations get large, the expression under the fourth root can become negative, leaving $\varepsilon\{4\}$ undefined. We will see that this can happen in the most central and the most peripheral centrality bins.

It was shown in [28] that in the MC-Glauber model, the real and imaginary parts of the complex ellipticity defined by Eq. (2.1), with the wounded nucleon density as weight function on the right hand side, both have approximately Gaussian fluctuations, with equal widths σ_ε . If this is the case, the magnitude ε_2 of this ellipticity exhibits fluctuations of Bessel-Gaussian type⁶ [29], leading to the identity [28]

$$\varepsilon\{4\} = \langle \varepsilon_{\text{RP}} \rangle. \quad (2.11)$$

For sufficiently large average ellipticities $\langle \varepsilon_2 \rangle$ (i.e. sufficiently large impact parameters), one may hope to be able to ignore the restriction that ε_2 can never fluctuate to negative values, and correspondingly assume that ε_2 exhibits Gaussian (instead of Bessel-Gaussian) fluctuations. In this case one has [28]

$$\begin{aligned} \varepsilon\{2\}^2 &= \langle \varepsilon_{\text{part}} \rangle^2 + \sigma_\varepsilon^2, \\ \varepsilon\{4\}^2 &= \sqrt{(\langle \varepsilon_{\text{part}} \rangle^2 - \sigma_\varepsilon^2)^2 - 2\sigma_\varepsilon^4}, \end{aligned} \quad (2.12)$$

⁶This takes into account that ε_2 can never fluctuate to negative values.

from which it follows that $\langle \varepsilon_2 = \varepsilon_{\text{part}} \rangle^4$ is the arithmetic mean of $\varepsilon\{2\}^4$ and $\varepsilon\{4\}^4$:

$$\frac{\varepsilon\{2\}^4 + \varepsilon\{4\}^4}{2\langle \varepsilon_{\text{part}} \rangle^4} = 1. \quad (2.13)$$

We will use Eqs. (2.11) and (2.13) (which hold irrespective of the fluctuation width σ_ε) in Sec. 2.2.1, and their analogues for the elliptic flow v_2 in Sec. 2.4.3, to test the assumptions of Bessel-Gaussian and Gaussian fluctuations of the event-by-event ellipticity and elliptic-flow fluctuations using the Monte Carlo Glauber (MC-Glauber) and Monte Carlo fKLN (MC-KLN) models.

If the hydrodynamic response were indeed linear, $v_2 \sim \varepsilon_{\text{part}}$, and non-flow effects could be ignored, the following identities would hold:

$$\frac{\langle v_2 \rangle}{\langle \varepsilon_{\text{part}} \rangle} = \frac{\bar{v}_2}{\bar{\varepsilon}_{\text{part}}} = \frac{v_2\{2\}}{\varepsilon\{2\}} = \frac{v_2\{4\}}{\varepsilon\{4\}}. \quad (2.14)$$

Assuming linear hydrodynamic response, one can compare the theoretically computed $\langle v_2 \rangle$ with the experimentally measured $v_2\{2\}$ or $v_2\{4\}$ if one normalizes the former by $\langle \varepsilon_{\text{part}} \rangle$ and the latter by $\varepsilon\{2\}$ or $\varepsilon\{4\}$, respectively, calculated *from the same initial-state model* [30,31]. In this context, the identity $\varepsilon\{4\} = \langle \varepsilon_{\text{RP}} \rangle$ (which holds if the ellipticity fluctuations are Gaussian) becomes particularly useful because it suggests that the measured $v_2\{4\}$ can be directly compared with a single-shot hydrodynamic v_2 obtained from a smooth reaction-plane-averaged initial density of ellipticity $\langle \varepsilon_{\text{RP}} \rangle$, without any corrections for flow fluctuations. Even better, $v_2\{4\}$ can be shown to be completely free of two-particle non-flow contributions [27,28]. These arguments have been used in [9] and provide a strong motivation for us to test the underlying assumptions (Gaussian ellipticity fluctuations and linear hydrodynamic elliptic flow response) in the present work.

We close this subsection by recalling the expression for the participant plane angle of a given event (see e.g. [24])

$$\Phi_2 = \frac{1}{2} \tan^{-1} \left(\frac{2\{xy\}}{\{y^2 - x^2\}} \right) \quad (2.15)$$

and for its transverse area

$$S = \pi \sqrt{\{x^2\}' \{y^2\}'}. \quad (2.16)$$

Both expressions assume that the events are properly centered at the origin.

2.1.2 Higher order eccentricity coefficients

The definition (2.1) can be generalized to higher ($n \geq 3$) harmonic eccentricity coefficients [21,22]:

$$\mathcal{E}_n := \varepsilon_n e^{in\Phi_n} = - \frac{\int dx dy r^2 e^{in\phi} e(x, y)}{\int dx dy r^2 e(x, y)} \quad (2.17)$$

where we call \mathcal{E}_n the n -th order complex eccentricity. Alternatively one can use r^n instead of r^2 as radial weight on the right hand side [10]:

$$\mathcal{E}'_n := \varepsilon'_n e^{in\Phi'_n} = - \frac{\int dx dy r^n e^{in\phi} e(x, y)}{\int dx dy r^n e(x, y)}. \quad (2.18)$$

Still another variant uses the entropy density $s(x, y)$ instead of the energy density $e(x, y)$ as weight function:

$$\mathcal{E}_n(s) := \varepsilon_n(s) e^{in\Phi_n(s)} = -\frac{\int dx dy r^2 e^{in\phi} s(x, y)}{\int dx dy r^2 s(x, y)}, \quad (2.19)$$

$$\mathcal{E}'_n(s) := \varepsilon'_n(s) e^{in\Phi'_n(s)} = -\frac{\int dx dy r^n e^{in\phi} s(x, y)}{\int dx dy r^n s(x, y)}. \quad (2.20)$$

We note that the r^2 -weighted eccentricity coefficients ε_n fall off faster with increasing harmonic order n than the r^n -weighted eccentricities ε'_n (see section 8.1). Also, as in Eq. (2.1), the minus sign in Eqs. (2.17)-(2.20) guarantees that, for a Gaussian density distribution that has only n^{th} -order eccentricity ε_n , the angle Φ_n points in the direction of the steepest density gradient, and thus in the direction of the corresponding hydrodynamically generated n^{th} -order harmonic flow v_n (see next subsection). It can be written as $-1 = e^{-in(\pi/n)}$ and amounts to a rotation of Φ_n by π/n . For example, if the profile is square-shaped, Φ_4 points to the sides instead of its corners.

As stated before, we will use the energy density as the default weight function; in cases of possible ambiguity, we will use the notations $\varepsilon_n(e)$, $\varepsilon_n(s)$ etc. to distinguish between energy- and entropy-density-weighted eccentricity coefficients and angles. Eccentricities ε without harmonic index n denote ellipticities (i.e. in the absence of n , $n = 2$ is implied).

The coefficients ε_n and angles Φ_n define the eccentricities and angles of the matter distribution in the participant plane. We note that the participant plane angles Φ_n associated with eccentricity coefficients of different harmonic order n do not, in general, agree (see Sec. 2.3.1). We will not study higher harmonic generalizations of the reaction-plane ellipticity (2.6).

2.1.3 Harmonic flow coefficients

We characterize the final observed momentum distribution $dN/(dy p_T dp_T d\phi_p)$ by “harmonic flow coefficients” constructed in analogy to Eq. (2.17), but without the extra minus sign:

$$V_n(y, p_T) := v_n(y, p_T) e^{in\Psi_n(y, p_T)} = \frac{\int d\phi_p e^{in\phi_p} \frac{dN}{dy p_T dp_T d\phi_p}}{\frac{dN}{dy p_T dp_T}}, \quad (2.21)$$

$$V_n(y) := v_n(y) e^{in\Psi_n(y)} = \frac{\int p_T dp_T d\phi_p e^{in\phi_p} \frac{dN}{dy p_T dp_T d\phi_p}}{\frac{dN}{dy}}. \quad (2.22)$$

where V_n are the complex flows.

In boost-invariant hydrodynamics, they are rapidity-independent, so we drop the argument y and keep in mind that we should only compare with midrapidity data at $y = 0$ where the assumption of boost-invariant longitudinal expansion is most justified. The spectra $\frac{dN}{dy p_T dp_T d\phi_p}$ are computed from the hydrodynamic output with the Cooper-Frye prescription [32] along an isothermal kinetic decoupling surface whose temperature is chosen in this chapter as $T_{\text{dec}} = 140$ MeV. Equation (2.21) defines the p_T -differential harmonic flow $v_n(p_T)$ and flow angle $\Psi_n(p_T)$, whereas Eq. (2.22) gives their p_T -integrated values v_n and Ψ_n . The orientation of the n^{th} -order harmonics of the final momentum distribution defines the n^{th} -order “event plane”. Again, different harmonic flows are usually associated with differently-oriented event planes. The first three harmonic flow coefficients are the directed flow (v_1), elliptic flow (v_2), and triangular flow (v_3).

2.1.4 Initial-state models

We use Monte Carlo versions [6,9] of the Glauber [5] and fKLN [8] models to generate fluctuating initial conditions for the entropy density in 200 A GeV Au+Au collisions. For the MC-Glauber model we assume a two-component (soft+hard) model with a small hard fraction ($\delta = 0.14$ [6]); we

also use a Woods-Saxon profile for the distribution of nucleon centers whose radius and surface-thickness parameters have been corrected for the finite nucleon size [6]. The resulting entropy density profile is normalized to the final charged-hadron multiplicity density dN_{ch}/dy in central collisions; after this normalization, the centrality dependence of the initial entropy production is fixed by the model (MC-Glauber or MC-KLN). To convert the initial entropy density to energy density, we use the equation of state (EOS) s95p-PCE which matches Lattice QCD data at high temperatures to a chemically frozen hadron resonance gas at low temperatures [11, 12], using $T_{\text{chem}} = 165$ MeV as chemical freeze-out temperature.

In the following we compute harmonic eccentricity and flow coefficients as functions of impact parameter b and collision centrality. The centrality classes are defined in terms of percentages of the total inelastic cross section, calculated from the distribution of the number of wounded nucleons $dN_{\text{event}}/dN_{\text{part}}$ in the optical Glauber model (i.e. without accounting for fluctuations in N_{part} at given impact parameter). Each centrality class is thus characterized by a range of impact parameters $b_{\text{min}} < b < b_{\text{max}}$ and an average value \bar{b} , together with a mean number of wounded nucleons \bar{N}_{part} . They are listed in Table B.1 [6].

2.1.5 Averaging procedures for the initial profiles

In this section, we will compare results obtained from event-by-event hydrodynamic simulations with traditional single-shot hydrodynamic simulations, where one first averages over many fluctuating initial profiles to obtain a smooth average profile, then evolves this smooth profile hydrodynamically. The question addressed in this comparison is to what extent the average harmonic-flow coefficients from event-by-event hydrodynamics can (or cannot) be faithfully represented by the harmonic-flow coefficients extracted (at much lower numerical expense) from the hydrodynamic evolution of an “average event”.

Taking the initial density profiles from the Monte Carlo generator and superimposing them directly without additional manipulations (such that the impact parameter directions for each collision are aligned) generates a “reaction-plane averaged” profile with ellipticity $\bar{\varepsilon}_{\text{RP}}$ (Eq. (2.7)). After recentering each event to the origin of the x - y -plane, we can compute event by event the reaction and participant plane ellipticities (Eqs. (2.6) and (2.2,2.3)) and evaluate their ensemble averages (2.8) and (2.4), respectively. To generate a smooth average profile with ellipticity $\bar{\varepsilon}_{\text{part}}$ (Eq. 2.5), we rotate each recentered event by the angle $\Phi_2(e)$ ($\Phi_2(s)$) if we want to determine the eccentricity of the average energy (entropy) density. For the calculation of entropy-weighted average eccentricities, we perform any ensemble average first and convert the result to energy density later; in this case all events are rotated by their $\Phi_2(s)$ angles. For energy-weighted ensemble averages, we convert s to e in each event first, rotate by $\Phi_2(e)$, and perform the ensemble average last. Other sequences or mixtures of these steps are technically possible but physically not meaningful. Note that the processes of computing the energy density from the entropy density via the EOS and of averaging the event profiles do not commute: The energy density obtained via the EOS from the ensemble-averaged entropy density profile is not the same as the ensemble-averaged energy density where the EOS is used in each event to convert s to e .

2.2 Eccentricities

2.2.1 Centrality dependence of different ellipticities

Fig. 2.1 shows a comparison between the different ellipticities defined in Sec. 2.1.1 as functions of the impact parameter b in panels (a) and (b) and as functions of collision centrality (as defined in Sec 2.1.4) in panels (c) and (d). For panels (a) and (b), we generated 10,000 initial profiles for each impact parameter (except for $b = 0, 1,$ and 2 fm for which we generated 30,000 events each), and the smooth initial conditions are averaged from them; for panels (c) and (d) we generated and averaged over 10,000 profiles for each centrality bin. Within the centrality bins, the impact parameters were sampled between b_{min} and b_{max} with $b db$ weight. Compared to panels (a) and

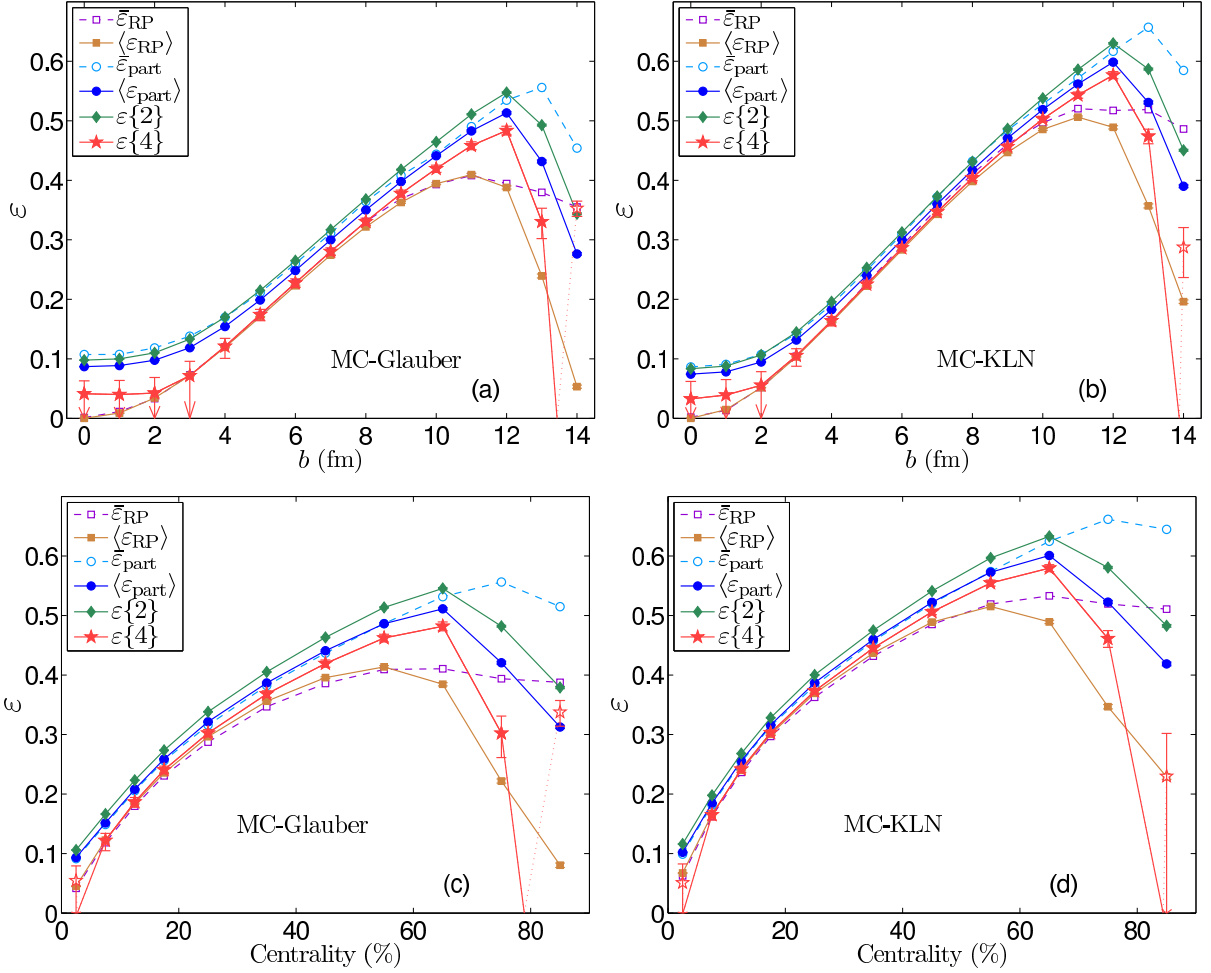


Figure 2.1: Different ellipticities as a function of impact parameter (top row) or collision centrality (bottom row), for the MC-Glauber (panels (a) and (c)) and the MC-KLN model (panels (b) and (d)). Panels (a,b) show e -weighted, panels (c,d) show s -weighted ellipticities. (See Fig. 2.4 below for a direct comparison between e - and s -weighted eccentricities.) Open stars indicate negative values for $\varepsilon\{4\}$ ⁴. Taken from [20].

(b), this leads to additional ellipticity fluctuations related to the fluctuating impact parameter, whereas in Fig. 2.1a,b, only N_{part} fluctuations at fixed b contribute.

As discussed in Sec. 2.1.1, Eq. (2.10), $\varepsilon\{4\}$ ⁴ can become negative when fluctuations grow large. Whenever this happens, we replace $\varepsilon\{4\}$ by $\sqrt[4]{|\varepsilon\{4\}^4|}$ and indicate this by an open star in Fig. 2.1 (connected by dotted lines to other points in the graph). One sees that $\varepsilon\{4\}$ ⁴ has a tendency to turn negative in the most peripheral collisions. In very central collisions, $\varepsilon\{4\}$ ⁴ becomes very small, with central values that can have either sign depending on whether we keep the impact parameter fixed (Figs. 2.1a,b) or average over events with different impact parameters in a given centrality bin (see the 0–5% centrality values in Figs. 2.1c,d). Statistical errors are large, however, and within errors $\varepsilon\{4\}$ ⁴ is compatible with zero for impact parameters $b < 3$ fm, i.e. in the most central (0–5% centrality) collisions. We indicate this by open-ended error bars for $\sqrt[4]{|\varepsilon\{4\}^4|}$, pointing from its upper limit all the way to zero.

Comparing panels (a,c) for the MC-Glauber model with panels (b,d) for the MC-KLN model we see great similarities in shape, but systematic differences in magnitude of the ellipticities. The ratio of the MC-KLN and MC-Glauber ellipticities is shown in Fig. 2.2. Except for the most

central and most peripheral collisions, the MC-KLN ellipticities exceed the MC-Glauber ones by an approximately constant factor of around 1.2. Please note the difference in the ratios for the reaction plane and participant eccentricities at small b . (The point for $\bar{\varepsilon}_{\text{RP}}$ at $b = 1$ fm is obtained from a ratio of very small numbers and probably not statistically robust – we had only 30,000 events to determine the ensemble-averaged density profile.) For the $\varepsilon\{4\}$ ratio we dropped all points where the statistical error for $\varepsilon\{4\}$ extended into the region of negative values for either the MC-Glauber or MC-KLN model.

Figure 2.1 shows that, for central and mid-peripheral collisions, the ensemble-averaged participant and reaction plane eccentricities $\langle\varepsilon_{\text{part}}\rangle$ and $\langle\varepsilon_{\text{RP}}\rangle$ agree very well with the mean eccentricities $\bar{\varepsilon}_{\text{part}}$ and $\bar{\varepsilon}_{\text{RP}}$ of the corresponding ensemble-averaged profiles. For strongly peripheral collisions ($b \gtrsim 10$ fm), however, the average of the ratio (Eqs. (2.3,2.4,2.8)) differs strongly from the ratio of averages (Eqs. (2.5,2.7)), indicating strong event-by-event fluctuations. We note that in very peripheral collisions, the average event ellipticity drops quickly with increasing b while the ellipticity of the average profile remains large; single-shot hydrodynamic calculations based on a smooth average initial profile thus overestimate the effective initial source ellipticity and produce more elliptic flow than expected from event-by-event hydrodynamic evolution of individual peripheral events. Still, as first emphasized in [31], the calculated v_2 from single-shot hydrodynamics decreases steeply at large collision centralities [9, 36, 71], due to the decreasing fireball lifetime, which contrasts with the initially reported experimentally observed behaviour [33, 34], but agrees

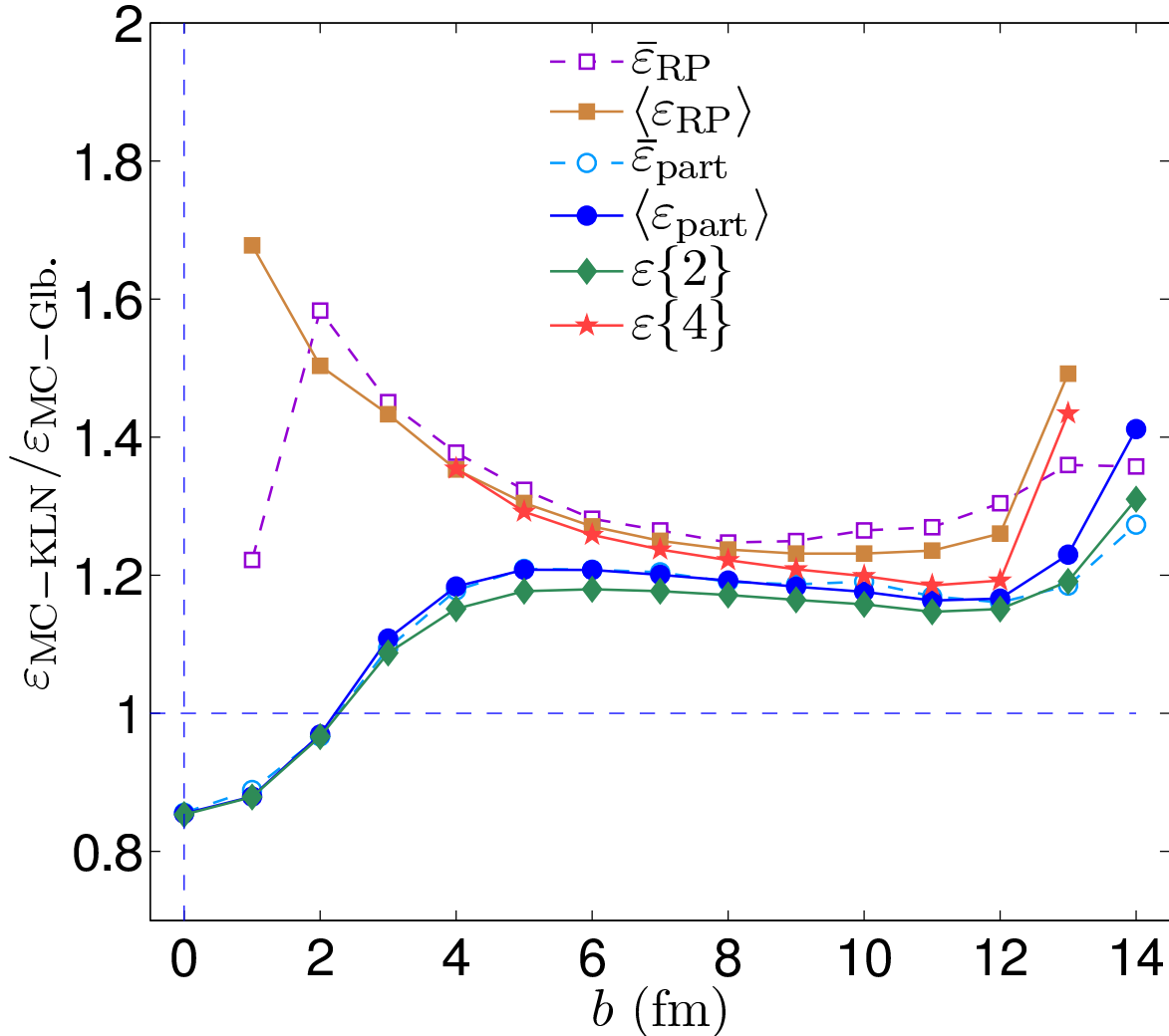


Figure 2.2: Impact-parameter dependence of the ratio of ellipticities obtained from the MC-KLN and MC-Glauber models as shown in Figs. 2.1a,b. Taken from [20].

qualitatively with a reanalysis [35] where non-flow effects have been largely eliminated and/or corrected for. We do point out that our Monte-Carlo simulations do not include fluctuations in the amount of entropy generated per nucleon-nucleon collision [10] which have important effects on the ellipticities in very peripheral collisions.

Comparing the curves for $\langle \varepsilon_{\text{part}} \rangle$, $\varepsilon\{2\}$, and $\varepsilon\{4\}$ in Fig. 2.1, we see that (as is manifest in the Gaussian model analysis in Eq. (2.12)) $\varepsilon\{2\}$ receives a positive and $\varepsilon\{4\}$ receives a negative contribution from event-by-event ellipticity fluctuations. In Fig. 2.3 we check, as a function of impact parameter, the validity of the identities (2.11) and (2.13), which follow from Bessel-

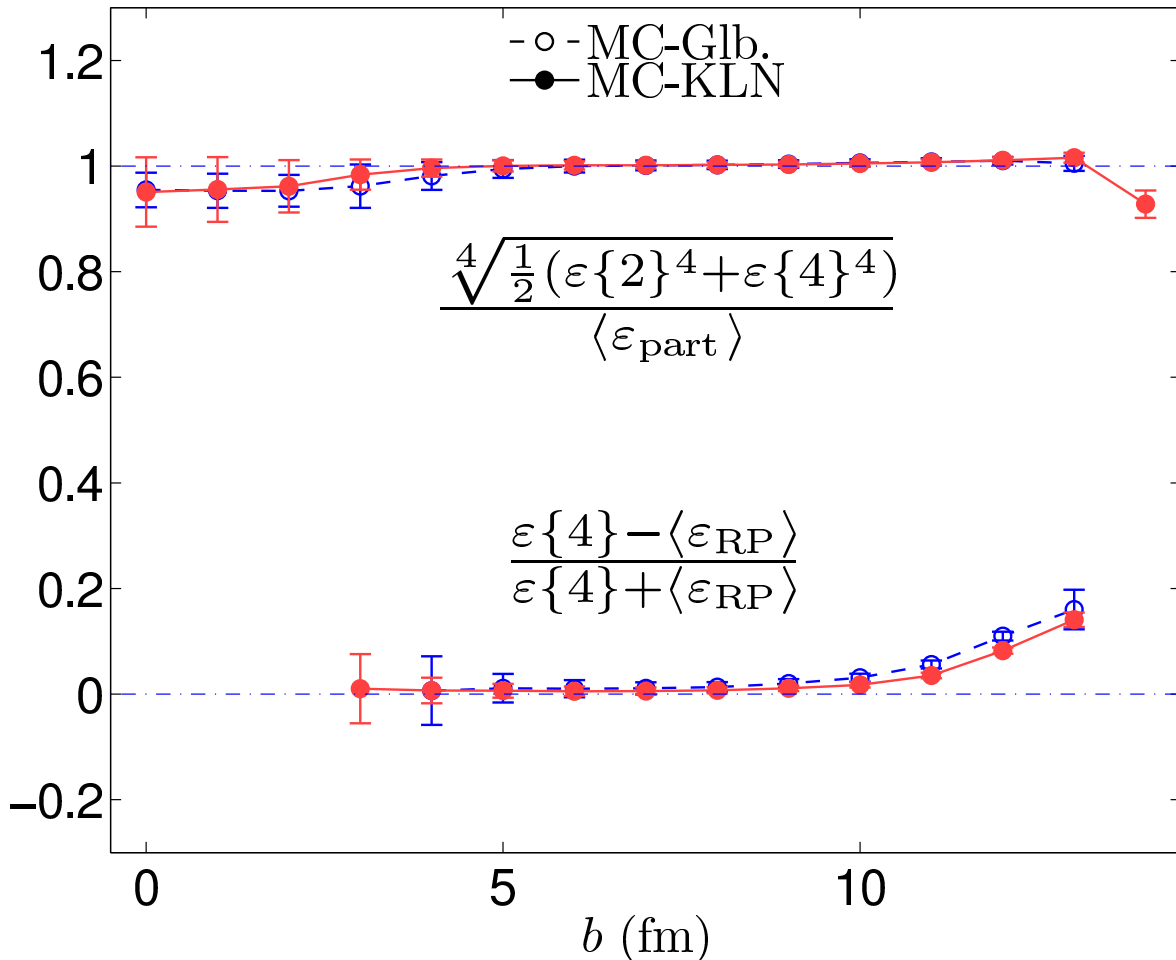


Figure 2.3: Checks of the assumption of Gaussian and Bessel-Gaussian fluctuations for $\varepsilon_{\text{part}}$ (see text for discussion). Taken from [20].

Gaussian and Gaussian $\varepsilon_{\text{part}}$ distributions, respectively. We see that both hold with good accuracy in the mid-central range ($b \lesssim 10$ fm for Eq. (2.11), $5 \lesssim b \lesssim 11$ fm for Eq. (2.13)) but break down in the most peripheral collisions. Both the Gaussian and Bessel-Gaussian hypotheses work slightly better for the MC-KLN than for the MC-Glauber model. Consistent with the analysis in Ref. [28], the Gaussian fluctuation hypothesis for $\varepsilon_{\text{part}}$ breaks down at small impact parameters, whereas (as theoretically expected [28]) the Bessel-Gaussian hypothesis appears to continue to hold, although we are unable to make this statement with statistical confidence. (For the ratio $(\varepsilon\{4\} - \langle \varepsilon_{\text{RP}} \rangle) / (\varepsilon\{4\} + \langle \varepsilon_{\text{RP}} \rangle)$, we again dropped all points for which the error band for $\varepsilon\{4\}$ reaches into negative territory.)

The assumption of Gaussian fluctuations of the real and imaginary parts of the complex ellipticity (2.1) is often used to argue that the average reaction-plane ellipticity $\langle \varepsilon_{\text{RP}} \rangle$ can serve as a

proxy for $\varepsilon\{4\}$ (see Eq. (2.11)), and that therefore reaction-plane averaged initial density profiles can be used in single-shot hydrodynamics (which ignores event-by-event fluctuations) to simulate the experimentally measured $v_2\{4\}$ values. Fig. 2.1 and the bottom curves in Fig. 2.3 show that $v_2\{4\}$ values obtained from single-shot hydrodynamic simulations with reaction-plane averaged initial conditions [9, 36] should not be trusted quantitatively for centralities $> 40\%$.

To summarize this subsection, all the simplifying assumptions that allow one to focus attention on the three quantities $\langle\varepsilon_{\text{part}}\rangle$, $\varepsilon\{2\}$, and $\varepsilon\{4\}$ only (by substituting $\langle\varepsilon_{\text{part}}\rangle$ for $\bar{\varepsilon}_{\text{part}}$ and $\varepsilon\{4\}$ for $\bar{\varepsilon}_{\text{RP}}$ or $\langle\varepsilon_{\text{RP}}\rangle$) hold well for central to mid-central collisions ($\leq 40\%$ centrality) but break down for peripheral collisions. For $> 40\%$ centrality there exists no substitute for event-by-event hydrodynamics if one aims for quantitative precision in the comparison with experimental elliptic flow data, since the latter are strongly affected by non-Gaussian event-by-event fluctuations at those centralities.

2.2.2 Ellipticities with different weight functions

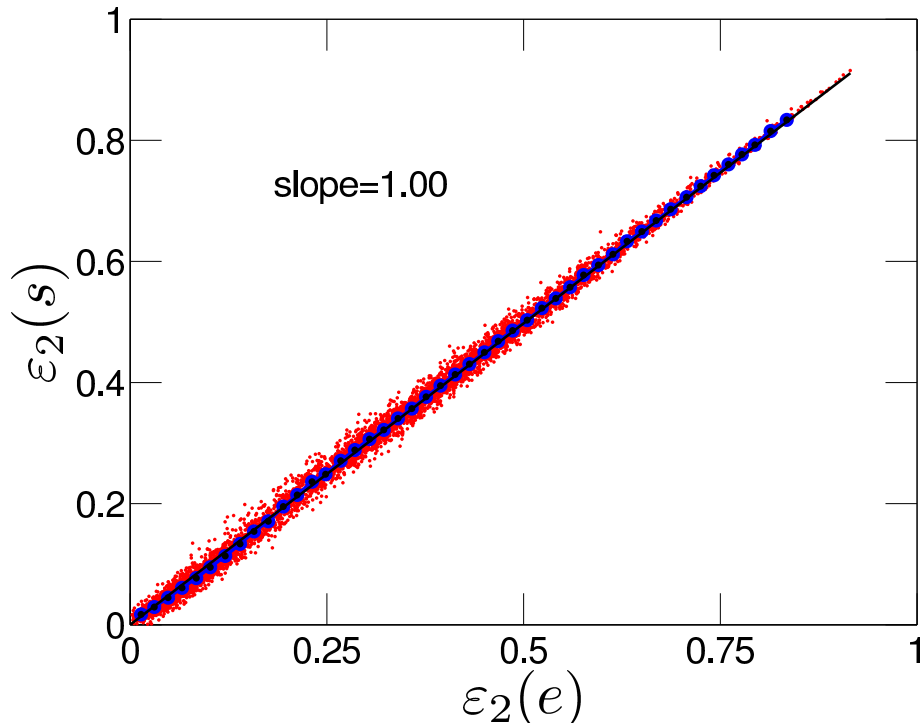


Figure 2.4: $\varepsilon_{\text{part}}(e)$ vs. $\varepsilon_{\text{part}}(s)$ for 6000 initial profiles from the MC-KLN model (1000 each for $b = 0$ fm, 0–5%, 15–20%, 20–30%, 30–40%, and 50–60% centrality). Taken from [20].

Figure 2.4 shows a comparison between the energy- and entropy-weighted ellipticities of the initial profiles generated with the MC-KLN model on an event-by-event basis. The scatter plot is based on 6000 events, 1000 each for $b = 0$ and for the following finite-width centrality bins: 0–5%, 15–20%, 20–30%, 30–40%, and 50–60%. This is not a realistic mix in the experimental sense, but permits us to explore the full range from very small to very large event ellipticities. The blue dots in Fig. 2.4 represent bin averages, and the solid black line is a linear fit through the origin. The fitted slope is 1.00, the scatter plot is seen to be tightly clustered around this fitted line, and only at small ellipticities $\varepsilon_2 < 20\%$ the e -weighted values are seen to be slightly larger on average than their s -weighted counterparts (see also Fig. 2.5a below).

2.2.3 Higher order harmonics

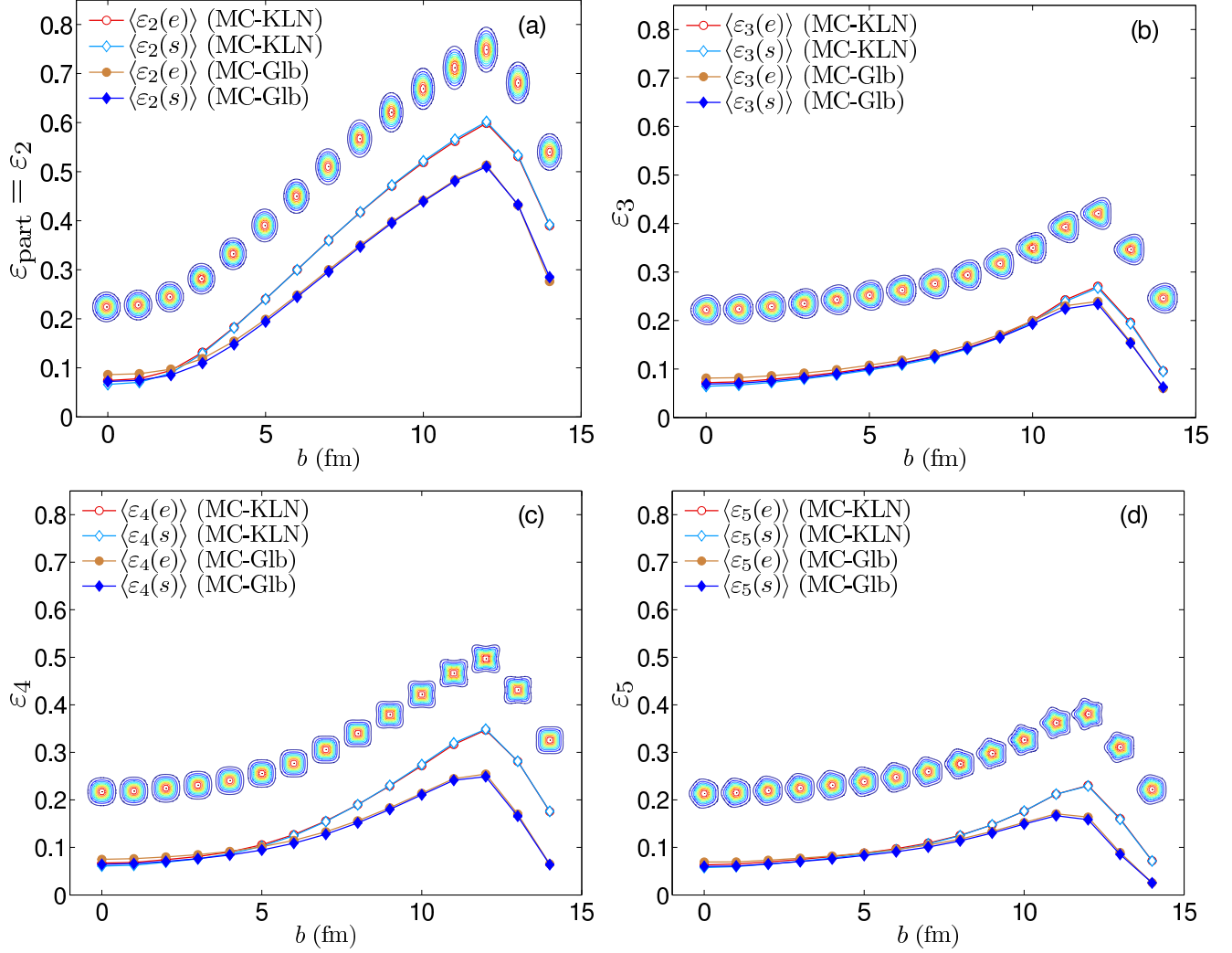


Figure 2.5: Harmonic eccentricity coefficients $\varepsilon_2 = \varepsilon_{\text{part}}$ (a), ε_3 (b), ε_4 (c) and ε_5 (d) as functions of impact parameter, calculated from the MC-Glauber (filled symbols, solid lines) and MC-KLN models (open symbols, dashed lines), using the energy density (circles) or entropy density (triangles) as weight function. The contour plots illustrate deformed Gaussian profiles $e(r, \phi) = e_0 \exp \left[-\frac{r^2}{2\rho^2} (1 + \varepsilon_n \cos(n\phi)) \right]$, with eccentricity $\varepsilon_n(e)$ taken from the MC-KLN model at the corresponding impact parameter. Taken from [20].

In Figs. 2.5a-d we compare the centrality dependences of the ensemble-averaged second to fifth harmonic eccentricity coefficients (energy- and entropy-weighted) from the MC-Glauber and MC-KLN models. The contour plots give a visual impression of the degree of deformation corresponding to the (larger) MC-KLN eccentricities, assuming (for illustration) the absence of any other eccentricity coefficients than the one shown in the particular panel.

First, one observes very little difference between the eccentricities of the entropy and energy density profiles, except for very central collisions ($b \lesssim 5$ fm for the MC-Glauber, $b \lesssim 3$ fm for the MC-KLN model) where the energy-weighted eccentricities lie systematically somewhat above the entropy-weighted ones (for all orders n studied here). The difference between s - and e -weighted eccentricities at small b is bigger in the MC-Glauber than in the MC-KLN model.

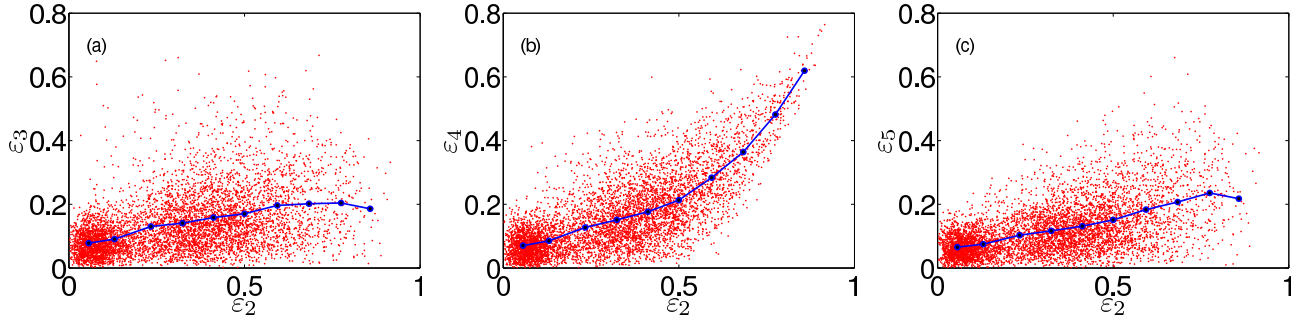


Figure 2.6: Scatter plots illustrating the event-by-event correlation of ε_3 (a), ε_4 (b), and ε_5 (c) with the fireball ellipticity $\varepsilon_2 = \varepsilon_{\text{part}}$, for the same set of 6000 event profiles analyzed in Fig. 2.4. The blue dots connected by a line indicate ε_2 -bin averages to guide the eye. Taken from [20].

Next, one notes the significantly larger ellipticities and quadrangularities of the MC-KLN distributions compared to those from the MC-Glauber model for all but the most central collisions. These are driven by geometry, i.e. by the almond-shaped deformation of the nuclear overlap zone in non-central collisions, which in the KLN-model is more eccentric than in the Glauber model. The third and fifth order harmonics, which are entirely due to fluctuations (and whose associated angles Φ_n are therefore completely uncorrelated to the reaction plane – see Ref. [10] and discussion below), show remarkably similar eccentricity values in the two initialization models, except for the most peripheral events. Comparing the viscous suppression of elliptic and triangular flow thus allow to distinguish experimentally between the MC-Glauber and MC-KLN models (see Chap. 3).

Third, in central collisions all four eccentricity coefficients are roughly of the same size. In peripheral collisions, the fluctuation-dominated eccentricity coefficients (ε_3 and ε_5) are generically smaller than the geometry-dominated ones (ε_2 , but also to some extent ε_4).⁷ This is less obvious when one defines the higher order eccentricities with r^n instead of r^2 weight [10], which tends to increase the values of the higher harmonics in peripheral collisions.

Even with “only” an r^2 weight, ε_4 and ε_5 are seen to become large enough around $b \sim 10\text{--}13$ fm that, if collective acceleration happens predominantly in the directions of steepest descent of the density profile, one has to expect cross-currents in the developing anisotropic flow patterns. These can lead to destructive interference and a correspondingly reduced efficiency of converting n^{th} -order eccentricities ε_n into n^{th} -order harmonic flows v_n [22]. In realistic situations this issue is exacerbated by the simultaneous presence of *several* large eccentricity components ε_n , which is expected to lead to a strongly nondiagonal and probably nonlinear response matrix relating v_n to ε_n [10]. This will be discussed in Sec. 2.3, and more in Sec. 8.4.

2.2.4 Eccentricity correlations

It is reasonable to ask whether and how the different harmonic eccentricity coefficients ε_n are correlated with each other. Figure 2.6 shows scatter plots of the correlations between $\varepsilon_{3,4,5}$ and the ellipticity ε_2 , which, for large ε_2 values, is dominated by geometric overlap effects. We note that, according to the definition (2.17), all eccentricity coefficients are positive definite, $\varepsilon_n \geq 0$. Keeping this in mind, Figs. 2.6a,c show that ε_3 and ε_5 are uncorrelated with the fireball ellipticity; the slight growth of $\langle \varepsilon_{3,5} \rangle$ with increasing ε_2 is related to the growth of the variances of their distributions in more peripheral collisions.

In contrast, the quadrangularity ε_4 shows a clear positive correlation with the ellipticity, see Fig. 2.6b. It is of geometrical origin: it reflects the football or almond shape of the overlap

⁷We checked that the centrality dependences of the ratios $\varepsilon_n/\varepsilon_2$ agree qualitatively, but not quantitatively, with Fig. 3 in Ref. [37]. We suspect that the differences, which are larger for the MC-Glauber than the MC-KLN model, are due to somewhat different Woods-Saxon and (in the MC-Glauber case) fluctuation-size parameters used in Ref. [37].

zone in non-central collisions which is a little sharper than a pure $\cos(2\phi)$ deformation. This is corroborated by the behavior of angle Φ_4 shown in Fig. 2.7a below, which, on average, points 45° relative to Φ_2 (which again points in x -direction). This means that the quadrangular component of the initial fireball definition is oriented like a diamond, with its corners on the x and y axes. Superimposing it on a pure $\cos(2\phi)$ deformation leads to a somewhat sharper shape of the density distribution.

2.3 Event-by-event hydrodynamics and flow fluctuations

In this section we analyze the results from event-by-event hydrodynamic evolution of the fluctuating initial profiles studied in the previous section. We focus on the anisotropic flow coefficients v_n , their relationship to the initial eccentricity coefficients ε_n , and the correlation between the n^{th} -order flow angles Ψ_n and the corresponding n^{th} -order participant-plane angles Φ_n associated with ε_n .

2.3.1 Correlations between participant plane, event plane, and reaction plane

One of the key characteristics of fluid dynamics is its ability to transform initial geometric deformation into a deformation of the final momentum distribution, via collective flow. This happens through spatially anisotropic hydrodynamic forces (i.e. pressure gradients) which cause anisotropic acceleration of the fluid. As a result, correlations between participant and event planes are expected: The angle Φ_n points in the direction of the largest pressure gradient associated with the n^{th} harmonic component of the spatial deformation of the initial density distribution, while Ψ_n points into the direction where the n^{th} harmonic component of the final collective flow is largest. Without interference between harmonics of different order, we would thus expect Φ_n and Ψ_n to point, on average and up to event-by-event fluctuations, in the same direction.

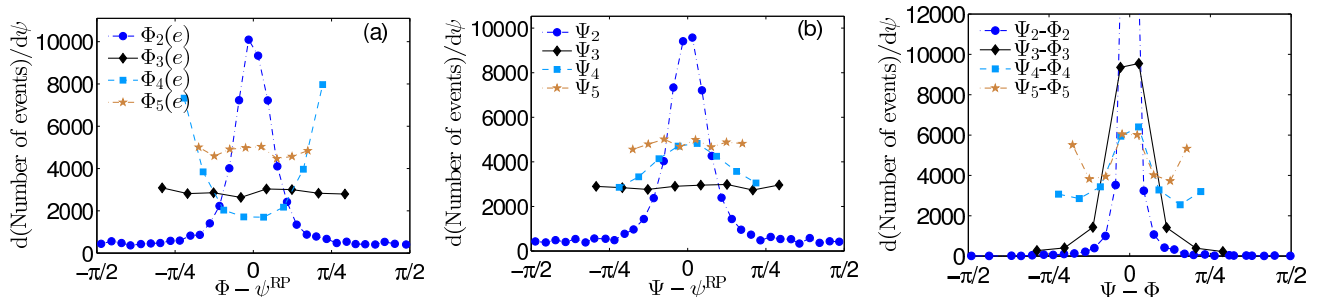


Figure 2.7: Event-by-event correlation of the participant plane (a) and event plane (b) angles with the reaction plane (ψ^{RP}), as well as the correlation between participant and event plane angles (c) for different harmonic eccentricity and flow coefficients. The same 6000 events as in Fig. 2.4 were analyzed after hydrodynamic evolution with $\eta/s = 0$ (ideal fluid). Taken from [20].

In Figs. 2.7a,b we show the distribution of participant- and event-plane angles associated with the n^{th} -order eccentricities and harmonic flows, relative to the x - z reaction plane. The analysis uses the same 6000 events as before, and evolves them with ideal fluid dynamics ($\eta/s = 0$). In panel (a) we see that $\Phi_{3,5}$ are completely uncorrelated with the reaction plane [10], as expected from the fact that the corresponding eccentricities are entirely fluctuation-driven, without contribution from the collision geometry. Panel (b) shows that the same holds true for $\Psi_{3,5}$, which is (at least superficially) consistent with the expectation that v_3 is mostly or entirely driven by ε_3 , and v_5 by

ε_5 . We will revisit this below. Φ_2 and Ψ_2 are strongly correlated with the reaction plane ψ^{RP} , at least for this mixed-centrality set of events. This is expected since, for non-central collisions, ε_2 is mostly controlled by the almond-shaped overlap geometry, and v_2 is mostly a collective flow response to this geometric deformation; event-by-event fluctuations contribute to ε_2 (and thus v_2), but in general do not dominate them.

The behavior of Φ_4 in Fig. 2.7a is interesting because it is on average strongly “anti-correlated” with the reaction plane, in the sense that it points (on average) at 45° relative to the x -axis. The geometric reason for this has already been discussed above in subsection 2.2.4. On the other hand, Fig. 2.7b shows that the angle Ψ_4 points on average *into* the reaction plane. This correlation of Ψ_4 with the reaction plane is somewhat weaker than the anti-correlation of Φ_4 with that plane seen in panel (a). Still, it suggests that quadrangular flow v_4 does not, on average, develop predominantly in the direction of the steepest pressure gradient associated with ε_4 , but in the direction of steepest ε_2 -induced pressure gradient.

Figure 2.7c, however, in which we analyze directly the correlation between the event and participant plane angles, paints a more subtle picture. It shows, surprisingly, a correlation peak at zero relative angle between Ψ_4 and Φ_4 , whereas the above discussion should have led us to expect a correlation peak at 45° . The resolution of this paradox is presented in the next subsection: the relative importance of geometric and fluctuation-induced contributions to ε_n , v_n , and their associated angles changes with collision centrality, with geometry playing a relatively larger role in peripheral collisions. One should therefore look at the angle correlations as a function of collision centrality. One finds that the correlation function peaks in Figs. 2.7a,b for the 4th-order angles relative to the reaction plane are almost entirely due to geometric effects in peripheral collisions, while in central collisions both Φ_4 and Ψ_4 are fluctuation-dominated and thus essentially uncorrelated with the reaction plane. On the other hand, precisely because in central collisions geometric effects such as geometrically driven elliptic flow do not dominate the hydrodynamic response to the fluctuation-driven higher-order eccentricities, Ψ_4 and Φ_4 remain relatively strongly correlated in near-central collisions. This is the reason for the peak at 0° for $n=4$ in Fig. 2.7c. (A hint of the “anti-correlation” at 45° is still visible in Fig. 2.7c, and it would be stronger if we had not (for unrelated reasons) strongly oversampled central collisions in our mixed-centrality sample.)

We close this discussion with the following additional observations about Fig. 2.7c: (i) The second-order participant and event planes are much more strongly correlated with each other than either one of them is with the reaction plane. This shows that even in very central collisions, where the source ellipticity is mostly fluctuation-driven and its angle therefore only weakly correlated with the reaction plane, elliptic flow develops event-by-event in the direction of the short axis of the ellipsoid. (ii) Even though the angles associated with ε_3 and v_3 are uncorrelated with the reaction plane (Figs. 2.7a,b), they are strongly correlated with each other. This indicates that v_3 is mostly driven by ε_3 , especially in the more central collisions, with relatively little interference from other harmonics. (iii) The 5th-order event and participant plane angles show correlation peaks both at 0 and $\pi/5$. As we will see in the following subsection, the former results from central and the latter from peripheral collisions. The peak at $\pi/5$ indicates significant cross-feeding between modes with $n=2, 3$, and 5.

2.3.2 Centrality dependence of event and participant plane correlations

Figure 2.8 looks at the correlation between the n^{th} -order EP and PP angles at different collision centralities. This generalizes a similar analysis for $n=2$ in Ref. [38] to higher harmonics. Plotted are the distributions of the absolute value of the difference between the two angles in the main graph and the root mean square of this distribution (i.e. the width around zero of the correlation) in the inset, as a function of collision centrality. Panel (a) shows that the second-order participant and event planes are strongly correlated at all collision centralities. This demonstrates that elliptic flow is generated almost exclusively by the source ellipticity. The variance of the correlation is

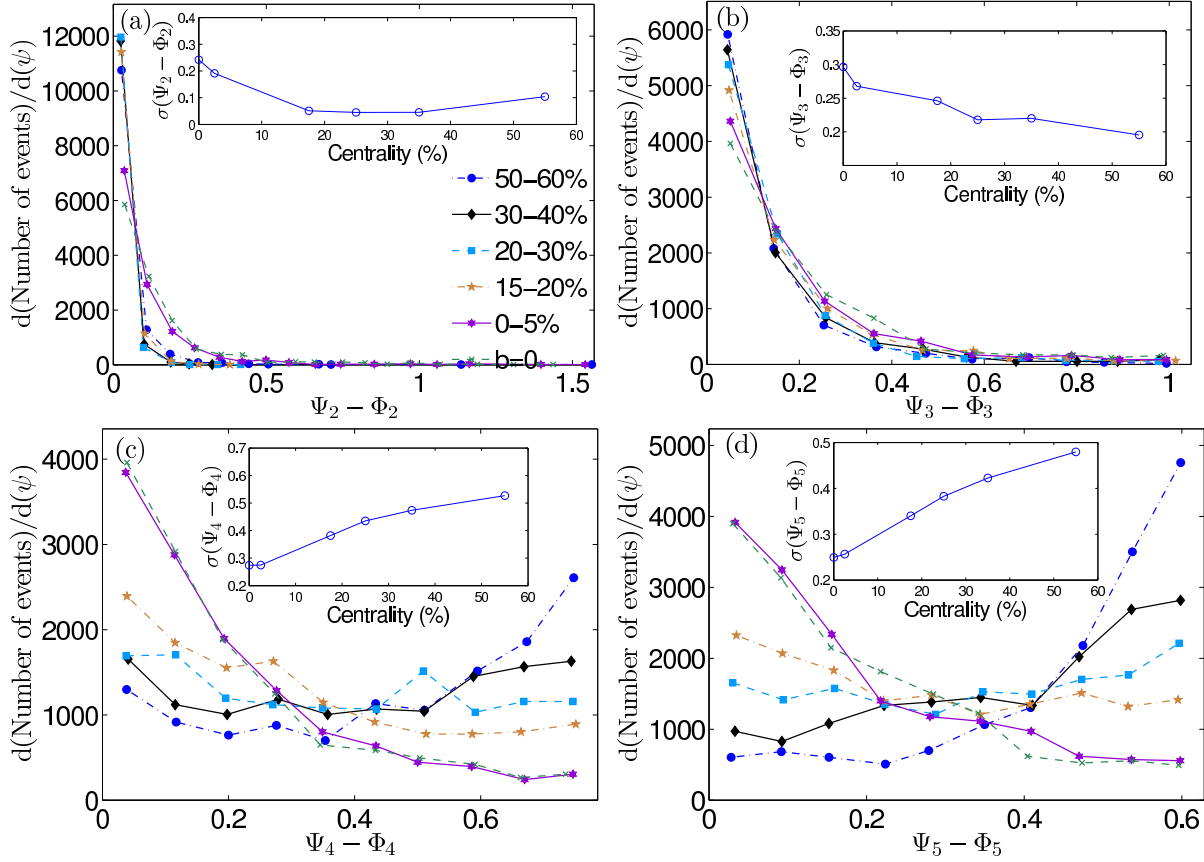


Figure 2.8: Event-by-event correlation between the absolute values of the event plane (Ψ_n) and participant plane (Φ_n) angles for the harmonics of order 2–5 (panels (a)-(d)), for events in different centrality classes as indicated in the legend. (The same set of MC-KLN events as in Fig. 2.4 was used.) The insets show the centrality dependence of the widths of these correlations around zero. All fireballs are evolved with $\eta/s = 0$ (ideal fluid hydrodynamics). Taken from [20].

~ 0.05 rad in the mid-central range (15-40% centrality) and increases in very central and very peripheral collisions due to growing ellipticity fluctuations.

A similar correlation exists for the 3rd-order participant and event planes, at all collision centralities, but with a larger variance of order $0.2 - 0.3$ rad (depending on centrality). The relatively strong correlation suggests that ε_3 is the dominant driver for v_3 [21].

For the 4th- and 5th-order participant and event planes the situation is complicated, as seen in panels (c) and (d). The planes are correlated with each other (i.e. the distributions peak at zero difference angle) in central collisions, become essentially uncorrelated in mid-central collisions and anti-correlated (i.e. peaked at a difference angle of π/n , $n=4,5$) in peripheral collisions. The anti-correlation in peripheral collisions indicates strong mode-mixing, driven by the large ellipticity ε_2 and strong elliptic flow v_2 at large impact parameters, which generates v_4 and v_5 contributions by coupling to lower harmonics, as described in the previous subsection. For v_4 in particular, a strong $\cos(2\phi)$ component in the collective flow velocity generates a v_4 of the final momentum distribution, without any need for nonzero ε_4 . At large impact parameters, ε_2 -induced quadrupolar flow from the initial elliptic deformation of the overlap region thus dominates over any contribution from initial quadrangular deformation. However, there are additional mode-coupling effects arising from the nonlinear hydrodynamic evolution. As we will see in Chap. 4, the flow angles Ψ_n reflected in the measured momentum distribution closely correlate with the angles of the hydrodynamic flow anisotropies, so there is a nonlinear contribution to the 4th harmonic of the collective-flow velocity. In near-central collisions, on the other hand, where all ε_n stem mostly from shape fluctuations, $v_{4,5}$ are dominantly driven by $\varepsilon_{4,5}$.

To study viscous effects we show Fig. 2.9, which is similar to Fig. 2.8, but using simulated data from both ideal and viscous ($\eta/s = 0.2$) hydrodynamic simulations, starting from identical initial conditions. Each impact parameter group has 1000 simulated events.

It can be seen that nonzero viscosity manifests itself in two distinct ways: (1) For flows that are not strongly affected by mode couplings, for example $v_{2,3}$ at any b , and v_4 at $b = 0$, the effect of shear viscosity is to reduce the fluctuations in $|\Psi_n - \Phi_n|$. Viscosity suppresses the randomness in the flow profile caused by the existence of hotspots in the initial density distribution, thus helping to build v_n up from ε_n and to align Ψ_n with Φ_n . (2) Viscosity also increases the strength of mode-coupling between different harmonics. In those cases where v_n receives large contributions from ε_m , $m \neq n$ (e.g. v_4 at large b , v_5 in general), the fluctuations in the angle difference $|\Psi_n - \Phi_n|$ receive multiple contributions, with each contributor possibly contributing positively or negatively, resulting in hard-to-predict net effects.

2.3.3 Harmonic flows and their corresponding initial eccentricities: nonlinear hydrodynamic response

It is often assumed that the harmonic flows v_n respond linearly to the eccentricities ε_n , at least as long as the latter are small. This assumption receives support from hydrodynamic simulations [22] as long as one probes deformed initial profiles with only a single non-vanishing harmonic eccentricity coefficient. In Fig. 2.10, we investigate the validity of this assumption with fluctuating MC-KLN events which feature nonzero ε_n values for all n .

Figure 2.10a generally provides support for the assumption of a linear dependence of the elliptic flow v_2 on initial ellipticity ε_2 , with two important caveats:

- (i) At small and large ellipticities, v_2 deviates upward from a best-fit line through the origin, indicating additional contributors to the elliptic flow. Indeed, for zero ellipticity $\varepsilon_2 = 0$ we find a nonzero average $\langle v_2 \rangle$. These are events with typically large nonzero values for eccentricities of higher harmonic order, which generate elliptic flow through mode-mixing (e.g. between ε_3 and ε_5). We see that this happens at all centralities, even for $b = 0$, due to event-by-event fluctuations of the eccentricity coefficients.
- (ii) The slope of the curve $\langle v_2 \rangle(\varepsilon_2)$ decreases in very peripheral collisions, indicating destructive interference via mode-mixing from other harmonics in the hydrodynamic evolution of the small and highly fluctuating fireballs created at large impact parameters.

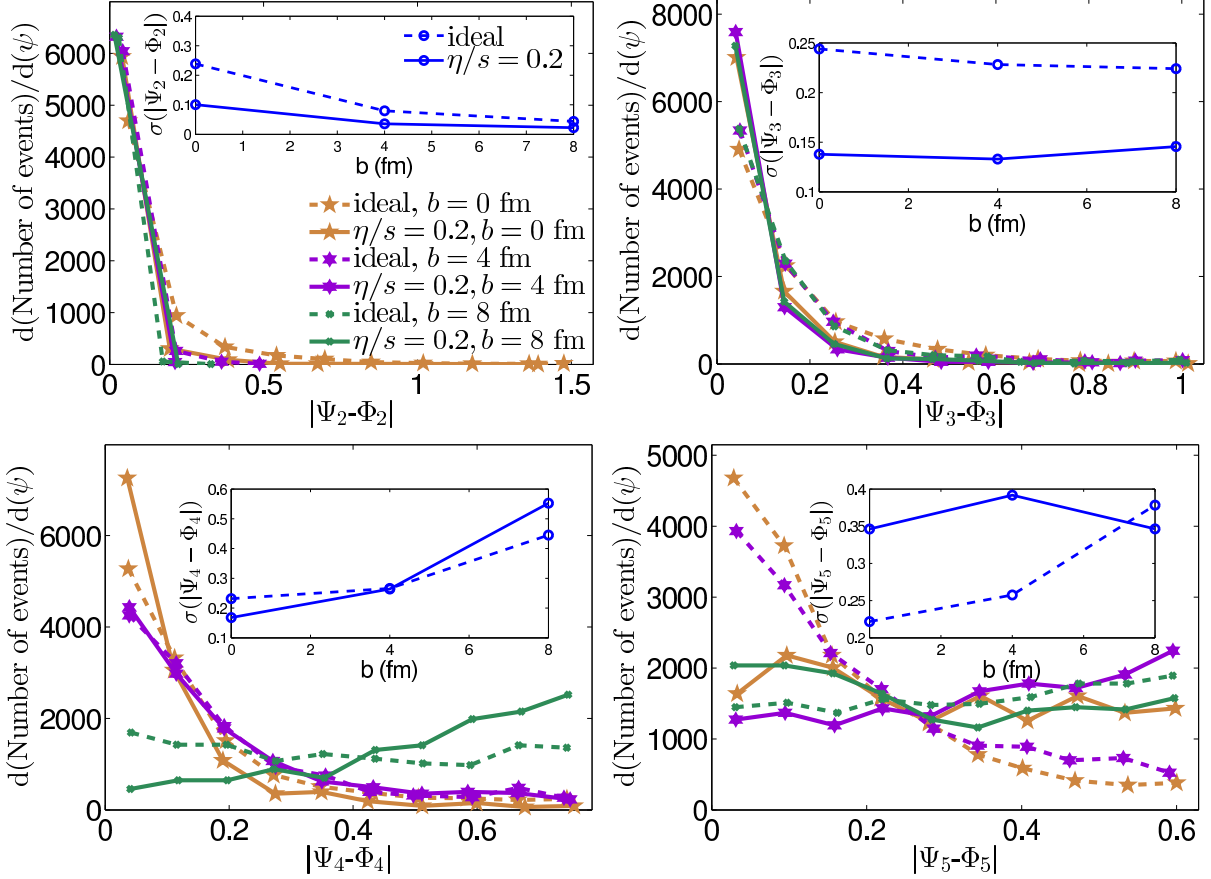


Figure 2.9: Event-by-event correlation between the absolute values of the event plane (Ψ_n) and participant plane (Φ_n) angles for the harmonics of order 2 – 5. 1000 events are simulated at each impact parameter, using both ideal hydrodynamics and viscous ones with $\eta/s = 0.2$, and grouped in eccentricity bins of sufficient width to have reasonable statistics in each bin.

The ε_3 -dependence of triangular flow $\langle v_3 \rangle$, shown in Fig. 2.10b, shows a qualitatively similar story, but the deviations from linear response are stronger, with significant nonzero triangular flow in events with zero initial triangularity, especially for larger impact parameters.

For $\langle v_4 \rangle$ and $\langle v_5 \rangle$, shown in Figs. 2.10c and 2.10d, mode-mixing effects are very strong, and a linear response of v_n to ε_n ($n = 4, 5$) can no longer be claimed. This is quite different from the results in [22], where v_4 was studied for a source that had only ε_4 deformation: in this case $v_4(\varepsilon_4)$ was found to be approximately linear for small ε_4 , with a downward bend at larger ε_4 values due to negative interference from cross-currents for sources with large quadranguliarities. (This approximately linear dependence survived in the p_T -integrated v_4 , even though it was noticed in a related study [39] that, for mid-central collisions, the differential quadrangular flow $v_4(p_T)$ at high p_T appears to be mostly determined by the elliptic deformation of the hydrodynamic flow profile generated by ε_2 .) Our study shows that it is unlikely that the anisotropic flow resulting from highly inhomogeneous initial profiles with nonzero eccentricity coefficients of all harmonic orders can be obtained by some sort of linear superposition of flows generated from sources with only a single nonzero harmonic eccentricity coefficient, as suggested in [40]. (We will discuss this topic in more detail in Chap. 4.) The hydrodynamic response $\{v_n\}$ to a set of initial eccentricity coefficients $\{\varepsilon_n\}$ is not only nondiagonal, but also (via mode-mixing) nonlinear, and there is no suitable single-shot substitute for event-by-event hydrodynamic evolution of fluctuating initial conditions.

The effect of viscosity can be studied using Fig. 2.11, which contains curves corresponding to both ideal and viscous ($\eta/s = 0.2$) hydrodynamic evolutions. In contrast to Fig. 2.10, the events

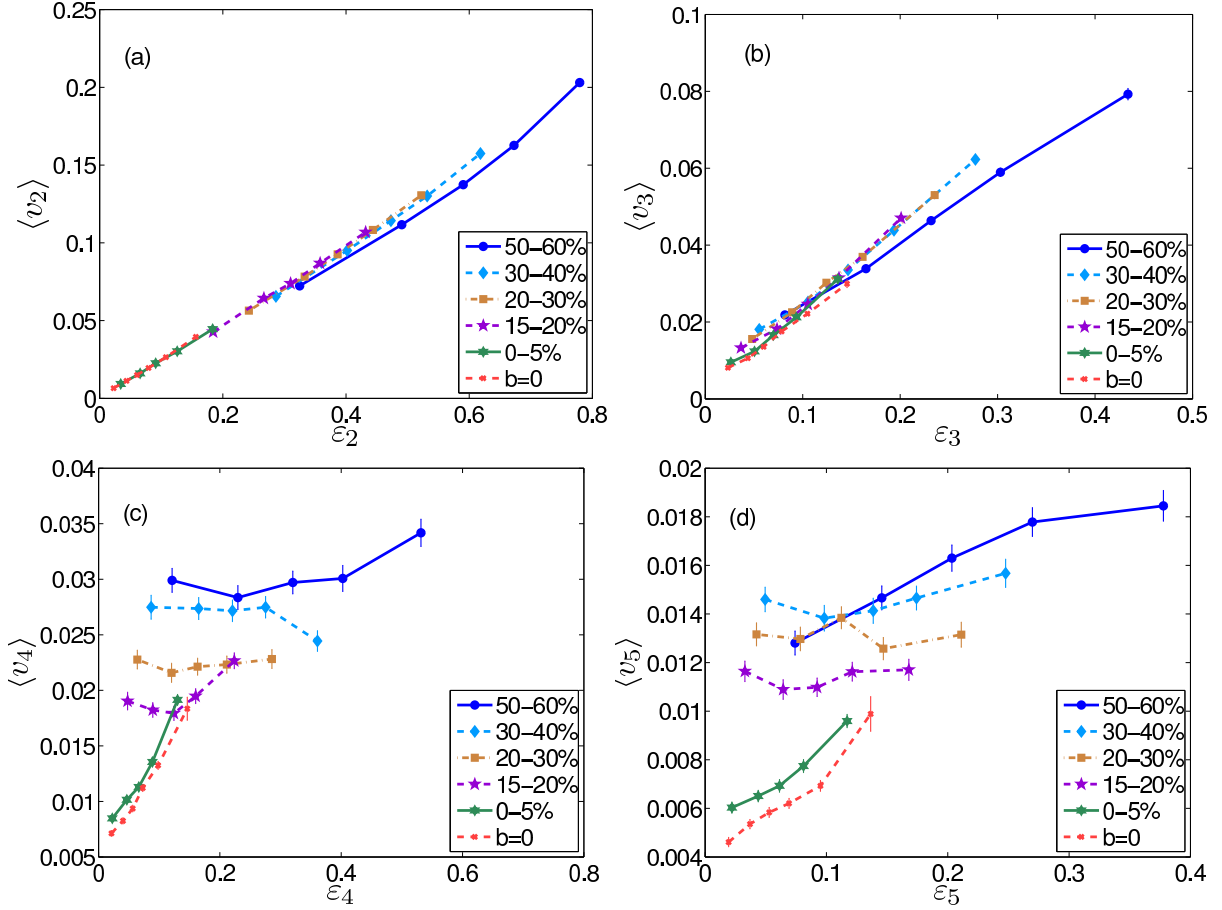


Figure 2.10: $\langle v_n \rangle(\varepsilon_n)$ for $n=2, 3, 4, 5$ (panels (a)-(d)), using ideal fluid dynamics. As in Fig. 2.4, each centrality class contains 1000 MC-KLN events, grouped in eccentricity bins of sufficient width to have reasonable statistics in each bin. Taken from [20].

are grouped directly by impact parameters. Again 1000 events are simulated for each impact parameter.

First it is clearly seen that the existence of viscosity reduces the response of v_n from ε_n , and this effect increases with increasing n . For elliptic and triangular flow, viscosity suppresses the conversion coefficient $v_{2,3}/\varepsilon_{2,3}$ more strongly for larger impact parameters, indicating larger viscous effects in more peripheral collisions. For $v_{4,5}$ viscosity wipes out the monotonicity of its dependence on $\varepsilon_{4,5}$ in central and semi-central collisions, meaning that it receives larger contributions from other sources than $\varepsilon_{4,5}$ — this is another way to state that viscosity increases nonlinear mode-coupling effects.

We note that in both ideal and viscous cases, nonlinear mode-mixing effects appear to be minimal for the elliptic and triangular flow (Figs. 2.10a,b, Figs. 2.11a,b). v_2 and v_3 remain therefore the best candidates for an extraction of the fluid’s viscosity, by studying (with quantitative precision) the fluid’s efficiency in converting initial spatial deformations into final momentum anisotropies and anisotropic flows. We will further elaborate on this theme in the next section.

2.4 Single-shot versus event-by-event hydrodynamics

We now discuss the effects of event-by-event initial-state fluctuations on the finally observed pion and proton p_T -spectra and anisotropic flow, comparing traditional single-shot hydrodynamic evolution of an appropriately constructed smooth average initial profile with event-by-event evolution of fluctuating initial conditions (with an ensemble average taken at the end). Since the

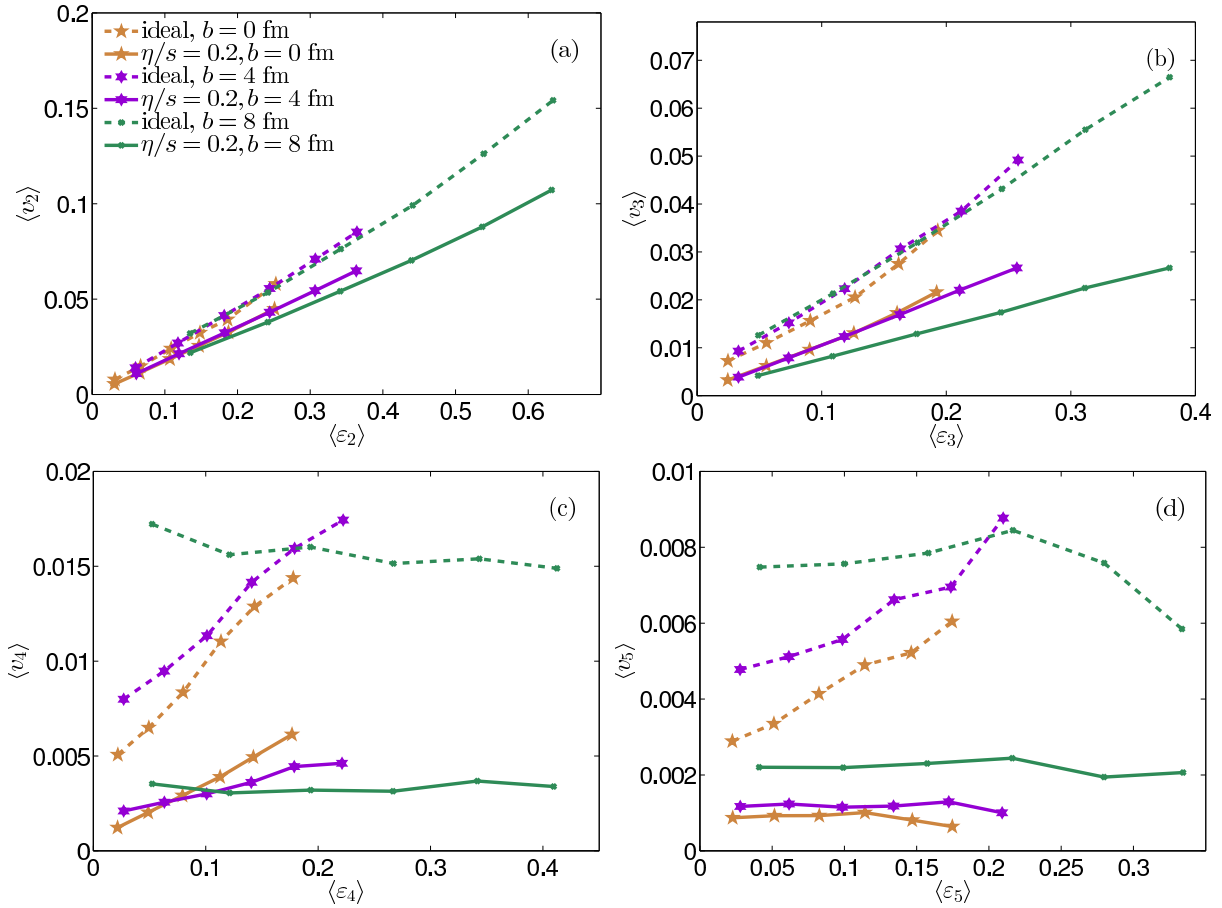


Figure 2.11: $\langle v_n \rangle(\langle \varepsilon_n \rangle)$ for $n = 2, 3, 4, 5$ (panels (a)-(d)). 1000 initial conditions are used in simulations for each impact parameter, using both ideal hydrodynamics and viscous runs with $\eta/s = 0.2$. Results are grouped in eccentricity bins of sufficient width to have reasonable statistics in each bin.

calculation of resonance decay feeddown corrections is computationally expensive but not expected to cause qualitative changes, we here concentrate on directly emitted (“thermal”) pions and protons. For the graphs shown in this section, we generated for each impact parameter 1000 fluctuating events from the MC-KLN model and propagated them either event-by-event or via a single-shot hydrodynamic simulation run down to a decoupling temperature of 140 MeV.

2.4.1 Transverse momentum spectra

In [41], Chatterjee *et al.* showed that thermal photon spectra from exploding heavy-ion collision fireballs with fluctuating initial conditions which were hydrodynamically evolved event-by-event are significantly harder than those obtained from single-shot hydrodynamic evolution of the corresponding ensemble-averaged smoother initial profiles. The authors of [41] attributed this effect to the existence of “hot spots” in the fluctuating initial conditions that radiate photons at a higher-than-average temperature. Figure 2.12 shows that the same hardening effect occurs in the pion and proton spectra even though these strongly interacting hadrons are emitted only at freeze-out, with the same decoupling temperature assumed in both types of evolution.⁸ This

⁸A similar effect was also seen in [38], whose authors further pointed out that the strength of this “hardening effect” depends on the fluctuation size parameter in the initial conditions (i.e. the area over which the entropy produced in a nucleon-nucleon collision is distributed).

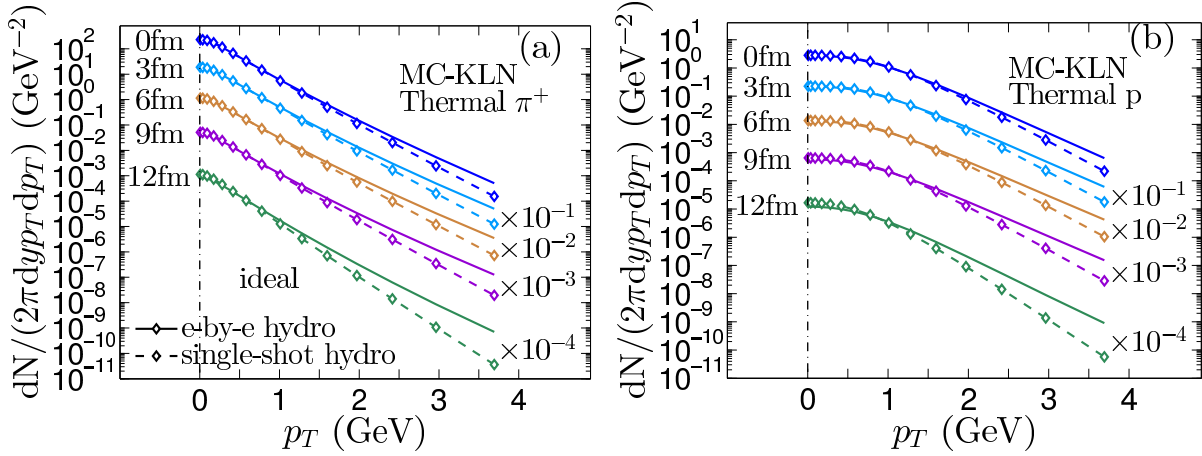


Figure 2.12: Transverse momentum spectra for directly emitted π^+ (left) and protons (right) from event-by-event (solid lines) and single-shot (dashed lines) ideal hydrodynamic simulations with MC-KLN initial conditions, for 200 A GeV Au+Au collisions at six selected impact parameters.

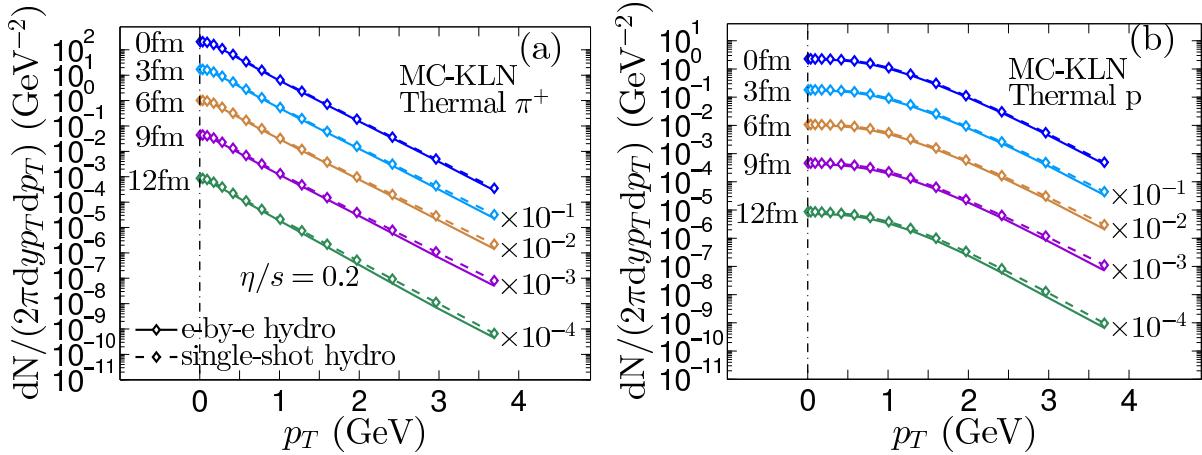


Figure 2.13: Same as Fig. 2.12, but for viscous hydrodynamics with $\eta/s = 0.2$.

proves that the effect is due to stronger radial flow in the event-by-event evolved fluctuating fireballs, driven by the stronger than average pressure gradients associated with the “hot spots” (i.e. over-dense regions) in the initial profile. The importance of initial-state fluctuation effects on the final p_T -spectra becomes stronger in peripheral collisions, where the initial fireballs are smaller and “hot spots” have a relatively larger influence. If stronger radial flow is the explanation of the fluctuation-driven hardening of the pion and proton spectra observed in Fig. 2.12, it is probably also an important contributor to the hardening of the photon spectra noted in Ref. [41], at least for low p_T (i.e. in the hydrodynamic regime).

Nonzero viscosity softens the hardening effect, as shown in Fig. 2.13. It is clearly seen that the difference in p_T -spectra between the two types of simulations is reduced in the viscous case. We attribute this reduction to the fact that the nonzero viscosity tends to quickly wash out density inhomogeneities from hot spots by dissipation, thereby reducing the difference between fluctuating and smooth initial conditions in the later stages of the expansion.

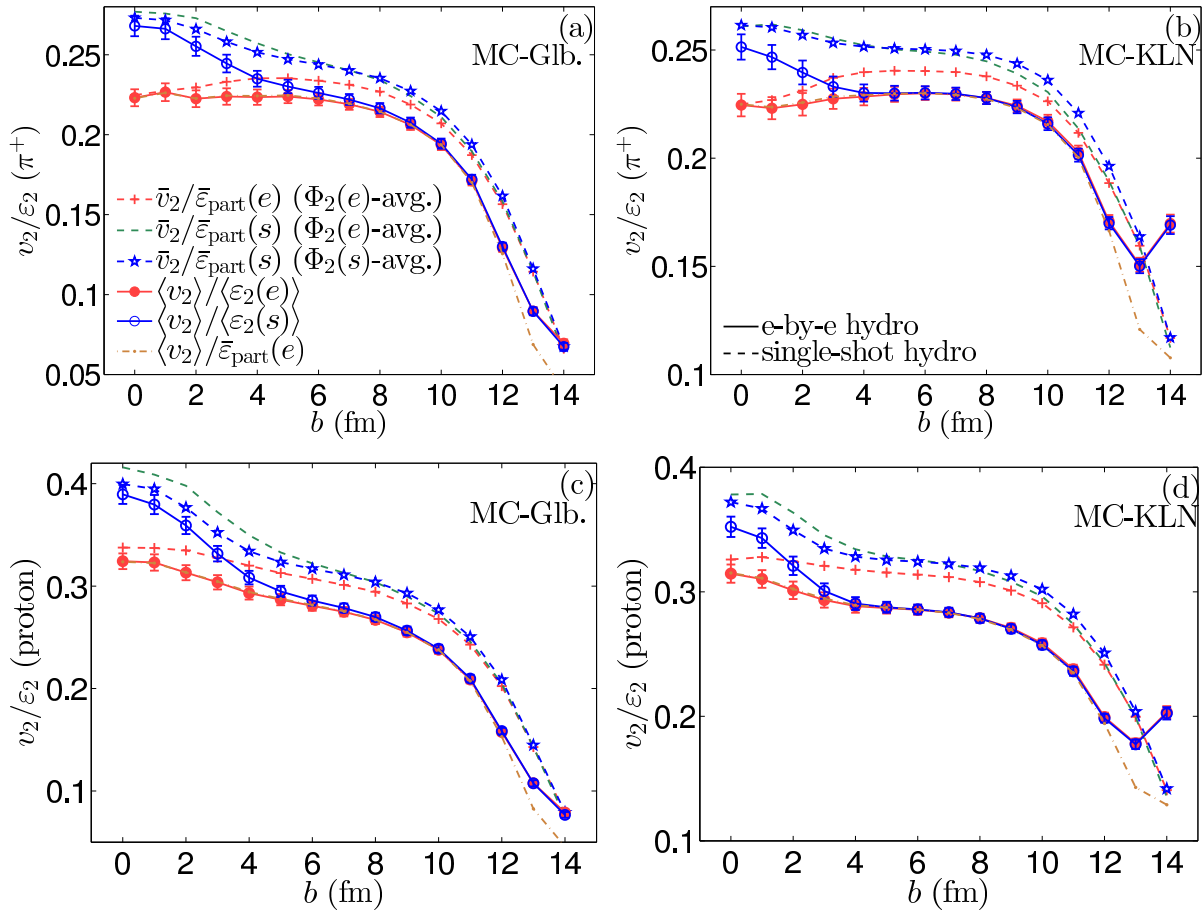


Figure 2.14: Eccentricity-scaled elliptic flow v_2/ε_2 as function of impact parameter, for pions (panels (a,b)) and protons (panels (c,d)), from the ideal fluid dynamic evolution of initial MC-Glauber (a,c) and MC-KLN (b,d) density profiles. Solid (dashed) lines correspond to event-by-event (single-shot) hydrodynamics. See text for discussion. Taken from [20].

2.4.2 Elliptic and triangular flow

In Figures 2.14 and 2.15, we compare the eccentricity-scaled elliptic and triangular flows, v_2/ε_2 and v_3/ε_3 , for pions and protons as a function of impact parameter, from single-shot (dashed lines) and event-by-event hydrodynamics (solid lines). These ratios represent the efficiency of the fluid for converting initial spatial deformations into final-state momentum anisotropies. This conversion efficiency is affected (to be more precise, reduced) by shear viscosity, so these ratios form the basis of many analyses that aim to extract this transport coefficient from experimental heavy-ion data.

For event-by-event hydrodynamics, we show two curves, using either the entropy- (blue open circles) or the energy-weighted (red solid circles) average eccentricities to normalize the average final flow $\langle v_n \rangle$. For the ellipticity (Fig. 2.14), this choice is seen to make a difference only in rather central collisions ($b < 4$ fm), but for the triangularity, the differences are significant out to average impact parameters probed in minimum-bias samples, $b \lesssim 8$ fm. As stated earlier, we prefer the energy-weighted eccentricities (solid circles) as deformation measures because energy density and pressure are closely related through the EOS, and it is the pressure gradients (and their anisotropies) that drive the collective flow (and its anisotropies).

For the single-shot hydrodynamic simulations, a question arises as to how exactly one should construct the ensemble-averaged smooth initial profile which is then evolved hydrodynamically. We have explored three reasonable procedures (variations of which have been used in the literature) and show them as dashed lines in Figs. 2.14 and 2.15. For the *lines labeled by stars*, we rotate

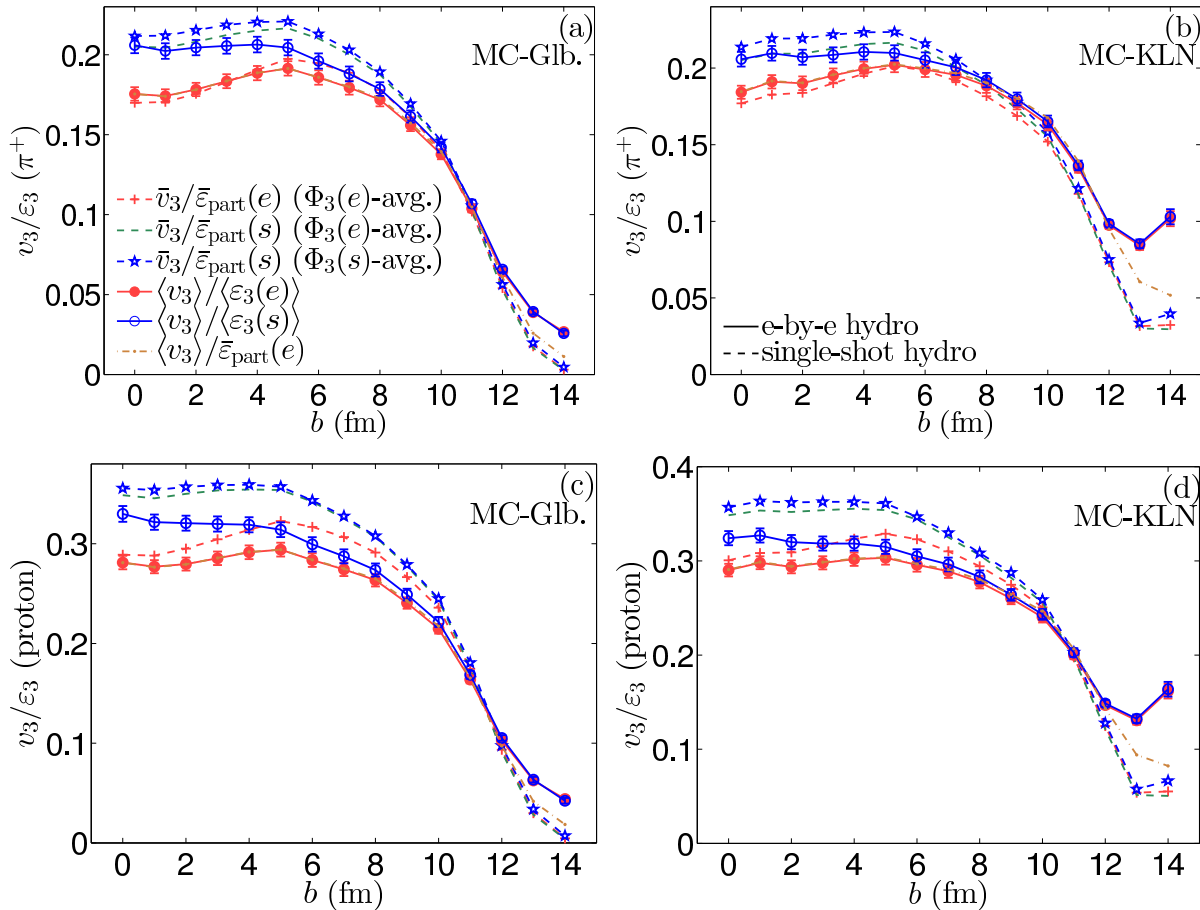


Figure 2.15: Same as Fig. 2.14, but for the eccentricity-scaled triangular flow v_3/ε_3 . Taken from [20].

the entropy density for each fluctuating event by the corresponding entropy-weighted participant-plane angle $\Phi_n(s)$ ($n=2,3$, see Eq. (2.19)),⁹ then average the rotated entropy profiles, compute the eccentricity $\bar{\varepsilon}_n(s)$ of the resulting average entropy profile and convert it to energy density using the EOS for input into the hydrodynamic code. For the *lines labeled by crosses*, we rotate the energy density for each fluctuating event (obtained from the EOS) by the corresponding energy-weighted participant-plane angle $\Phi_n(e)$ (see Eqs. (2.1,2.2)), compute the averaged rotated energy density profile and its eccentricity $\bar{\varepsilon}_n(e)$, and use it directly as hydrodynamic input. For the *dashed lines without symbols*, finally, the averaged initial energy density (and therefore the final \bar{v}_n) are exactly the same as for the lines with crosses, but the final \bar{v}_n is scaled by the entropy-weighted (rather than energy-weighted) eccentricity of the averaged initial profile, where the entropy density is obtained from the smooth averaged energy density via the EOS.

The differences between the different dashed lines illustrate the uncertainties associated with the choice of averaging procedure for the initial state. Keeping in mind that a 20% reduction in v_2/ε_2 corresponds (very roughly) to an increase of η/s by an additive term $1/4\pi$ [30], one sees that these differences are not negligible if one aims for quantitative precision in the extraction of the specific shear viscosity. Comparing the three dashed lines, we see that it doesn't make much difference whether we use the s -weighted or e -weighted participant-plane angles to rotate the events before superimposing them (the dashed lines without symbols and with stars are all very close to each other), but that in the more central collisions we obtain significantly different values for the conversion efficiencies $\bar{v}_n/\bar{\varepsilon}_n$ if we normalize by e - or s -weighted mean eccentricities.

⁹Note that for computation of \bar{v}_3 , we rotate the events by a different angle before averaging than for \bar{v}_2 , i.e. \bar{v}_3 and \bar{v}_2 are obtained from two different single-shot hydrodynamic runs, starting from different averaged initial-energy-density profiles.

Even though they look similar in Fig. 2.5a, at small impact parameters $\bar{\varepsilon}_{\text{part}}(e)$ and $\langle\varepsilon_2(e)\rangle$ are larger than $\bar{\varepsilon}_{\text{part}}(s)$ and $\langle\varepsilon_2(s)\rangle$, respectively, and this is the main reason why the red and blue lines in Fig. 2.14 diverge at small b , for both event-by-event (solid lines) and single-shot hydrodynamics (dashed lines).

An apples-to-apples comparison between event-by-event and single-shot hydrodynamics (and between theory and experimental data) therefore must ensure that the same (or at least conceptually compatible) eccentricities are used to normalize the anisotropic flow coefficients that are to be compared. In Figs. 2.14, 2.15, we should therefore compare blue solid with blue dashed or red solid with red dashed lines, but not curves of different colors.

Even this is not good enough if one wants to accurately assess the relative space-to-momentum anisotropy conversion efficiency in single-shot and event-by-event hydrodynamics: in the single-shot hydro curves, we use $\bar{\varepsilon}_{\text{part}}$ to normalize the final elliptic flow, whereas the event-by-event hydro results were normalized with $\langle\varepsilon_2\rangle \equiv \langle\varepsilon_{\text{part}}\rangle$. While each of these eccentricity measures makes perfect sense in its own context, they differ at large impact parameters, $\bar{\varepsilon}_{\text{part}}$ being larger (see Figs. 2.1a,b). To avoid this problem, we have added in Figs. 2.14 and 2.15 an additional “mixed ratio” (dash-dotted purple line), which normalizes the ensemble-averaged anisotropic flow $\langle v_n \rangle$ ($n=2,3$) from event-by-event hydrodynamics (used in the ratio $\langle v_n \rangle / \langle \varepsilon_n \rangle$ denoted by solid lines with solid red circles) by the mean e -weighted eccentricity $\bar{\varepsilon}_n$ from single-shot hydrodynamics (used in the ratio $\bar{v}_n / \bar{\varepsilon}_n$ denoted by dashed lines with crosses). This dot-dashed purple line agrees almost perfectly with the solid red line with circles over most of the impact parameter range, except for peripheral collisions with $b \gtrsim 10$ fm where $\bar{\varepsilon}_n$ and $\langle \varepsilon_n \rangle$ begin to diverge. The red dashed lines with crosses and purple dash-dotted lines show the anisotropic flows from single-shot and event-by-event hydrodynamics normalized by the *same* eccentricity measure characterizing the fluctuating event sample. Their comparison allows an unambiguous assessment of the different efficiencies of single-shot and event-by-event hydrodynamics in converting initial eccentricities to final momentum anisotropies. Their ratio is shown in Fig. 2.16.

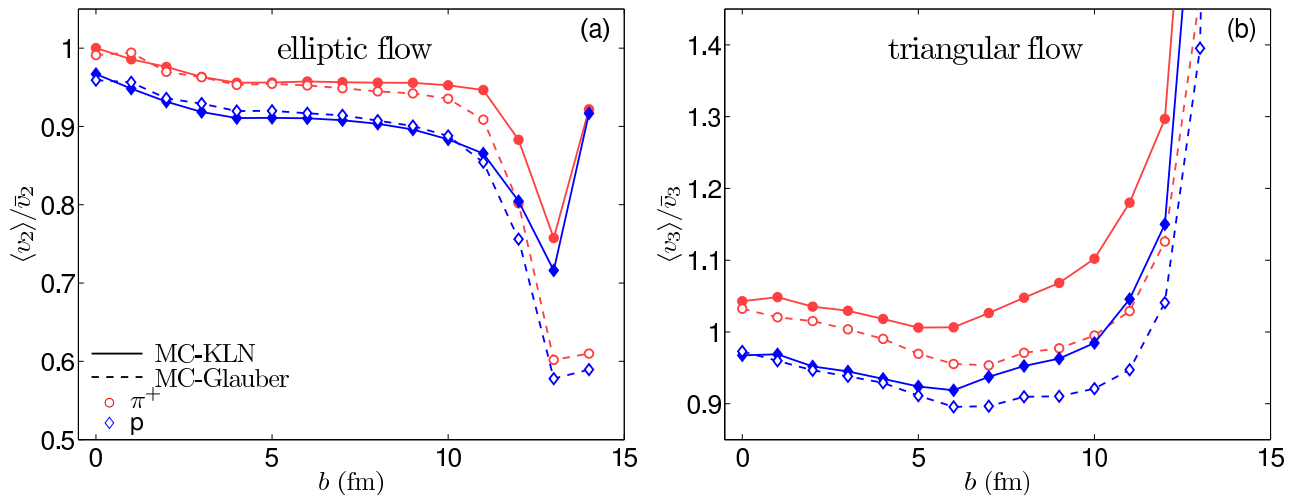


Figure 2.16: Ratio of the average flow coefficient $\langle v_n \rangle$ from event-by-event ideal hydrodynamics and the corresponding mean \bar{v}_n from single-shot ideal hydrodynamics, as a function of impact parameter in 200 A GeV Au+Au collisions, for $n=2$ (a) and $n=3$ (b). Shown are the ratios for directly emitted pions (circles) and protons (diamonds) from fluctuating events using the MC-Glauber (dashed lines) and MC-KLN models (solid lines). Average events for computing \bar{v}_n using single-shot hydrodynamics were obtained by rotating the energy density of each event by $\Phi_n(e)$ before superimposing them. Taken from [20].

From Fig. 2.16a, one concludes that, for ideal hydrodynamics, event-by-event fluctuations on average reduce the efficiency of the fluid in converting initial source ellipticity into elliptic flow.

Over most of the centrality range, this reduction is about 4% for pions and about twice as large for protons and it is similar for MC-KLN and MC-Glauber initial profiles. In very central collisions, the ratio of conversion efficiencies for event-by-event vs. single-shot hydrodynamics is closer to 1, but it degrades strongly in very peripheral collisions where event-by-event evolution generates on average 30–40% less elliptic flow than single-shot hydrodynamics. The generic tendency of the event-by-event hydrodynamic evolution of fluctuating initial profiles to generate less elliptic flow than expected from hydrodynamic evolution of the corresponding smooth average profile has been observed before [42, 43]; our systematic study in Fig. 2.16a quantifies this effect over the full range of collision centralities.

The situation with triangular flow, shown in Fig. 2.16b, is quite different: event-by-event propagation of initial-state fluctuations can lead to an increase or decrease of the triangular flow compared to single-shot hydrodynamics, depending on particle mass (pions or protons), the nature of the fluctuations (MC-Glauber or MC-KLN), and collision centrality. Contrary to elliptic flow, in peripheral collisions event-by-event evolution leads to significantly *larger* average triangular flow than single-shot hydrodynamics.

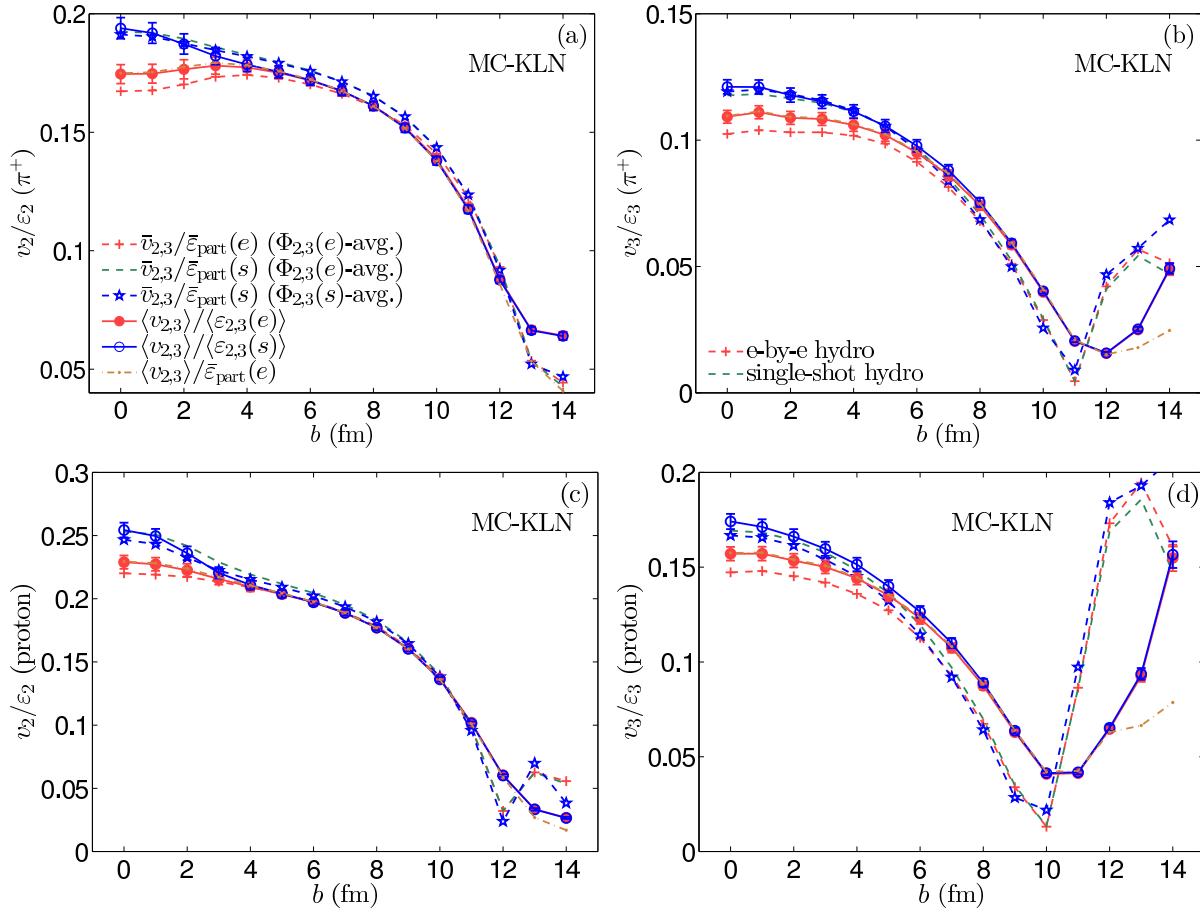


Figure 2.17: Eccentricity-scaled elliptic flow v_2/ε_2 (left) and v_3/ε_3 (right) as functions of impact parameter, for pions (panels (a,b)) and protons (panels (c,d)), from viscous ($\eta/s = 0.2$) fluid dynamic evolution of initial MC-KLN density profiles. Solid (dashed) lines correspond to event-by-event (single-shot) hydrodynamics. See text for discussion, and Fig. 2.14, 2.15 for a comparison with ideal fluid dynamics.

The analogous plots to Fig. 2.14 and Fig. 2.15 using viscous ($\eta/s = 0.2$) hydrodynamic simulations with MC-KLN initial conditions are shown in Fig. 2.17. Comparing the ideal and viscous

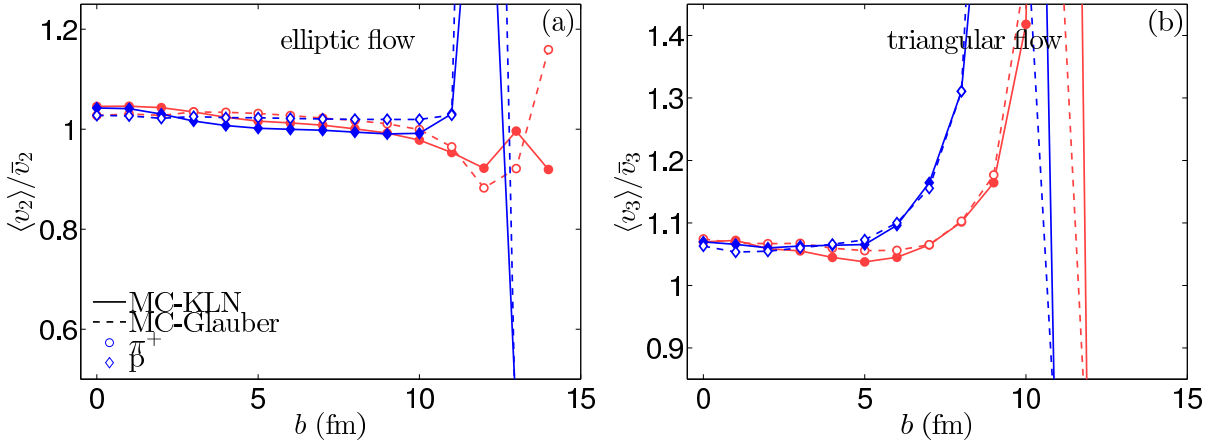


Figure 2.18: Same as Fig. 2.16, but for viscous hydrodynamic evolution with $\eta/s = 0.2$.

results, we see that viscosity greatly reduces the gap between event-by-event and single-shot simulations, both for π^+ and protons, for both elliptic and triangular flow. This is consistent with viscosity damping inhomogeneities by dissipation, making the density distributions smoother, at least at the late times.

To make the statement more quantitative, we show the corresponding ratio plot in Fig. 2.18. Comparing to Fig. 2.16, it is seen from panel (a) that, except for extremely peripheral collisions ($b \geq 10$ fm), the $\sim 10\%$ gap between the elliptic flows calculated from the two types of simulations is reduced to $\sim 3\%$. For the triangular flow, the story is somewhat different: although the curves from event-by-event and single-shot simulations appear to be closer to each other in Fig. 2.17b,d than in Fig. 2.15b,d, the relative difference between the two types of simulations is actually slightly larger, rising from $\pm 5\%$ to $\sim 8\%$.

If one aims for quantitative calculations with accuracy better than 5% or for a study of higher-order flows, event-by-event hydrodynamic evolution is an essential and indispensable ingredient; however if one has larger accuracy tolerance, one might try to extract η/s from v_2 and v_3 using single-shot simulations. Unfortunately, it turns out that v_2 and v_3 are not enough to constrain η/s very well unless one has complete control over the initial fluctuation spectrum which, as already shown in this chapter, is not true for the MC-KLN and MC-Glauber models. This will be discussed in more detail in the following chapters.

2.4.3 Elliptic flow fluctuations

Similar to what is shown in Figs. 2.1a,b for the initial source ellipticities, Fig. 2.19 shows the elliptic flow measures $\langle v_2 \rangle$, $v_2\{2\}$, and $v_2\{4\}$ from event-by-event hydrodynamics, together with \bar{v}_2 from single-shot hydrodynamic evolution of the corresponding averaged initial profile, for pions and protons, using MC-Glauber and MC-KLN initializations, respectively. $v_2\{2\}$ and $v_2\{4\}$ are defined in analogy to Eqs. (2.9,2.10) by

$$v_2\{2\}^2 = \langle v_2^2 \rangle, \quad (2.23)$$

$$v_2\{4\}^4 = 2\langle v_2^2 \rangle^2 - \langle v_2^4 \rangle. \quad (2.24)$$

Here v_2 is calculated event by event via Eq. (2.22) from the Cooper-Frye spectrum at freeze-out (with zero statistical uncertainties since it is determined with mathematical precision by the event-by-event hydrodynamic output).

As in Fig. 2.1, open stars show the central values for $\sqrt[4]{|v_2\{4\}^4|}$ whenever $v_2\{4\}^4$ turns negative, and open-ended error bars indicate that the error band for $v_2\{4\}^4$ ranges from positive to negative values. Similar to the ellipticities shown in Fig. 2.1, the latter happens at small impact parameters, but for the MC-Glauber model the b -range over which this happens for $v_2\{4\}$ (for both pions and protons) is somewhat larger than for $\varepsilon\{4\}$. Still, $v_2\{4\}$ is compatible with zero over this

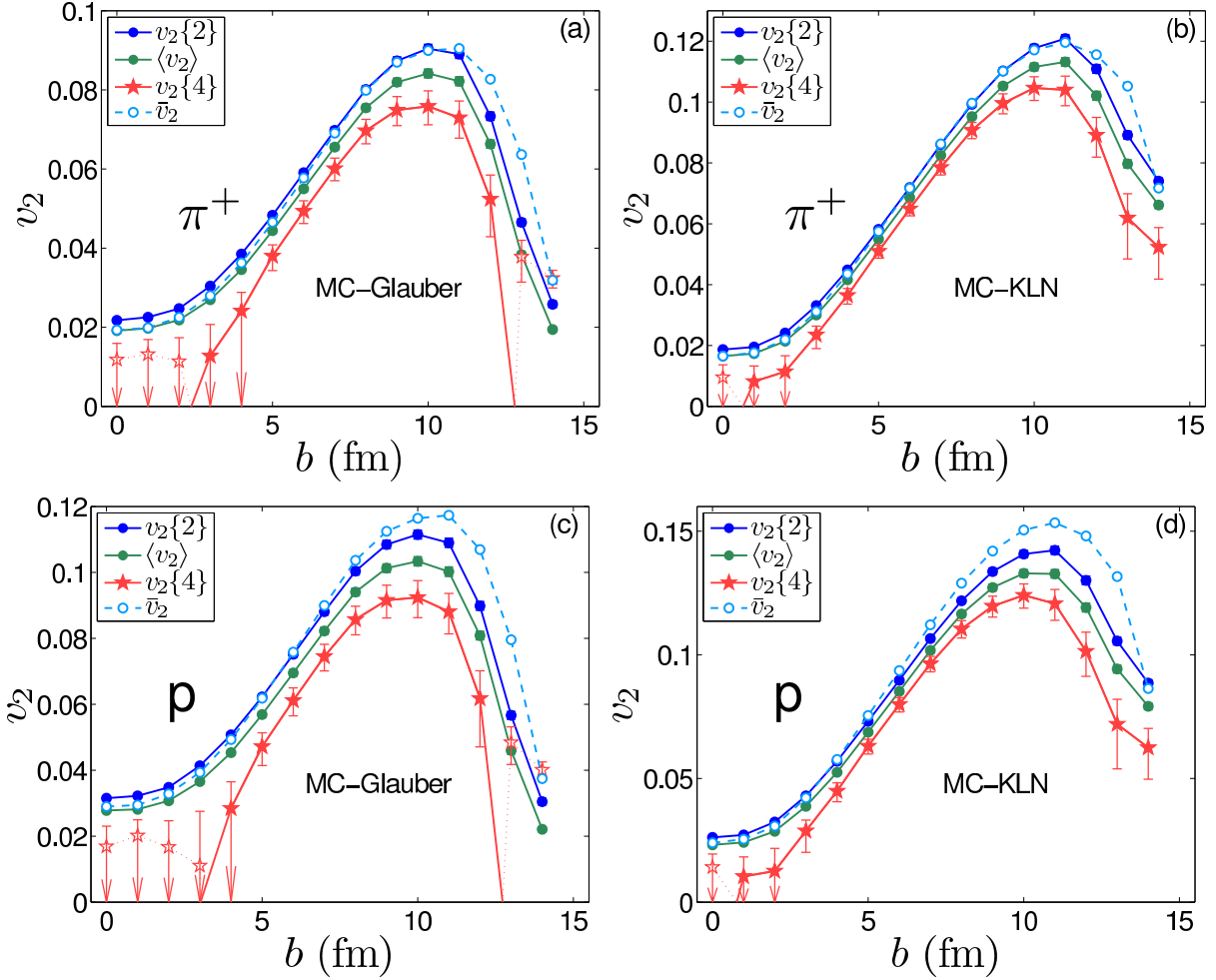


Figure 2.19: Different measures for the final elliptic flow v_2 (similar to Fig. 2.1) for directly emitted pions (a,b) and protons (c,d) as functions of impact parameter from event-by-event ideal fluid dynamics for $T_{\text{dec}} = 140$ MeV, using MC-Glauber (a,c) and MC-KLN (b,d) initial conditions for 200 A GeV Au+Au collisions. Taken from [20].

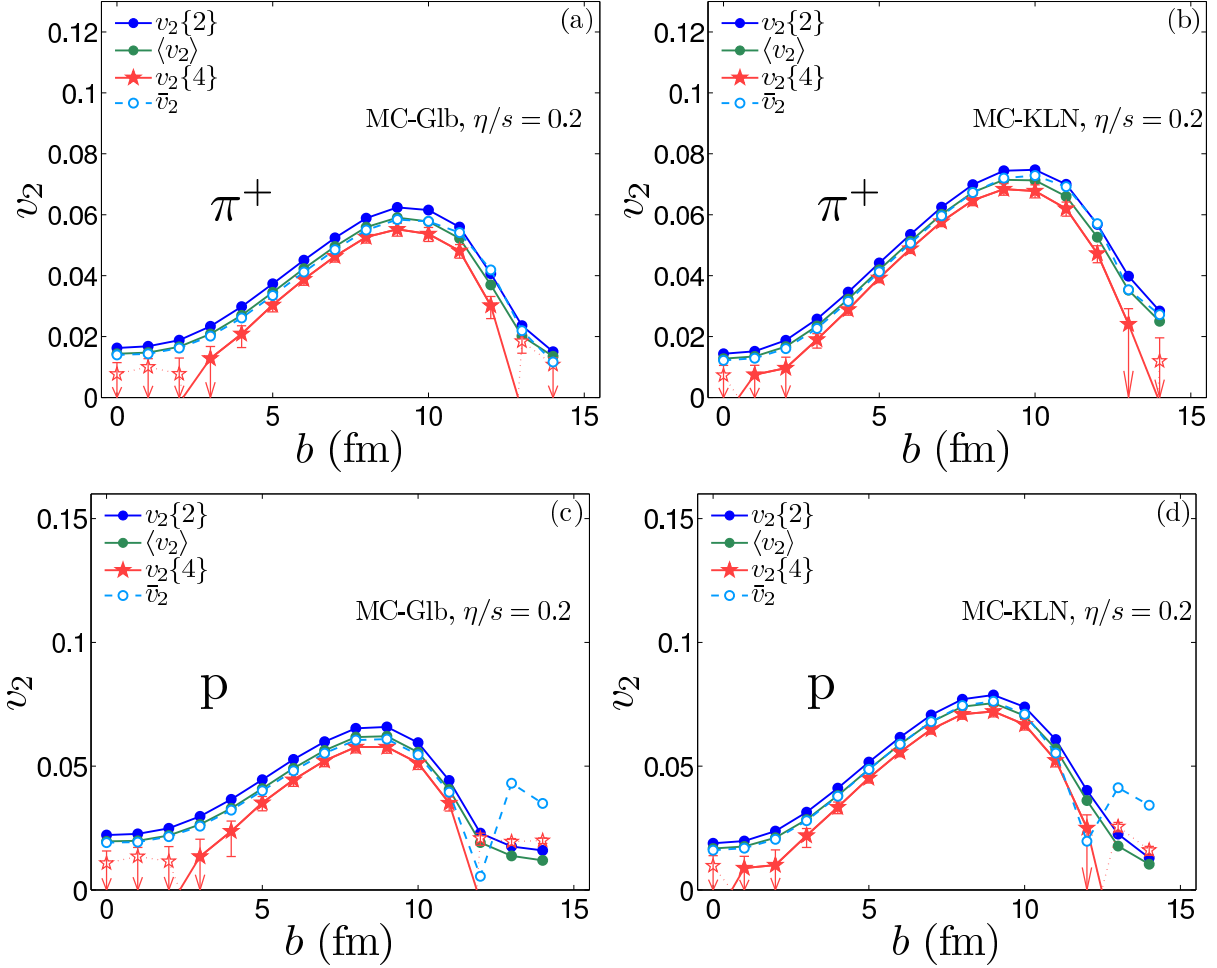


Figure 2.20: Similar to Fig. 2.19 but with $\eta/s = 0.2$.

entire range, and we do not find statistically significant negative values for $v_2\{4\}$ at small impact parameters. At large $b > 12$ fm, $v_2\{4\}$ turns negative for both pions and protons when we use MC-Glauber initial conditions, whereas it remains positive for MC-KLN initial profiles.

By comparing \bar{v}_2 (open circles in Fig. 2.19) with $\langle v_2 \rangle$ (solid green circles), one sees that in mid-central to peripheral collisions the v_2 -suppression from event-by-event hydrodynamic evolution is of the same order as or (especially for protons) even larger than the difference between $v_2\{2\}$ and $\langle v_2 \rangle$ (solid blue vs. solid green circles) that arises from event-by-event flow fluctuations. As a result, $v_2\{2\}$ from event-by-event hydrodynamics lies in peripheral collisions even below \bar{v}_2 from single-shot hydrodynamics, in spite of its fluctuation-induced enhancement.

Corresponding results from viscous hydrodynamic simulations with $\eta/s = 0.2$ are shown in Fig. 2.20. We see that viscosity suppresses the elliptic flow, consistent with what we concluded in previous sections. We also see that the event-by-event fluctuation of v_2 is also suppressed, giving much smaller error bars compared to the ideal case as shown in Fig. 2.19. Again we attribute this effect to the fact that viscosity dissipates hot-spots and thus to some extent reduces the event-by-event fluctuations caused by the randomness of the initial nucleons positions.

Similar to Eqs. (2.11)-(2.13) we can test whether the v_2 fluctuations from event to event have Gaussian or Bessel-Gaussian distributions. This is done in Fig. 2.21. The upper set of curves (thick lines) tests the v_2 -analogue of relation (2.13), whereas the lower set (thin lines) tests the validity of Eq. (2.11). (In the lower set of curves, we dropped all b -values for which the error band for $v_2\{4\}$ extends to negative values.) Just as we saw for the initial ellipticities in Fig. 2.3, both

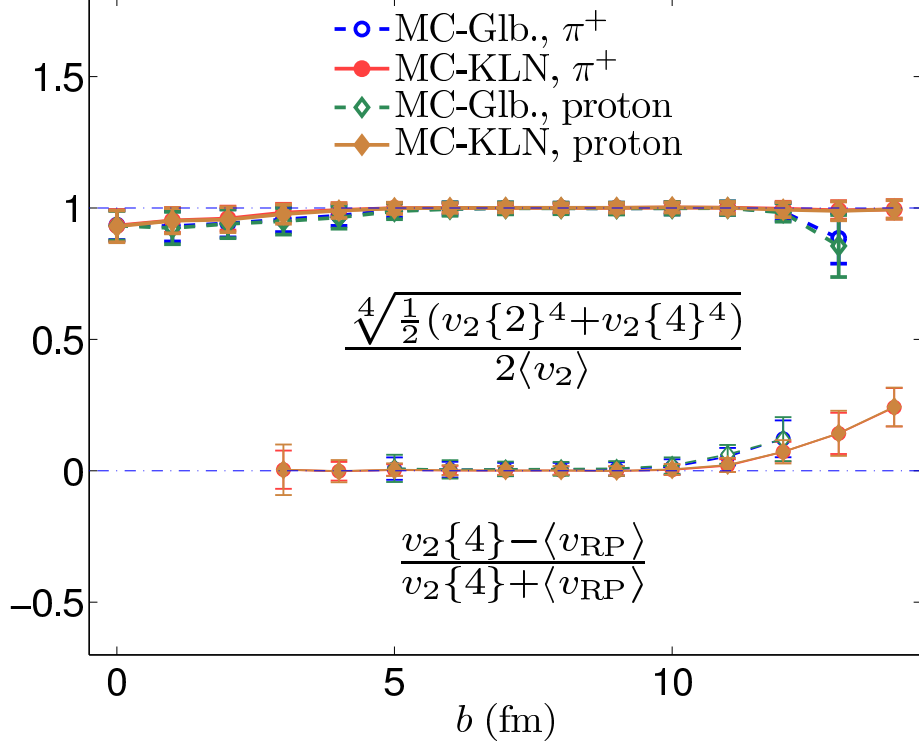


Figure 2.21: Similar to Fig. 2.3, but for the elliptic flow v_2 of pions and protons using ideal fluid dynamics. See text for discussion. Taken from [20].

the Gaussian and Bessel-Gaussian hypotheses for v_2 -fluctuations are seen to hold quite well in mid-central ($4 \lesssim b \lesssim 10$ fm) collisions. The Bessel-Gaussian hypothesis breaks down in peripheral collisions ($b > 10$ fm). We expect that the hypothesis holds (as expected [28]) in central collisions although it is not clearly seen from the plot which is generated using only 1000 events per b -value. The assumption of Gaussian v_2 -fluctuations breaks down in central collisions ($b < 5$ fm), as expected. For the MC-Glauber model, it also breaks down in very peripheral collisions, whereas for MC-KLN initial conditions the final elliptic flow exhibits a nice Gaussian distribution all the way to the largest impact parameters.

We checked that viscosity leads only to small changes in the ratios shown in Fig. 2.21, and we therefore refrain from plotting them for the viscous simulations.

Overall, a comparison of Figs. 2.21 and 2.3 (as well as of Figs. 2.19 and 2.1) shows that the statistical properties of v_2 fluctuations are qualitatively similar but quantitatively different from those of the initial ellipticity fluctuations. This is consistent with the fact that the main driver for elliptic flow is the initial ellipticity, but that eccentricity coefficients of higher harmonic orders affect the evolution of v_2 weakly but measurably through nonlinear mode-coupling effects.

2.5 Chapter summary

We summarize a few key results from this chapter:

- The average and mean ellipticities $\langle \varepsilon_2 \rangle$ and $\bar{\varepsilon}_2$ agree with excellent accuracy over a wide range of impact parameters, but diverge in very peripheral collisions ($\geq 60\%$ centrality) where $\bar{\varepsilon}_2 > \langle \varepsilon_2 \rangle$ (both for participant-plane and reaction-plane averaged profiles).
- The average energy and entropy density weighted eccentricities agree with excellent accuracy over a wide range of impact parameters, except for central collisions ($b \lesssim 4$ fm) where $\langle \varepsilon_n(e) \rangle > \langle \varepsilon_n(s) \rangle$.
- Whether the fluctuating entropy density distributions for individual events are first converted to energy density and then rotated by $\Phi_n(e)$ and averaged, or first rotated by $\Phi_n(s)$ and averaged and then converted to energy density has very little influence on the shape of the resulting smooth average initial energy density profile for single-shot hydrodynamics. We prefer the conversion

to energy density as the first step, since in event-by-event hydrodynamics the energy density gradients of each event generate (through the EOS) the pressure gradients that drive the evolution of collective flow.

- The shortcut of using reaction-plane averaging to generate a smooth profile for single-shot hydrodynamics with ellipticity approximately equal to $\varepsilon\{4\}$ of the ensemble, in the hope of generating with a single hydrodynamic run an elliptic flow \bar{v}_2 that can be directly compared with $v_2\{4\}$ measurements, works only in the 0–40% centrality range. For peripheral collisions, this method cannot be trusted.

- The assumption of Bessel-Gaussian fluctuations for initial source ellipticity and final elliptic flow work well for $b \lesssim 10$ fm but breaks down in more peripheral collisions. For more peripheral collisions, the hypothesis that ε_2 and v_2 are Gaussian distributed works better than the Bessel-Gaussian assumption, but it breaks down for $b < 5$ fm. For MC-Glauber initial conditions, directly emitted pions and protons feature negative values of $v_2\{4\}$ ⁴ in very peripheral collisions. The fluctuations of initial source ellipticities and final elliptic flow values have qualitatively similar but quantitatively different statistical properties.

- Except for rather central collisions, the eccentricities $\langle\varepsilon_2\rangle$, $\langle\varepsilon_4\rangle$ and $\langle\varepsilon_5\rangle$ from the MC-KLN model are all significantly larger than those from the MC-Glauber model. In contrast, $\langle\varepsilon_3\rangle$ is numerically very similar for the two models over most of the impact parameter range. The viscous suppression of triangular flow v_3 thus allows for a determination of the QGP shear viscosity $(\eta/s)_{\text{QGP}}$ that is free from the large model uncertainties that arise from the different MC-Glauber and MC-KLN ellipticities when using v_2 for such an extraction; or alternatively, an extraction of sheer viscosity using both v_2 and v_3 simultaneously can be used to study the correctness of initial condition models, see Chap. 3.

- The second- and fourth-order eccentricities ε_2 and ε_4 are strongly correlated by collision geometry, and v_4 receives strong contributions even from a purely elliptical deformation of the final flow velocity distribution. These complications make v_4 a poor candidate for systematic studies of viscous effects on the evolution of collective flow. Similar comments apply to v_5 since it couples via mode-coupling to triangularity from fluctuations and to ellipticity from collision geometry. This mixture of contributions from conceptually different origins complicates a systematic analysis. In general, flow coefficients v_n of high harmonic order ($n > 3$) show poor correlation with the eccentricity coefficients ε_n of the same harmonic order, except for very central collisions where all eccentricities are driven by fluctuations alone (and not by overlap geometry).

- In spite of nonlinear mode-coupling effects, the basic response of elliptic flow v_2 to ellipticity ε_2 , and of triangular flow v_3 to triangularity ε_3 , is approximately linear. These two observables thus remain prime candidates for systematic studies of viscous effects on collective hydrodynamic flow.

- Event-by-event hydrodynamics generates harder p_T -spectra for the emitted hadrons than single-shot hydrodynamic evolution of the corresponding averaged initial profile. This is due to additional radial flow generated by large pressure gradients arising from “hot spots” in the initial fluctuating density distribution. The hardening effect is particularly strong in peripheral collisions which produce small fireballs that fluctuate strongly; it is reduced by shear viscosity.

- Event-by-event hydrodynamic evolution of fluctuating initial conditions leads to smaller average elliptic flow than obtained by evolving the corresponding averaged initial condition in a single shot. This suppression depends somewhat on collision centrality, and for ideal fluids it is generically of order 4-5% for pions and 8-10% for protons. The effect is sufficiently large to possibly lead to a significant over-estimate of the fluid’s specific shear viscosity if one extracts it from elliptic flow measurements by comparing with single-shot hydrodynamic simulations. The discrepancy between event-by-event and single-shot hydrodynamics decreases, however, in viscous fluid dynamics. More related studies are reported in Chap. 3.

Chapter 3: Using simultaneously measured elliptic and triangular flow to resolve initial condition ambiguities

This chapter focuses on a simultaneous comparison of both elliptic and triangular flow from viscous fluid dynamics with measurements in Pb+Pb collisions at the LHC. Using initial density distributions from the MC-Glauber and MC-KLN models, we show that the data favor a small specific shear viscosity $(\eta/s)_{\text{QGP}} \sim 1/(4\pi)$ for the quark-gluon plasma. Using this viscosity value, the relative magnitude of the elliptic and triangular flow is well described with MC-Glauber initial conditions while the MC-KLN initial conditions require twice as large viscosity to reproduce the elliptic flow and then under-predict triangular flow by about 30%. We show that compatibility of the experimental data with larger values for the specific shear viscosity of the QGP would require initial-state models whose density distributions fluctuate more strongly, yielding significantly larger triangular deformations on average than those obtained from both the MC-Glauber and MC-KLN models. The material in this chapter is based on [44] and [45].

3.1 Introduction

Much attention has been given to the extraction of the specific shear viscosity (η/s) of the quark-gluon plasma from elliptic flow data in relativistic heavy-ion collisions [9, 12, 30, 34, 36, 43, 46–54].

A major road block in this effort is insufficient knowledge of the initial shape of the thermalized fireball created in these collisions, whose initial ellipticity is uncertain by about 20% [6, 20, 55–57] (Fig. 2.5). As shown in Chap. 2, this induces an $\mathcal{O}(100\%)$ uncertainty in the value of $(\eta/s)_{\text{QGP}}$ extracted from elliptic flow [30, 49]. After the discovery of triangular flow in heavy ion collisions at RHIC [21, 58, 59] and LHC energies [60–62], followed by the confirmation of its collective hydrodynamic nature [10, 21, 22, 63–66] and the realization that shear viscosity suppresses higher-order harmonic flow coefficients more strongly than elliptic flow [22, 43, 54, 67, 68], it was suggested [37, 45, 58, 60, 69] that a combined analysis of the elliptic and triangular flow coefficients v_2 and v_3 could yield a more precise value for the QGP shear viscosity and thereby reduce or eliminate the model uncertainty in the initial deformation of the QGP fireball and its event-by-event fluctuations. This chapter focuses on such an analysis, using Pb+Pb collision data collected by the ALICE collaboration at the LHC [70].

3.2 Justification for using single-shot simulations

Event-by-event viscous hydrodynamic simulations with full inclusion of unstable resonance decays are at present numerically too costly for systematic flow studies over a range of viscosities, collision energies, centralities, and collision systems. To study the possibility of replacing event-by-event simulations by less costly single-shot ones, we draw on our intuition based on previous hydrodynamic simulations for Au+Au collisions at $\sqrt{s} = 200$ A GeV (Chap. 2). The initial conditions under comparison are from the MC-Glauber and the MC-KLN models (see Sec. 1.3).

We have shown in Chap. 2 that, for ideal hydrodynamic simulations, the eccentricity-scaled elliptic and triangular flows $v_{2,3}/\varepsilon_{2,3}$ calculated from single-shot and event-by-event hydrodynamics show 5 – 10% differences (Figs. 2.14, 2.15), for both light (thermal pions) and heavy (protons)

particles; the differences for viscous hydrodynamic simulations with $\eta/s = 0.2$ are even smaller (Fig. 2.17). This suggests that for viscous hydrodynamic simulations with sufficiently large viscosity η/s , single-shot hydrodynamics can substitute well for event-by-event evolution for the purpose of calculating v_2/ε_2 and v_3/ε_3 . For ideal hydrodynamic simulations, there is a $\sim 7\%$ inaccuracy caused by this substitution, however this is already much smaller than the $\sim 20\%$ uncertainty in ellipticity induced by the ambiguity between the MC-Glauber and MC-KLN models. Therefore a (relatively) quick study using single-shot simulations with both elliptic and triangular flows becomes a meaningful proposition for gaining new information beyond the previous studies based on v_2/ε_2 alone.

However there is a subtlety: the experimental flow data are mostly determined with two-particle and four-particle correlations methods which give $v_{2,3}\{2\}$ and $v_{2,3}\{4\}$ instead of $\langle v_2 \rangle$. Following [27] we try to normalize the flow by the correspondingly calculated eccentricity, that is, $\langle v_n \rangle$ by $\langle \varepsilon_n \rangle$, $v_n\{2\}$ by $\varepsilon_n\{2\}$, $v_n\{4\}$ by $\varepsilon_n\{4\}$, and the results are shown in Fig. 3.1.

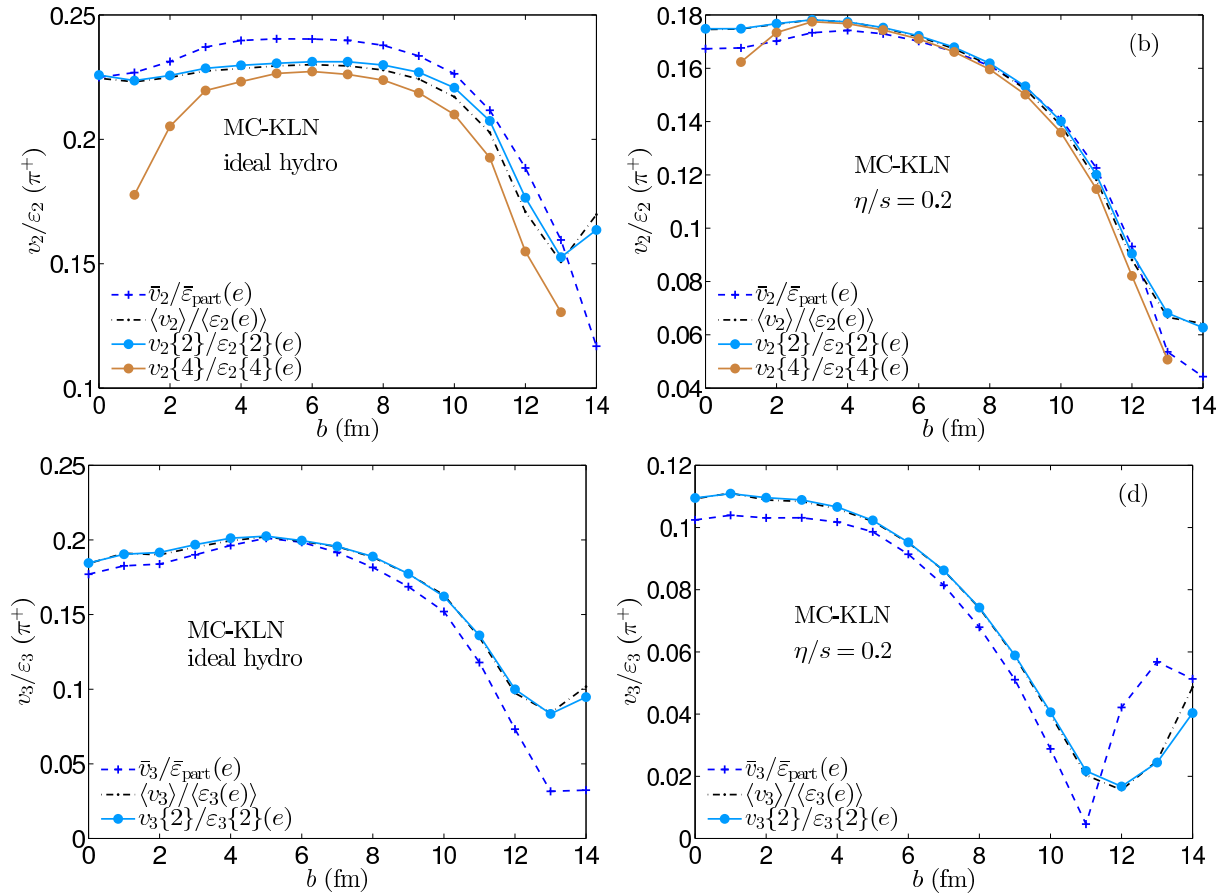


Figure 3.1: $\langle v_n \rangle / \varepsilon_n$, $v_n\{2\} / \varepsilon_n\{2\}$, and $v_n\{4\} / \varepsilon_n\{4\}$ for $n = 2$ (ab) and $n = 3$ (cd), using thermal pions from ideal hydrodynamics (ac) and viscous ($\eta/s = 0.2$) hydrodynamics (bd), from the MC-KLN model calculations for Au+Au collisions at the RHIC energy. The blue dash curves represent results from single-shot calculations and the rest are from event-by-event calculations.

Fig. 3.1(ab) shows that, for the elliptic flow, the process of normalizing the flow by the correspondingly calculated eccentricity gives very similar scaled flow in the ideal fluid case (Fig. 3.1(a)), and almost completely equal scaled flow in the viscous case (Fig. 3.1(b)). There are 5% \sim 10% differences between $\bar{v}_2/\bar{\varepsilon}_2$ and $v_2\{2\}/\varepsilon_2\{2\}$ or $v_2\{4\}/\varepsilon_2\{4\}$ when small η/s is used (Fig. 3.1(a)); with $\eta/s = 0.2$, this difference has almost vanished (Fig. 3.1(b)).

The scaled triangular flows are shown in Fig. 3.1(cd). It is clear that $v_3\{2\}/\varepsilon_3\{2\}$ is very close to $\langle v_3 \rangle / \langle \varepsilon_3 \rangle$ and $\bar{v}_3 / \bar{\varepsilon}_3$, which are almost identical in both the ideal (Fig. 3.1(c)) and viscous (Fig. 3.1(d)) cases. For triangular flow, we do not show $v_3\{4\}/\varepsilon_3\{4\}$ since the values for both numerator and denominator are small and plagued by large statistical errors.

We take the results of this study as justification for applying a similar single-shot approach to the LHC data in the remaining of this chapter.

3.3 Setup for the simulations

We use the (2+1)-dimensional viscous hydrodynamic simulation code VISH2+1, with longitudinal boost-invariance, describing numerically the transverse evolution of the heavy-ion collision fireball near midrapidity. As in past work [6, 20, 30, 49, 50, 57], we use the MC-Glauber and the MC-KLN models.

The MC-KLN calculations were done using a Monte-Carlo sample of initial state profiles with identical properties as those used in [71] for the calculation of transverse momentum spectra and elliptic flow in 2.76 A TeV Pb-Pb collisions at the LHC. To compute the nuclear thickness function $T_A(\mathbf{r}_\perp; b)$, we use an inelastic nucleon-nucleon cross section $\sigma_{NN} = 62$ mb at LHC energies. For the x dependence of the gluon structure function in the MC-KLN model, we used the power $\lambda = 0.28$ [6]; the normalization factor for the initial entropy density was fixed by hand to reproduce the measured charged hadron multiplicity density $dN_{\text{ch}}/d\eta$ for the 5% most central collisions [72]; the measured dependence of $dN_{\text{ch}}/d\eta$ on collision centrality [73] is then automatically reproduced reasonably well by the model [71] (see Fig. 3.2(a)). MC-KLN runs were done with $\eta/s = 0.2$ which, for this type of initial conditions, was shown to yield a good overall description of the measured transverse momentum spectra and elliptic flow in 200 A GeV Au-Au collisions at RHIC [71] and gave an impressively accurate prediction for the unidentified and identified charged-hadron spectra and elliptic flows in 2.76 A TeV Pb-Pb collisions at the LHC [71, 74].

For the MC-Glauber runs, we generated a new set of initial configurations that differ from those used for 200 A GeV Au-Au collisions in [30] by the wounded-nucleon-to-binary-collision ratio. Taking the initial entropy density

$$s(\mathbf{r}_\perp; b) = \kappa \left(\frac{1-x}{2} n_{\text{WN}}(\mathbf{r}_\perp; b) + x n_{\text{BC}}(\mathbf{r}_\perp; b) \right), \quad (3.1)$$

we determine κ and x by a two-parameter fit to the ALICE data [73] shown in Fig. 3.2(a). Due to viscous entropy production during the hydrodynamic evolution, which itself depends on collision centrality, the fitted value for x depends on the assumed shear viscosity. For MC-Glauber initial conditions, we took $\eta/s = 0.08$ since this value was shown in [54, 60, 68] to provide a reasonable description of the charged hadron $v_2(p_T)$ and $v_3(p_T)$ data measured by the ALICE experiment; this results in $x = 0.118$ for Pb-Pb collisions at the LHC. Both the MC-Glauber and MC-KLN initial conditions are hydrodynamically evolved with equation of state (EOS) s95p-PCE [12], which matches numerical results from lattice QCD at high temperatures to a hadron resonance gas at low temperatures [11] and implements chemical freeze-out at $T_{\text{chem}} = 165$ MeV. The hydrodynamic output is converted to final hadron distributions along an isothermal decoupling surface of temperature $T_{\text{dec}} = 120$ MeV, using the Cooper-Frye prescription.

In Chap. 2 [20], we showed that, due to similar fluctuation mechanisms, the MC-KLN and MC-Glauber models generate similar third-order eccentricities ε_3 , whereas the ellipticity ε_2 , which is mostly controlled by collision geometry, is about 20% larger in the MC-KLN model. Event-by-event ideal and viscous hydrodynamic simulations with both realistically-fluctuating [20] (Recall Fig. 2.14, 2.15, 2.17) and doubly-deformed Gaussian initial conditions [45] (with simultaneously nonzero ε_2 and ε_3 eccentricities) have shown that the hydrodynamic conversion efficiencies for translating initial spatial eccentricities into final flow anisotropies [10, 40, 75], although different for v_2/ε_2 and v_3/ε_3 , are very similar in the MC-KLN and MC-Glauber models. The similarities in ε_3 and differences in ε_2 between these models should thus straightforwardly reflect themselves

in analogous differences in v_2 and v_3 [45, 69], allowing for an experimental distinction between the models.

For all the reasons discussed in Sec. 3.2, we use the single-shot approach. For a meaningful comparison with experiment, we include the full cascade of resonance decays in the final state. We compare with recent data from Pb-Pb collisions at the LHC, and we use the properly normalized ratios v_n/ε_n for our comparison. The results are shown in next few sections. Our approach here differs from that in [22] by replacing the singly-deformed Gaussian parametrization of the initial density used there by the ensemble average of realistically-fluctuating, non-Gaussian initial profiles and from [43, 54, 68] by employing a more realistic EOS that accounts for the important effects of chemical non-equilibrium hadronic evolution on the elliptic flow v_2 [76]. In [60] it was shown that, with the approach used in [22], MC-KLN initial conditions with $\eta/s = 0.16$ cannot describe the p_T -integrated v_3 measured in 2.76 A TeV Pb-Pb collisions, whereas the MC-Glauber based event-by-event calculations (with $\eta/s = 0.08$) of Schenke *et al.* [54] appear to describe $v_3(p_T)$ at selected centralities reasonably well.

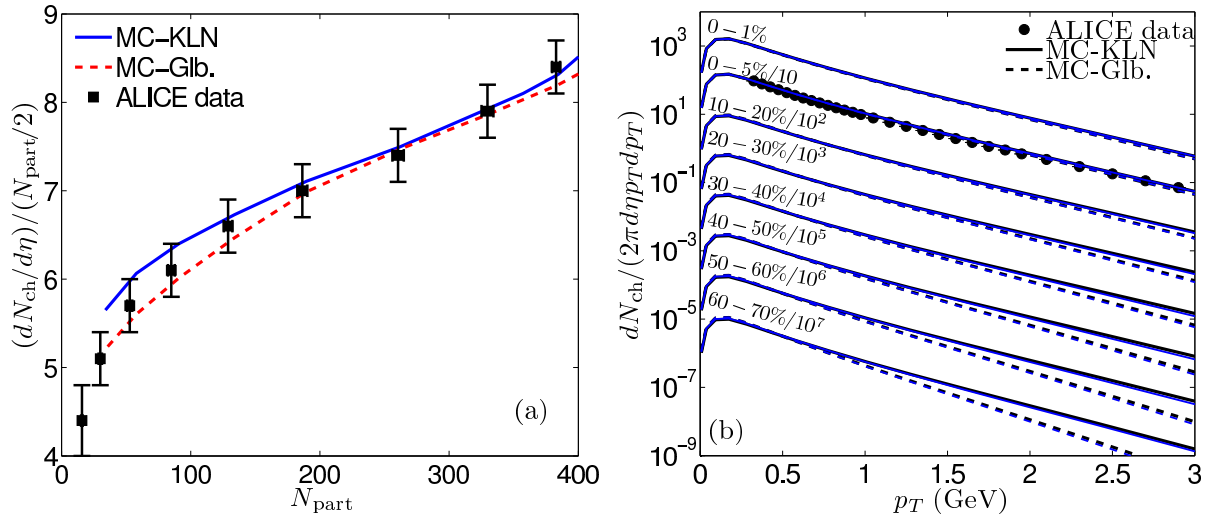


Figure 3.2: (a) (Color online) Centrality dependence of charged particle multiplicity density as a function of N_{part} from the MC-Glauber (dashed) and MC-KLN (solid) models, compared with ALICE measurements [73] for 2.76 A TeV Pb-Pb collisions. (b) Charged particle p_T -spectra from the MC-Glauber and MC-KLN models for different centralities. The most central (0–5%) results are compared with ALICE data [70]. From [44].

3.4 Transverse momentum spectra

Fig. 3.2(b) shows the charged hadron p_T -spectra for 2.76 A TeV Pb-Pb collisions at different centralities, for both MC-Glauber ($\eta/s = 0.08$) and MC-KLN ($\eta/s = 0.2$) initial conditions. For the most central (0–5%) collisions, the spectra from both models agree well with published ALICE data. In more peripheral collisions, the MC-KLN spectra are harder than those from MC-Glauber initial conditions. This is a consequence of larger radial flow caused by larger transverse viscous pressure gradients in the MC-KLN case, where the fluid is taken to have 2.5 times larger shear viscosity than for the MC-Glauber simulations in order to obtain the same elliptic flow [30, 49]. In peripheral collisions, these viscous effects are stronger than in more central collisions where the fireball is larger [77]. As shown in [20, 38] and Chap. 2, event-by-event evolution of fluctuating initial conditions generates, for small values of η/s , flatter hadron spectra than single-shot hydrodynamics, especially in peripheral collisions, due to stronger radial flow driven by hot spots in the fluctuating initial states. Proper event-by-event evolution of the latter is therefore expected to

reduce the difference between the MC-Glauber and MC-KLN curves, as explained in Sec. 3.6, since this effect is relatively strong for $\eta/s=0.08$ (MC-Glauber) [20] but almost absent for $\eta/s=0.2$ (MC-KLN).

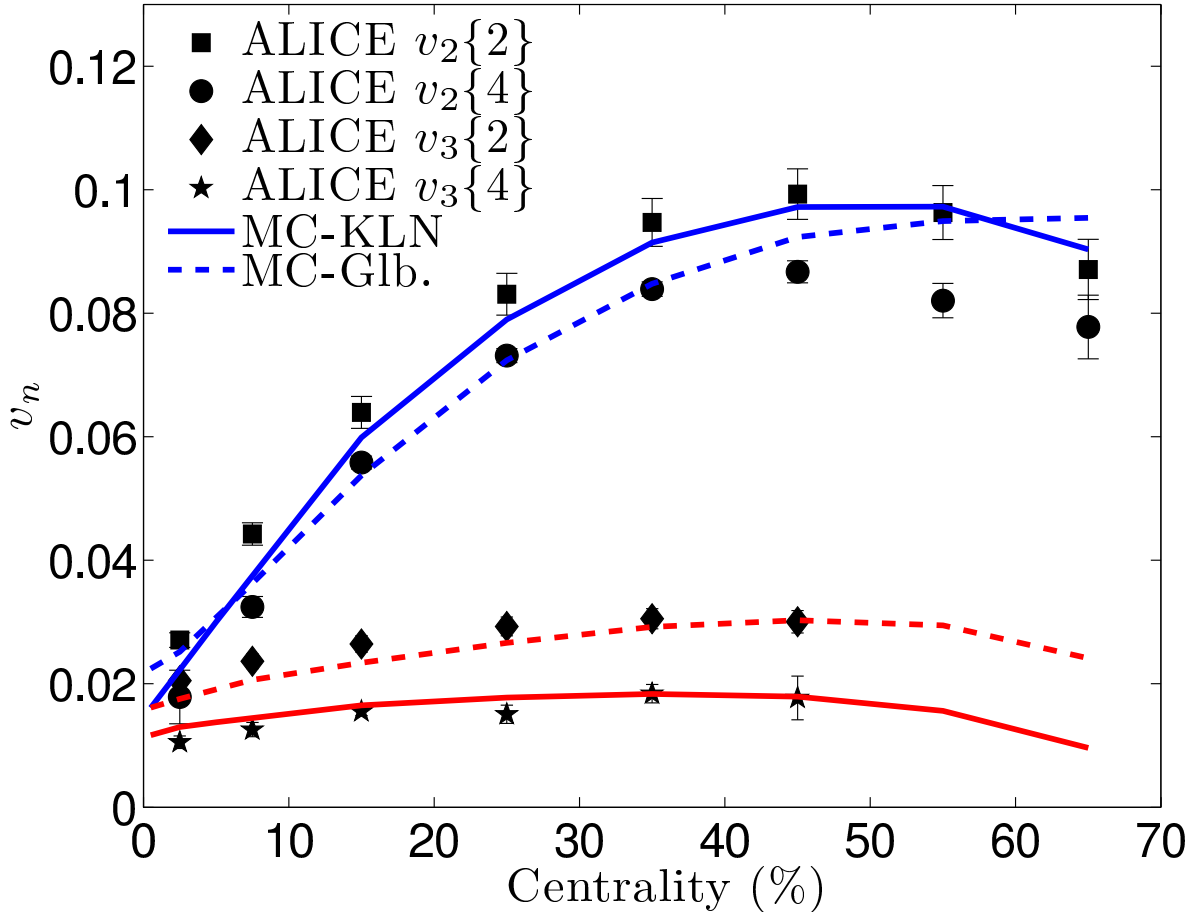


Figure 3.3: Charged hadron \bar{v}_2 and \bar{v}_3 vs. centrality, compared with ALICE $v_2\{2\}$, $v_2\{4\}$, $v_3\{2\}$, and $v_3\{4\}$ data for 2.76 A TeV Pb+Pb [60]. From [44].

3.5 p_T -integrated elliptic and triangular flow

In Fig. 3.3, we compare our p_T -integrated \bar{v}_2 and \bar{v}_3 as functions of centrality with ALICE $v_2\{2\}$, $v_2\{4\}$, $v_3\{2\}$, and $v_3\{4\}$ data, extracted from 2- and 4-particle correlations [60] (also see Chap. 2). For both models, $\bar{v}_{2,3}$ from the averaged smooth initial conditions lie between the experimental $v_{2,3}\{2\}$ and $v_{2,3}\{4\}$ values. This is consistent with the theoretical expectation [28, 78] that $v_n\{2\}$ ($v_n\{4\}$) is shifted up (down) relative to the average flow by event-by-event flow fluctuations and was also found elsewhere [30, 51, 54]. Upon closer inspection, however, and recalling that ideal single-shot hydrodynamics with smooth initial condition was shown in [20] and in Chap. 2 to generate \bar{v}_2 similar to $v_2\{2\}$ from the corresponding event-by-event evolution, it seems that the MC-KLN is favored since it produces \bar{v}_2 results closer to the $v_2\{2\}$ data. Unfortunately, a similar argument using \bar{v}_3 can be held against the MC-KLN model. To eliminate the interpretation difficulties associated with a comparison of average flows from single-shot evolution of averaged initial conditions with data affected irreducibly by naturally existing event-by-event fluctuations, we proceed to a comparison of eccentricity-scaled flow coefficients.

Assuming linear response of $v_{2,3}$ to their respective eccentricities $\varepsilon_{2,3}$ (which was found to hold in Chap. 2 and in [20] with reasonable accuracy for v_2 and v_3 , but not for higher order anisotropic flows) we follow [27] and scale the flow $\bar{v}_{2,3}$ from single-shot hydrodynamics by the eccentricity $\bar{\varepsilon}_{2,3}$ of the ensemble-averaged smooth initial energy density, while scaling the experimental $v_{2,3}\{2\}$ and $v_{2,3}\{4\}$ data by the corresponding fluctuating eccentricity measures $\varepsilon_{2,3}\{2\}$ and $\varepsilon_{2,3}\{4\}$, respectively, calculated from the corresponding models. As shown in Sec. 3.2, this procedure is justified for $v_{2,3}\{2\}$ and $v_2\{4\}$; we do not perform comparisons using $v_3\{4\}/\varepsilon_3\{4\}$ because of the lack of statistical confidence in our theoretical calculations.

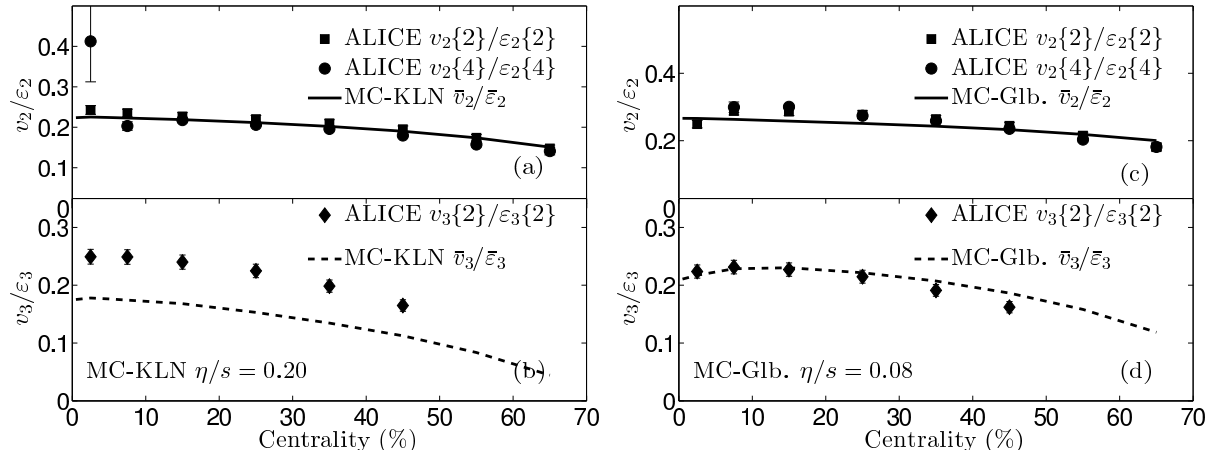


Figure 3.4: Eccentricity-scaled, p_T -integrated $\bar{v}_{2,3}$ for the hydrodynamically evolved MC-KLN (a,b) and MC-Glauber (c,d) models, compared with ALICE $v_{2,3}$ data for 2.76 A TeV Pb-Pb collisions [60] scaled by their corresponding eccentricities (see text). From [44].

The eccentricity-scaled elliptic and triangular flow coefficients for the MC-KLN and MC-Glauber models are shown in Figs. 3.4(a,b) and Fig. 3.4(c,d), respectively, and compared with the corresponding data from ALICE [60]. The first thing to note is the impressively accurate agreement between the experimentally measured $v_2\{2\}/\varepsilon_2\{2\}$ and $v_2\{4\}/\varepsilon_2\{4\}$, showing that for elliptic flow the idea of scaling “each flow with its own eccentricity” [27] works very well. Secondly, both $v_2\{2\}/\varepsilon_2\{2\}$ and $v_2\{4\}/\varepsilon_2\{4\}$ measured by ALICE agree well with the viscous hydrodynamic calculations for both the MC-Glauber and MC-KLN models, confirming that for each model the correct value of η/s has been used as far as elliptic flow is concerned.

The bottom panels in Fig. 3.4 show the triangular flow v_3 . Clearly, with the viscosities needed to reproduce v_2 , the MC-KLN model badly disagrees with the experimental data. The measured triangular flow is too big to accommodate a specific shear viscosity as large as 0.2. Within the present approach, the only possibility to avoid this conclusion is that somehow the MC-Glauber and MC-KLN models both under-predict the initial third-order eccentricity ε_3 by about 50%. With MC-Glauber initial conditions and $\eta/s=0.08$, on the other hand, the ALICE data agree well with viscous hydrodynamics, even if the measured centrality dependence of $v_3\{2\}/\varepsilon_3\{2\}$ is slightly steeper than the calculated one.

Summarizing Fig. 3.4, the only possibility to have a large $\eta/s \sim 0.2$ for the QGP that is compatible with large ALICE v_3 data is to require an initial-condition model that produces much larger triangularities than the MC-Glauber and the MC-KLN models [79].

3.6 p_T -differential elliptic and triangular flow

As a cross-check, we compare our calculations also to the p_T -differential anisotropic flow data at one collision centrality (30–40%) [60]. The corresponding comparison between data and theory is

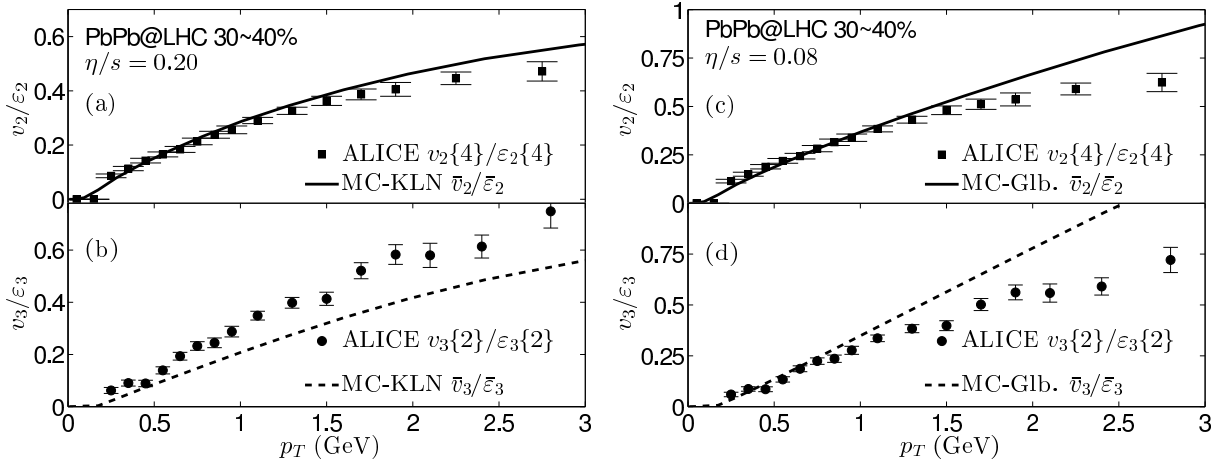


Figure 3.5: Eccentricity-scaled, p_T -differential elliptic and triangular flow for 2.76 A TeV Pb-Pb collisions from viscous hydrodynamics with MC-KLN (a,b) and MC-Glauber (c,d) initial conditions. The ALICE data [60] are scaled according to their corresponding eccentricities, see text. From [44].

shown in Fig. 3.5; as in Fig. 3.4, we compare the eccentricity-scaled flows, plotting $\bar{v}_{2,3}/\bar{\varepsilon}_{2,3}$ for the models and $v_2\{4\}/\varepsilon_2\{4\}$ ($v_3\{2\}/\varepsilon_3\{2\}$) for the elliptic (triangular) flow data. As seen in the upper panels, both initial-state models describe the measured elliptic flow well up to $p_T \sim 1-1.5$ GeV/c; at larger p_T , they over-predict $v_2(p_T)$ for charged particles – a problem noticed before [36, 71] and possibly related to an imperfect model description of the measured final chemical composition [74]. The disagreement at larger p_T is worse for MC-Glauber initial conditions; this is likely related to our earlier observation in Fig. 3.2(b) that our the MC-Glauber p_T -spectra are steeper than the MC-KLN ones in peripheral collisions – an artifact of our single-shot approach and possibly remedied by a proper event-by-event hydrodynamical simulation.

Fig. 3.5(b) shows again the disagreement between theory and experiment for triangular flow when we use MC-KLN initial conditions: the model strongly under-predicts the data at all p_T , i.e. it gives the wrong slope for $v_3(p_T)$. With MC-Glauber initial conditions and correspondingly lower shear viscosity $\eta/s = 0.08$ (Fig. 3.5(d)), the measured $v_3(p_T)$ is well described up to $p_T \sim 1$ GeV/c but over-predicted at larger p_T . Again, the latter can be at least partially attributed to the fact that MC-Glauber p_T -spectrum from our single-shot hydrodynamic approach is too steep at this collision centrality, which can be corrected by performing the hydrodynamic evolution properly event by event.

3.7 Chapter summary

Using a single-shot viscous hydrodynamic approach without any hadronic after-burner but properly implementing hadronic chemical freeze-out at $T_{\text{chem}} \approx 165$ MeV and including a full set of resonance decays, we have shown that a combined analysis of the ALICE data for elliptic and triangular flow from 2.76 A TeV Pb-Pb collisions leads to a strong preference for initial conditions from the Monte-Carlo Glauber model, combined with a low value for the QGP shear viscosity $\eta/s \simeq 0.08$, and disfavors the considerably larger viscosities of $\eta/s \sim 0.2$ that are required to reproduce the measured elliptic flow when assuming the more eccentric Monte-Carlo KLN initial profiles.

The analysis presented in this chapter was restricted to only these two initial-state models, and only to elliptic and triangular flows. While this analysis, published in [44], was the first combined analysis of two different flow harmonics, it was later superseded by analyses that included several higher order harmonics [4, 80–82]. From the later work one must conclude that neither the MC-KLN model with $\eta/s = 0.2$ nor the MC-Glauber model with $\eta/s = 0.08$ can simultaneously explain all flow harmonics. An additional ingredient is missing from both of these models in order

to produce the correct initial density fluctuation spectrum: In addition to the fluctuating nucleon positions, fluctuations of the quark and gluon fields inside the nucleons must be accounted for. Models that do this were recently developed in [79, 80, 83].

Chapter 4: Hydrodynamic event-plane correlations in Pb+Pb collisions

In this chapter, we show that correlations between the flow angles associated with higher harmonics measured by the ATLAS collaboration have hydrodynamic origin. The correlation strength is found to be sensitive to both the initial conditions and the shear viscosity of the expanding fireball medium. The material in this chapter is based on [84].

4.1 Introduction

In this chapter, we follow the conventions to define the eccentricity coefficients ε_n with associated participant plane angles Φ_n [10, 21, 40](Chap. 1) as:

$$\begin{aligned}\mathcal{E}_1 &:= \varepsilon_1 e^{i\Phi_1} = -\frac{\int r dr d\phi r^3 e^{i\phi} e(r, \phi)}{\int r dr d\phi r^3 e(r, \phi)}, \\ \mathcal{E}_n &:= \varepsilon_n e^{in\Phi_n} = -\frac{\int r dr d\phi r^n e^{in\phi} e(r, \phi)}{\int r dr d\phi r^n e(r, \phi)}, \quad (n > 1)\end{aligned}\tag{4.1}$$

where $e(r, \phi)$ is the initial energy density distribution in the plane transverse to the beam direction at the collision point $z=0$. The final momentum distributions of the emitted charged hadrons are characterized, as in previous chapters, by their anisotropic flow coefficients v_n and their associated flow (event plane) angles Ψ_n [10, 20, 85](Chap. 1):

$$V_n := v_n e^{in\Psi_n} = \frac{\int p_T dp_T d\phi_p e^{in\phi_p} \frac{dN_{\text{ch}}}{d\eta dp_T d\phi_p}}{\int p_T dp_T d\phi_p \frac{dN_{\text{ch}}}{d\eta dp_T d\phi_p}}.\tag{4.2}$$

As pointed out in [86, 87], a complete understanding of the entire spectrum of harmonic flow coefficients v_n is expected to yield strong constraints on the initial conditions and dynamical evolution of heavy-ion collisions, in particular the transport coefficients of the fireball medium. The authors of [40, 88–92] added that correlations between the event plane angles Ψ_n of different harmonic order can yield valuable additional insights into the initial conditions. Such correlations were measured with good precision by the ATLAS Collaboration in Pb+Pb collisions at the LHC [93]. In this chapter, we demonstrate that some of the measured final-state event-plane correlations have a qualitatively different centrality dependence from the corresponding initial-state participant-plane correlations, and that this characteristic change between initial and final state is correctly reproduced by hydrodynamic evolution. This provides additional strong support for the validity of the hydrodynamic paradigm in relativistic heavy-ion collisions. Furthermore, we show that the measured event-plane correlations are not only sensitive to the initial conditions, but also to the shear viscosity of the hydrodynamic medium, thus providing an independent constraint for this key transport coefficient.

4.2 Methodology

We evolve fluctuating initial energy density profiles for Pb+Pb collisions at $\sqrt{s} = 2.76$ ATeV using event-by-event viscous hydrodynamics. To explore the sensitivity to model uncertainties in the initial state, we have evolved events from two sets of initial conditions obtained from the Monte-Carlo Glauber and the Monte-Carlo KLN models [6, 56]¹⁰. We divided each set into centrality classes according to the number N_{part} of wounded nucleons (see tables B.2-B.7); for each centrality class, we evolved 11,000 events for each of the two initial condition models. Model parameters were tuned to reproduce the p_T spectra and elliptic flows of unidentified charged particles and identified hadrons, as reported in [44, 71](Chap. 3). As explained in Chap. 3, this results in a choice of specific shear viscosity $\eta/s=0.08$ for MC-Glauber initial conditions and the larger value $\eta/s=0.2$ for MC-KLN initial conditions. Both the QGP phase and the hadronic phase are evolved hydrodynamically; particle momentum distributions are calculated with the Cooper-Frye prescription, taking into account strong decays of all hadron resonances with masses up to 2.25 GeV.¹¹ From the resulting charged hadron distribution we calculate for each event the flow angles Ψ_n according to

$$v_n e^{in\Psi_n} = \frac{\int_{0.5 < |\eta| < 2.5} d\eta \int_{p_{\text{min}}} p_T dp_T d\phi_p e^{in\phi_p} \frac{dN_{\text{ch}}}{d\eta dp_T dp_T d\phi_p}}{\int_{0.5 < |\eta| < 2.5} d\eta \int_{p_{\text{min}}} p_T dp_T d\phi_p \frac{dN_{\text{ch}}}{d\eta dp_T dp_T d\phi_p}}, \quad (4.3)$$

employing the same pseudorapidity range $0.5 < |\eta| < 2.5$ and lower p_T cutoff $p_T > p_{\text{min}} = 0.5$ GeV as used in the experimental analysis [93].^{12,13} From these event plane angles we compute for each event $\cos(k_1 \Psi_{n_1} + \dots + k_m \Psi_{n_m})$ for the two-plane ($m=2$) and three-plane ($m=3$) correlations listed in Tables 1 and 2 of Ref. [93] and shown in the figures below, and then average this quantity over all events in the given centrality class. We compare these event-plane correlations with the corresponding correlations between the initial-state participant plane angles, Φ_n , calculated from the initial energy density profile of each propagated event according to Eq. (4.1) and then averaged over events in a similar way.

4.3 Results

Figures 4.1 and 4.2 show the initial and final state two-plane correlations, for the eight different combinations of angles and weight factors explored by the ATLAS experiment [93]. Each correlation function is plotted against collision centrality, with peripheral collisions (small N_{part} values) on the left and central collisions (large N_{part}) on the right. Fig. 4.1 shows that several

¹⁰As mentioned in Chap. 3, it was realized later that neither the MC-Glauber model nor the MC-KLN model can give a complete description to all the flow data, but the transition to the emerging new initial-condition models had not happened when this thesis was written; the only initial-condition models that are available to us are the MC-Glauber and the MC-KLN models.

¹¹We found, however, that the event-plane correlations discussed below are almost identical for all particle species, so including resonance decays is not essential for this work.

¹²The ATLAS results were obtained with two independent methods: (a) using a calorimetric measurement of transverse energy E_T over rapidity range $0.5 < |\eta| < 4.8$, and (b) using charged particle tracks with $p_T > 0.5$ GeV and $0.5 < |\eta| < 2.5$. The data from method (a) have better precision but are fully compatible with those from method (b), within error bars. Since we cannot simulate the calorimetric response of ATLAS theoretically, we compute the event-plane correlations according to method (b), but compare them in the figures to the more precise data obtained from method (a).

¹³It was however realized only recently that the flow analysis performed by the ATLAS collaboration suffers from inaccuracies caused by the event-plane method, and an analysis with the scalar-product method yields much better agreement between theory and experimental data [94].

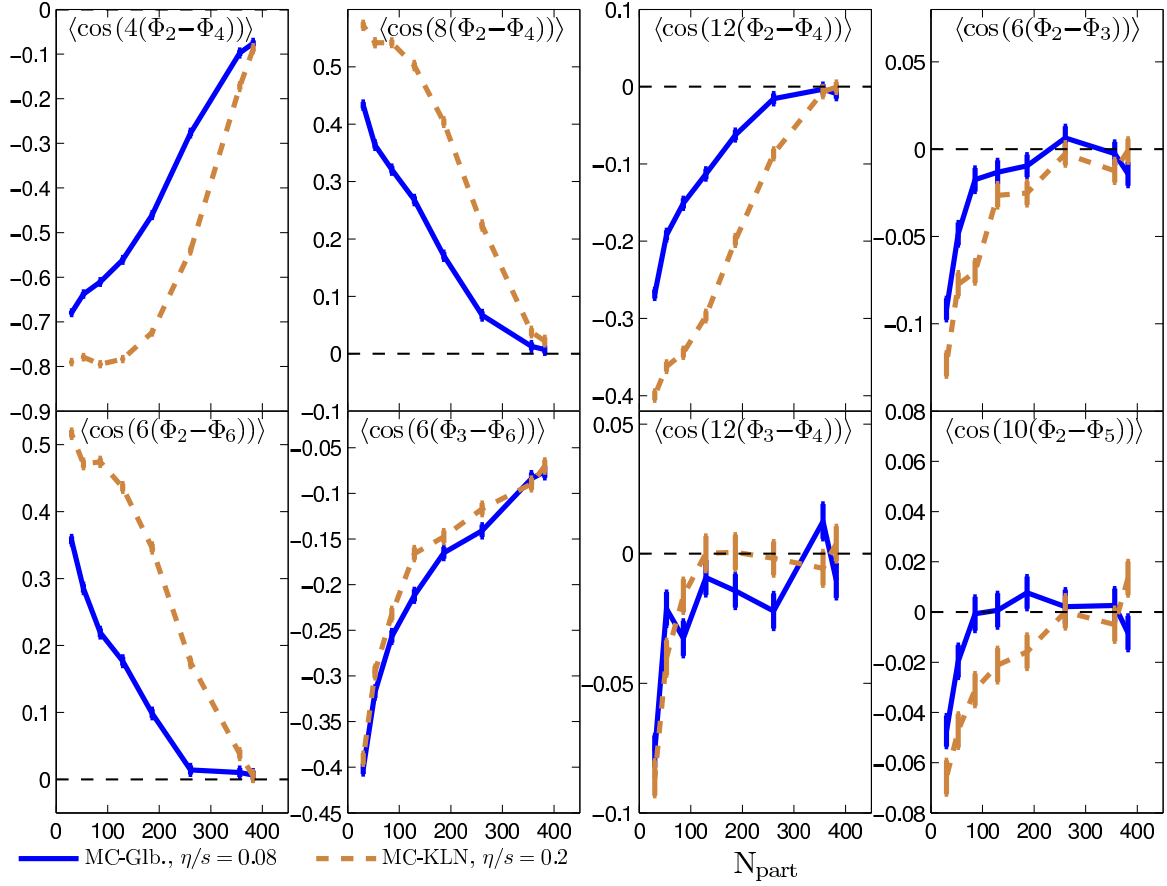


Figure 4.1: Two-plane correlations $\langle \cos(jk(\Phi_n - \Phi_m)) \rangle$, where j is an integer and k is the least common multiple (LCM) of n and m [90, 92], between pairs of participant-plane angles $\Phi_{n,m}$ for the harmonics (n, m) and multipliers j studied in Ref. [93]. Solid (dashed) lines show results for initial density profiles obtained from the MC-Glauber (MC-KLN) model. From [84].

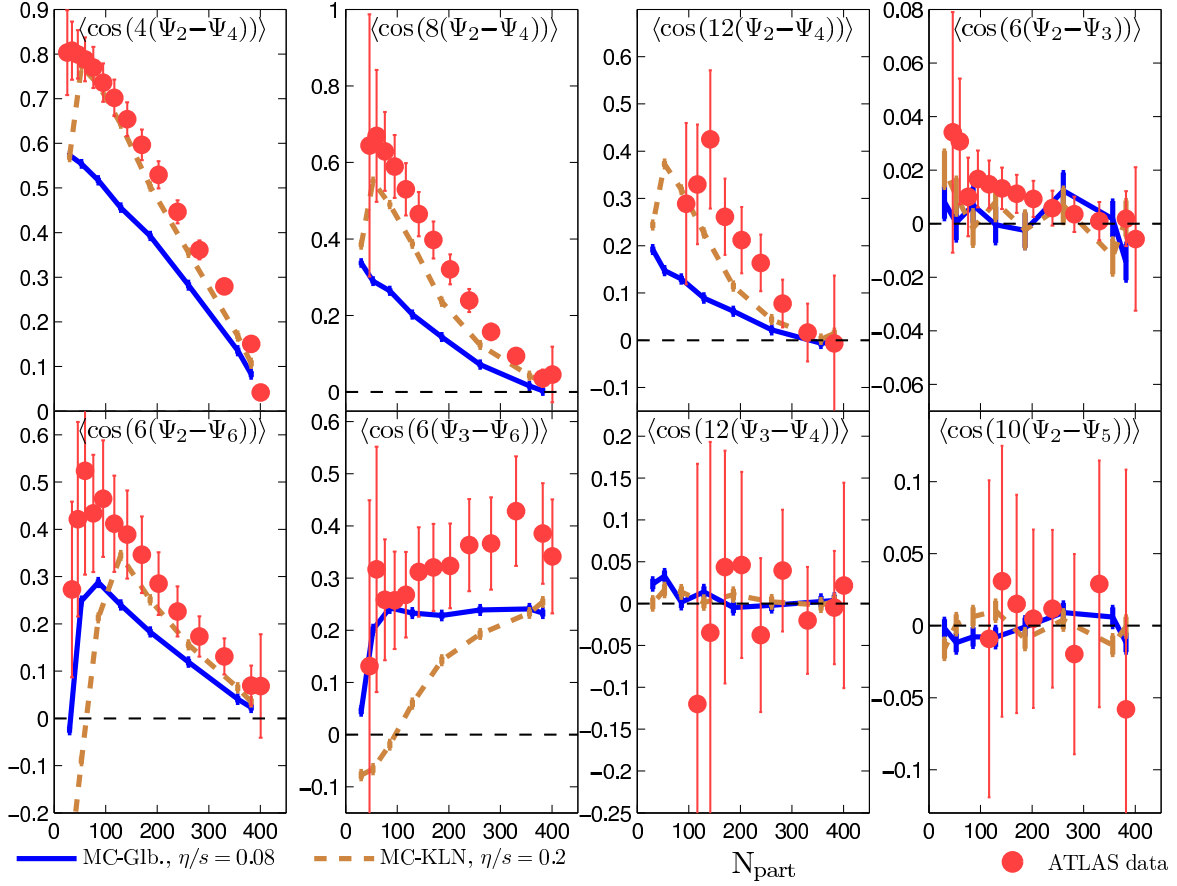


Figure 4.2: Similar to Fig. 4.1, but for the corresponding final-state event-plane angles $\Psi_{n,m}$. Filled circles show the experimental values measured by ATLAS [93]. The MC-Glauber (solid) and MC-KLN (dashed) initial profiles used in Fig. 4.1 were propagated individually using viscous hydrodynamics with $\eta/s=0.08$ and 0.2 , respectively. From [84].

of these correlations are quite sensitive to the model used to generate the initial energy density profiles (MC-Glauber vs. MC-KLN). These model differences in the initial state manifest themselves in corresponding model differences between the final-state event-plane correlations shown in Fig. 4.2, but they are additionally modified by the different shear viscosities η/s (0.08 and 0.2, respectively) used to evolve the initial conditions from the two models. This is most clearly seen in the “3-6 correlation”, where the two models give almost identical initial-state participant-plane correlations $\langle \cos(6(\Phi_3 - \Phi_6)) \rangle$ (second lower panel from the left in Fig. 4.1) whereas the corresponding final-state event-plane correlators $\langle \cos(6(\Psi_3 - \Psi_6)) \rangle$ exhibit significant model differences. This demonstrates the sensitivity of these event-plane correlations to the specific shear viscosity of the expanding fireball medium.

It is worth emphasizing that several of these two-plane correlators exhibit dramatically different centrality dependences for the initial-state participant-plane and the final-state event-plane angles (see, for example, the upper left, two upper right and second lower left panels in Figs. 4.1 and 4.2). The difference is largest in peripheral collisions (small N_{part}). This effect is caused by a dynamical rotation of the event-plane angles during the hydrodynamic evolution, driven by large elliptic flow in non-central collisions which leads to mode coupling between the angles Φ_n and $\Phi_{n\pm 2k}$ (where k is an integer and the largest coupling coefficient should correspond to $k=1$).¹⁴

Figures 4.3 and 4.4 show a number of three-plane correlations studied by the ATLAS experiment [93], with the initial-state participant-plane correlators plotted in Fig. 4.3 and the corresponding final-state event-plane correlators in Fig. 4.4, together with the experimental data. Again, we observe characteristic sign changes between several of the initial-state correlations and their corresponding final-state correlators. Even if neither of the two initial-state models (MC-Glauber and MC-KLN) reproduces the experimental data exactly, we find it impressive that the hydrodynamic model reproduces all the qualitative features of the centrality dependences of the 14 different measured event-plane correlation functions correctly: where the data show strong (weak) correlations, the same is true for the theoretical results, and where the data show correlations that increase (decrease) from peripheral to central collisions, the same holds for the theoretical predictions, without any parameter tuning. This provides very strong support for the hydrodynamic model description of the fireball evolution from a new set of observables that is quite independent of all previously studied observables (p_T -spectra, anisotropic flow coefficients v_n , and HBT radii).

We note that the nonlinear mode coupling first discovered in [20] (see Chap. 2) and the event-plane rotations driven by this nonlinear effect, are key to the qualitative agreement between theory and data in Figs. 4.2 and 4.4. It was recently shown that the measured correlation can also be reproduced with the AMPT model [94], a microscopic model that also features strong collective flow and an approach to approximate local thermal equilibrium [96]. We doubt that a similar agreement can be obtained with dynamical models that do not rely on a large degree of local thermalization in the expanding fireball, or from an approach based on linear [40, 88, 97] hydrodynamic response to the initial-state density fluctuations. Inclusion of first-order nonlinear terms in the hydrodynamic response [98] appears to yield event-plane correlations with qualitatively similar features as shown here [99], but quantitative success likely requires a numerical approach that fully accounts for the intrinsic nonlinearity of viscous hydrodynamics.

A closer look at Figs. 4.1 and 4.3 shows that the MC-KLN model tends to produce stronger correlations between the initial-state participant-plane angles Φ_n than the MC-Glauber model. We observe that hydrodynamic evolution translates the stronger initial-state participant-angle correlations into stronger final-state event-plane correlations, even though the signs of some of the correlators featuring the strongest correlation strengths flip between initial and final state. This is especially true for the two-plane correlations shown in Fig. 4.1, while the three-plane correlators

¹⁴This is different from the mode coupling at freeze-out [95] caused by an elliptic (quadrupole) deformation of the collective flow velocity appearing in the exponent of the Boltzmann factor in the Cooper-Frye expression for the final-particle momentum distribution that couples v_n with $v_{n\pm 2k}$. In contrast, in the presence of strong elliptic flow, the nonlinear hydrodynamic evolution *before freeze-out* leads to mode coupling between the modes n and $n\pm 2k$ (k integer) for the entire complex flow vector on the left-hand side of Eq. (4.2). We will come back to this point later in this chapter.

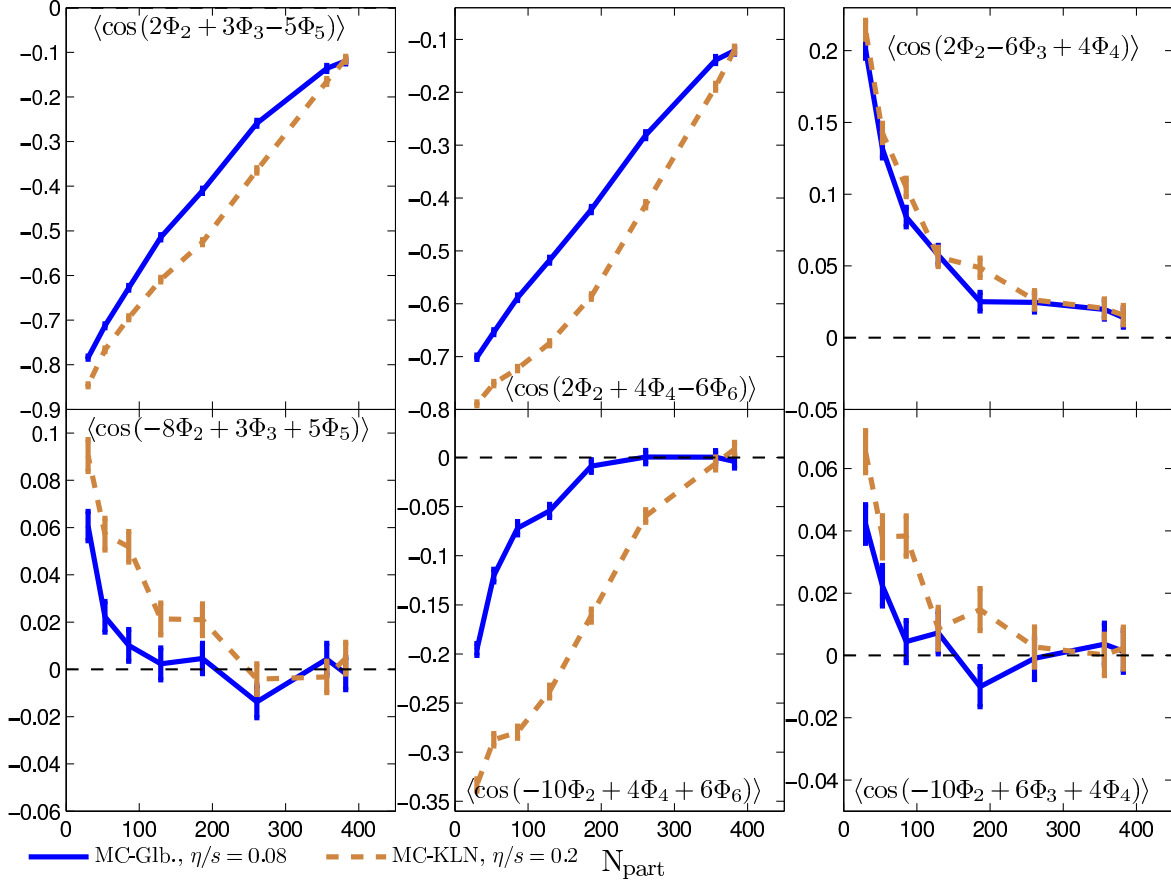


Figure 4.3: Similar to Fig. 4.1, but for selected [93] three-plane correlators of the form $\langle \cos(c_l l \Phi_l + c_n n \Phi_n + c_m m \Phi_m) \rangle$, where the c_i are integers satisfying $c_l l + c_n n + c_m m = 0$ [90]. From [84].

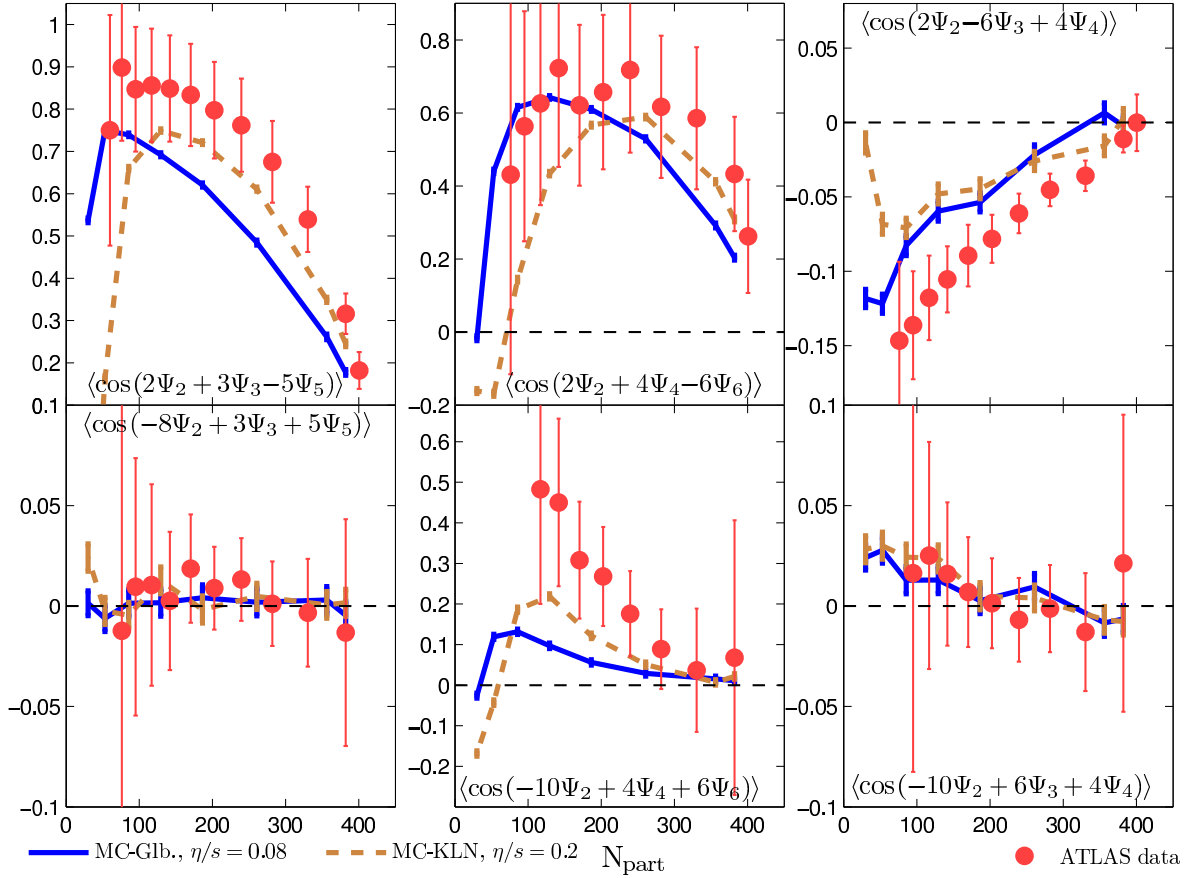


Figure 4.4: The final-state event-plane correlators corresponding to the initial-state correlators between three participant planes of different harmonic order shown in Fig. 4.3. Solid and dashed lines show results from viscous hydrodynamics with MC-Glauber and MC-KLN initial conditions, evolved with $\eta/s=0.08$ and 0.2 , respectively; filled circles show ATLAS data [93]. From [84].

exhibit some exceptions to this “rule” in the most peripheral collisions. The experimental data appear to prefer the stronger angle correlations in the initial profiles from the MC-KLN model, even though this model gives an elliptic-to-triangular flow ratio v_2/v_3 that is much larger than measured [44], caused by a larger $\varepsilon_2/\varepsilon_3$ ratio than in the MC-Glauber model [20] (see Chap. 2). These observations show that a combined analysis of both the anisotropic flow coefficients v_n and their associated flow angles Ψ_n (and the correlations among them) promises to yield powerful constraints on initial state models for the fireball energy density profiles created in heavy-ion collisions.

Finally, to demonstrate that the mode-coupling effect responsible for the observed event-plane angle correlations is dynamically generated during the hydrodynamic evolution rather than at the freeze-out stage, we show angle correlations similar to the ones shown above, but calculated using the flow velocity. We define the anisotropies of the transverse fluid velocity along the freeze-out surface as:

$$\bar{V}_n e^{in\bar{\Psi}_n} = \frac{\int_{\Sigma} |d^3\sigma| v_{\perp}^n e^{in\phi(v_{\perp})}}{\int_{\Sigma} |d^3\sigma| v_{\perp}^n} \quad (4.4)$$

In Fig. 4.5 we show the correlations between the so-defined flow velocity angles $\bar{\Psi}_n$ ¹⁵. It is seen that the correlations shown in Fig.4.5 between the anisotropy angles calculated using the fluid velocity are impressively similar to those shown in Figs. 4.1 and 4.2. They still show differences which should be attributed to either the “freeze-out mode-coupling” effect or a viscous correction to the equilibrium hadron emission function, or to the resolution effects discussed in [94]. Still the qualitative similarity between the correlation patterns calculated from the fluid velocity and from anisotropic flows from hydrodynamical simulations is an interesting finding in the following sense: the fluid velocity, which is a result of *only* the dynamical process, cares little about the mechanism for particle emissions and thus is not affected by final-stage effects (for example, resonance decay, or the choice of forms for the viscous correction terms to the distribution function, etc.). Therefore the fact that the correlations calculated from the fluid velocity are similar to those from the anisotropic flow data provides strong evidence that the correlations among anisotropic flow angles are generated during the dynamical evolution rather than at the freeze-out stage.

Even though more detailed studies will be necessary to fully explore the event-plane correlations discussed in this chapter, the calculations presented here suggest that very likely neither the MC-Glauber nor the MC-KLN initial conditions will ultimately provide a quantitatively satisfactory description of the experimental data from the ATLAS Collaboration [93]. While this statement is backed up by the study in Chap. 3, however, a recent study shows that the quantitative disagreement between theory results and experiments is very likely to be an artifact of the event-plane method used in the experimental flow analysis [94]. We have not performed the same analysis using our own simulated results, but no matter what the outcome might be, the question of how to turn the multitude of anisotropic flow observables (magnitudes and angles) that are already measured and will be measured into a focused search for the correct initial-state model is an interesting and welcome new challenge for the theory community.

¹⁵We checked that almost identical results are obtained if the power v_{\perp}^n is replaced by v_{\perp}^2 in the integrand of the numerator and the denominator in eq. (4.4).

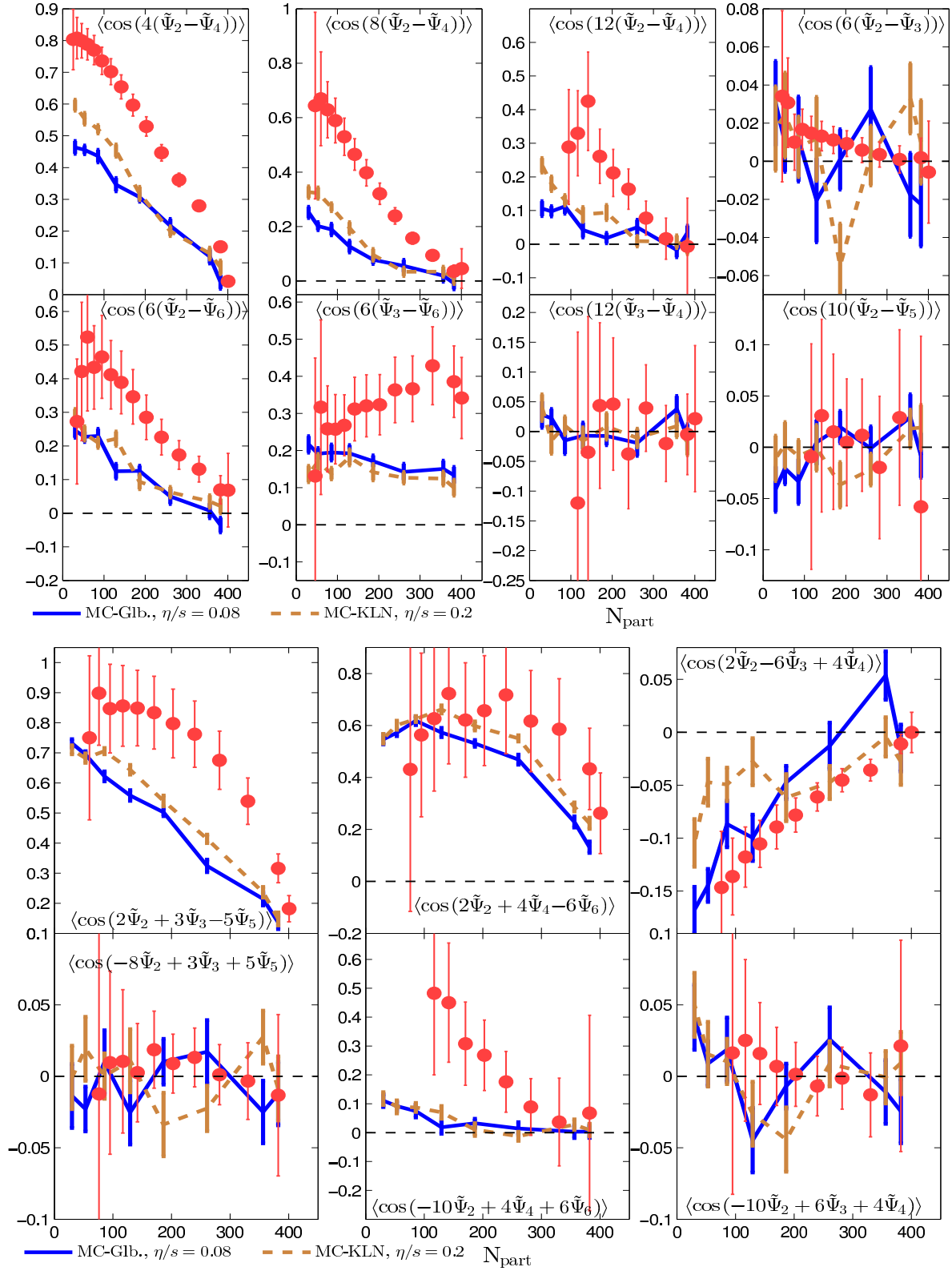


Figure 4.5: Correlations similar to Fig.4.2 (top) and Fig.4.4 (bottom), but with anisotropy angles calculated from fluid velocity, see text for details.

Chapter 5: Resonance decay contributions to higher-order anisotropic flow coefficients

The computation of resonance decays at the end of a hydrodynamic calculation in order to obtain the complete spectra of stable hadrons is numerically very costly and therefore often omitted. In this chapter, we show that, in hydrodynamic simulations for relativistic heavy-ion collisions, strong resonance decay calculations can be performed with fewer species of particle resonances than usually implemented while preserving good accuracy in single-particle spectra and flow anisotropies. Such partial resonance calculations boost computational efficiency by a factor of 10, which is essential for large scale event-by-event simulations. The material in this chapter is based on [100].

5.1 Chapter introduction

In event-by-event hydrodynamic simulations, due to the limited number of final-state particles in each event, observables can be measured with good statistical precision only as ensemble averages, which requires the simulation of a large number of events. Due to algorithmic progress over the last few years, the hydrodynamic evolution part is no longer the bottleneck in such event-by-event studies; at least for (2+1)-dimensional simulations (which assume longitudinal boost-invariance), the largest fraction of the computer time is spent converting the hydrodynamic output into final particle distributions, either on a “switching surface” between a macroscopic hydrodynamic description of the QGP fluid and a microscopic kinetic evolution of the dilute late hadronic-rescattering stage [55, 101] or on a “kinetic decoupling” surface marking the transition from a strongly coupled fluid directly to a noninteracting gas of free-streaming hadrons. The high numerical cost of this “hydro-to-particle conversion” process results from the large number of unstable hadron resonances that need to be included and whose post-freeze-out decays (mostly due to strong-interaction processes, although for some comparisons with experimental data that have not been corrected [102, 103] for weak-decay feed-down, weak and electromagnetic decays must also be considered) modify the finally observed particle distributions.

The hydro-to-hadron conversion algorithm is based on the Cooper-Frye formula [32], which expresses the final hadron momentum distribution as an integral of the local equilibrium (for ideal fluid dynamics) or slightly off-equilibrium (in viscous fluids) distribution function for the particle species in question over the conversion surface. Contributions to the spectra of experimentally measured *stable* particles from the strong decays of unstable resonances are then calculated from the single-particle spectra for the resonances [104]. This requires the calculation of the directly emitted (“thermal”) particle momentum distributions for all ~ 300 hadron species with mass typically up to 2 GeV via Cooper-Frye integrals, followed by the evaluation of the phase-space integrals [104] for all contributing decay channels. On a typical personal computer with a single CPU core in year 2012 this calculation takes about 2-3 hours, compared to 10-15 minutes for the preceding hydrodynamic evolution.

The ~ 2 GeV cutoff in resonance mass is dictated by requiring convergence of the relative particle yields of the measured hadronic final state after all unstable resonances have been allowed to decay. (The pion yields are especially sensitive to resonance feeddown.) Experimental evidence points to chemical decoupling at a temperature of $T_{\text{chem}} \approx 165$ MeV, i.e. close to the (pseudo)critical temperature for the quark-hadron phase transition [105]; at this temperature,

only resonances with masses above 2 GeV are sufficiently strongly Boltzmann-suppressed that their decay contributions to stable particle yields can be safely ignored.

Here we show that for an accurate determination of the pion and proton anisotropic flow coefficients v_n , a much smaller number of resonances needs to be taken into account than for the hadron yields, and that even the shape of the azimuthally averaged pion and proton transverse momentum spectra can be reliably determined by accounting for only a small subset of the ~ 300 resonance species mentioned above. These are the observables needed for an extraction of the QGP shear viscosity from heavy-ion collision experiments [30]. In this chapter, we show that by rearranging the resonance decay table in the order of decreasing importance for the calculation of p_T -spectra and v_n coefficients instead of increasing mass, good convergence for these observables can be achieved with a significantly reduced set of only about 20-30 resonances. This speeds up the computation by a factor of 10 – a significant gain in efficiency for the iterative determination of the QGP shear viscosity.

The analysis presented here uses final states generated with the same (2+1)-dimensional boost-invariant viscous hydrodynamic code `VISH2+1` for 200 A GeV Au+Au collisions at the Relativistic Heavy-Ion Collider (RHIC) and for 2.76 A TeV Pb+Pb collisions at the Large Hadron Collider (LHC) at various collision centralities, with previously determined [30,44,71] hydrodynamic input parameters. We find very similar results at both collision energies and therefore show here only plots for LHC collisions. Since the decay contributions from different resonances to the mentioned observables depend only on their decay channels and transverse momentum distributions, we expect little sensitivity to the assumption of longitudinal boost-invariance implicit in our approach and expect our reordered resonance decay tables to perform equally well for both (2+1)-d and (3+1)-d hydrodynamic simulations, and for a wide range of input parameters, such as QGP viscosity, thermalization time, initial entropy and energy density, etc.

5.2 Resonance ordering

The momentum distributions of directly emitted (“thermal”) resonances of species i are computed from the Cooper-Frye formula [32]:

$$E \frac{dN_i}{d^3p} = \frac{dN}{dy p_T dp_T d\phi_p} = \frac{g_i}{(2\pi)^3} \int_{\Sigma} p^\mu d^3\sigma_\mu (f_{i0} + \delta f_i). \quad (5.1)$$

Here Σ is the hydro-to-hadron conversion hypersurface, $d^3\sigma_\mu$ is its surface normal vector, $f_{i0} = 1/[e^{\beta(p \cdot u - \mu_i)} \mp 1]$ is the Bose or Fermi thermal equilibrium distribution function, and δf_i accounts for viscous corrections (driven by the viscous pressure tensor $\pi_{\mu\nu}(x)$ on the conversion surface) of the local phase-space distribution along Σ . We assume the quadratic form [106,107]:

$$\delta f = \frac{1}{2} f_0 (1 \pm f_0) \frac{p^\mu p^\nu}{T^2} \frac{\pi_{\mu\nu}}{(e + p)}. \quad (5.2)$$

Resonance decays increase the total yields of the stable hadrons and change their momentum distributions. For kinematic reasons, most of the light decay daughters have low transverse momenta, thus modifying the shape of light stable hadrons (pions, kaons) particle spectra mostly in the region $p_T < 1.5$ GeV [104]. We denote the total decay contribution to the momentum distribution of stable hadron species i by $\delta(dN_i/(dy d^2p_T))$, and the total spectrum (obtained by adding this to the thermally emitted spectrum $dN_i^{\text{th}}/(dy d^2p_T)$) by $dN_i^{\text{tot}}/(dy d^2p_T)$. (We here include only strong and electromagnetic decays.) The p_T -integrated total yield $\delta(dN_i/dy)$ of decay products of species i is denoted by δN_i , with $N_i^{\text{tot}} = N_i^{\text{th}} + \delta N_i = N_i^{\text{th}} + \sum_j \tilde{b}_{j \rightarrow i} N_j^{\text{th}}$, where the sum is over resonances j and $\tilde{b}_{j \rightarrow i}$ is the effective branching ratio (see Eq. (5.5) below) for the decay $j \rightarrow i$.

The contribution to δN_i from a particular resonance j is not only influenced by its mass (through the Boltzmann suppression factor $\sim e^{-E_j/T}$), but also by its spin degeneracy factor g_j and its branching ratio $\tilde{b}_{j \rightarrow i}$ into the decay channel that feeds stable particle species i . For each

name	mass (GeV)	total contribution (%)
ω	0.78260	15.398
ρ^0	0.77580	11.179
ρ^+	0.77580	11.098
.....

Table 5.1: Example of the π^+ contribution table for $T_{\text{conv}} = 120$ MeV.

stable hadron species i , it is therefore a different set of resonances that makes the most important contributions. Our goal is to order the resonances in decreasing order of importance for each stable particle species i . We here assume that the conversion surface has constant temperature T_{conv} . The different hadron resonances have T_{conv} -dependent nonequilibrium fugacities λ_j that ensure constant stable particle ratios equal to their chemical equilibrium values at T_{chem} and $\mu_B = 0$, independent of the hydro-to-hadron conversion temperature T_{conv} . While the actual fractions contributed by each resonance to the stable particle yields depend on T_{conv} , the ordering of these fractions is largely T_{conv} -independent.

We start from the resonance table in the AZHYDRO package,¹⁶ which includes 319 species of hadrons (counting different isospin states such as π^+ , π^0 , π^- as separate species) with rest masses up to 2.25 GeV. After fixing the value of T_{conv} we look up the non-equilibrium fugacity λ_j for each of these 319 species from the EOS s95p-PCE tables constructed in Ref. [11]. For each stable particle species i , we then generate an ordered list of resonances j that can decay directly into i . Note that, in this ordering, we account not only for direct decay contributions, but also for multi-step decay cascades, where j first decays into an unstable resonance k which further decays (directly or through more intermediate steps) into the stable species i .

Table 5.1 shows the beginning of this contribution table for positively charged pions, for a conversion temperature $T_{\text{conv}} = 120$ MeV. The “total contribution” percentages $c_{j \rightarrow i}$ in the third column are computed as

$$c_{j \rightarrow i} = \frac{N_i^{(j)}}{\sum_{j'} N_i^{(j')}} = \frac{\tilde{b}_{j \rightarrow i} N_j^{\text{th}}}{\sum_{j'} \tilde{b}_{j' \rightarrow i} N_{j'}^{\text{th}}}, \quad (5.3)$$

$$N_j^{\text{th}} = g_j m_j^2 \sum_{k=1}^{\infty} \frac{(\pm)^{k+1}}{k} \lambda_j^k K_2 \left(k \frac{m_j}{T} \right), \quad (5.4)$$

where the effective branching ratios $\tilde{b}_{j \rightarrow i}$ in Eq. (5.3) account for multi-step decay cascades as follows:

$$\tilde{b}_{j \rightarrow i} = b_{j \rightarrow i} + \sum_{k_1} b_{j \rightarrow k_1} b_{k_1 \rightarrow i} + \sum_{k_1, k_2} b_{j \rightarrow k_1} b_{k_1 \rightarrow k_2} b_{k_2 \rightarrow i} + \dots \quad (5.5)$$

The sum over k in (5.4) takes care of quantum statistical effects, with the upper (lower) sign for bosons (fermions). For all hadrons except pions, accurate results can be obtained by keeping only the first term $k=1$, i.e. by ignoring quantum statistical effects. Even for pions, a few k -terms suffice for good precision (in our calculations we truncate the series in (5.4) at $k=10$). The complete ordered resonance decay contribution tables for π^+ , K^+ , p , Λ , Σ^+ and Ξ^- are given in the Appendix (Sec. C). Horizontal lines in the tables indicate where the cumulative resonance decay contributions $c_i^{\text{cut}} = \sum_{j=1}^{j^{\text{cut}}} c_{j \rightarrow i}$ exceed certain threshold percentages (as indicated) of the total resonance decay contribution to species i .

In the following section, we show the stable hadron p_T -spectra and their anisotropic flow coefficients as functions of these cumulative decay contribution percentages c_i^{cut} in order to assess how

¹⁶AZHYDRO is available at <http://www.physics.ohio-state.edu/~froderma/>.

many resonances from these ordered decay tables should be included for an accurate computation of these observables.

5.3 Results and discussion

Using the ordered tables described in Sec. 5.2 and truncating the sum over resonance decay contributions at j_{cut} values corresponding to various different cumulative resonance decay contribution thresholds c_i^{cut} , we performed calculations for π^+ , K^+ , and p . We tested individual bumpy as well as (ellipticity-aligned and ensemble-averaged) smooth initial conditions at both RHIC and LHC energies for a variety of collision centralities. Since the results were found all to be qualitatively similar, we show only a small selection, focussing on pions and protons from one bumpy Pb-Pb event from the 0–10% centrality class and from the smooth averaged initial condition corresponding to the 60–70% centrality class, both at LHC energy ($\sqrt{s} = 2.76$ A GeV).

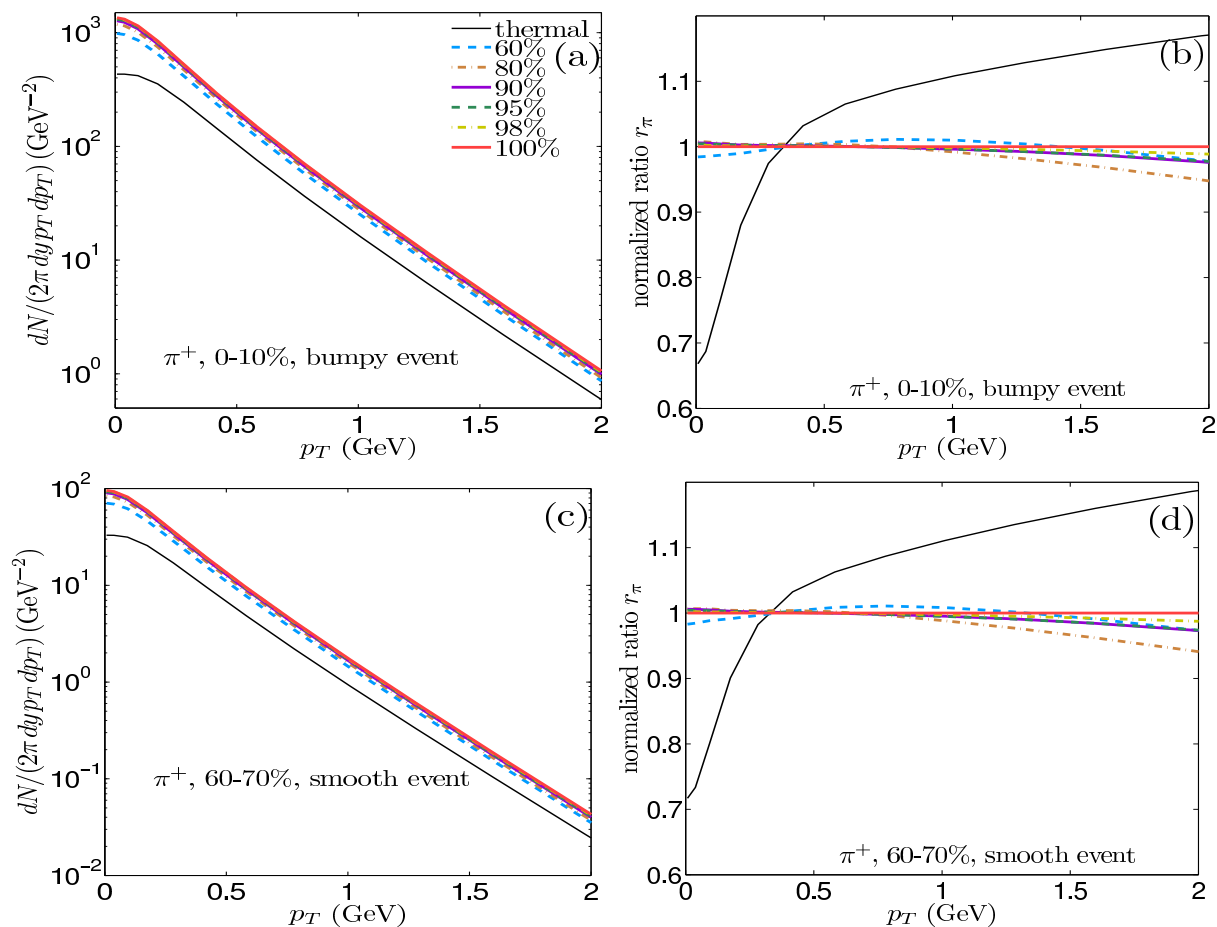


Figure 5.1: Transverse momentum spectra of π^+ , for a bumpy central (0-10% centrality, top panels) and a smooth peripheral (60-70% centrality, bottom panels) Pb-Pb collision at LHC energies. Panels (a) and (c) present the absolutely normalized spectra, while panels (b) and (d) show the normalized ratio $r_\pi(p_T)$ defined in Eq. (5.6). Different lines correspond to different cumulative resonance decay contributions between 0% (“thermal”) and 100%. See text for discussion. From [100].

Figure 5.1 shows the pion p_T -spectra for the bumpy central collision in the upper panels and the smooth peripheral event in the lower panels. The left panels show the usual semilogarithmic

plots of the absolutely normalized p_T -distribution. As is well-known, the directly emitted (“thermal”) pions constitute only about 50-60% of all observed pions, the rest coming from resonance decays. The “thermal” spectrum also has the wrong shape: resonance-decay pions predominantly contribute to the low- p_T part of the spectrum, making it steeper. However, this shape difference between the truncated and full resonance-decay spectrum disappears almost completely already when including only the 9 strongest decay channels, accounting for just 60% of the total pion yield from resonance decays. This is shown in the right panels of Fig. 5.1 where we plot the ratio

$$r_i(p_T) = \frac{\frac{dN_i^{\text{th}}}{dy p_T dp_T} + \frac{1}{\sum_{j=1}^{j_{\text{cut}}} c_{j \rightarrow i}} \sum_{j=1}^{j_{\text{cut}}} \frac{dN_i^{(j)}}{dy p_T dp_T}}{\frac{dN_i^{\text{th}}}{dy p_T dp_T} + \sum_{j=1}^{j_{\text{max}}} \frac{dN_i^{(j)}}{dy p_T dp_T}} \quad (5.6)$$

for $i = \pi$ as a function of p_T . ($N_i^{(j)}$ is the contribution to particle species i from decays of particle species j (see Eq. (5.3)), and j_{max} is the index of the last resonance in the ordered resonance decay table from Sec. 5.2.) The numerator includes only resonance decays up to j_{cut} , but we renormalize those decay contributions by the cumulative decay contribution c_i^{cut} corresponding to the same j_{cut} value. (c_i^{cut} is easily calculated from Eqs. (5.3,5.4) and directly obtained by summing the entries in the third column of the resonance decay table.) This renormalization corrects for the missing yield from the truncation of the decay table. The remaining effect (after missing yield renormalization) of the truncation on the *shape* of the p_T -spectrum is seen in panels (b) and (d) of Fig. 5.1: Whereas without any resonance decays the ratio $r_\pi(p_T)$ changes by almost a factor 2 between $p_T = 0$ and 2 GeV, this variation is reduced to less than 5% already for $c_\pi^{\text{cut}} = 60\%$ for both bumpy and smooth initial conditions in both central and peripheral collisions.

In Fig. 5.2, we show in the same way the proton spectra. Again the shape of the spectra can be accurately reproduced by taking into account a small fraction of all decay contributions (note the expanded vertical scale in Figs. 5.2b,d): after renormalization to account for the missing yield, just the 4 strongest of 75 decay channels (three charge states of the $\Delta(1232)$ resonance and one charge state of $\Delta(1600)$), corresponding to 60% of the total resonance decay yield for protons, reproduce the full proton spectrum with $< 5\%$ error between $p_T = 0$ and 2 GeV.

We conclude that, by accounting for the missing yield through appropriate renormalization, the correctly normalized total pion and proton spectra can be obtained, with shape errors $< 5\%$, by including only the strongest decay channels accounting for the leading 60% of the total resonance decay yields. A quick look at the tables in the Appendix shows that this will reduce the number of resonance decays (and thus computer time) by at least a factor 10.

We now proceed to a discussion of the differential and p_T -integrated anisotropic flow coefficients v_n defined by eq. (2.21) and eq. (2.22). In the formula, the spectrum $dN/(dy p_T dp_T d\phi_p)$ includes all contributions from the ordered resonance decay table for the considered stable species up to a certain threshold j_{cut} , with the truncated resonance decay contribution renormalized for the missing yield by a factor $1/c_i^{\text{cut}}$ as shown in the numerator of Eq. (5.6). In Figs. 5.3 and 5.4, we specify the cumulative decay contribution percentage c_i^{cut} to indicate the truncation level corresponding to each curve.

Figure 5.3 shows the differential elliptic and triangular flows for pions and protons, for one single bumpy central (0-10% centrality) event. We see that once again excellent agreement with the full resonance decay calculation is already obtained when including only the small subset of resonances that account for the top 60% of the resonance decay yields. We checked that this result is generic, i.e. it does not depend on the selected event (although the elliptic and triangular flows do).

For the p_T -integrated harmonic flow coefficients v_n , we show in Fig. 5.4 results for all harmonic orders from $n = 1$ to 9, again for pions and protons and for a bumpy central as well as a smooth peripheral event. For the smooth averaged initial condition, the odd harmonics vanish by symmetry. For fluctuating initial conditions, the v_n values shown here and their relative size depend

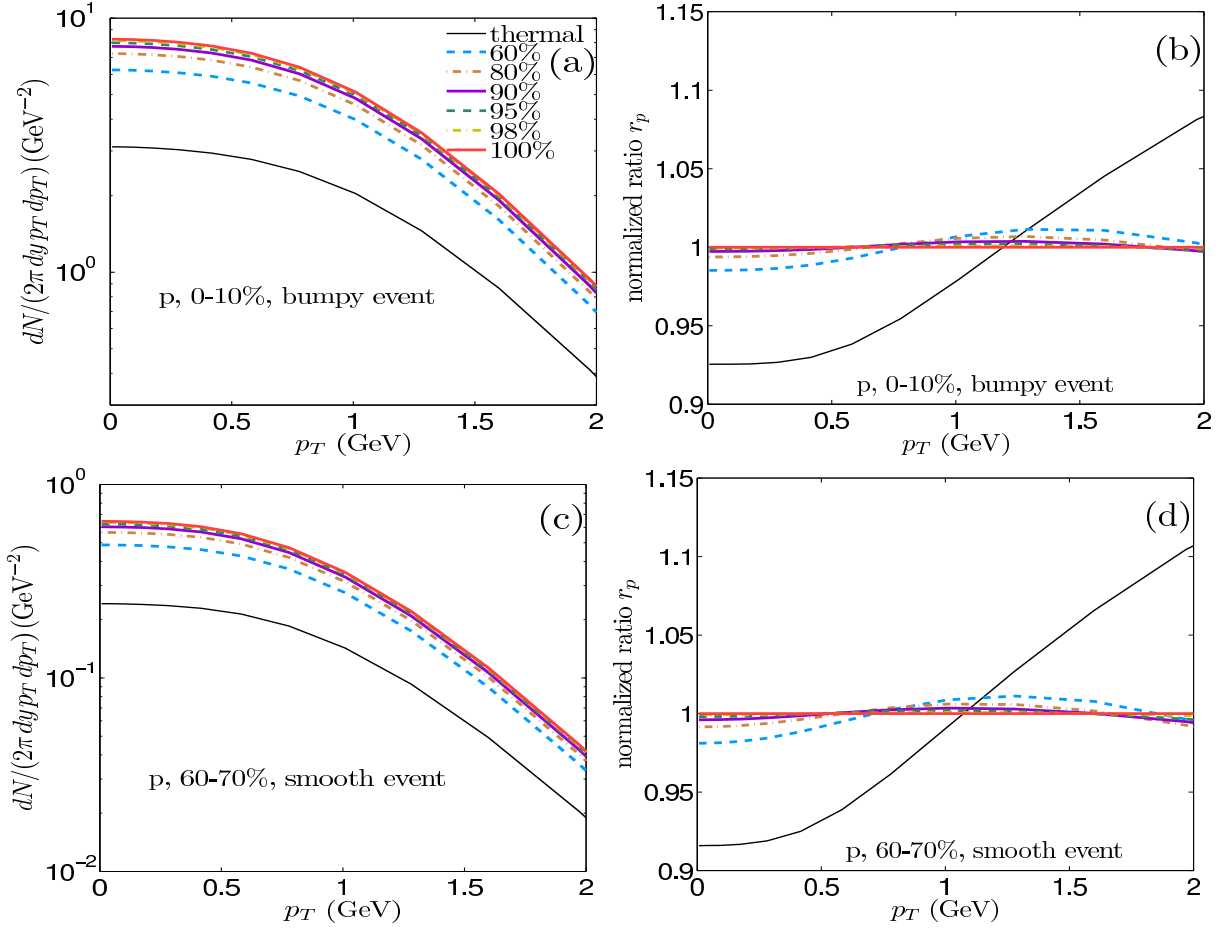


Figure 5.2: Same as Fig.5.1, but for protons. From [100].

on the randomly selected event. All plots shown in this chapter are based on one and the same bumpy central collision event.

For each harmonic order n , Fig. 5.4 shows two sets of results. The left set corresponds to results obtained by using the truncated resonance decay spectra shown in Figs. 5.1a,c and 5.2a,c, without missing yield renormalization. The right set uses the renormalized truncated decay spectra as defined in the numerator of Eq. (5.6). One observes a much faster convergence towards the full result in the right sets than in the left sets. The reason is that, by renormalizing the truncated resonance decay contributions for the missing yield, the correct mixing ratio between direct thermal and indirect decay contributions is ensured and the shape of the total p_T -spectrum is approximated much more accurately than without renormalization (see Figs. 5.1b,d and 5.2b,d). Figure 5.4 demonstrates that, when using the renormalized truncated decay spectra, accounting for just the top 60% decay contributions (i.e. including only the 9 strongest decay channels contributing to pions and the 4 strongest decay channels contributing to the proton spectra) reproduces the full results for the harmonic flow coefficients v_n with excellent precision: the lines corresponding to different c_i^{cut} values $\geq 60\%$ are almost indistinguishable.

Future precision extractions of the QGP viscosity may require highly precise v_n values. For such a purpose one can adjust j_{cut} to include a larger fraction of all resonance decays if needed.

For a given precision, the required minimal j_{cut} truncation indices and cumulative resonance decay fractions c_K^{cut} for kaons lie between those for pions and protons. The c_i^{cut} for $i = \pi, K, p$ are almost identical at RHIC and LHC energies, i.e. only weakly sensitive to radial flow.

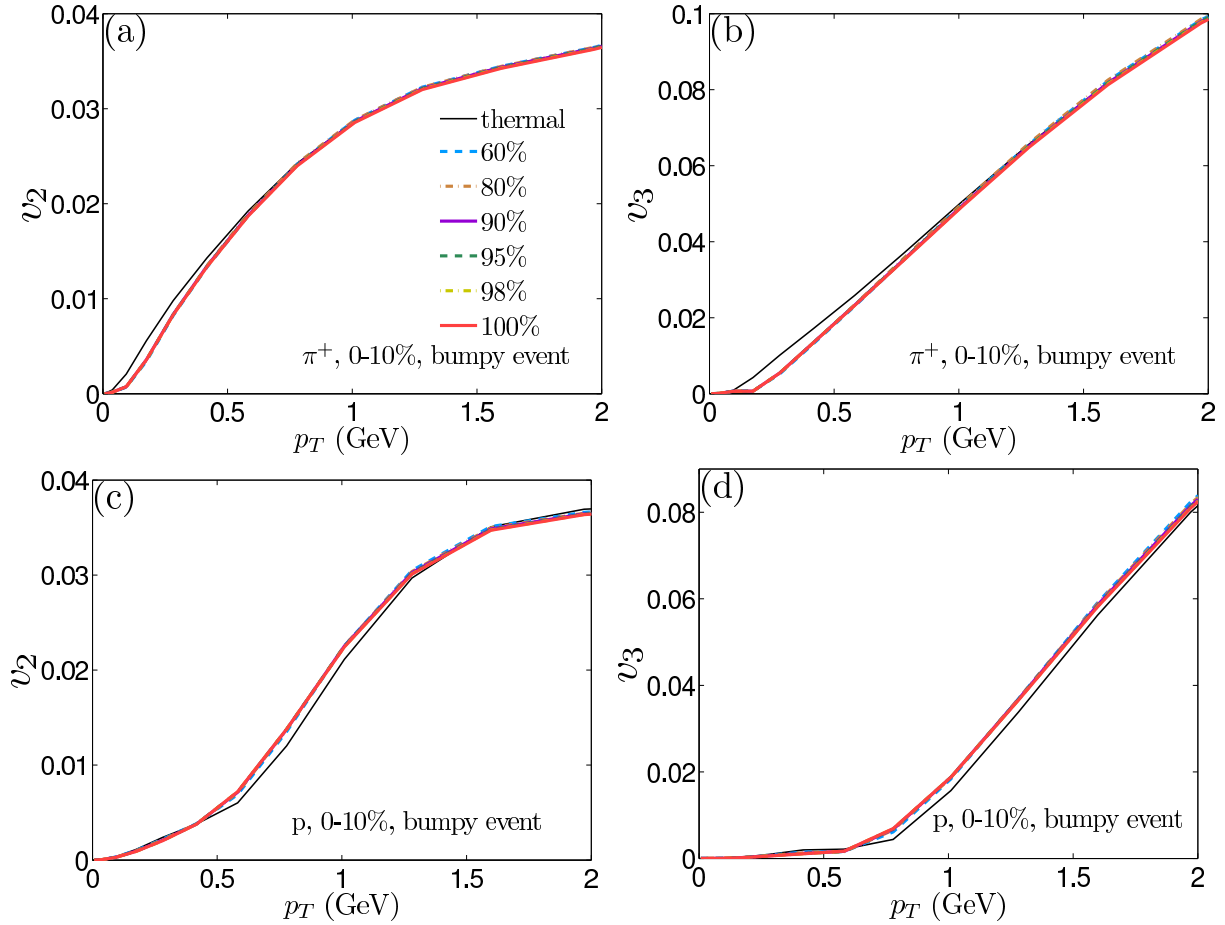


Figure 5.3: The differential elliptic (v_2 , left panel) and triangular flow (v_3 , right panel), for π^+ (upper panels) and p (lower panels), for one bumpy Pb-Pb event from the 0–10% centrality class at LHC energy. As in Fig. 5.1, lines of different styles and colors correspond to different cumulative resonance decay fractions. From [100].

5.4 Chapter conclusions

In this chapter, we showed that for a sufficiently accurate determination of the differential anisotropic flow coefficients $v_n(p_T)$, only those resonances need to be included that generate the top 60% of the largest decay contributions to the stable particle yields. For the single particle spectra, correct normalization of the total yield requires a renormalization of the truncated resonance decay yield as given in the numerator of Eq. (5.6). With this renormalization, good convergence of the slope of the pion spectra and of the p_T -integrated anisotropic flow coefficients v_n requires inclusion of only the 9 strongest contributing channels for pions and only the 4 strongest channels for protons, accounting in both cases for just 60% of the total decay yield. This reduces the number of resonance decay channels to be evaluated by a factor >10 , without loss of precision, leading to a similar reduction of the total computing time for the final stable hadron distributions.

In hybrid model calculations [101], the late hadronic stage is described microscopically by a Boltzmann cascade that propagates a reduced set of resonances until final kinetic decoupling. In this case, the spectra of all unstable resonances that are explicitly included in the Boltzmann cascade must be generated on the conversion surface. This is still only a small subset of all resonances included in the resonance decay tables. The optimal ordering of the resonance decay tables for the purpose of generating input for the late-stage Boltzmann cascade and the corresponding optimized truncation fractions c_i^{cut} are left as an open question.

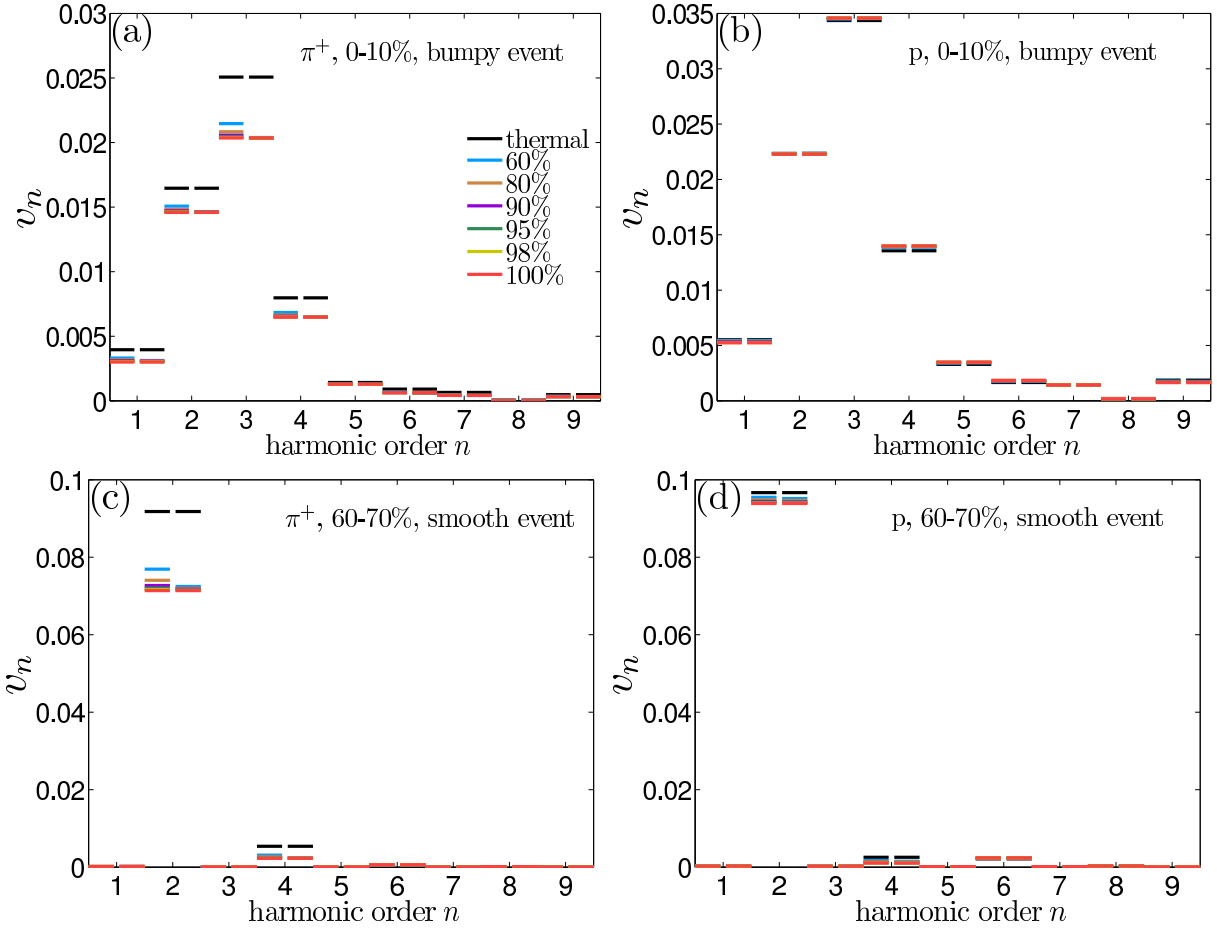


Figure 5.4: The p_T -integrated anisotropic flow coefficients v_n , $n = 1, \dots, 9$, for π^+ (a,c) and p (b,d), for a bumpy central (0-10%) collision event (a,b) and a smooth averaged peripheral (60-70%) collision event (c,d). Line colors and styles as in Figs. 5.1-5.3. For a discussion of the two sets of lines for each harmonic order n see text. From [100].

Chapter 6: Fluctuating flow angles and anisotropic flow measurements

Event-by-event fluctuations in the initial density distributions of the fireballs created in relativistic heavy-ion collisions lead to event-by-event fluctuations of the final anisotropic flow angles, and density inhomogeneities in the initial state cause these flow angles to vary with the transverse momentum of the emitted particles. In this chapter, we show that these effects lead to characteristically different transverse momentum dependencies for anisotropic flow coefficients extracted from different experimental methods. These differences can be used to experimentally constrain flow angle fluctuations in the final state of heavy-ion collisions which, in turn, are sensitive to the initial-state density fluctuations and the shear viscosity of the expanding fireball medium.

The material in this chapter is based on [108]; although for completeness, the whole material is included, only part of the content was contributed by the author.

6.1 Chapter introduction

Due to quantum fluctuations of the positions of the nucleons inside the colliding nuclei and of the positions of the colored quark and gluon constituents inside each nucleon, the density of the fireball matter created in collisions between ultra-relativistic heavy ions is highly inhomogeneous in the transverse plane, even for collisions with identical impact parameters. It has been shown in this thesis that the initial density inhomogeneities lead to highly anisotropic pressure gradients, causing an anisotropic collective expansion of the fireball, whose harmonic flow coefficients v_n and associated flow angles Ψ_n (both defined below) fluctuate from collision to collision [24].

While v_n fluctuations and the effect of their variance on different methods for measuring v_n have been studied extensively over the last few years, flow angle fluctuations and correlations have only recently found attention [20, 40, 84, 92, 93, 98, 109–111]. Gardim *et al.* [111] pointed out that, since the fluctuating flow angles Ψ_n depend on transverse momentum p_T and rapidity y , the usually assumed (and experimentally observed [112–115]) factorization of the azimuthal oscillation amplitudes of the two-particle angular correlations into a product of single-particle flow coefficients is slightly broken even if these correlations are entirely due to collective flow. We show here that the p_T -dependence and fluctuating nature of the flow angles Ψ_n also affects the p_T -dependence of the experimentally measured differential flow coefficients $v_n(p_T)$, and that it does so in different ways for different experimental methods of determining $v_n(p_T)$.

For each collision event, the momentum distribution of finally emitted particles can be characterized by a set of harmonic flow coefficients v_n and flow angles Ψ_n through the complex quantities (see also Chap. 2)

$$\begin{aligned} V_n &= v_n e^{in\Psi_n} := \frac{\int p_\perp dp_\perp d\phi e^{in\phi} \frac{dN}{dy p_\perp dp_\perp d\phi}}{\int p_\perp dp_\perp d\phi \frac{dN}{dy p_\perp dp_\perp d\phi}} \\ &\equiv \{e^{in\phi}\}, \end{aligned} \tag{6.1}$$

$$\begin{aligned} V_n(p_\perp) &= v_n(p_\perp) e^{in\Psi_n(p_\perp)} := \frac{\int d\phi e^{in\phi} \frac{dN}{dy p_\perp dp_\perp d\phi}}{\int d\phi \frac{dN}{dy p_\perp dp_\perp d\phi}} \\ &\equiv \{e^{in\phi}\}_{p_\perp}. \end{aligned} \tag{6.2}$$

Here ϕ is the azimuthal angle of the particle's transverse momentum p_T and the curly brackets denote the average over particles from a single collision.¹⁷ Eq. (6.1) defines the flow coefficients and associated flow angles for the entire event, whereas Eq. (6.2) is the analogous definition for the subset of particles in the event with a given magnitude of the transverse momentum p_\perp . We suppress the dependence of both types of flow coefficients on the rapidity y . As mentioned before, v_n are the integrated anisotropic flows and $v_n(p_\perp)$ are the differential flows. By definition, both v_n and $v_n(p_\perp)$ are positive definite. Hydrodynamic simulations show that in general the flow angles Ψ_n depend on p_\perp and that, as a function of p_\perp , $\Psi_n(p_\perp)$ wanders around the “average angle” Ψ_n that characterizes the integrated flow v_n of the entire event (see Fig. 6.1 below and also Fig. 2

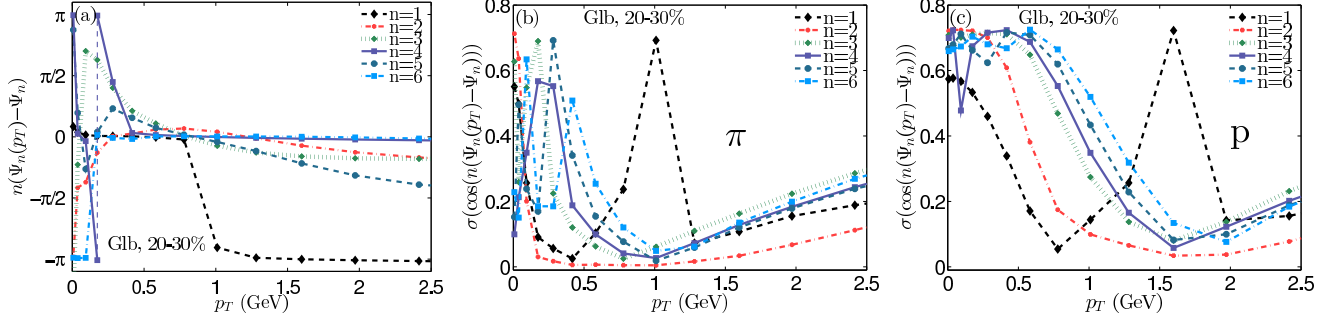


Figure 6.1: (a) p_\perp dependence of the flow angles $\Psi_n(p_\perp)$ relative to their average value Ψ_n ($n=1, \dots, 6$), for pions from a single but typical Pb+Pb collision event at LHC energies in the 20–30% centrality class, computed with the viscous hydrodynamic code VISH2+1 using an initial density profile from the MC-Glauber model and $\eta/s=0.08$. Note the flip of the dipolar ($n=1$) flow angle from 0 to $-\pi$ (happening around $p_\perp \sim 0.9$ GeV in this particular event); this reflects the constraint from total transverse momentum conservation [116]. (b,c) The variance σ of the cosine of the flow angle fluctuations (which is free of ambiguities of the angles by multiples of $2\pi/n$) as a function of p_\perp , for pions (b) and protons (c) from 11,000 hydrodynamic events in the same centrality class from which the event in (a) was taken. The variance is minimal around $p_\perp = 1$ GeV for pions and around $p_\perp = 1.5\text{--}2$ GeV for protons (except for the dipolar flow angle which flips by π exactly in that momentum region, see panel (a)). It is smallest for the elliptic flow angle fluctuation $\Psi_2(p_\perp) - \Psi_2$, and it becomes large for all flow harmonics at low p_\perp . From [108].

in Ref. [110]). Some theoretical and experimental definitions of v_2 have yielded values that turn negative over certain p_\perp ranges; we will see that this is due to defining the flows of each event relative to a fixed azimuthal angle (for example, relative to the direction of the impact parameter of the collision in theoretical calculations, or relative to the integrated elliptic flow angle Ψ_2 in experiment), and that the same thing can happen for higher-order harmonic flow coefficients when defining them relative to a fixed (i.e. p_\perp -independent) flow angle Ψ_n . The subject of this chapter is to elucidate the origins of such differences between different anisotropic flow measures and, in particular, the manifestation of event-by-event fluctuations of the p_\perp -dependent flow coefficients $v_n(p_\perp)$ and flow angles $\Psi_n(p_\perp)$ in different experimental flow measures.

¹⁷The average can include all charged particles or only particles of a specific identified species; we will not clutter our notation to account for these different possibilities.

6.2 Differential flows from the event-plane method and from two-particle correlations

The key experimental difficulty is that, due to the finite number of particles emitted in each collision, the left hand sides of Eqs. (6.1,6.2) cannot be determined accurately for a single event. The V_n are characterized by probability distributions that depend on the studied class of events (system size, collision energy and centrality) from which each collision takes a sample. Experimental flow measurements rely on a number of different methods that amount to taking different moments of that probability distribution by averaging over large numbers of events. Understanding the nature of these moments and reconstructing them from theoretical event-by-event dynamical simulations are essential steps in a meaningful comparison between theory and experiment.

Our main interest lies in the event-by-event fluctuations in the initial state of the collision fireball. These are primarily caused by the finite number of nucleons (or effective collision centers) in the colliding nuclei and unrelated to detector capabilities. In addition, there are fluctuations related to the finite number of particles produced (or detected) in the event which depend on collision energy and (in part) on detector capabilities. They reflect the fact that in practice the final state of the fireball evolution, which in principle (with the appropriate dynamical evolution model) can be *predicted* from the initial state with perfect precision, cannot be *measured* with perfect precision, due to finite sampling statistics. In this chapter, we are not interested in the fluctuations arising from finite sampling statistics; instead we focus on the hydrodynamical consequences of unavoidable event-by-event fluctuations in the initial state over which we have no control since they are rooted in the internal structure of the colliding nuclei, and which we therefore have to live with in any case even after we correct the measurements for finite final-state multiplicity effects.

The most extensively used experimental methods for measuring anisotropic flows are the event-plane and two-particle correlation methods [85]. We begin with a discussion of the latter. Two-particle azimuthal correlations receive contributions from the anisotropic collective flow as well as from non-flow correlations; the latter can be minimized by appropriate experimental cuts and corrected for [25, 85]. Again, we are not interested in non-flow correlations and will here simply ignore their existence, assuming that they have been corrected for in the experimental analysis.

Two-particle correlation measures of anisotropic flow are based on correlators of the type

$$\langle \{ e^{in(\phi_1 - \phi_2)} \} \rangle \quad (6.3)$$

where ϕ_1 and ϕ_2 are the azimuthal angles around the beam direction of two particles with transverse momenta p_{T1} and p_{T2} , and $\langle \dots \rangle$ denotes the average over $N_{\text{ev}} \gg 1$ events from a set of given characteristics (e.g. of collisions in a certain centrality bin),

$$\langle \mathcal{O} \rangle = \langle \{ \mathcal{O} \} \rangle := \frac{1}{N_{\text{ev}}} \sum_{i=1}^{N_{\text{ev}}} \{ \mathcal{O} \}_i, \quad (6.4)$$

whereas $\{ \dots \}_i$ is the average of the observable \mathcal{O} over all (or a specified subset of all) particle pairs in the event i :

$$\{ e^{in(\phi_1 - \phi_2)} \}_i = \frac{1}{N_{\text{pairs}}^{(i)}} \sum_{\text{pairs} \in i} e^{in(\phi_1 - \phi_2)}. \quad (6.5)$$

Different chosen subsets for the event-wise average $\{ \dots \}_i$ define different correlation measures for the anisotropic flow coefficients, as we will explain below. In this chapter, we will always correlate pairs of particles of the same kind (e.g. protons with protons or charged hadrons with charged hadrons, but not protons with charged hadrons), unless specifically stated otherwise. We will also assume that they have the same rapidity y ; the generalization to particles with different rapidities is straightforward, following the procedure discussed below when we go from particles with the same to particles with different p_{\perp} .

The magnitudes $v_n(p_\perp)$ of the anisotropic flow coefficients defined in Eq. (6.2) fluctuate from event to event according to some probability distribution $P(v_n(p_\perp))$. Let us denote the rms mean of this distribution by $v_n[2](p_\perp) := \sqrt{\langle v_n^2(p_\perp) \rangle}$, and similarly the rms mean for the integrated flow v_n by $v_n[2] := \sqrt{\langle v_n^2 \rangle}$. These rms means can be obtained from two-particle correlators of the type (6.3) as follows:

$$\begin{aligned} v_n^2[2](p_\perp) &= \langle \{e^{in(\phi_1-\phi_2)}\}_{p_\perp} \rangle = \langle \{e^{in\phi_1}\}_{p_\perp} \{e^{-in\phi_2}\}_{p_\perp} \rangle, \\ v_n^2[2] &= \langle \{e^{in(\phi_1-\phi_2)}\} \rangle = \langle \{e^{in\phi_1}\} \{e^{-in\phi_2}\} \rangle. \end{aligned} \quad (6.6)$$

Note that for the differential flow in the first line of equation (6.6), both particles are taken from the same p_\perp bin, and that the event-wise pair averages $\{e^{in(\phi_1-\phi_2)}\}$ factorize in each event due to our assumptions (absence of non-flow two-particle correlations, independent hydrodynamic emission of particles 1 and 2). Due to $1 \leftrightarrow 2$ symmetry under particle exchange, the exponential can be replaced by the cosine, and we get

$$\begin{aligned} v_n^2[2](p_\perp) &= \left\langle \frac{\int d\Delta\phi \cos(n\Delta\phi) \frac{dN_{\text{pairs}}}{dy_1 dy_2 p_{T1} dp_{T1} p_{T2} dp_{T2} d\Delta\phi} \Big|_{p_{T1}=p_{T2}}}{\int d\Delta\phi \frac{dN_{\text{pairs}}}{dy_1 dy_2 p_{T1} dp_{T1} p_{T2} dp_{T2} d\Delta\phi} \Big|_{p_{T1}=p_{T2}}} \right\rangle, \\ v_n^2[2] &= \left\langle \frac{\int d\Delta\phi \cos(n\Delta\phi) \frac{dN_{\text{pairs}}}{dy_1 dy_2 d\Delta\phi}}{\int d\Delta\phi \frac{dN_{\text{pairs}}}{dy_1 dy_2 d\Delta\phi}} \right\rangle, \end{aligned} \quad (6.7)$$

where $\Delta\phi = \phi_1 - \phi_2$ and the pair distribution has already been integrated over the average angle $\tilde{\phi} \equiv (\phi_1 + \phi_2)/2$.

Note that in Eqs. (6.7), the single-event averages are normalized by the number of pairs in the event, before averaging over events. This is important: since the pair multiplicity fluctuates from event to event and within a multiplicity bin, and multiplicity anti-correlates with impact parameter with which the magnitudes of some of the anisotropic flow coefficients are geometrically correlated, this event-wise normalization avoids biasing the measured flow coefficients towards their values in events with larger than average multiplicity.

Our definition of the integrated flow $v_n[2]$ agrees with the standard definition for the ‘‘two-particle cumulant’’ flow $v_n\{2\}$ [117–119], but the same is not true for the differential flow $v_n[2](p_\perp)$ which differs from $v_n\{2\}(p_\perp)$. The experimental definition of $v_n\{2\}(p_\perp)$ is [117–119]

$$\begin{aligned} v_n\{2\}(p_\perp) &:= \langle \{e^{in\phi_1}\}_{p_{T1}} \{e^{-in\phi_2}\} \rangle / v_n\{2\} \\ &= \left\langle v_n(p_\perp) v_n \cos[n(\Psi_n(p_\perp) - \Psi_n)] \right\rangle / v_n[2]. \end{aligned} \quad (6.8)$$

Here only the first of the two particles within an event is taken from the desired p_\perp bin and particle species; it is correlated with *all* other particles detected in the event, with obvious statistical advantages compared with $v_n[2](p_\perp)$ which requires both particles to be of the same kind and from the same p_\perp bin. The normalization factor is the total rms flow of all charged hadrons. The last expression shows that $v_n\{2\}(p_\perp)$ reduces to $v_n[2](p_\perp) = \sqrt{\langle v_n^2(p_\perp) \rangle}$ if and only if the flow angle Ψ_n does not depend on p_\perp , the event-by-event fluctuations of $v_n(p_\perp)$ affect only its normalization but not the shape of its p_\perp dependence, and the v_n fluctuations of the particle species of interest are proportional to those of all hadrons. All of these assumptions are violated in hydrodynamic simulations of bumpy expanding fireballs. The difference between $v_n\{2\}(p_\perp)$ and $v_n[2](p_\perp)$, is thus sensitive to event-by-event fluctuations of the p_\perp -dependent difference $\Psi_n(p_\perp) - \Psi_n$ between the flow angle of particles with momentum p_\perp and the average event flow angle,¹⁸ in addition to the (largely independent) fluctuations in the magnitudes of v_n and $v_n(p_\perp)$.

¹⁸More precisely, $v_n\{2\}(p_\perp)$ depends on the difference between $\Psi_n(p_\perp)$ of the particles of interest and the average flow angle Ψ_n of all detected particles. We checked numerically that the average hydrodynamic flow angles Ψ_n for

Another approach to isolating effects arising from the p_{\perp} -dependence of the flow angles is a comparison of the p_{\perp} -dependent rms flow $v_n[2](p_{\perp})$ with the so-called event-plane flow^{19,20}

$$\begin{aligned}
v_n\{\text{EP}\}(p_{\perp}) &:= \left\langle \frac{\int d\phi \cos[n(\phi - \Psi_n)] \frac{dN}{dy p_{\perp} dp_{\perp} d\phi}}{\int d\phi \frac{dN}{dy p_{\perp} dp_{\perp} d\phi}} \right\rangle \\
&= \Re \left\langle \{e^{in\phi}\}_{p_{\perp}} e^{-in\Psi_n} \right\rangle = \Re \left\langle v_n(p_{\perp}) e^{in(\Psi_n(p_{\perp}) - \Psi_n)} \right\rangle \\
&= \left\langle v_n(p_{\perp}) \cos[n(\Psi_n(p_{\perp}) - \Psi_n)] \right\rangle.
\end{aligned} \tag{6.9}$$

The equality in the second line arises from Eq. (6.2). Here for each event the ‘‘average flow angle’’ Ψ_n is first obtained by computing the \mathbf{Q}_n vector [120]

$$\mathbf{Q}_n = Q_n e^{in\Psi_n} := \frac{1}{N} \sum_{k=1}^N \omega_k e^{in\phi_k} \tag{6.10}$$

(where N is the number of detected particles in the event) and determining its phase. In principle, different choices for the weights ω_k can be considered [85], but for consistency with Eq. (6.9) one must choose $\omega_k = 1$. The ‘‘average angle’’ Ψ_n for the event extracted from \mathbf{Q}_n in general depends on the types of particles included in the sum in Eq. (6.10). As noted in footnote 2, however, the average flow angle for particles emitted from a hydrodynamic source is (within numerical precision) the same for all particle species, and the precision of extracting Ψ_n in experiments can thus be maximized by including all detected particles in the \mathbf{Q}_n vector (6.10).²¹

The last line in Eq. (6.9) makes it clear that the differential event-plane flows $v_n\{\text{EP}\}(p_{\perp})$ are sensitive to the event-by-event fluctuations of the p_{\perp} -dependent flow angles $\Psi_n(p_{\perp})$ around the ‘‘average flow’’ angle Ψ_n . Just like the finite-number statistical fluctuations²² of the flow angle reconstructed from \mathbf{Q}_n around the ‘‘true’’ flow angle of the event, these fluctuations smear out the azimuthal oscillations of the transverse momentum spectra and thus reduce the oscillation amplitudes $v_n\{\text{EP}\}(p_{\perp})$. In contrast to the former, they arise from fluctuations in the initial state and thus cannot be eliminated by improving or accounting for the resolution of the measurement of

identified pions and protons agree with great precision with the average flow angles for all particles in the event: computing the ensemble average of $\langle \cos[n(\Psi_n^{\pi} - \Psi_n^p)] \rangle$ for all harmonics n and all collision centralities, we found deviations of less than 1–2% in all cases except for some of the high-order harmonics with $n > 6$, whose calculation is plagued by numerical errors at low $p_{\perp} \lesssim 0.2$ GeV arising from the finite grid spacing of our square numerical grid used in solving the hydrodynamic equations.

¹⁹One can replace the cosine function in this definition by the exponential, omitting taking the real part in the second line, since the flow-angle fluctuations are symmetrically distributed such that the imaginary part vanishes after taking the event average (this has been verified numerically).

²⁰Note that we define the n^{th} -order event-plane flow relative to the n^{th} -order flow plane Ψ_n , and not relative to the elliptic flow plane Ψ_2 as sometimes done.

²¹Since in this paper we ignore finite particle statistical fluctuations in the final state, we know Ψ_n with infinite precision for each particle species, and we will simply use these particle-specific values in our numerical results below.

²²Due to the finite number of particles detected in each event, the accuracy of determining Ψ_n is limited by finite number statistics, and an accurate experimental estimation of the event-plane flow $v_n\{\text{EP}\}$ requires an ‘‘event-plane resolution correction’’ [85]. As shown in [24, 25] (see also the discussion in [111]), which moment of the underlying v_n distribution is actually measured by the total event-plane flow $v_n\{\text{EP}\}$ depends on this event-plane resolution: for perfect resolution, $v_n\{\text{EP}\}$ approaches the average flow $\langle v_n \rangle$, whereas in the case of poor resolution, it is closer to the rms flow $v_n[2] = v_n\{2\}$ [24, 25]. The mathematical analysis in [25] applies only to the integrated flow which allows one to ignore the p_{\perp} -dependence of v_n fluctuations as well as initial-state-related, p_{\perp} -dependent fluctuations of the flow angles that are not caused by finite multiplicity in the final state. In view of the latter, event-plane resolution effects on differential flow measurements and their correction require a new analysis.

the final state. They carry valuable physical information about the initial state and the dynamics of its evolution into the final state.

We can remove the sensitivity of the measured quantity to the p_\perp -dependent fluctuations of the flow angle by first computing *for each event* the magnitude $v_n(p_\perp)$ of $\{e^{in\phi}\}_{p_\perp} = V_n(p_\perp)$, before summing over events:

$$\begin{aligned} \langle v_n(p_\perp) \rangle &= \langle |\{e^{in\phi}\}_{p_\perp} e^{-in\Psi_n}| \rangle = \langle |\{e^{in\phi}\}_{p_\perp}| \rangle \\ &= \left\langle \sqrt{\{\cos(n\phi)\}_{p_\perp}^2 + \{\sin(n\phi)\}_{p_\perp}^2} \right\rangle. \end{aligned} \quad (6.11)$$

Since the quantity inside the event average does not depend on the average flow angle Ψ_n , this observable is not subject to an event-plane resolution correction. However, due to finite multiplicity in the final state, the right hand side will still in general be positive and non-zero experimentally even if there is no underlying anisotropic flow in the event. Again, how to properly account for such finite sampling statistical effects requires additional analysis.

By comparing $\langle v_n(p_\perp) \rangle$ (6.11) with $v_n[2](p_\perp)$ (6.6, 6.7), $v_n\{2\}(p_\perp)$ (6.8), and $v_n\{\text{EP}\}(p_\perp)$ (6.9), we can experimentally assess and separate the relative importance of event-by-event fluctuations in the magnitudes and directions of the anisotropic flows as functions of p_\perp .

Let us now proceed to two-particle correlations between particles of different (but specified) momenta. Since in the first line of Eq. (6.7), both particles are taken from the same bin in p_\perp , the flow angle $\Psi_n(p_\perp)$ drops out from the expression. This is not true for azimuthal correlations between two particles with different p_\perp [111]. In this case, one finds [66, 111]

$$\begin{aligned} \tilde{V}_{n\Delta}(p_{T1}, p_{T2}) &:= \langle \{e^{in(\phi_1 - \phi_2)}\}_{p_{T1}p_{T2}} \rangle \\ &= \langle \{e^{in\phi_1}\}_{p_{T1}} \{e^{-in\phi_2}\}_{p_{T2}} \rangle = \langle V_n(p_{T1}) V_n^*(p_{T2}) \rangle \\ &= \langle v_n(p_{T1}) v_n(p_{T2}) e^{in(\Psi_n(p_{T1}) - \Psi_n(p_{T2}))} \rangle \\ &= \left\langle v_n(p_{T1}) v_n(p_{T2}) \cos[n(\Psi_n(p_{T1}) - \Psi_n(p_{T2}))] \right\rangle. \end{aligned} \quad (6.12)$$

Due to parity symmetry, $\tilde{V}_{n\Delta}(p_{T1}, p_{T2})$ is real: while the quantity inside the event average $\langle \dots \rangle$ is in general complex for each individual event, its imaginary part averages to zero when summed over many events.

To properly account for multiplicity fluctuations, in Eq. (6.12) the averages $\{ \dots \}_{p_{T1}}$ within an event are once again normalized by the total number of particles included in the average, similar to Eq. (6.7). For this reason, $\tilde{V}_{n\Delta}(p_{T1}, p_{T2}) = \langle \{\cos(n\Delta\phi)\}_{p_{T1}, p_{T2}} \rangle$ defined in Eq. (6.12) is not identical with the experimental quantity $V_{n\Delta}(p_{T1}, p_{T2})$, which is obtained from a Fourier decomposition with respect to the difference angle $\Delta\phi$ of the two-particle distribution obtained by summing over many events, without normalizing the contribution from each event by the corresponding event multiplicity [66, 112–115]. For a meaningful comparison between theory and experiment, one should either normalize on the experimental side the contribution from each event to the two-particle distribution by the number of pairs in the event, or weight the theoretical prediction for $v_n(p_{T1})v_n(p_{T2})e^{in(\Psi_n(p_{T1}) - \Psi_n(p_{T2}))}$ for each event i with a factor $N_{\text{pairs}}^{(i)}/\langle N_{\text{pairs}} \rangle$ before summing over events. We prefer the first option, since it avoids the geometric bias arising from the correlation between collision geometry and particle multiplicity.

Equation (6.12) makes it obvious that the two-particle correlation coefficient $\tilde{V}_{n\Delta}(p_{T1}, p_{T2})$ does not factorize into a product of single-particle anisotropic flow coefficients [111]. There are two contributions to this breaking of factorization: p_\perp -dependent event-by-event fluctuations of the magnitude of the flow coefficient v_n , and p_\perp -dependence of the flow angles Ψ_n [111] (which also fluctuate from event to event). It is possible to define a non-factorizing correlator that is only affected by the fluctuations of $v_n(p_\perp)$ but is insensitive to the flow angles:

$$\left\langle v_n(p_{T1}) v_n(p_{T2}) \right\rangle = \left\langle \sqrt{\{\cos(n\Delta\phi)\}_{p_{T1}, p_{T2}}^2 + \{\sin(n\Delta\phi)\}_{p_{T1}, p_{T2}}^2} \right\rangle. \quad (6.13)$$

It is obtained experimentally by first obtaining the magnitude of $\{e^{in\phi_1}\}_{p_{T1}}\{e^{-in\phi_2}\}_{p_{T2}}$ for each event, normalizing it to the number of pairs used for its computation, and then adding the results for many events. Its sensitivity to finite-number statistical effects should be similar to Eq. (6.11) and needs to be explored. By comparing the quantity $\tilde{V}_{n\Delta}(p_{T1}, p_{T2})$ from Eq. (6.12) with $\langle v_n(p_{T1})v_n(p_{T2}) \rangle$ from Eq. (6.13) one can assess the importance of the p_{\perp} -dependence and event-by-event fluctuations of the flow angles Ψ_n (which affect the former but not the latter).

6.3 The effect of flow fluctuations on differential v_n measures

In this section we compare the differential flows $v_n(p_{\perp})$ extracted from the 22,000 viscous hydrodynamic simulations per centrality bin of 2.76 A TeV Pb+Pb collisions at the LHC (11,000 each with MC-Glauber and MC-KLN initial density profiles) that were generated [84]. We use the Cooper-Frye prescription to compute from the hydrodynamic output on the freeze-out surface the single-particle distributions $dN/(dy p_{\perp} dp_{\perp} d\phi)$ as continuous functions of p_{\perp} and ϕ (i.e. we do not sample the distribution to generate a finite number of particles per event, but pretend that the spectrum is sampled infinitely finely – this avoids the need to correct for effects arising from finite-number statistics, such as imperfect event-plane resolution). All resonance decays are included in the final stable-hadron spectra. The details of the hydrodynamic simulations, initial conditions and freeze-out parameters are not important for the qualitative study presented here, but they can be found in Refs. [44, 71, 84]. Here we only note that MC-Glauber (MC-KLN) initial conditions were hydrodynamically evolved with specific shear viscosity $\eta/s = 0.08$ (0.2).

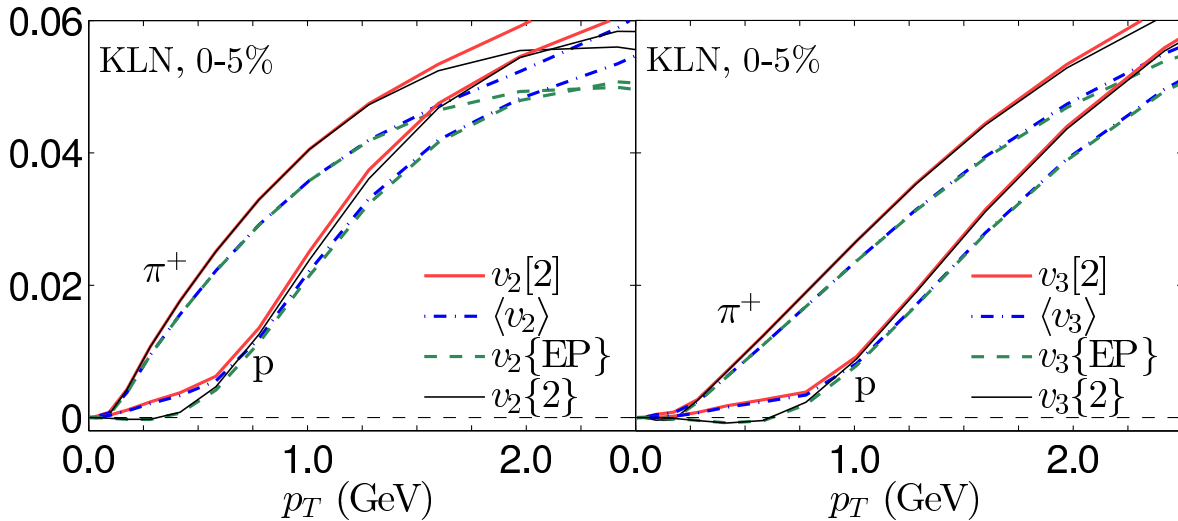


Figure 6.2: Comparison between the different definitions of the differential flows $v_n[2](p_{\perp})$ (6.6,6.7), $v_n\{2\}(p_{\perp})$ (6.8), $v_n\{EP\}(p_{\perp})$ (6.9), and $\langle v_n(p_{\perp}) \rangle$ (6.11), for pions and protons from central (0–5% centrality) Pb+Pb collisions at $\sqrt{s} = 2.76$ A TeV, computed with the viscous hydrodynamic code VISH2+1. See text for discussion. From [108].

We present results for pions and protons, representing light and heavy particle species. Qualitatively, although not quantitatively, the same generic features are observed with MC-KLN and MC-Glauber model initial density profiles, and we show examples of both. Figures 6.2 and 6.3 show elliptic and triangular flows in their left and right panels, for central (Fig. 6.2) and peripheral (Fig. 6.3) Pb+Pb collisions. The curves for $v_{2,3}[2]$ and $\langle v_{2,3} \rangle$, which are not affected by flow angle fluctuations (Eqs. (6.6) and (6.11)), should be compared with those for $v_{2,3}\{2\}$ and $v_{2,3}\{EP\}$,

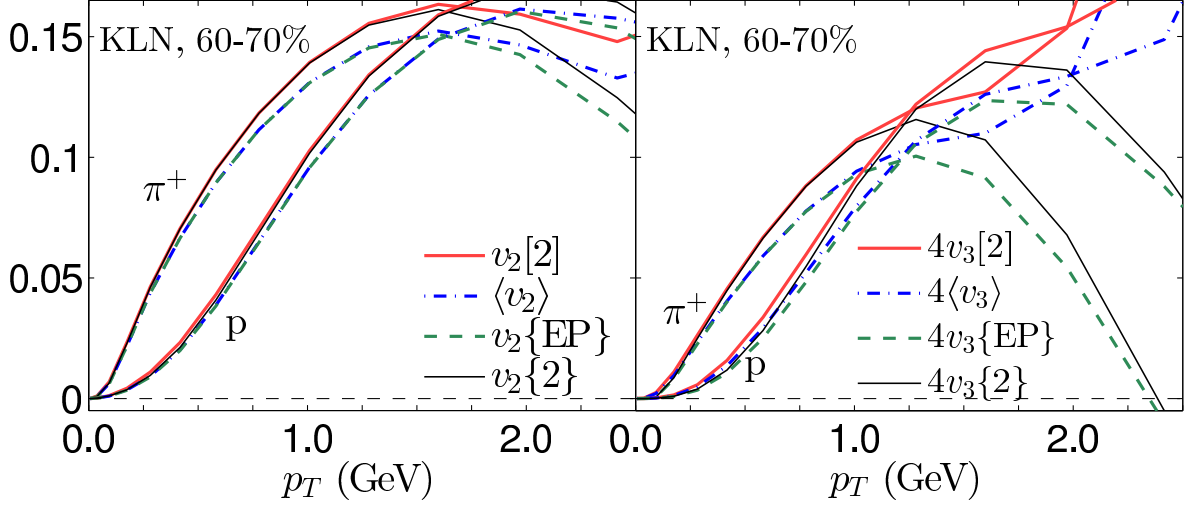


Figure 6.3: Same as Fig. 6.2, but for peripheral Pb+Pb collisions at 60–70% centrality. From [108].

which *are* affected by the p_{\perp} -dependence of the flow angles Ψ_n and their event-by-event fluctuations (Eqs. (6.8) and (6.9)): for protons with transverse momenta below about 1 GeV, flow angle fluctuations are seen to cause a significant suppression of the latter (in some cases even leading to negative elliptic flow values).²³ For the much lighter pions, flow angle fluctuation effects are almost invisible at low p_{\perp} . For protons they gradually disappear, too, as one goes from central (Fig. 6.2) to peripheral (Fig. 6.3) collisions.²⁴

Event-by-event fluctuations of the *magnitudes* of $v_{2,3}$ are accessible by comparing $\langle v_{2,3} \rangle$ with $v_{2,3}[2] = \langle v_{2,3}^2 \rangle^{1/2}$. When plotting the ratios $v_{2,3}[2](p_{\perp})/\langle v_{2,3} \rangle(p_{\perp})$ for central (0–5% centrality) collisions, where anisotropic flows are caused exclusively by fluctuations, with negligible geometric bias from a non-zero average deformation of the nuclear overlap region, we found for both pions and protons a constant (i.e. p_{\perp} -independent) value of $2/\sqrt{\pi} \approx 1.13$. This is expected [28, 121]: If the flow angle Ψ_n is randomly distributed relative to the reaction plane, the components of $V_n(p_{\perp})$ along and perpendicular to the reaction plane are approximately Gaussian distributed around zero, and the magnitude $v_n(p_{\perp})$ of the complex flow coefficient is Bessel-Gaussian distributed with $\sqrt{\langle v_n^2(p_{\perp}) \rangle} = \frac{2}{\sqrt{\pi}} \langle v_n(p_{\perp}) \rangle$ (see Eqs. (4) and (5) in Ref. [28]). A similar p_{\perp} -independent ratio is not observed at larger impact parameters: even for triangular flow, which continues to be fluctuation-dominated also at non-zero impact parameters, we observe deviations of the ratio $v_3[2](p_{\perp})/\langle v_3 \rangle(p_{\perp})$ from $2/\sqrt{\pi}$ at both low and high p_{\perp} ; for elliptic flow these deviations are larger and significant at all p_{\perp} .

Interestingly, for central collisions we found approximately the same constant value $2/\sqrt{\pi}$ for the ratio $v_{2,3}\{2\}(p_{\perp})/v_{2,3}\{\text{EP}\}(p_{\perp})$ (except near the p_{\perp} values where either the numerator or denominator passes through zero). Looking at the definitions (6.8) and (6.9), this suggests an approximate factorization of the p_{\perp} -dependent flow angle fluctuations (which enter through

²³Note that the factor $\cos[n(\Psi_n(p_{\perp}) - \Psi_n)]$ in Eqs. (6.8) and (6.9) is maximal if $\Psi_n(p_{\perp})$ is always aligned with Ψ_n . The suppression of, say, $v_n\{\text{EP}\}(p_{\perp})$ relative to $\langle v_n \rangle(p_{\perp})$ does therefore not indicate a definite momentum tilt of the emitting source at a given p_{\perp} relative to the average Ψ_n , but simply reflects a nonzero difference $\Psi_n(p_{\perp}) - \Psi_n$ that fluctuates from event to event, suppressing the value of $\cos[n(\Psi_n(p_{\perp}) - \Psi_n)]$ for either sign of the difference.

²⁴The curves shown in Figs. 6.2, 6.3 include the decay products from unstable hadronic resonances. We have observed that for protons the flow angle fluctuation induced difference at low p_{\perp} between $(v_{2,3}[2], \langle v_{2,3} \rangle)$ on the one hand and $(v_{2,3}\{2\}, v_{2,3}\{\text{EP}\})$ on the other hand doubles if only directly emitted (“thermal”) particles are included in the analysis. Resonance decays thus dilute the sensitivity of the proposed observables to flow angle fluctuations by about 50%.

the factor $\cos[n(\Psi_n(p_\perp) - \Psi_n)]$ that cancels between numerator and denominator if it fluctuates independently) from the fluctuations of the magnitude $v_n(p_\perp)$, as well as an approximate p_\perp -independence of the $v_{2,3}$ fluctuations.

To follow up on these observations and gain deeper insight into the relative importance of flow angle fluctuations in different p_\perp ranges, let us look at Figs. 6.2, 6.3 and note that the frequently measured quantity $v_{2,3}\{2\}(p_\perp)$ behaves like the event-plane flow $v_{2,3}\{\text{EP}\}(p_\perp)$ at low p_\perp and like the differential rms flow $v_{2,3}[2](p_\perp)$ at intermediate p_\perp . This suggests that it is dominated by flow angle fluctuations at low p_\perp and by fluctuations of the magnitude of $v_{2,3}(p_\perp)$ at higher p_\perp . In central collisions, the proton $v_{2,3}\{2\}(p_\perp)$ even turns negative at low p_\perp , whereas $v_{2,3}[2](p_\perp)$ is by definition always positive. A related observation is that the proton event-plane flow $v_{2,3}^p\{\text{EP}\}(p_\perp)$ in Fig. 6.2 approximately agrees with $v_{2,3}^p\{2\}(p_\perp)$ at low p_\perp (where flow angle fluctuations seem to have strong effects) but with the mean flow $\langle v_{2,3}^p(p_\perp) \rangle$ at higher p_\perp (where flow angle fluctuation effects are weak). This is reminiscent of the behavior of the p_\perp -integrated event-plane flow, which approaches the mean flow for good event-plane resolution. Flow angle fluctuations appear to have similar effects on flow measures as a decrease in flow angle resolution. The difference is that the former is a physical effect due to initial-state fluctuations, whereas the latter is a finite-sampling statistical effect in the final state and affected by detector performance.

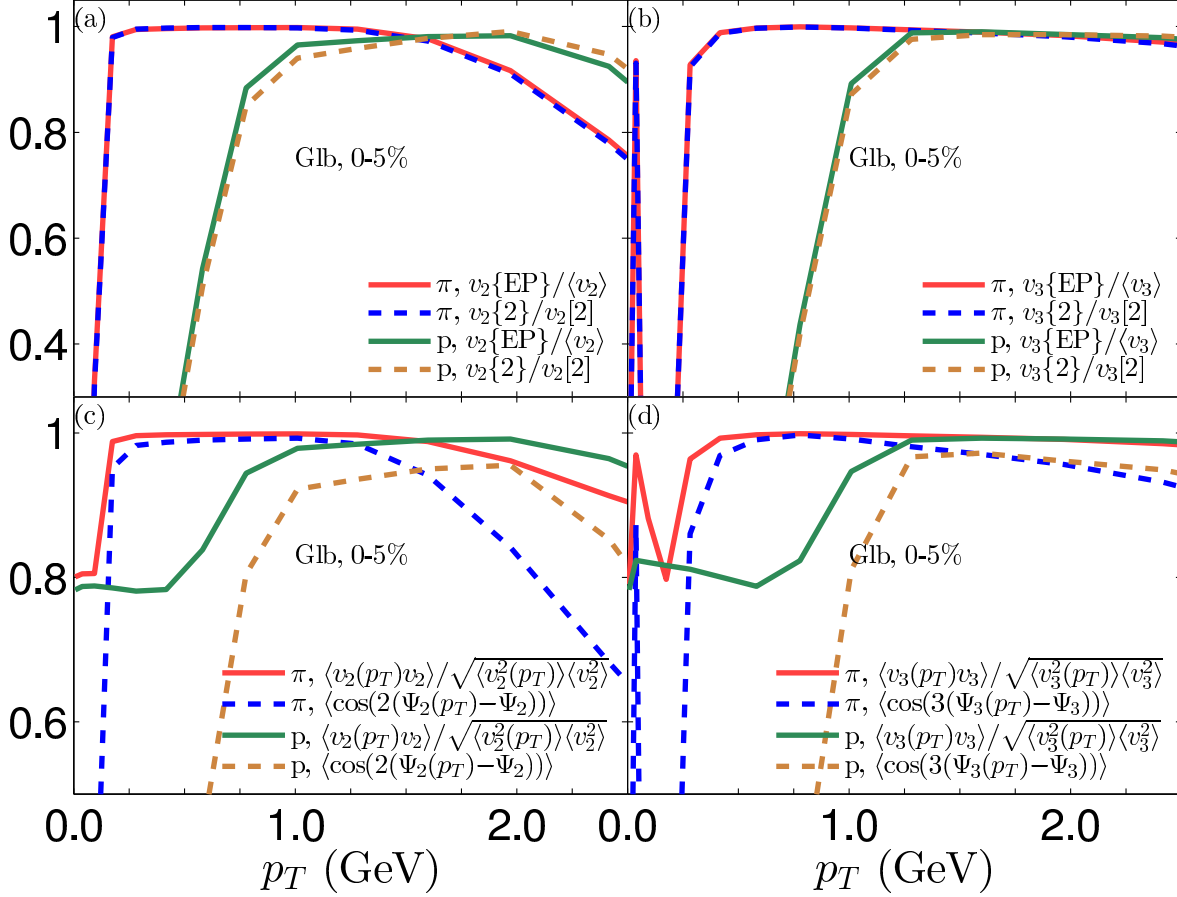


Figure 6.4: (a,b) Ratios of differently defined elliptic (a) and triangular (b) flow coefficients for pions and protons as functions of p_{\perp} . (c,d) p_{\perp} -dependence of the separate fluctuations of the magnitudes v_n and the angles Ψ_n for pions and protons as discussed in the text. All curves from viscous hydrodynamics with $\eta/s = 0.08$ for central 2.76 A TeV Pb+Pb collisions with MC-Glauber initial conditions. Results for MC-KLN initial conditions evolved with $\eta/s = 0.2$ look very similar. From [108].

To make these qualitative observations quantitative, we plot in the upper two panels of Fig. 6.4 the ratios $v_{2,3}\{2\}/v_{2,3}\{2\}$ and $v_{2,3}\{\text{EP}\}/\langle v_{2,3}\rangle$ as functions of p_{\perp} , for both pions and protons. (We focus here on the results from Fig. 6.2 for central collisions, where all anisotropic flows are fluctuation-dominated.) In each case the numerator is sensitive to the flow angle fluctuations while the denominator is not. However, numerator and denominator are also differently affected by fluctuations in the magnitudes of v_n . Both ratios are seen to behave very similarly, staying close to 1 at intermediate p_T but dropping steeply at low p_{\perp} and more moderately at high p_{\perp} . The steep drop at low transverse momenta sets in at $p_{\perp} \sim 1$ GeV for protons, but at much smaller $p_{\perp} < 0.25$ GeV for pions. We do not have a full understanding of this mass dependence, beyond the qualitative observation that the minimum of the variance of the flow angle fluctuations shown in Figs. 6.1b,c is shifted to higher p_{\perp} for protons compared to pions, and that quite generally strong radial flow shifts all flow anisotropies to higher p_{\perp} values for heavier particles.

The lower two panels of Fig. 6.4 demonstrate that the behavior of the ratios shown in the two upper panels is strongly dominated by flow angle fluctuations. The dashed lines in Figs. 6.4c,d show the flow angle fluctuations $\langle \cos[n(\Psi_n(p_{\perp}) - \Psi_n)] \rangle$ in isolation. Their p_{\perp} dependence alone is almost sufficient to completely explain the shape of the curves in panels (a) and (b). The solid lines in Figs. 6.4c,d show that at intermediate p_{\perp} fluctuations in the magnitudes of the p_{\perp} -dependent flow $v_n(p_{\perp})$ and the p_{\perp} -integrated v_n tend to be correlated with each other ($v_n(p_{\perp}) \propto v_n$) while

they appear to fluctuate more independently at low and high p_\perp . At high p_\perp this decorrelation contributes to the suppression of the ratios shown in panels (a,b). At low p_\perp , the decorrelation of the p_\perp -dependent flow *magnitude* fluctuations $v_n(p_\perp)$ from the p_\perp -integrated flow v_n does not become effective until after the ratios have already been suppressed by flow *angle* fluctuations, and its effect is therefore subdominant.

In summary, we see for central collisions that at low p_\perp the differences between $v_n\{2\}(p_\perp)$ and $v_n[2](p_\perp)$, as well as between $v_n\{\text{EP}\}(p_\perp)$ and $\langle v_n(p_\perp) \rangle$, are dominated by flow angle fluctuations, whereas at high p_\perp fluctuations of both the flow angles and flow magnitudes must be considered to explain their differences. At intermediate p_\perp , flow angle fluctuations appear to be unimportant, $v_n(p_\perp)$ fluctuates in sync with the p_\perp -integrated v_n , and the differences between $v_n\{2\}(p_\perp)$ and $v_n[2](p_\perp)$, as well as between $v_n\{\text{EP}\}(p_\perp)$ and $\langle v_n(p_\perp) \rangle$, vanish.

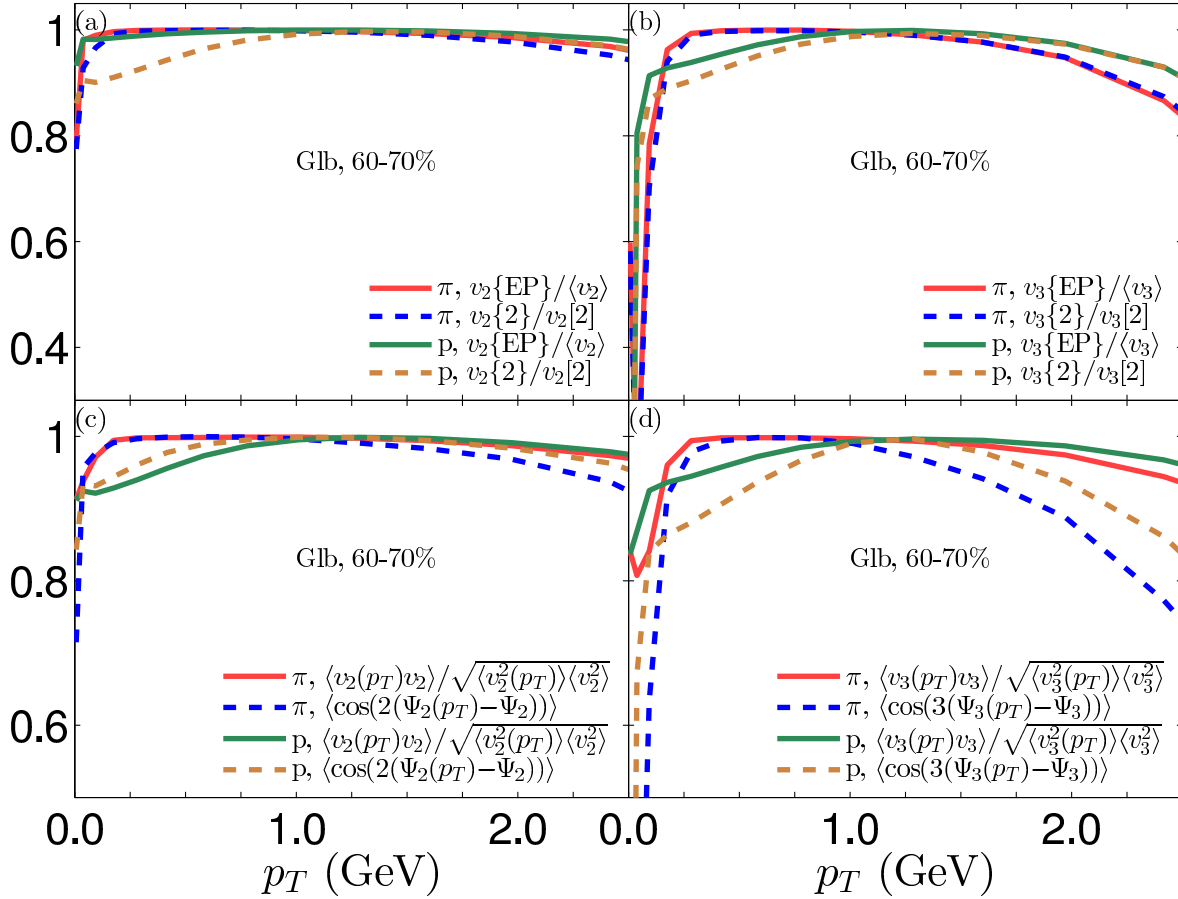


Figure 6.5: Same as Fig. 6.4, but for peripheral collisions at 60–70% centrality. From [108].

Figure 6.5 shows the same ratios as Fig. 6.4 for peripheral Pb+Pb collisions, again using MC-Glauber initial conditions with $\eta/s = 0.08$.²⁵ Compared to central collisions (shown in Fig. 6.4), the flow angle fluctuation effects at low p_\perp are much weaker and appear to be shifted to lower transverse momenta, for both pions and protons. At high $p_\perp \gtrsim 1$ GeV, Figs. 6.5c,d show that effects from fluctuations of the flow angles (dashed lines) dominate over those from fluctuations of the flow magnitudes (solid lines).

²⁵The main difference with results from MC-KLN initial conditions with $\eta/s = 0.2$ (not shown) is that the latter exhibit stronger suppression effects from the flow fluctuation factor $\cos[n(\Psi_n(p_\perp) - \Psi_n)]$ in the high- p_\perp region $p_\perp \gtrsim 1$ GeV (see also Fig. 6.3).

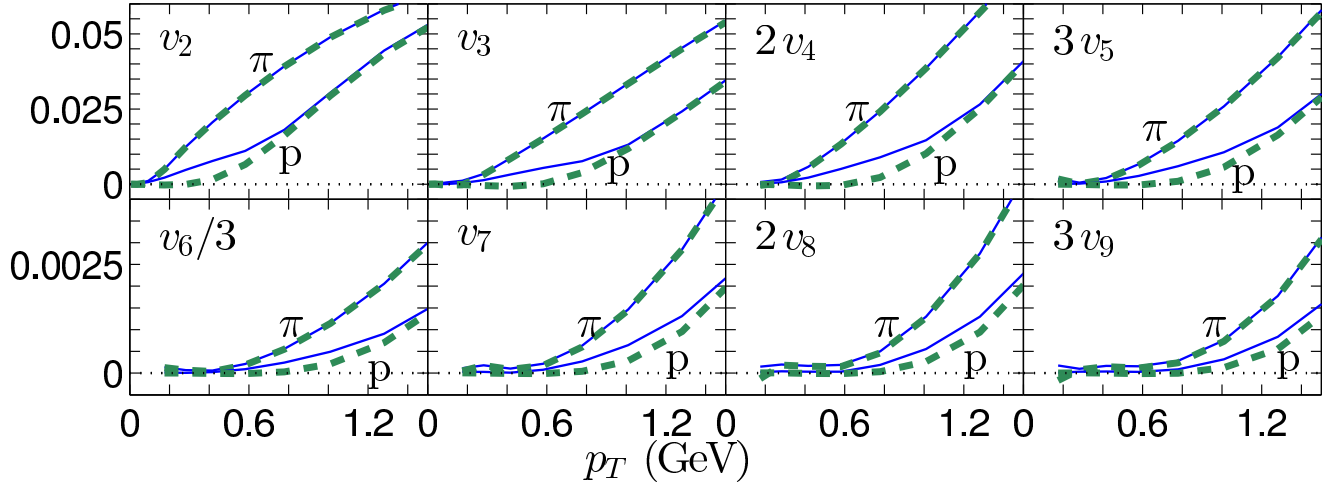


Figure 6.6: Similar to Figs. 6.2,6.3, but with MC-Glauber initial conditions for Pb+Pb collisions in the 0–10% centrality bin. For clarity only $v_n\{\text{EP}\}(p_\perp)$ (Eq. (6.9), thick dashed) and $\langle v_n(p_\perp) \rangle$ (Eq. (6.11), thin solid) are shown, but for all harmonics from $n=2$ to $n=9$ (scaled by appropriate factors for best visibility). This set of plots focusses on the low- p_\perp region $p_\perp < 1.5$ GeV, where the effects from flow angle fluctuations are strongest. See text for discussion. From [108].

Finally, in Figure 6.6 we explore (for near-central collisions) how the flow angle fluctuation effects, which push the event-plane flow $v_n\{\text{EP}\}$ at low- p_\perp below the value of the average flow $\langle v_n \rangle$, evolve as the harmonic order n increases. (For $n \geq 4$, we do not show results below $p_\perp = 0.2$ GeV for technical reasons explained in footnote 2.) For pions, flow angle fluctuations are invisible in the shown p_\perp region for all flow harmonics; for protons, they are clearly visible for all harmonic flows. The relative magnitude of their effect on the difference $\langle v_n \rangle(p_\perp) - v_n\{\text{EP}\}(p_\perp)$ at any fixed p_\perp decreases as n increases, but the difference remains nonzero over a larger p_\perp range for the higher harmonics.

6.4 Non-factorization of flow-induced two-particle correlations

The breaking of factorization of flow-induced two-particle correlations by flow fluctuations was first emphasized by Gardim *et al.* [111]. Their study was based on simulations using ideal fluid dynamics, which are here repeated with viscous fluid dynamics. A comparison of Figs. 6.7, 6.8 below with the plots shown in Ref. [111] shows that viscous effects reduce the amount by which event-by-event fluctuations break factorization. We here explore the relative role played in this context by fluctuations in the magnitudes and angles of the flows.

To this end we define the following two ratios, both symmetric in p_{T1} and p_{T2} :

$$\begin{aligned}
 r_n(p_{T1}, p_{T2}) &:= \frac{\tilde{V}_{n\Delta}(p_{T1}, p_{T2})}{\sqrt{\tilde{V}_{n\Delta}(p_{T1}, p_{T1})\tilde{V}_{n\Delta}(p_{T2}, p_{T2})}} \\
 &= \frac{\langle V_n(p_{T1})V_n^*(p_{T2}) \rangle}{\sqrt{\langle |V_n(p_{T1})|^2 \rangle \langle |V_n(p_{T2})|^2 \rangle}} \\
 &= \frac{\langle v_n(p_{T1})v_n(p_{T2}) \cos[n(\Psi_n(p_{T1}) - \Psi_n(p_{T2}))] \rangle}{\sqrt{\langle v_n^2(p_{T1}) \rangle \langle v_n^2(p_{T2}) \rangle}};
 \end{aligned} \tag{6.14}$$

$$\tilde{r}_n(p_{T1}, p_{T2}) := \frac{\langle v_n(p_{T1})v_n(p_{T2}) \cos[n(\Psi_n(p_{T1}) - \Psi_n(p_{T2}))] \rangle}{\langle v_n(p_{T1})v_n(p_{T2}) \rangle}. \tag{6.15}$$

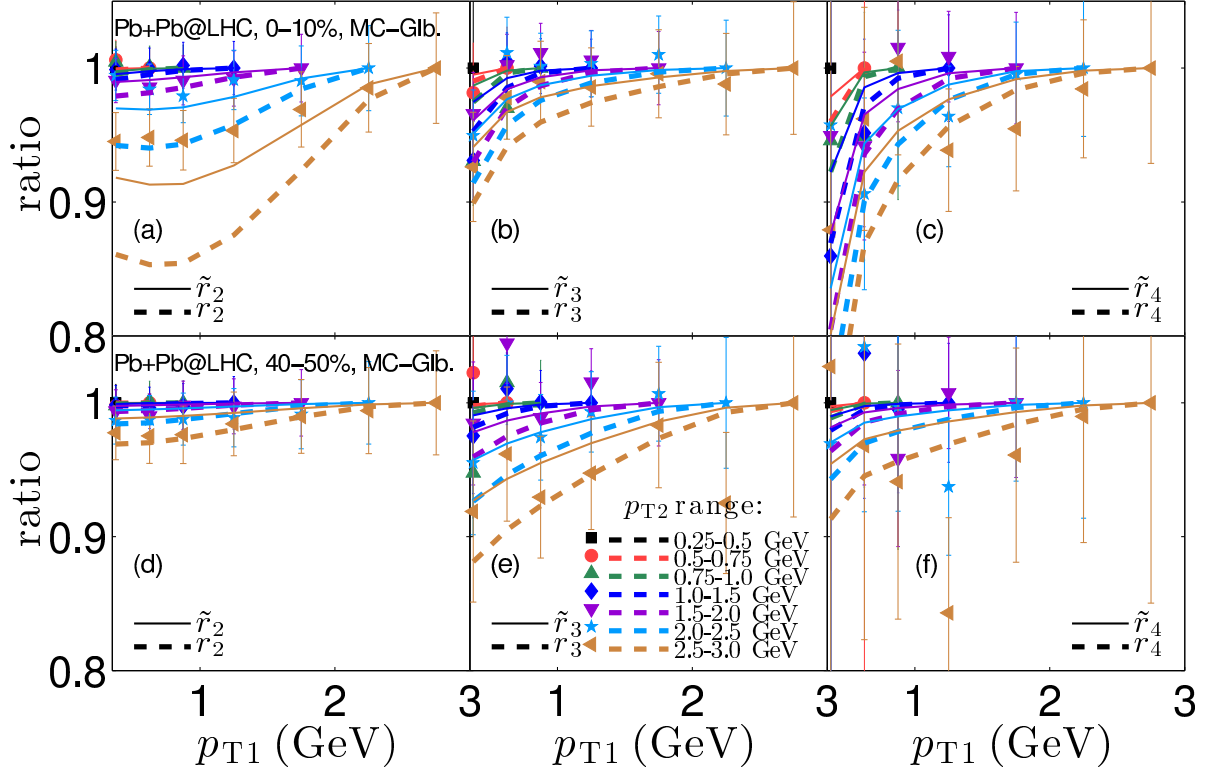


Figure 6.7: The ratios $r_{2,3,4}(p_{T1}, p_{T2})$ (thick dashed lines) and $\tilde{r}_{2,3,4}(p_{T1}, p_{T2})$ (thin solid lines), defined in Eqs. (6.14) and (6.15), as functions of p_{T1} for different p_{T2} ranges, as indicated. Filled symbols represent ALICE data for Pb-Pb collisions at $\sqrt{s} = 2.76$ A TeV [113]. The lines are the corresponding viscous hydrodynamic calculations with MC-Glauber initial conditions, using specific shear viscosity $\eta/s = 0.08$. Panels (a,b,c) show $r_{2,3,4}$ and $\tilde{r}_{2,3,4}$ for central (0–10%) collisions, panels (d,e,f) show the same ratios for peripheral (40–50%) collisions. From [108].

The ratio r_n , first introduced and studied with ideal fluid dynamics in [111], is sensitive to fluctuations of both the magnitudes $v_n(p_\perp)$ and angles $\Psi_n(p_\perp)$ of the complex anisotropic flow coefficients $V_n(p_\perp)$ defined in Eq. (6.2). The second ratio \tilde{r}_n , on the other hand, differs from unity only on account of flow angle fluctuations. By comparing the two ratios with each other and with experimental data, we can isolate the role played by flow angle fluctuations in the breaking of factorization of the event-averaged two-particle cross section. In the absence of non-flow correlations both ratios are always ≤ 1 .

Figures 6.7 show these ratios for all charged hadrons as functions of $p_{T1} \leq p_{T2}$ for fixed ranges of p_{T2} , indicated by different colors.²⁶ Figs. 6.7a,b,c focus on central, Figs. 6.7d,e,f on peripheral collisions; in both cases, we used MC-Glauber initial conditions and evolved them with VISH2+1 using $\eta/s = 0.08$ for the specific shear viscosity. In central collisions, the hydrodynamic simulations appear to overpredict the factorization breaking effects, while in peripheral collisions, theory and data agree somewhat better. More precise experimental data would be desirable. The comparison of r_n (dashed lines) with \tilde{r}_n shows that a significant fraction ($\sim 50\%$ or more) of the effects that cause the breaking of factorization arises from flow angle fluctuations. This seems to hold at all the transverse momenta shown in the figures. A comparison of the top and bottom rows of panels in Fig. 6.7 shows that factorization-breaking effects are stronger for harmonics that are fluctuation dominated (*i.e.* all harmonics in central collisions and the odd harmonics (especially

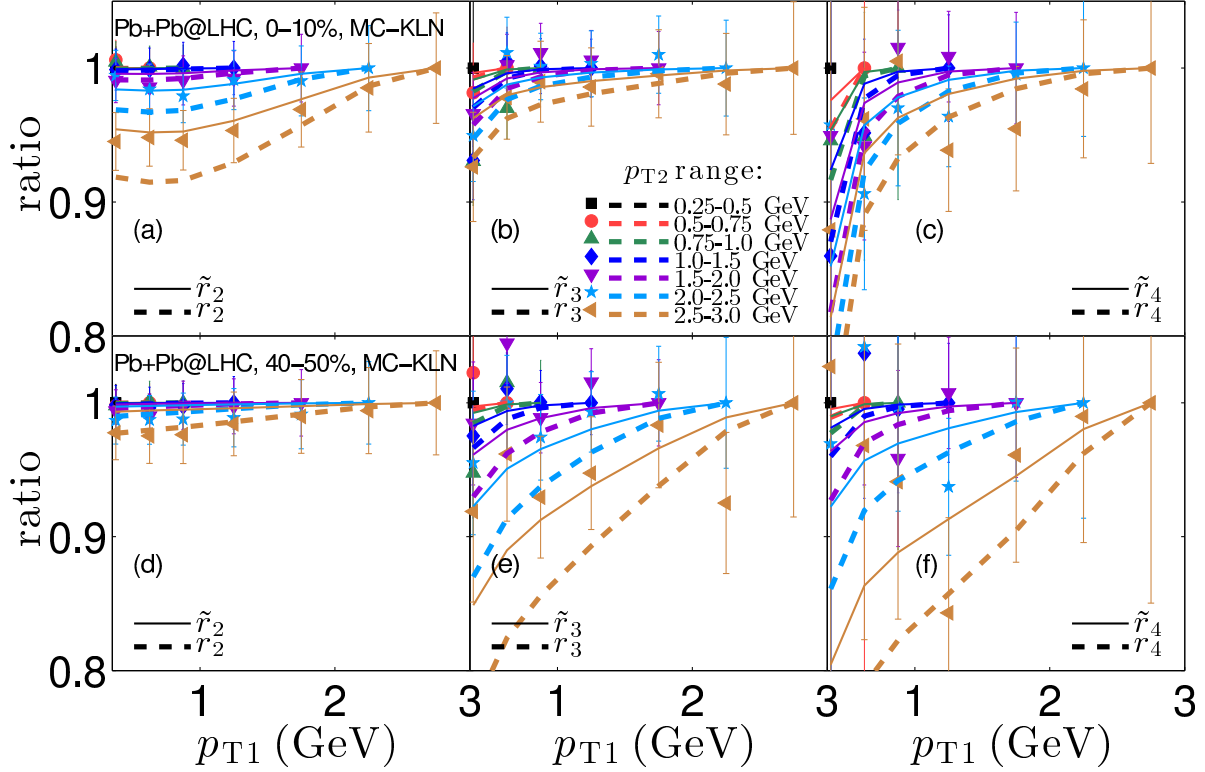


Figure 6.8: Same as Fig. 6.6, but for MC-KLN initial conditions that have been evolved hydrodynamically with $\eta/s=0.2$ (a shear viscosity value that is 2.5 times larger than the one used in Fig. 6.6). From [108].

v_3) in peripheral collisions) and appear to weaken for v_2 and v_4 in peripheral collisions, where both the magnitudes $v_{2,4}$ and the flow angles $\Psi_{2,4}$ are mostly controlled by collision geometry.

To explore the effects of shear viscosity of the expanding fluid on the breaking of factorization, we show in Figure 6.8 the same data as in Fig. 6.7, but compared with hydrodynamic calculations that use MC-KLN initial conditions evolved with $\eta/s=0.2$ (a 2.5 times larger viscosity than used in Fig. 6.7). Obviously, the MC-KLN model produces a different initial fluctuation spectrum than the MC-Glauber model, so not all of the differences between Figs. 6.7 and 6.8 can be attributed to the larger viscosity. However, in conjunction with the ideal fluid results reported in [111], the comparison of these two figures strengthens the conclusion that increased shear viscosity tends to weaken the fluctuation effects that cause the event-averaged two-particle cross section to no longer factorize.

6.5 Chapter summary

All experimental precision measures of anisotropic flow in relativistic heavy-ion collisions are based on observables that average over many collision events. It has been known for a while that both the magnitudes v_n and flow angles Ψ_n of the complex anisotropic flow coefficients V_n fluctuate from event to event, but only very recently it became clear that not only the v_n , but also their associated angles Ψ_n depend on p_\perp , and that the difference $\Psi_n(p_\perp) - \Psi_n$ between the p_\perp -dependent and p_\perp -averaged flow angles also fluctuates from event to event. Here in this chapter we pointed out that these flow angle fluctuations leave measurable traces in experimental observables from which the ensemble-averaged p_\perp -dependent anisotropic flows are extracted. We have introduced several new flow measures and shown how their comparison with each other and with flow measures that

²⁶The p_{T2} ranges are adjusted to the experimental data, and the ratios were computed by first averaging the numerator and denominator over the given p_{T2} range.

are already in wide use allows to separately assess the importance of event-by-event fluctuations of the magnitudes and angles of $V_n = v_n e^{in\Psi_n}$ on experimentally determined flow coefficients.

Viscous hydrodynamic simulations show that flow angle fluctuations affect the p_\perp -dependent flow coefficients of heavy hadrons (such as protons) more visibly than those of light hadrons (pions). In near-central collisions, where anisotropic flow is dominated by initial density fluctuations rather than overlap geometry, the effects from flow angle fluctuations appear to be strongest for particles with transverse momenta $p_\perp \lesssim m$. A precise measurement and comparison of $\langle v_n(p_\perp) \rangle$ (Eq. (6.11)), $v_n\{\text{EP}\}(p_\perp)$ (Eq. (6.9)), $v_n[2](p_\perp)$ (Eqs. (6.6,6.7)), and $v_n\{2\}(p_\perp)$ (Eq. (6.8)) for identified pions, kaons and protons with transverse momenta $p_\perp < 2 \text{ GeV}$ should be performed to confirm the hydrodynamically predicted effects from flow angle fluctuations. The theoretical interpretation of these measurements requires a reanalysis of finite-sampling statistical effects on the p_\perp -dependent differential flows, stemming from the finite multiplicity of particles of interest in a single event, which we did not consider here. The proposed comparison holds the promise of yielding valuable experimental information to help constrain the distribution of initial density fluctuations in relativistic heavy ion collisions and may prove crucial for a precision determination of the QGP shear viscosity.

We also showed that flow angle fluctuations are responsible for more than half of the hydrodynamically predicted factorization breaking effects studied in Ref. [111] and in Sec. 6.4 above, and that these effects are directly sensitive to the shear viscosity of the expanding fluid, decreasing with increasing viscosity. By combining the study of various types of differential anisotropic flow measures with an investigation of the flow-induced breaking of the factorization of two-particle observables into products of single-particle observables, one can hope to independently constrain the fluid's transport coefficients and the initial-state fluctuation spectrum.

Chapter 7: Sampling particles from the Cooper-Frye distribution

This chapter explains the methodology of sampling particles from the emission function calculated with the Cooper-Frye formula along the freeze-out surface. I will focus on the correctness and efficiency of the sampling algorithm. The material product of this methodology are the iS and the iSS code packages, which are among the core packages used in our group’s simulations. For completeness, both the required mathematical background and some technical details are given in this chapter.

The main structure of the chapter is outlined as follows: Sec. 7.2 provides the background on random variables and general sampling methodologies. The calculation of particle emission is briefly explained in Sec. 7.3. The actual sampling algorithm for particle momenta and space-time position is given in Sec. 7.4. Finally, a number of code checks are performed in Sec. 7.5.

The material is based on a document for the iSS code that is not yet published. The code was developed together with Chun Shen, who shares equal credit for this effort.

7.1 iS and iSS overview

The name “iS” stands for “iSpectra”; iS is a fast Cooper-Frye particle momentum distribution calculator along the conversion surface. Its output is a continuous function, evaluated at discrete momenta provided by the users, for the invariant momentum distributions of the desired hadron species. The code “iSS”, whose name stands for “iSpectraSampler”, goes one step further by generating individual particles, using the calculated particle momentum distributions as the relative emission probability. iSS is an “event generator” which generates a complete collision event of emitted hadrons, similar to the events created in the experiment. Both codes are written keeping the following factors in mind:

- **Readability and extendability.** The most important goal is to create a cleanly written framework that calculates particle momentum distributions and performs sampling, whose components and output can be used easily for further physics analyses and tests of new physical ideas. To achieve this, the entire program is divided into modules according to their functionalities, the structures and the algorithms are documented with comments, and long but informative names are chosen for variables and function names.
- **Efficiency.** Both the iS and iSS codes are written aiming for intensive hybrid event-by-event calculations where every CPU cycle counts. To achieve the necessary degree of efficiency, much effort is put into optimizing the algorithms at different levels of the calculations.
- **Easy maintainability and re-usability.** The framework is divided into different carefully chosen functionality modules, for better interoperability and to maximize re-usability.

Although the codes are meant to serve as a basic framework upon which additional physical analysis modules can be added, some such modules are already implemented, as will be explained in the following sections. An external parameter file and several tables allow for easy adjustment of parameters and choosing among multiple choices between available modules.

7.2 Random variables and sampling methods

7.2.1 Random variable, PDF and CDF

A random variable X is a variable that takes different values within a set S every time it is sampled. If S is a discrete set, then X can be characterized by specifying the probability of it taking each element in S ; if S is a continuous set, then X is characterized by the probability density function (PDF) $f(X)$, defined such that $\int_{X \in A} f(X) dX$ gives the probability of finding X in a subset A .

The cumulative distribution function (CDF) $F(X)$ is formally defined to be the function that gives the probability of finding $X' \leq X$:

$$F(X) = \int^{-X} f(X') dX' \tag{7.1}$$

The “inverse CDF” is the inverse function of $F(X)$.

By definition $f(X)$ is non-negative and it integrates to 1, and $F(X)$ is non-decreasing and $F(X \rightarrow -\infty) = 0$, $F(X \rightarrow \infty) = 1$.

In this chapter, a variable is “ n -dimensional” if the dimension of the set S is n . The PDF and CDF definitions are also valid for multi-dimensional random variables, where for the CDF the notion of $X \leq x$ should be understood component by component.

7.2.2 Sampling 1d random variables according to the inverse CDF

The inverse CDF sampling is best understood if we partition the range $[0, 1]$ of the CDF into n intervals with equal lengths R_i , and their pre-image in the domain space are denoted as $D_i := F^{-1}(R_i)$. By definition of CDF, the probability that $F(X)$ lies inside any R_i is the same, therefore the probability for X to lie in any D_i is the same. By throwing another uniform random variable in $[0, 1]$, we can sample an index i which means that the sampled $X \in D_i$. By taking $n \rightarrow \infty$, we see that the process becomes: uniformly randomly sample a value $T \in [0, 1]$, then find the sampled $X = F^{-1}(T)$.

If the range of the CDF is not properly normalized to $[0, 1]$ but $[A, B]$, the process given above can be extended trivially by shift and scaling.

7.2.3 Direct sampling of 1d random variables according to their PDF: special accept-reject method

Another intuitive sampling method is to sample the PDF directly using the accept-reject method. It starts with sampling a uniformly randomly chosen value for X , then use another continuous random variable T uniform in $[0, 1]$ to decide whether to accept or reject the sample: if the sampled trial variable value is greater than $f(X)$, then it is rejected; otherwise it is accepted. By doing so it is ensured that the probability of keeping X is proportional to $f(X)$, which is what we want.

One immediate improvement on efficiency is that instead of comparing the test variable to $f(X)$, we can also compare it to $k f(X)$, where k is a factor such that $k f(X) \leq 1$ for all X . A larger k values means less rejections and larger efficiency, and max efficiency is attained by choosing $k = 1/\max(f(X))$.

Like the inverse CDF method, if the PDF is not properly normalized, a scaling in T can be used to generalize the method.

Note that the accept-reject method for sampling PDF does not require the PDF to be properly normalized; the only requirement is that the probabilities used to make accept-reject selections need to be less than 1.

7.2.4 Sampling a 1d random variable using envelope distribution: general accept-reject method

A random variable Y on S with PDF $g(y)$ is considered as an envelope distribution to X on S with PDF $f(x)$ if there exists a constant k so that $k g(s) \geq f(s), \forall s \in S$.

Given an envelope distribution, the random variable X can be sampled using a two-step accept-reject procedure. First samples of Y according to the distribution $g(y)$ are generated using any appropriate method, then each sample $Y = s$ is accepted as a sample of X with probability $p(s) = f(s)/(k g(s))$.

The reasoning is simply based on a re-expressing the probability of an event as a product of the probability of another event and a conditional probability: the probability of generating a sample $X = s$ is $f(s)$, and it equals the probability $g(s)$ of first generating a sample $Y = s$, multiplied by the conditional probability of getting $X = s$ knowing $Y = s$, which is proportional to $f(s)/(k g(s))$.

As a special case, when g is a constant, sampling using the envelope distribution reduces to the case of direct sampling of PDF method explained in Sec. 7.2.3.

The efficiency of using an envelope distribution function is analyzed in Sec. 7.2.6.

Often an envelope distribution can be constructed as a sum of step functions, see Sec. 7.2.7.

7.2.5 Sampling 1d random variable using grouping

Another less intuitive method to sample X is to use the grouping method, which divides S into subsets and first samples the subset the next sample belongs to, then samples the element inside that subset. To illustrate it consider a simple case where $S = \{0, 1, 2, 3\}$ and $f(0) = f(1) = f(2) = f(3) = 1/4$.

The way to divide S into groups is not unique but suppose S is divided into $S_0 = \{0, 1\}$ and $S_1 = \{2, 3\}$, then the probability of finding $X \in S_0$ is $f(0) + f(1) = 1/2$ and the probability of finding $X \in S_1$ is $f(2) + f(3) = 1/2$.

The subsets are first sampled, which is equivalent to sampling a random variable Y on the indices $\{0, 1\}$ of the subsets with PDF $g(0) = g(1) = 1/2$. Next elements in that subset S_Y are sampled according to the PDF $f(x)$ but restricted to S_Y .

In general, after S is partitioned into subsets $S_i, i = 0, \dots, n$, first subsets are sampled using the induced “group-index-variable” Y on $\{0, \dots, n\}$ with PDF $g(i) = \int_{X \in S_i} f(x) dx$, then X is sampled with restricted PDF $f_{\text{restricted}}(x) = f(x) \Theta(X \in S_i)$.

The grouping method can be used recursively, where S_i are sub-divided into finer sub-subsets.

How S should be divided into subsets, and the efficiency of the grouping method are explained in Sec. 7.2.6.

7.2.6 Sampling efficiency

So far, four different sampling methods have been explained:

1. sampling using inverse CDF (Sec. 7.2.2)
2. direct PDF sampling (Sec. 7.2.3)
3. sampling with envelope distribution (Sec. 7.2.4)
4. sampling using grouping (Sec. 7.2.5)

Among them, (1) and (2) are direct sampling methods while (3) and (4) are composite in the sense that they involve sampling a second random variable, using any desired direct sampling method. For sampling with the envelope distribution method, the way to sample the envelope distribution is unspecified; and for sampling using grouping, both the way to sample groups and the way to sample elements within the group are left open.

In this section, sampling efficiencies are compared for methods (1)-(4). Here the “sampling efficiencies” are measured in terms of the number of times $f(x)$ is evaluated, while all other calculations are assumed to pose no costs. I will abbreviate *the number of evaluations of $f(x)$* in this section as “NOE”. When sampling a large number of samples, another good measurement of efficiency is the average number of times $f(x)$ needs to be calculated in order to produce 1 accepted sample, which is the reciprocal of the “acceptance rate”.

In almost all cases, $f(x)$ either has an analytic expression or can be pre-tabulated. In cases where $F(x)$ can be calculated analytically or pre-tabulated, the time spent on evaluating $F(x)$ is similar to that of evaluating $f(x)$. In such cases, the sampling using inverse CDF method is no doubt the most efficient one, since each time $F(x)$ is evaluated, it gives one sample with 100% acceptance. However in many cases, $F(x)$ cannot be evaluated analytically or pre-tabulated²⁷, and its calculation requires numerical integration of $f(x)$. It is for these cases that the efficiencies of different methods matters, and the following comparisons are all done under such conditions.

For demonstration, it is assumed that $f(x)$ is discrete and S is a finite set with N elements. Assume also that a total number of M samples is desired. In such a case, the evaluation of $F(x)$ for all $x \in S$ requires NOE= N .

Two extreme scenarios for X are used: scenario (A) assumes that the distribution function $f(x) = 1/N$ is uniform, and scenario (B) assumes that the distribution function $f(x)$ is delta-like: f is 1 for one special element and 0 for others. A realistic distribution can have any shape in between, and the sampling efficiency of it is expected to also lie in between; a flat distribution should have sampling efficiency close to scenario (A) and a sharply peaked one close to scenario (B).

It can be shown that if an event has success probability $1/N$, then the average waiting time to have one success in a series of repeated independent sampling is $N - 1$, that is, on average the N -th sample is the successful one.

Starting with scenario (A) where $f(x)$ is uniform, the direct PDF sampling method (2) in the most optimized case where $f_m = \max\{f\} = 1/N$ (see Sec. 7.2.3) gives full acceptance: every sample of X is accepted because the acceptance probability is 1. Thus NOE is M . The sampling using inverse CDF method (1), as explained requires N NOE for constructing the inverse CDF plus M NOE for actual sampling.

For scenario (B) where $f(x)$ is delta-like, the direct PDF sampling method (2) in the most optimized case requires MN NOE since each sampling has $1/N$ success rate and there are M desired samples. The inverse CDF sampling method (1) requires again N NOE for constructing $F(x)$ plus M NOE for sampling.

The results are summarized in the Table 7.2.6.

NOE	flat distribution	delta-like distribution
direct PDF	M	MN
inverse CDF	$M + N$	$M + N$

Table 7.1: Summary for waiting times (NOE per M successful sampling) between direct PDF sampling and inverse CDF sampling methods.

Therefore for a flat distribution, the direct PDF sampling method, when used properly, is most efficient. For distributions with peaks, the sampling using inverse CDF method is always superior than the direct PDF sampling method, except for $M = 1$. In general for $M \gg N$ or $M \sim N$, using inverse CDF sampling will practically almost always grant excellent efficiency; only for $M \ll N$ should the direct PDF sampling method be considered.

²⁷One common situation is that $f(x) = f(x; \alpha)$ depends on another continuous parameter and $F(x; \alpha)$ cannot be calculated analytically, thus there are “infinitely many” $F(x)$ that need to be tabulated.

From our study of scenario (B), it is also clear that an accurate estimate for the maximum of the PDF is crucial for the direct PDF sampling method: an overestimate of the maximum by a factor of 2 would decrease the success rate by a factor of 2, thus doubling the sampling time.

As a quick summary, for steep distributions, the sampling using the inverse CDF method is superior; for flat and general unknown distributions, to generate a small number of samples the direct PDF sampling is faster, while for large samples, the inverse CDF method is faster.

The envelope distribution function method (3) first samples according to the envelope distribution, after which it uses the accept-reject method to sample the target distribution (see Sec. 7.2.4). The envelope distribution can be sampled by direct PDF sampling or inverse CDF sampling. However if direct PDF sampling is used for the envelope function, then sampling with the envelope distribution method has no advantage over the direct PDF sampling method since the over-all probability for accepting a sample is still the same as the one in the direct PDF sampling. The sampling using the envelope method is only more efficient when the envelope variable can be sampled using the inverse CDF method and its CDF can be calculated analytically or pre-tabulated, or at least its evaluation takes a much shorter time.

To see why using envelopes improves the sampling efficiency, consider a simple example of scenario (B): $S = \{0, 1, 2, 3\}$ and X has PDF $f(0) = 1, f(1) = f(2) = f(3) = 0$, which is delta-like. The direct PDF sampling method requires on average $N = 4$ NOE to acquire one sample. Consider using an envelope distribution Y with PDF $g(0) = g(1) = 1/2, g(2) = g(3) = 0$. By assumption, the sampling of Y takes only 1 NOE, which yields either $Y = 0$ or $Y = 1$. Next consider using an accept-reject method to sample X , but since the possible sample spaces has been restricted to $\{0, 1\}$ from sampling Y , the sampling of X using direct PDF sampling has a much larger acceptance rate, and the average NOE is 2. The over-all required NOE is $1(\text{for } Y) + 2(\text{for } X) = 3$, which is smaller than the 4 NOE required for direct PDF sampling.

The efficiency of sampling using the envelope method depends on the choice of envelope, and the closer the shape of g is to f , the better the efficiency. In the extreme case that the envelope becomes the original distribution, $g = f$, the acceptance becomes 100% and the sampling using the envelope method degenerates into the sampling using the inverse CDF method (assuming the envelope distribution is sampled using the inverse CDF method for efficiency).

As a summary, the efficiency of sampling using the envelope method is greater than the direct PDF sampling method but worse than the inverse CDF sampling method. Only when the inverse CDF cannot be analytically calculated or pre-tabulated and when the NOE spent on constructing CDF is significant should the sampling using envelopes method be tried. The envelope distribution should be so constructed that: (1) its shape resembles the desired distribution²⁸; (2) its CDF can be pre-tabulated, calculated analytically, or computed numerically with only low expenses.

Often an envelope function can be numerically constructed as a sum of step functions, which only requires evaluation of f at a few locations, and a general-purpose example is given in Sec. 7.2.7.

The last method to analyze is the grouping method (4). Similar to the envelope method, its efficiency varies depending on the choice of groups.

As a case study, consider the set S is divided into l_1 subsets: $S_{i_1}, i_1 = 1, \dots, l_1$, and each subset is further divided into l_2 sub-subsets: $S_{i_1, i_2}, i_2 = 1, \dots, l_2$, and so on. Assume ‘‘on the ground level’’ each sub-sub-...-subset contains only one element, that is, $S_{i_1, i_2, \dots}$ is an element. Assume that at each level, the probability of X being in any subset is the same: $p(X \in S_{i_1, i_2, \dots, i_k}) = l_1^{-1} l_2^{-1} \dots l_k^{-1}$. Assume for now that we use direct PDF sampling method to sample groups at each level. The efficiency for sampling using such a grouping is discussed in the next paragraph.

For sampling subsets at the 1st level S_{i_1} , the success rate is $1/l_1$ and the average NOE is l_1 . Next, knowing which 1st level subset X belongs to, to sample the 2nd level subsets S_{i_1, i_2} requires similarly an average NOE l_2 . Continuing this it is clear that the total NOE required in the end is $l_1 + l_2 + \dots$. Note that l_j 's are subject to the constraint $l_1 l_2 \dots = N$, and recall that the direct PDF sampling method requires N NOE, it is then clear that the sampling using grouping method is much more efficient.

The best efficiency is attained when $l_1 = l_2 = \dots = 2$. In such extreme case, the required NOE is naively estimated as $2 + 2 + \dots \sim 2 \log_2(N)$ but in fact it is just 1. The reason is that $l_j = 2$

²⁸However there is one constraint: the envelope function, when multiplied by a constant, should be larger than the original distribution (see 7.2.4).

is different from $l_j > 2$ because even a “failure” in the sampling can also tell us which subset X belongs to. For example, if X does not belong to S_0 , then it must belong to S_1 . Therefore both “success” and “failure” can be used to inquire the subset X belongs to and in the end only 1 NOE is required²⁹.

In fact, when all l_j 's are 2, the grouping sampling method becomes the sampling using inverse CDF method. To see this, first notice that we can re-order the set S so that $S_0 = \{x, F(x) < 1/2\}$ and $S_1 = \{x, F(x) > 1/2\}$ ³⁰ etc., which in general gives that:

$$S_{i_1, i_2, \dots, i_k} = \left\{ x : \frac{i_1}{2^1} + \frac{i_2}{2^2} + \dots + \frac{i_k}{2^k} < F(x) < \frac{i_1}{2^1} + \frac{i_2}{2^2} + \dots + \frac{i_k + 1}{2^k} \right\}. \quad (7.2)$$

Then it is clear that what the grouping method does is just a binary search for the element $S_{i_1, i_2, \dots}$ with a given sequence $(i_1 i_2 \dots)$. The sequence becomes a real number in $[0, 1]$ when its elements are interpreted as digits in binary code: $(i_1 i_2 \dots)_2 = i_1 2^{-1} + i_2 2^{-2} + \dots$. In this way, the grouping method can be interpreted as: For a uniformly chosen real number $t_0 \in [0, 1]$, first express it in binary code, then perform a binary search for the element x that, according to eq. (7.2), satisfies $F(x) = t_0$. Therefore the grouping sampling method is just a particular numerical implementation (binary search for inverse) of the inverse CDF sampling method.

We just showed that in this extreme case, the grouping sampling and inverse CDF methods become identical. For general cases, such as when not all l_j 's are 2's, or when some of the subsets are sampled using inverse CDF methods, its efficiency lies between the direct PDF sampling and the inverse CDF methods.

In reality, the grouping method is much slower than the sampling using inverse CDF method, since even choosing a random number between 0 and 1 for $\log_2(N)$ number of times costs a significant number of computations. The grouping method, like the sampling with envelope method, should only be tried when the inverse CDF cannot be analytically calculated or pre-tabulated. If part of the sampling (usually the sampling of the groups) uses the inverse CDF sampling method, then for a grouping scheme, the larger the portion of the entire sampling that is done with the inverse CDF sampling method, the more efficient the whole process becomes.

As a summary, the efficiency of the grouping sampling method is greater than that of the direct PDF sampling but less than that of the inverse CDF sampling. It should only be attempted if the inverse CDF cannot be calculated analytically or pre-tabulated, or is too time consuming when constructed numerically. When each level of the group is sampled using the direct PDF sampling method, it achieves better efficiency when more levels of groups are used, with fewer groups at each level. Also, the more groups are sampled using the inverse CDF method, the more efficient the method.

7.2.7 Automatically generated stair function envelope distribution

Many distributions are piecewise monotonic. Within one such monotonic interval $[a, b]$, an envelope function can be constructed using constant function. Taking the proportional constant to be $k = 1$ (see Sec. 7.2.4), due to the monotonicity of the PDF, the envelope can be taken as a constant function $g = c$ where $c = \max\{f(a), f(b)\}$. Given that the real axis is divided into a series of intervals on each of which f is monotonic, a stair-shaped envelope function can be generated by using a constant envelope function on each monotonicity interval. Such a construction only involves evaluating $f(x)$ at those boundary points that separate the intervals, and the inverse CDF of a stair function is easily calculable; therefore when the number of monotonicity intervals is small, constructing and sampling with such a stair-shaped envelope function becomes efficient.

For example, assuming one wants to sample a Gaussian distribution $f(x) = e^{-x^2}$ on $[0, 100]$. When using direct PDF sampling, 95% of the time the suggested sample for X lies in the interval $[5, 100]$ and its acceptance is below $e^{-25} \ll 1\%$ and it almost always is rejected. However, if a

²⁹Again, all other calculations, like throwing $\log_2(N)$ random dices, are considered to have negligible time here.

³⁰The boundary of the interval is irrelevant only for continuous distribution but it is ignored here for simplicity.

two-stair envelope distribution Y with PDF $g = 1, x \in [0, 5]$, and $g = e^{-25}, x \in [5, 100]$ is used, then the acceptance rate for X will be greatly increased because sampling Y will only give a tiny chance to suggest a sample above 5 for X . Furthermore, the construction of such an envelope including its inverse CDF only requires 2 evaluations of $f(x)$, at $x = 0$ and $x = 5$, which is negligible compared to the NOE required in direct PDF sampling, which is typically $> 10,000$ (inverse acceptance rate).

In many cases, the encountered distribution function has a unique maximum located at its “mode” and is monotonically decreasing on both sides when x goes away from the mode. Examples include the Gaussian distribution function, the negative binomial distribution (NBD), etc. For such distribution functions, one way to automatically generate an envelope is to start with its mode, and construct stair-shaped envelope functions whose width for each step is, for example, its standard deviation, and which reaches out for a few (e.g. 6) multiples of it. Such a stair-shaped envelope function can be constructed without knowing the analytic form of the inverse CDF and it only requires ~ 10 more NOE. For rapidly dropping distributions like Gaussian and NBD, the time constructing the envelope is negligible compared to the time spent on typical direct PDF sampling.

For piecewise monotonic distributions like the Gaussian and NBD distributions, if they do not have *parameter dependence*, their inverse CDF should be calculated in advance and pre-tabulated to provide maximum sampling efficiency; if however they do have parameter dependence and tabulating their inverse CDF becomes impossible, the automatically constructed stair-shaped envelope can greatly boost performance compared to a brute-force PDF sampling method.

7.2.8 Generating genuine continuous samples

For a variable X defined on a continuous set S , it can be sampled using the direct PDF sampling method (or other composite methods) with continuum PDF, which will produce samples that can take any continuous values in S ³¹. However, when X is sampled using numerically constructed discretized inverse CDF, the generated samples are on a discrete set upon which the CDF is constructed. When the discrete set is dense, such a discrete sampling hardly even causes any practical problems. If the discrete set is not so dense and genuine continuous samples are preferred, the continuum can still be approximately restored by an additional random process: instead of using a sample in the discrete set, a “perturbed” sample, which is generated by assigning an additional random shift whose range is half of the discretization spacing, can be used. Such a process generates samples close to the continuous sampling method while maintaining the efficiency of the inverse CDF sampling method (the cost for the additional random process is by our assumption ignored, see Sec. 7.2.6).

7.2.9 Sampling multi-dimensional random variables

For multi-dimensional random variables, the direct PDF sampling method, the sampling with envelope method, and the grouping sampling method can be generalized naturally, but it is not clear how the most efficient sampling method, the inverse CDF sampling method, can be generalized to multi-dimensional case for a continuous set S , while the solution for a discrete S is simple. Since almost all functions are discretized on a computer, in this section the discussion is restricted to the case that S is discrete.

When S is discrete³², it can be “flattened” into a 1d set by re-ordering its elements in any desired fashion. In this way, any random variable X on S can be treated as a 1d random variable and all the sampling methods and their sampling efficiency analyses explained in previous sections directly apply.

For example, supposing $S = \{(x, y)\}$ resembles the $[0, 1] \times [0, 1]$ area, after discretizing along both directions the interval $[0, 1]$ into 10 points, $S = \{(x_i, y_j)\}, x_i, y_j = 0.1, \dots, 1$. The set S can

³¹This is also true if the inverse CDF has an analytical expression, which is really rare.

³²The following argument actually only requires a weaker assumption that S can be made into an ordered set.

be ordered, for example, as:

$$S = \{(0.1, 0.1), \dots, (1, 0.1), (0.2, 0.1), \dots, (0.2, 1), \dots, \dots, (1, 1)\} \quad (7.3)$$

Therefore any “2d” random variable X on S can be treated as a 1d random variable on the re-ordered set. Higher-dimensional random variables can be “flattened” similarly.

As explained (Sec. 7.2.6), sampling using the inverse CDF is the most efficient method: if it can be calculated analytically or pre-tabulated, or if a large number of samples are desired so the time spent on constructing the CDF numerically is negligible, the sampling using inverse CDF method should always be used. Otherwise the sampling with envelope or grouping methods should be tried before using the direct PDF sampling method.

When applying the grouping sampling method to multi-dimensional variables, it is very natural to divide S into subsets according to one of the dimensions. For example, the set S in eq. (7.3) can be divided into 10 groups $S_i = \{(0.1 \times i, 0.1), (0.1 \times i, 0.2), \dots\}$. By doing so, the sampling using grouping method essentially samples $X = (X_1, X_2)$ by first sampling X_1 then sampling X_2 .

For multi-dimensional random variables, there is yet one more practical constraint: even if the CDF of the variable can be pre-calculated, it cannot be tabulated due to memory shortage. In such situations, one practical solution is to tabulate not the CDF for the multi-dimensional variable, but only for the CDF corresponding to higher level groups created in grouping sampling. To give an example, suppose that discretization into 100 points is too much so that the inverse CDF cannot be stored for $X = (X_1, X_2)$ on S given in eq. (7.3), but the inverse CDF for the variable X_1 , which controls the sampling of groups S_i , requires only 10 points as it has a much larger chance to fit into the memory.

7.2.10 Possible issues

Deviations due to limited number of samples

It may seem trivial that, with a limited number of samples, the statistically calculated quantities, for example the mean and standard deviation, have statistical errors compared to the exact values calculated from the distribution function. However during numerical calculations, some situations may still seem to give “counterintuitive” results when using exotic distributions. For example, if X takes the value 0 with $1 - 10^{-1000}$ probability and 10^{1000} with 10^{-1000} probability, it has mean 1 but in almost any actual sampling process the mean is 0. Therefore when sampling distributions with fast-dropping tails, the mean calculated from samples is expect to deviate from the exact value, especially for a highly skewed distribution.

Discretizing continuous distribution

When continuous distributions are discretized, the weight on each discretized point should be the integral of the PDF (probability) around that point, instead of being the PDF itself (probability density) at that point. The difference only matters if the discretization is on an irregular lattice. For example, assuming that X is uniform on $[0, 3]$ and one discretization is $[0, 2]$ represented by the middle point $x = 1$ and $[2, 3]$ represented by middle point $x = 2.5$, then the weight at $x = 1$ should be twice that at $x = 2.5$, in order to generate twice as many samples in $[0, 2]$ than $[2, 3]$. This requires using the integral of the PDF on $[0, 2]$ and $[2, 3]$ as the sampling weights instead of the values of the PDF at $x = 1$ and $x = 2.5$ as the sampling weights; that is, weights are probabilities, not probability densities.

One scenario in which irregular lattice discretization is encountered is during the sampling on a lattice specified by Gauss quadrature. Assuming that a function is numerically costly to evaluate but it needs to be integrated, then the numerical integral can be efficiently calculated by summing its values on only a few lattice points given by Gauss quadrature, during which process values of it on the lattice are stored to avoid repeated calculation. If such a discretization of this function is used later as a PDF in sampling, then samples should be generated not using the values of the function on the lattice, but using the integral of it on each interval, that is, with the specified Gauss weight.

7.3 Sampling the particle momentum distribution

The iS and iSS codes read the hydrodynamic variables along the conversion surface generated from the hydrodynamical simulation, then calculate the particle momentum distribution and observables, and also sample particles accordingly. Both codes calculate the particle momentum distribution using the Cooper-Frye formula for the emission function which, together with the details for calculating related observables and sampling, will be explained in this section.

7.3.1 Emission function and Cooper-Frye formula

The emission function is the function that determines how many particles on average will be emitted from a given location on the conversion surface. In general, it depends on (x^μ, p^ν) , where the 4-vector $x = (\tau, \vec{x}_\perp, \eta_s)$ has the following components: the proper time τ ; the transverse location \vec{x}_\perp , and the space-time rapidity η_s on the conversion surface. The 4-vector $p = (E, \vec{p}_\perp, y)$ has the following components: the energy E , the transverse momentum \vec{p}_\perp , and the particle rapidity y . All the out-going particles are on-shell, and the 4-vector x^μ is constrained to be on the conversion surface, so there are only 6 free components on which the emission function depends.

The conversion surface is conventionally denoted as Σ ; it is a 3-dimensional set of points in 4-dimensional space-time. An infinitesimal piece of Σ is characterized by its surface normal vector $d^3\sigma_\mu$, whose norm gives the 3-volume of the element and whose components give the direction.

The Cooper-Frye formula has been widely used to calculate the emission function, whose differential form is the following:

$$dN(\tau, \vec{x}_\perp, \eta_s, \vec{p}_\perp, y) = gp^\mu d^3\sigma_\mu \frac{d^3p}{E(2\pi)^3} f(x, p). \quad (7.4)$$

Here g is the spin degeneracy, and f is the distribution function taking the form³³:

$$f(x, p) = f_0 + \delta f = \frac{1}{e^{(p \cdot u - \mu)/T} \pm 1} + \frac{\chi(p^2) p^\mu p^\nu \pi_{\mu\nu}}{2T^2(e + p)} f_0(1 \mp f_0). \quad (7.5)$$

e , p , T , u^μ are the energy density, pressure, temperature, and 4-flow velocity of the fluid, respectively; and μ is the chemical potential of the particle; the function χ is a function of only p^2 ; $\chi = 1$ corresponds to the quadratic ansatz for δf .

In numerical calculations, it is natural to separate the rapidity dependence from the surface element as $d^3\sigma_\mu = \tau d\eta_s d^2\tilde{\sigma}_\mu$. It is also convenient to use the variable $\eta'_s = y - \eta_s$ and to write $d^2p_\perp = p_\perp dp_\perp d\phi$. With these choices, the emission function eq. (7.4) assumes the form:

$$\frac{dN}{dy}(\tau, \vec{x}_\perp, \eta'_s, \vec{p}_\perp, y) = g (\tau d\eta'_s d^2\tilde{\sigma}_\mu(x_\perp)) \frac{p_\perp dp_\perp d\phi}{(2\pi)^3} p^\mu f(x, p). \quad (7.6)$$

The emission function drops rapidly with increasing $|\eta'_s|$ or p_\perp , and this influences the sampling efficiency, as will be explained in Sec. 7.4.

The differential emission function given by eq. (7.4) is not necessarily always positive since, depending on the shape of Σ , $p^\mu d^3\sigma_\mu$ can become negative; for sampling with probability methods, we need, however, a positive-definite emission probability density. This issue and its possible treatments are discussed in Sec. 7.4.

7.3.2 Spectra and flow calculations

The azimuthally averaged spectrum is calculated from $dN/(dy p_\perp dp_\perp d\phi)(\vec{p}_\perp)$ as:

$$\frac{dN}{2\pi dy p_\perp dp_\perp} = \frac{1}{2\pi} \int_0^{2\pi} d\phi \frac{dN}{dy p_\perp dp_\perp d\phi}(\vec{p}_\perp). \quad (7.7)$$

³³All through this chapter, the upper sign is for fermions and lower sign is for bosons.

and the differential anisotropic flows v_n 's are the Fourier coefficients with respect to the azimuthal angles of the same distribution:

$$v_n e^{in\Psi_n} = \frac{\int p_\perp dp_\perp d\phi dN/(dy p_\perp dp_\perp d\phi) e^{in\phi}}{\int p_\perp dp_\perp d\phi dN/(dy p_\perp dp_\perp d\phi)}. \quad (7.8)$$

Therefore the calculation of spectra and flow requires the calculation of the distribution function $dN/(dy p_\perp dp_\perp d\phi)$, which from eq. (7.6) is calculated as:

$$\frac{dN}{dy p_\perp dp_\perp d\phi} = \frac{g}{(2\pi)^3} \tau \int_\Sigma d\eta'_s d^2\tilde{\sigma}_\mu p^\mu f(x, p). \quad (7.9)$$

In numerical calculations, the distribution function $dN/(dy p_\perp dp_\perp d\phi)$ is represented as an array whose elements are calculated using eq. (7.9). Usually to achieve high numerical accuracy, a dense conversion surface discretization is used, and the numerical integrals in eq. (7.9), which involve numerical sums over the conversion surface, become very time consuming. Therefore a quadrature rule that requires a smaller size of the $dN/(dy p_\perp dp_\perp d\phi)$ array while not losing accuracy means less computing time for the integral over the conversion surface, resulting in better efficiency. Gauss quadrature, which requires much fewer sampling points, is thus used in our codes for both the p_\perp and ϕ integrals.

The integral over η'_s in eq. (7.9) can also be done using Gauss quadrature. Under the boost-invariant assumption, the integrand is an even function and the integral further reduces to one along only the positive axis, which is then calculated using 15-point Gauss quadrature.

Further optimization for performing the numerical integral in eq. (7.9) involves adjusting the order of the integration loops, using local variables, pre-tabulating mathematical functions, etc. The resulting code iS is ~ 7 times faster compared to the previous used AZSpectra code.

Note that a negative differential emission function is physically allowed in all the integrals in this section, since only $dN/dy d^2p_\perp$ (i.e. a momentum distribution integrated over Σ) and $dN(\vec{x}_\perp, \eta, \tau)$ (i.e. the spatial emission density integrated over momentum) have to be always positive definite. However, for the sampling algorithms to work, the integrands need to be replaced by their absolute values, or the negative contributions must be set to zero by hand. While this gives physically incorrect results, it is necessary for testing the sampling algorithm. This is explained in detail in Sec. 7.4.

7.4 Sampling the emission function

We now discuss how to sample the emission function to generate particles whose space-time and momentum distributions are given by the differential emission function (7.6). Required information are the total emitted number of particles, their species, the emission location, and their momenta. The space-time information of the particles comes from the location on the conversion surface from where they are emitted. Their momentum information is sampled according to the Cooper-Frye formula (eq. (7.4) or (7.6)).

In numerical calculations, the conversion surface is generated from the hydrodynamic calculation, and it is discretized into surface cells which are labeled by the ‘‘conversion surface cell index’’, denoted as l_{conv} in this section. The space-time information \vec{x}_\perp , τ , and η_s on the conversion surface cell are functions of this index. For a boost-invariant system, the conversion surface is invariant under a shift in the η_s direction, and only the conversion surface at $\eta_s = 0$ is stored. Therefore only the \vec{x}_\perp and τ information are expressed through the conversion surface cell index, and the $\eta'_s = \eta_s - y$ dependence is kept explicitly. Finally, for boost-invariant systems, the η'_s -integrated emission function does not depend on particle rapidity; the rapidity y dependence of the particle can always be sampled additionally in the end with a uniform distribution in a given rapidity range, which together with η'_s determines η_s . Therefore the quantities that the differential emission function dN depends on in practice are: the conversion surface cell index l_{conv} , the transverse momentum p_\perp and ϕ , and the relative space-time rapidity η'_s .

Of these 4 quantities, the conversion surface cell index is already discretized, and the other 3 can be discretized or kept as continuous quantities. As explained in Sec. 7.2.8, continuous samples can still be approximately generated from samples on a discrete set, so the issue of whether the generated samples assume continuous or discrete values will be largely ignored in this section, and the main focus is on the efficiency of the sampling algorithm.

7.4.1 The purely numerical approach

The straightforward approach is where all required quantities are calculated numerically.

For a given species of particle, the average total yield N is calculated by numerically integrating the differential emission function over all its dependences. By storing all the partial sums encountered in the numerical integration, the inverse CDF for the flattened variable (see Sec. 7.2.9) can be generated at the same time. As explained in Sec. 7.2.6, the inverse CDF sampling method is the most efficient one, and it should be used for the generation of particle samples.

However in practice, the inverse CDF for the full differential dN can hardly fit into the current generation computer memory. In a typical calculation, we have $\sim 30,000$ surface cells, 720 discretized \vec{p}_\perp points, and 40 discretized η'_s points, giving an array of size 864MB, already dangerously large. In the most central Pb-Pb collisions at 2.76A GeV energy at the LHC, the number of conversion surface cells exceeds 100,000, and the memory demand reaches 3GB. My personal design philosophy is to leave flexible memory spaces to allow for unexpected extreme cases, for possible future modifications, etc. Furthermore, it is soon realized that input/output to files is more costly than the sampling time difference between the inverse CDF sampling method and the one that is currently used, as explained below.

From Sec. 7.2.6, it is clear that, if the inverse CDF sampling method cannot be applied, then the other two composite sampling methods should be tried. For a multi-dimensional random variable dN , it is most natural to use the grouping sampling method (see Sec. 7.2.9), with the sampling of groups being efficiently handled by the inverse CDF sampling method.

As explained, the variable dN effectively depends on a tuple of 4 quantities: the conversion surface cell index l_{conv} , the transverse momentum magnitude p_\perp , the transverse momentum angle ϕ , and the relative rapidity η'_s . Their discretized sizes are $\sim 30,000$, 15, 48, and 40, respectively. The total sampling space size is the product of these numbers, which will be divided into groups. Recall that the sampling of groups is done using the efficient inverse CDF sampling method, thus the larger the groups the more efficient the process becomes (see Sec. 7.2.6). With the memory limitations and the desire for code simplicity, the largest group can be formed using the surface index and the relative rapidity, leaving out the transverse momentum degrees of freedom. Such a grouping gives groups of size $\sim 30,000 \times 40$ which easily fit into memory, and their partially integrated emission function

$$\frac{dN}{dyd\eta'_s}(l_{\text{conv}}, \eta'_s, y) = g\tau(l_{\text{conv}})d^2\tilde{\sigma}_\mu(l_{\text{conv}}) \int \frac{p_\perp dp_\perp d\phi}{(2\pi)^3} p^\mu f(x, p) \quad (7.10)$$

will be used in the inverse CDF sampling.

Each emitted particle is generated by first sampling the group it belongs to using the inverse CDF method, which gives a conversion surface cell index l_{conv} and a relative rapidity η'_s . Once having them, the transverse momentum of this particle is then sampled using the direct PDF sampling method, which is efficient since it is the transverse momentum information \vec{p}_\perp for only *one* particle that needs to be sampled, which falls into the category of “generating a small number of samples”, see Sec. 7.2.6.

Another small advantage is that direct sampling with the PDF generates samples with continuous \vec{p}_\perp distributions, which reduces the discretization error for quantities that depend sensitively on angular distributions, for example the high-order anisotropic flows.

The efficiency of the direct PDF sampling relies strongly on the estimate of the maximum (Sec. 7.2.6). These maxima for the p_\perp -weighted differential emission function can be approximated by their maxima on the discrete lattice in momentum space, and they are stored during the calculation of the total multiplicity.

Other grouping configurations have also been tried, including one with a single inverse CDF function for the whole differential emission function. Indeed the efficiency from inverse CDF sampling method is the fastest, and it is 30% \sim 50% faster than the one proposed above, when clocked for pure sampling without writing to files. When writing to files is turned on, the speed difference is no more than \sim 10%, and \sim 60% of the time is spent on writing to files. In fact, significantly more time would be spent on writing to files had there not been a manually constructed “buffer” for file writing, which is explained in Sec. 7.4.4.

7.4.2 Semi-analytic approach

For a boost-invariant system, the flow rapidity is equal to the space-time rapidity, and it follows that the distribution function is a function of only η'_s instead of both y and η_s . By changing variables, the invariant integral measure d^3p/E can also be written as $d^3p/E = dy p_\perp dp_\perp d\phi = -d\eta'_s p_\perp dp_\perp d\phi$. Therefore the emission function calculated in each cell of the conversion surface:

$$\frac{dN}{dy}(l_{\text{conv}}, y) = g\tau(l_{\text{conv}})d^2\tilde{\sigma}_\mu(l_{\text{conv}}) \int d\eta'_s \int \frac{p_\perp dp_\perp d\phi}{(2\pi)^3} p^\mu f(x, p) \quad (7.11)$$

is a scalar under boosts. The semi-analytic approach takes advantage of this invariance and evaluates dN/dy in the local fluid rest frame.

First it can be shown that the integral of δf is zero. To see this³⁴, write the integral as

$$\left(\int \frac{d^3p}{E(2\pi)^3} \chi(p^2) p^\mu p^\rho p^\sigma f_0(1 \mp f_0) \right) \pi_{\rho\sigma} \quad (7.12)$$

The quantity in the parentheses is a contravariant rank-3 tensor that depends only on u^μ , therefore it can only be a sum of tensors composed from u^μ and $g^{\mu\nu}$. If the indices ρ or σ is carried by u , then by transversality of u^μ and $\pi^{\mu\nu}$, the corresponding contraction upon ρ or σ gives zero; otherwise the term contains $g^{\rho\sigma}$ which also leads to zero when contracted with $\pi_{\rho\sigma}$ by the tracelessness of $\pi^{\mu\nu}$.

Thus the full distribution function f can be replaced by the equilibrium distribution in the local rest frame:

$$f_0(x, p) = \frac{1}{e^{(p^\nu u_\nu - \mu)/T} \pm 1} = \frac{1}{e^{(E - \mu)/T} \pm 1} \quad (7.13)$$

where the last equality used that $u^\mu = (1, 0, 0, 0)$ in local rest frame. From the symmetry of p^μ , it is clear that:

$$\begin{aligned} \int \frac{d^3p}{E(2\pi)^3} p^\mu f_0(x, p) &= \int \frac{d^3p}{E(2\pi)^3} p^0 \frac{1}{e^{(p^\nu u_\nu - \mu)/T} \pm 1} g^{\mu 0} \\ &= \int \frac{d^3p}{(2\pi)^3} \frac{1}{e^{(E - \mu)/T} \pm 1} g^{\mu 0} \end{aligned} \quad (7.14)$$

³⁴As an alternative argument, first write the integral measure as d^3p , then it is clear that the integral involving δf is proportional to:

$$\int \frac{d^3p}{E(2\pi)^3} \chi(p^2) p^\mu p^\rho p^\sigma \pi_{\rho\sigma} f_0(1 \mp f_0) = \int \frac{d^3p}{(2\pi)^3} \chi(p^2) p^\rho p^\sigma \pi_{\rho\sigma} g^{\mu 0} f_0(1 \mp f_0)$$

since for $\mu \neq 0$ the integrand is odd in p^i and thus integrates to 0. Similarly ρ has to be the same as σ to produce non-zero results. Since in the local rest frame $\pi^{\rho 0} = \pi^{0\sigma} = 0$, the integral in eq. (7.12) for $\mu = 0$ can thus be written as:

$$\int \frac{dp_x dp_y dp_z}{(2\pi)^3} \chi(p^2) (p_x^2 \pi_{xx} + p_y^2 \pi_{yy} + p_z^2 \pi_{zz}) f_0(1 \mp f_0)$$

Next notice that by symmetry, p_x^2 , p_y^2 , and p_z^2 can be replaced by $p^2/3$ and then it follows from the traceless condition of $\pi^{\mu\nu}$ that the integral over δf is zero.

And finally,

$$\int \frac{d^3p}{(2\pi)^3} \frac{1}{e^{(E-\mu)/T} \pm 1} = \frac{T^3}{2\pi} \int d(p/T) \frac{(p/T)^2}{e^{\sqrt{(p/T)^2 + (m/T)^2 - (\mu/T)} \pm 1}} \quad (7.15)$$

and the last integral can be pre-calculated and tabulated for rescaled mass m/T and rescaled chemical potential μ/T .

Furthermore in the local rest frame for any 4-vector A , its 0-th component can be written as $A^0 = A^0 u_0 = A^\mu u_\mu$ where the last expression can be evaluated in any frame; thus in the local rest frame, $d^2\tilde{\sigma}_0$ becomes $d^2\tilde{\sigma}_\mu u^\mu$ in the lab frame. Therefore eq. (7.11) becomes:

$$\frac{dN}{dy}(l_{\text{conv}}, y) = g\tau(l_{\text{conv}}) d^2\tilde{\sigma}_\mu(l_{\text{conv}}) u^\mu \frac{T^3}{2\pi} \int d(p/T) \frac{(p/T)^2}{e^{\sqrt{(p/T)^2 + (m/T)^2 - (\mu/T)} \pm 1}} \quad (7.16)$$

Using eq. (7.16), the emission function on each conversion surface cell in eq. (7.11) can be calculated without performing the numerical integral, but by evaluating an algebraic expression with results read from a pre-calculated table. This is the most important step in this fast semi-analytic sampling approach.

As mentioned, the variable dN depends on a tuple of 4 quantities: conversion surface cell index l_{conv} , transverse momentum magnitude p_\perp , transverse momentum angle ϕ , and relative rapidity η'_s . The semi-analytic sampling approach is a grouping sampling method that divides the full $(l_{\text{conv}}, p_\perp, \phi, \eta'_s)$ sampling space into groups labeled by l_{conv} . The probability for a sampled particle to belong to each group is given by dN/dy in eq. (7.16). The groups are sampled by the inverse CDF method, which gives the conversion surface cell index from which a particle is emitted; once a particle is known to be emitted from a certain conversion surface cell, its (p_\perp, ϕ, η'_s) dependence is sampled using the direct PDF sampling method.

Recall from Sec. 7.2.6 that the efficiency of the direct PDF sampling method depends intensively on the closeness of the estimated maximum of the PDF to the real one. Compared to the purely numerical approach (Sec. 7.4.1), the maximum of the differential dN *cannot* be extracted numerically since there is no more numerical integration thus no more numerical scan of the integrand over the sampling space, and it has to be estimated analytically.

In the following derivation, the maximum is closely related to the function:

$$G(E; A) = \frac{E^A}{e^{\beta(E-\mu)} \pm 1}, \quad A > 0 \quad (7.17)$$

where $\beta = T^{-1}$. By setting its derivative to zero the extrema can be found by solving:

$$(1 \mp f_0) = \frac{A}{\beta E} \iff \begin{cases} xe^x = y; x = \beta E - A, y = Ae^{\beta\mu - A}, \text{ fermions (upper)} \\ xe^{-x} = y; x = A - \beta E, y = Ae^{\beta\mu - A}, \text{ bosons (lower)} \end{cases} \quad (7.18)$$

This equation is transcendental and it cannot be solved algebraically; however, the solution to the equations expressed in terms of x and y can be pre-calculated and tabulated. For fermions (upper sign), the solution always exists and it is expressed by the Lambert W-function; for bosons (lower sign) the equation only has real solutions when $y < 1/e$, and it yields two solutions; the one needed is the one satisfying $x \in [0, 1]$. In the following, the solution to this equation will be denoted as E_{max}^\pm when it exists.

The maximum of $G(E; A)$ with constraint $E \geq m$ will be denoted as $G_{\text{max}}^{(A)}$ and it depends on several conditions:

1. For fermions (upper sign), $G(E)$ has a single peak at E_{max}^+ and the constraint maximum is $G(E_{\text{max}}^+)$ if $E_{\text{max}}^+ > m$ and otherwise is $G(m)$.

2. For bosons (lower sign) with $Ae^{\beta\mu-A} > 1/e$, eq. (7.18) has no solution and the maximum is $G(m)$.
3. For bosons (lower sign) with $Ae^{\beta\mu-A} \leq 1/e$, $G(E)$ has two extrema in (μ, ∞) with the larger one being the maximum and given by E_{\max}^- . If $E_{\max}^- < m$ then the maximum is $G(m)$; otherwise the maximum is the larger one between $G(m)$ and $G(E_{\max}^-)$.

In the following, an estimate is given of the maximum of the differential emission function:

$$F(x, p) = d^2 \tilde{\sigma}_\mu p^\mu f(x, p) \quad (7.19)$$

Write $F = F_0 + \delta F$ corresponding to f_0 and δf , respectively. Note that F_0 and δF are scalars whose evaluations, including their maximum, are frame independent. Their maxima are thus estimated in the local rest frame, but expressed using quantities in the lab frame.

For a boost-invariant system, $d^2 \tilde{\sigma}_3 := d^2 \tilde{\sigma}_{\eta_s} = 0$ and the conversion surface cell volume in the local rest frame can be estimated as:

$$\begin{aligned} d^2 \tilde{\sigma}_\mu p^\mu &= d^2 \tilde{\sigma}_0 E + d\vec{\sigma}_\perp \cdot \vec{p}_\perp \\ &\leq E (|d^2 \tilde{\sigma}_0^{\text{L.R.F.}}| + |d^2 \tilde{\sigma}_\perp^{\text{L.R.F.}}|) = E (|d^2 \tilde{\sigma}_0^{\text{L.R.F.}} u^0| + |d^2 \tilde{\sigma}_\perp^{\text{L.R.F.}}|) \end{aligned} \quad (7.20)$$

As explained earlier in this section, in the lab frame $d^2 \tilde{\sigma}_0^{\text{L.R.F.}} u^0$ should be replaced by $d^2 \tilde{\sigma}_\mu u^\mu$. The quantity $d^2 \tilde{\sigma}_\perp^{\text{L.R.F.}}$ in the lab frame has the form $\sqrt{d\sigma_\mu d\sigma_\nu \Delta^{\mu\nu}}$, where $\Delta^{\mu\nu} = u^\mu u^\nu - g^{\mu\nu}$ is the spacial projection operator, and it can be explicitly calculated by an actual boost from $d\tilde{\sigma}$ in the lab frame as:

$$\begin{aligned} (d^2 \tilde{\sigma}_\perp^{\text{L.R.F.}})^2 &= d^2 \tilde{\sigma}_0^2 ((u^1)^2 + (u^2)^2) + d^2 \tilde{\sigma}_1^2 (1 + (u^1)^2) + d^2 \tilde{\sigma}_2^2 (1 + (u^2)^2) \\ &\quad + 2d^2 \tilde{\sigma}_0 d^2 \tilde{\sigma}_1 u^0 u^1 + 2d^2 \tilde{\sigma}_0 d^2 \tilde{\sigma}_2 u^0 u^2 + 2d^2 \tilde{\sigma}_1 d^2 \tilde{\sigma}_2 u^1 u^2 \end{aligned} \quad (7.21)$$

For the equilibrium contribution F_0 , it is clear from eq. (7.20) and eq. (7.19) that the remaining part is to calculate the maximum for the function:

$$E f_0 = \frac{E}{e^{(E-\mu)/T} \pm 1} = G(E; 1) \quad (7.22)$$

and the solution is $G_{\max}^{(1)}$.

Next I give an estimate to the maximum of the off-equilibrium part with choice $\chi(p^2) = p^\beta$:

$$\delta F = d^2 \tilde{\sigma}_\mu p^\mu f_0 (1 \mp f_0) \frac{p^\alpha p^\mu p^\nu \pi_{\mu\nu}}{2T^2 (e + p)} \quad (7.23)$$

The conversion surface cell volume is again estimated as in eq. (7.20) and eq. (7.21). For a boost-invariant system $\pi_{3i} = 0$; in the local rest frame, the rotational freedom in the transverse direction can be used to set $\pi_{xy} = 0$; it then follows from the Hölder inequality and the fact that $|p_{x,y,z}| \leq p \leq E$ that

$$\begin{aligned} p^\mu p^\nu \pi_{\mu\nu} &= p_x^2 \pi_{xx} + p_y^2 \pi_{yy} + p_z^2 \pi_{zz} \leq E (|p_x| |\pi_{xx}| + |p_y| |\pi_{yy}| + |p_z| |\pi_{zz}|) \\ &\leq E \left(E \sqrt{\pi_{xx}^2 + \pi_{yy}^2 + \pi_{zz}^2} \right) = E^2 \sqrt{\pi^{\mu\nu} \pi_{\mu\nu}} \end{aligned} \quad (7.24)$$

The quantity $\pi^{\mu\nu} \pi_{\mu\nu}$ is a scalar and thus can be evaluated using $\pi^{\mu\nu}$ from the lab frame. Using that $p^\beta \leq E^\beta$ and after combining all the power of E 's and assuming that $f_0 < 1$, the rest is straightforward:

$$E^{\beta+3} f_0 (1 \mp f_0) \leq \alpha E^{\beta+3} f_0 = \alpha G(E; \beta + 3) \leq \alpha G_{\max}^{(\beta+3)} \quad (7.25)$$

where $\alpha = 1$ for fermions (upper sign) and $\alpha = 2$ for bosons (lower sign).

To summarize, the maximum for the differential dN that integrates to the one given in eq. (7.11) is estimated as:

$$(dN/dy)_{\max} = \frac{g}{(2\pi)^3} \tau (|d^2 \tilde{\sigma}_\mu u^\mu| + |d^2 \tilde{\sigma}_\perp^{\text{L.R.F}}|) \left(G_{\max}^{(1)} + \frac{\sqrt{\pi^{\mu\nu} \pi_{\mu\nu}}}{2T^2(e+p)} G_{\max}^{(\beta+3)} \right) \quad (7.26)$$

where $d^2 \tilde{\sigma}_\perp^{\text{L.R.F}}$ is given in eq. (7.21).

The validity of the assumption $f_0 < 1$ depends on the choice of the conversion surface cell temperature, chemical potential, etc. It is practically true almost all the time, although there are instances where it is violated. If a more rigorous result is desired, the inequality 7.25 can be replaced by the following one:

$$E^{\beta+3} f_0 (1 \mp f_0) \leq |E^{\beta+3} f_0| + |E^\gamma f_0| |E^{\beta+3-\gamma} f_0| \leq G_{\max}^{\beta+3} + G_{\max}^\gamma G_{\max}^{\beta+3-\gamma} \quad (7.27)$$

where $0 \leq \gamma \leq \beta + 3$ is a parameter one can tune to sharpen the inequality.

The efficiency of direct PDF sampling with maximum given by eq. (7.26) can be tested numerically by studying the ratio between the real maximum encountered in actual sampling and $(dN/dy)_{\max}$. This ratio varies: it is 80% \sim 95% for pions, which take most of the sampling time due to their large multiplicity, and it can be as low as \sim 50% for some heavy particles.

There is yet another approximate treatment for the maximum: the observed numerical maximum from the large number of samples is very close to the real maximum; therefore when a huge number of samples are needed, the observed numerical maximum from some portion of the samples can be used to approximate the real distribution maximum for the rest of the sampling process. Such a ‘‘dynamic maximum’’ mechanism has been implemented and it can be enabled by switching parameters, as explained in detail in Sec. D.

7.4.3 Comparison between the approaches

Both methods use the grouping sampling method, with groups sampled by the inverse CDF method and sampling within groups by the direct PDF sampling method. The grouping between these two approaches are different, and the main difference is how the PDF for the probability distribution of the group random variables is constructed: the numerical approach constructs it numerically and the semi-analytic approach construct it semi-analytically. The total amount of time spent on sampling can be split into two parts: the part for calculating the total multiplicity and constructing the PDF for the group variable and its inverse CDF, and the part for the actual sampling.

For the construction of the group variable PDF and its inverse CDF, the numerical approach takes a much longer time, due to the numerical summation over a huge array. As a comparison, the semi-analytic approach takes almost no time at this stage; in fact most of the time it takes is to read the pre-calculated tables from files.

For the actual sampling, the numerical approach takes a much shorter time per particle sample compared to the semi-analytic approach, and the reasons are explained in the following.

The first reason is that due to the different grouping scheme, the semi-analytic approach needs to sample one more degree of freedom η'_s compared to the numerical approach.

The second reason is that the numerically estimated maximum in the numerical approach is closer to the real maximum compared to the analytically estimated maximum in the semi-analytic approach. However, it should be warned that the numerically estimated maximum in the numerical approach is from a discrete \vec{p}_\perp lattice and it is not the exact maximum on the continuum \vec{p}_\perp space, although the actual difference is so tiny that it generates only $< 10^{-6}$ portion of defects.

Because of the different characteristics of the two approaches, the numerical approach is suitable for a large number of repeated sampling while the semi-analytic approach is suitable for a small number of repeated sampling. For clarity, I define M -repeated sampling such that with a given conversion surface, $M \times N$ number of particles will be sampled, where N is the total number of particle calculated from the Cooper-Frye formula; thus a large number of repeated sampling means $M \gg 1$ and a small number of repeated sampling means $M \approx 1$.

The sampling time is tested with a realistic conversion surface containing 34,516 conversion surface cells. The calculated thermal π^0 yield is ~ 136 . The test is done using one CPU core with 2.2GHz frequency.

First the two approaches are tested with 500 repeated sampling. The numerical approach takes 16.67s to calculate the group variable PDF and its inverse CDF and the total multiplicity for π^0 ; a similar amount of time is spent for each of the rest of the 320 species of the particles³⁵. The sampling for π^0 takes 0.74s and much less for heavy particles due to the smaller number yields. The total execution time for all species of particles is 1530s.

The semi-analytic approach takes 17.78s to calculate the group variable PDF and its inverse CDF³⁶ for all 320 species of particles. It then take ~ 13.1 s to sample π^0 , and much less time for the heavy particle species due to their rareness. The total execution time is 83s.

Next, they are tested for 200 repeated samplings. As expected, the running time for the numerical approach does not change much, since most of its time is spent on calculating the group variable PDF and its inverse CDF, and the run time for the semi-analytic approach becomes $17.78 + 33.05$ s.

Finally they are tested for 50,000 repeated samplings. The time spent on constructing the group variable PDF and its inverse CDF does not change and the numerical approach spent 67s on sampling π^0 , while the semi-analytic approach spent 1340s on sampling π^0 .³⁷

The comparison is summarized in table 7.4.3.

500 repeated sampling	pure numerical	semi-analytic
calculate dN/dy matrices	16.67s for π^0 $\sim \times 100$ for rest of particles	17.78s for all particles (15s for loading tables)
actual sampling	0.74s for π^0 faster for heavier particles	13.1s for π^0 faster for heavier particles
total	1530s	83s
200 repeated total	\sim same	$17.78 + 33.0$ s
50,000 repeated π^0	67s	1,340s

Table 7.2: Efficiency comparison between pure numerical and semi-analytic methods. The test case has 34,516 conversion surface cells and $dN/dy|_{\pi^0} \sim 136$. See the text for detailed explanations.

As a quick summary, for a small number of repeated samplings, the semi-analytic approach is ~ 18 times faster and should be used; for a large number of repeated samplings, the numerical approach is ~ 20 times faster and should be used.

Another subtlety is that due to numerical inaccuracy, especially with fluctuating initial conditions, the trace of $\pi^{\mu\nu}$ is not exactly zero. Therefore the dN/dy for one piece of the conversion surface calculated from the semi-analytic approach, which assumes the traceless of the $\pi^{\mu\nu}$, is not exactly the same as that calculated from the numerical approach. However, with our $\pi^{\mu\nu}$ regulation treatment in the hydrodynamical simulation (Sec. 8.2), the difference is small. It has been checked that only for small dN/dy can the difference become as large as $\sim 2\%$ and only for extremely small dN/dy can the difference becomes as large as $\sim 10\%$.

³⁵Another ‘‘grouping optimization’’ is used here to speed up the calculations so the actual time spent is $\sim 16.67 \times 120$, see Sec. 7.4.4.

³⁶A high precision table for the integral in eq. (7.16) is used here; when a low-precision (~ 5 times larger table spacing when tabulating) table is used it takes ~ 2 s.

³⁷The rest of the species are not tested, but we expect the sampling time ratio between the two sampling methods to be roughly the same for other species of particles.

7.4.4 Other optimizations and implemented models

Particle grouping

Within the Cooper-Frye formalism, two particles that are both fermions or both bosons are considered the same if they have the same mass, chemical potential, and spin degeneracy. Such particles can be grouped and the emission function needs only to be calculated once for each group. At least a particle and its anti-particle belong to the same group, which cuts the total number of particles that need to be calculated from 320 to ~ 150 . Furthermore, if high accuracy is not necessary, particles with mass and chemical potential difference within a certain threshold can also be grouped to speed up the calculation. These particles still need to be of the same type, meaning that they are both fermions or both bosons, and have the same spin degeneracy.

An automatic particle grouping treatment is implemented. Such a treatment first orders all particles according to their mass, then during the loop over particle species for calculating the emission function, if two successive particles with the same type have mass and chemical potentials with the given threshold, the previous result from the first particle will be reused.

Determining total number yield

The Cooper-Frye formula gives average particle yields, which usually is not an integer; however the actually particle yield in each sampling has to be an integer. The way to get the integer number yield from the average value is model dependent. So far three models have been implemented.

The first model separates the average particle yield into an integer and a fractional part, and the fractional decimal is used as the probability to sample one more particle. For example, if the average pion yield is 15.2, then during the actual sampling 20% of the time 16 pions are generated instead of 15.

The second model also separates the average particle yield into an integer and a fractional part. However, instead of being used as the probability of sampling one more particle, the fractional part is used as the mean number of particle in a negative binomial distribution. The actual yield of the particle then is the integer yield plus a number sampled from the negative binomial distribution.

The third model uses the average particle yield (not only the fractional part) as the mean for a negative binomial distribution to sample the actual integer number yield.

These three models yield the same average yields of particles theoretically, however when performing code checks, one should bare in mind the issue mentioned in Sec. 7.2.10.

How to switch between these models and to tune their associated parameters are explained in Sec. D.

There are other models that can be used to determine the number yield. For example, the total energy on the conversion surface can be used as one such constraint. Such a sampling model is only partially implemented, but can be completed relatively easily³⁸.

It should be emphasized again that the purpose of the iSS code is to create an easy-to-use framework in which additional physics models can be implemented and tested relatively easily. For this reason, the currently implemented models are more for demonstration purpose: the justification and comparison between models are left for future work.

File-writing buffer

When using the numerical approach to sample a large amount of samples, the efficiency of writing particle information into files becomes the bottleneck of the sampling subroutine. It was once tested on a scenario that the sampling itself takes only 14s, while without properly handling, the process of writing to files takes 66s. The frequent access to files causes a drop in efficiency, and an internal string buffer is then created to temporarily store the samples, and the buffer is only written to files when a large amount of data is accumulated. This string buffer mechanism

³⁸The advantage of using total energy to constrain the total number yield is that only one numerical integral needs to be done on the conversion surface instead of for all 320 species of particles, and it is computationally cheap. However, after the discovery of the “semi-analytic” (Sec. 7.4.2) approach, the total number yield calculation does not cost heavy computation time anymore and the sampling using the total energy method became less appealing to us.

is tested to be faster than the default buffer provided by the operating system, and its size can be tuned. With optimized buffer size, the time for writing for the example mentioned above is reduced to 23s.

7.5 Code verification

The sampling algorithm is tested by comparing quantities calculated directly from the emission function with those calculated using actual generated samples. The results are shown in this section, but the subtlety regarding locally-negative emission functions needs to be elaborated on first. For clarity, the quantities calculated directly from the emission function in this section are referred to as “theoretical results” and the quantities calculated from actual generated samples are referred to as “results from samples”.

The emission function used in the sampling needs to be non-negative, but its actual calculated value from the Cooper-Frye formula may not be necessarily so, and when it is not, it physically describes particles that flow from the hadron gas phase into the quark-gluon plasma phase. These are rare and usually are ignored during calculation, although they are required for ensuring energy conservation for the whole system. The different treatments of the negative emission function therefore create only tiny differences; but in a code checking for the sampling procedure, such systematic uncertainties had better be excluded. In the following, two different treatments for negative emission functions are given, and it will be explained that a slightly unphysical treatment is the one most suitable for a code check. (After the code has been verified, it was only used in the physically correct mode.)

The simplest treatment is to set the differential emission function given in eq. (7.6) to zero whenever it is negative, which is referred to as the “enforced-positivity” treatment. Such a treatment ignores those particles flying back into the quark-gluon plasma phase, and it is considered to be slightly unphysical; but then the emission function is a perfectly legitimate PDF from which particles can be sampled. For comparison, the same treatment needs to be applied when calculating theoretical results, which means that there then has to be a theta function enforcing the positivity of the emission function in any integrals involving the emission function. The conclusion is that an accurate code check for the sampling *algorithm* is possible with such a positivity requirement as long as the theoretical calculations are modified accordingly.

Note that this treatment for the emission function is not commonly used in previous calculations of theoretical results, where the negative emission function is kept “as-it-is” to maintain energy conservation. The integrated elliptic flow calculated from these two treatments has been checked to give $\sim 1\%$ difference.

There are two approaches used for the sampling (see Sec. 7.4). The enforced-positivity method is possible within the numerical approach, where the differential emission function is numerically calculated and thus open to modification. This treatment is not possible within the semi-analytic approach, because the emission function is enclosed in analytic integrals and it needs to stay unmodified in order for the integrals to be solved analytically.

Another treatment is to keep the sign of the emission function “as long as possible”, and only enforcing it to be positive when necessary. This treatment will be referred as the “semi-positivity” treatment in the following. For the current two sampling approaches, which both use the grouping sampling method (Sec. 7.2.5), this treatment means that the emission probabilities from group variables are calculated, either as analytic integrals or numerical sums, allowing negative contributions. It is only after the group variable for particle emission has been sampled that during the next stage of the sampling (within groups) the particles are sampled with the enforced-positivity emission function.

However, no theoretical calculations can accommodate the semi-positivity requirement for the emission function used in the sampling. This is because in the sampling procedure, the emission function is first used unmodified in the integration and then enforced to be positive later during the sampling of the integrand, and such a “timing” treatment has no associated analytic modifications to the theoretical integrals. Because of this, the theoretical integrals need to be solved at least in the same order, such that the same sequence of treatments can be applied for an honest comparison; for example, for elliptic flows where the spatial integral is performed before the momentum integral,

the semi-positivity requirement cannot be implemented because the sampling procedure solves the momentum integral first.

Note that for the first approach, the emission probabilities for group variables are calculated by integrals of only the positive part of the emission function, and they are different from those calculated from the second approach, which has no such constrains. This means that the different treatment not only alters the distributions of the particle samples within each group, that is, the momentum distributions of particles at given spacial locations, but it also alters the distribution of group variables, which is the spacial distribution of the particles.

For code comparison, the enforced-positivity treatment for negative emission functions is used. As explained above, this means that only the purely numerical sampling approach (Sec. 7.4.1) is feasible. The comparison is performed using an averaged Monte-Carlo Glauber initial condition corresponding to RHIC collisions in the 30 – 40% centrality bin. Samples are generated from 50,000 repeated samplings.

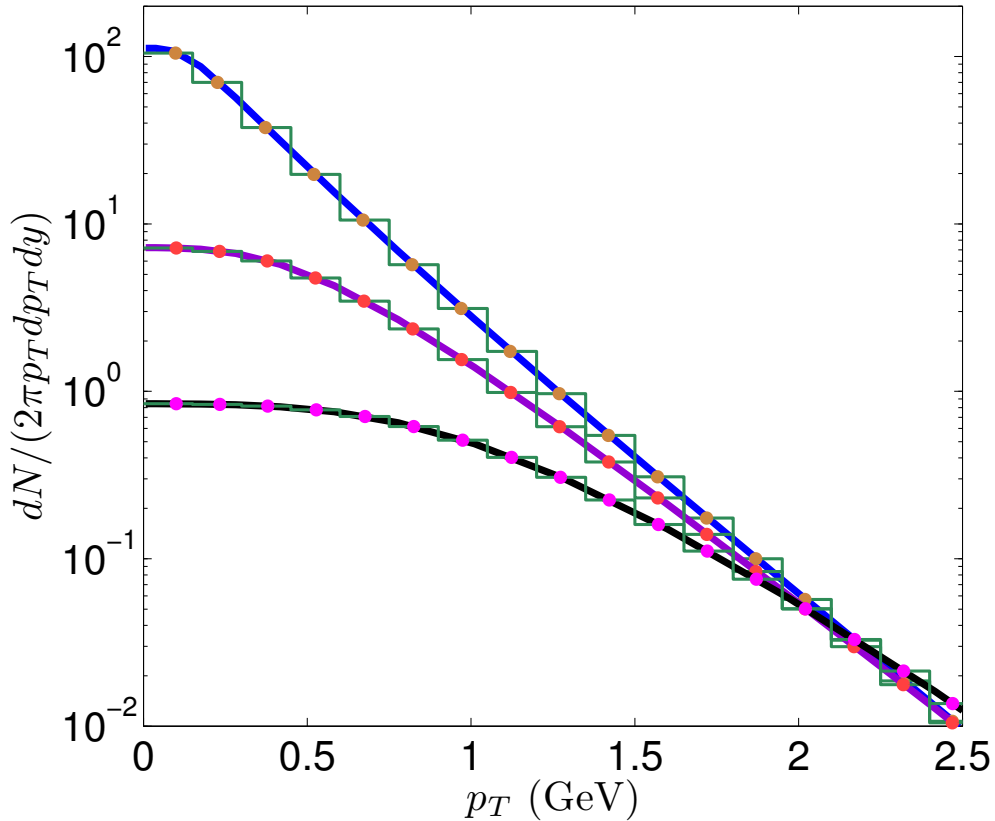


Figure 7.1: p_{\perp} -spectra comparison for thermal pions, kaons, and protons, calculated by integrating emission function (solid curves) or from samples (dots). For other details, see the text.

The p_{\perp} -spectra from theoretical results and samples for thermal pions, kaons, and protons are compared in Fig. 7.1.

The spectra calculated from samples agree with the theoretically calculated spectra up to $p_{\perp} \sim 2.5$ GeV, beyond which the signal becomes noisy due to low statistics.

The differential elliptic flow from theoretical results and samples for thermal pions, kaons, and protons are compared in Fig. 7.2.

The differential elliptic flow calculated from samples agrees with the theoretically calculated flows up to $p_{\perp} \sim 2.5$ GeV, where the signal starts to become noisy due to low statistics. For the integrated v_2 , the sampled results agree with theoretical results to first 5 significant decimals

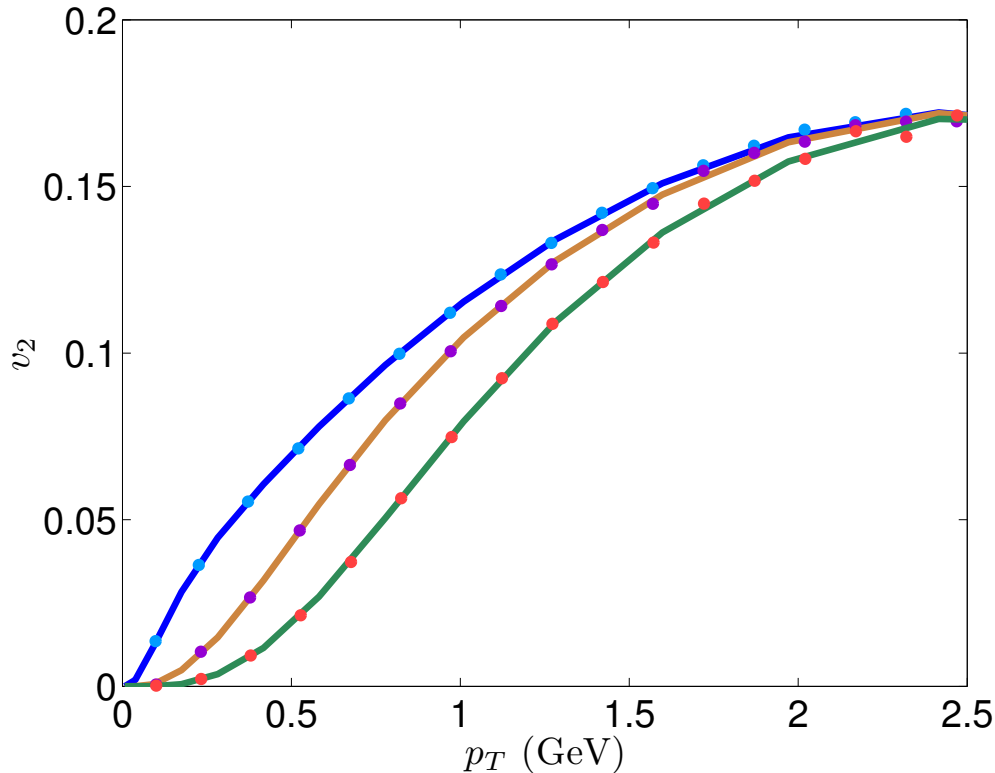


Figure 7.2: Differential elliptic flow comparison for thermal pions, kaons, and protons, calculated theoretically (solid curves) or from samples (dots). See the text for details.

for pions, 4 for kaons, and 3 for protons due to the decrease in statistics; such highly accurate agreements give confidence in the verification of the codes and the sampling algorithm.

The emission rate as a function of the proper time $dN/(d\tau dy)$ for thermal pions, kaons, and protons are compared in Fig. 7.3. The agreement between the theoretical results and those from the samples are excellent.

The distributions of the emission functions in terms of η_s at $y = 0$ calculated theoretically and from samples are compared in Fig. 7.4 using thermal pions, kaons, and protons. The results from samples agree with those calculated theoretically. Note that the bins used to average the samples need to be chosen according to those used in the theoretical calculations (see Sec. 7.2.10), where they are separated by the location of the points used by the Gauss quadrature (see also Sec. D).

In Fig. 7.5, the angular distribution of the emission function $dN/(d\phi dy)$ calculated theoretically and from samples are compared for thermal pions, kaon, and protons. The results from samples agree well with those calculated theoretically. Here again the bins used to average samples need to be chosen according to those used in the theoretical calculations (see Sec. 7.2.10), which are separated by the location points for Gauss quadrature (see also Sec. D).

As explained earlier in this section, only the pure numerical sampling approach is appropriate for a high-accuracy code check. For the semi-analytic sampling approach, the semi-analytic results for the emission probability from each conversion surface cells have been checked to agree well with the numerical results, except when the emission function is tiny. Possible issues stem from the non-positivity of the differential emission function and from the non-tracelessness of $\pi^{\mu\nu}$ produced by the hydrodynamics code (see more details in Sec. 7.4.3).

Still, as a physical comparison rather than a code check, the results from samples generated from the semi-analytic approach can be compared to the theoretical ones. For one bumpy initial

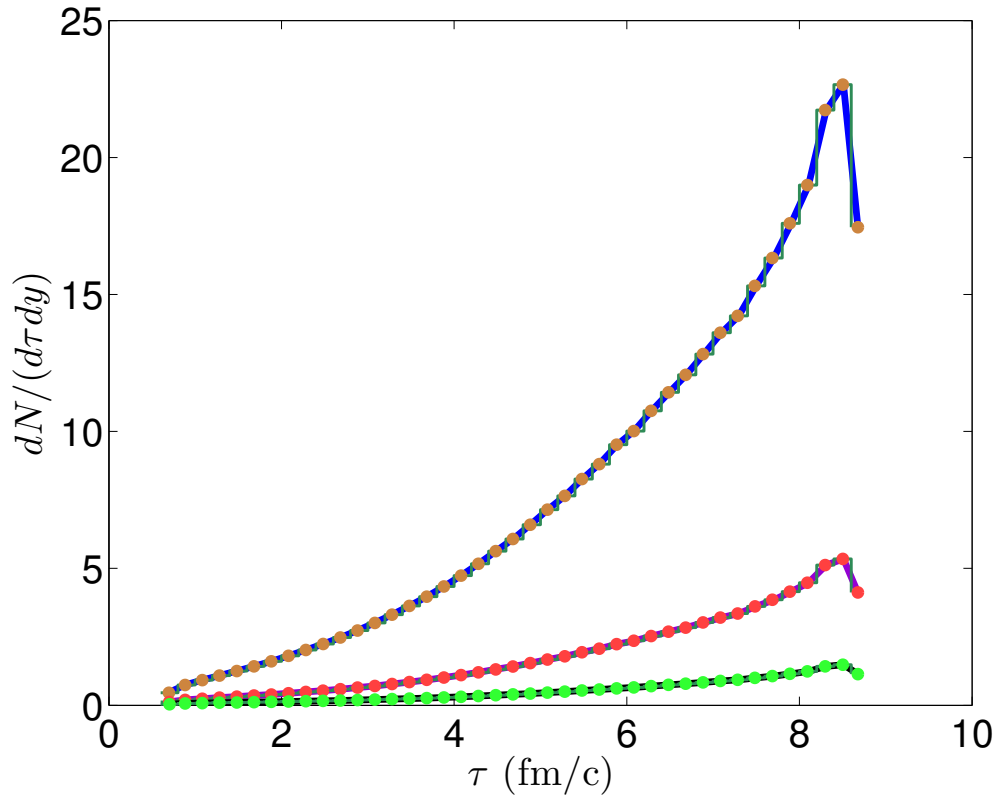


Figure 7.3: Emission rate $dN/(d\tau dy)$ for thermal pions, kaons, and protons, calculated theoretically (solid curves) and from samples (dots). See the text for details.

condition and 5,000 samples, the spectra and the differential flows are compared in Fig. 7.6. Here the spectra and differential flows are calculated without any modifications to the emission function, and samples are generated by semi-analytic approach with naturally the semi-positivity modification as explained. The agreement on spectra is good, but the agreement on differential flow for kaons and protons are bad. This is expected since, for bumpy initial conditions, the emission function can become negative at random locations, which (by enforcing it to be positive) generates numeric noise in the signal for the momentum anisotropy that influences the elliptic flow more than the spectra, which rely only on the averaged flow.

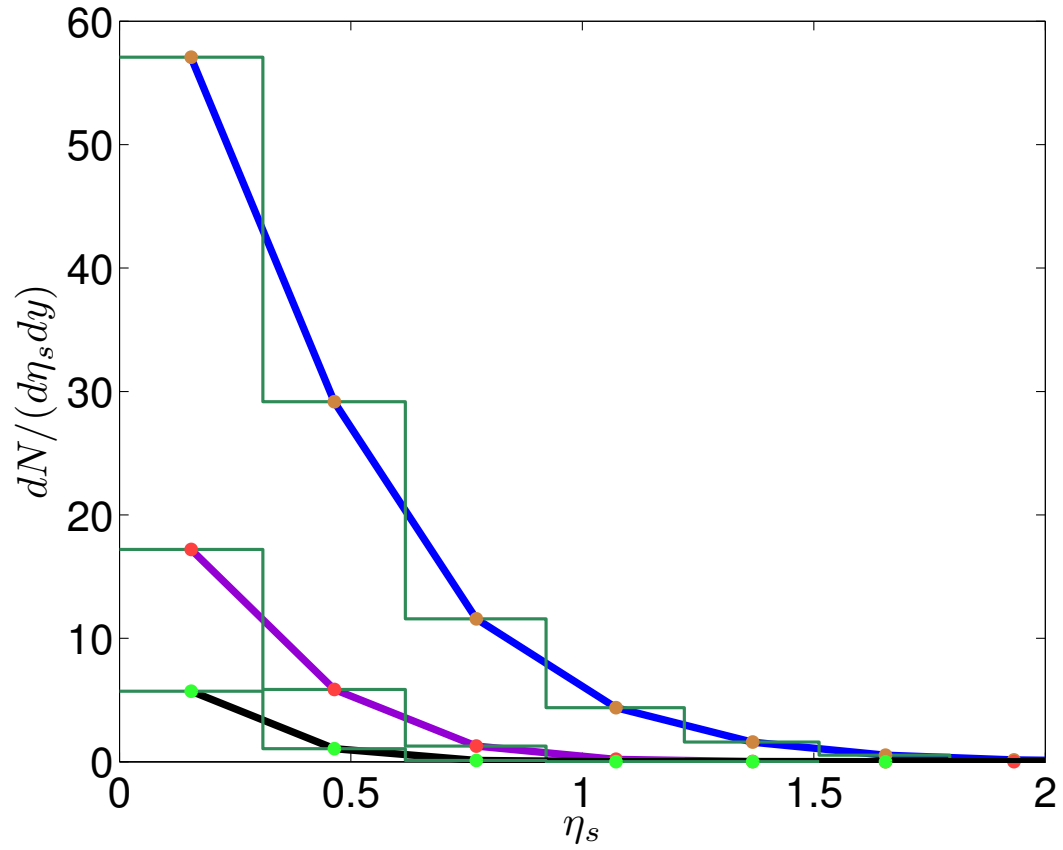


Figure 7.4: Distribution of the emission functions in terms of η_s at $y = 0$ for thermal pions, kaons, and protons, calculated theoretically (solid curves) and from samples (dots). See the text for details.

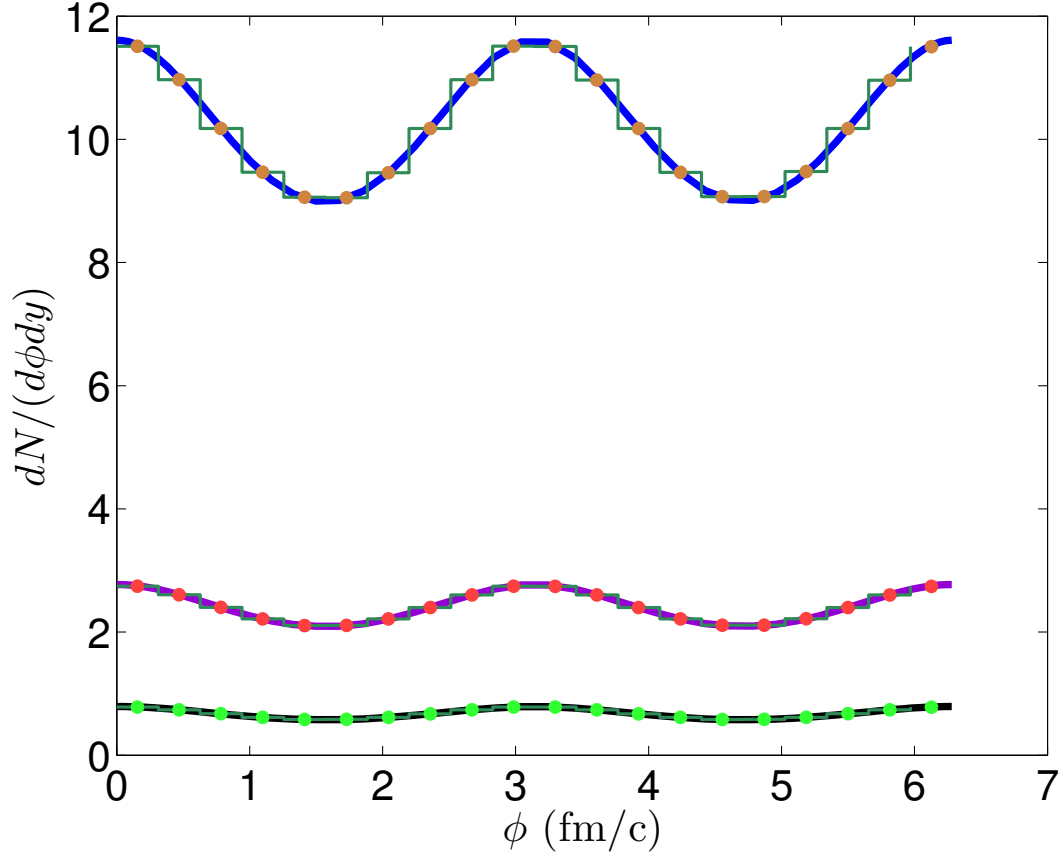


Figure 7.5: Angular distribution of the emission function for thermal pions, kaons, and protons, calculated theoretically (solid curves) and from samples (dots). See the text for details.

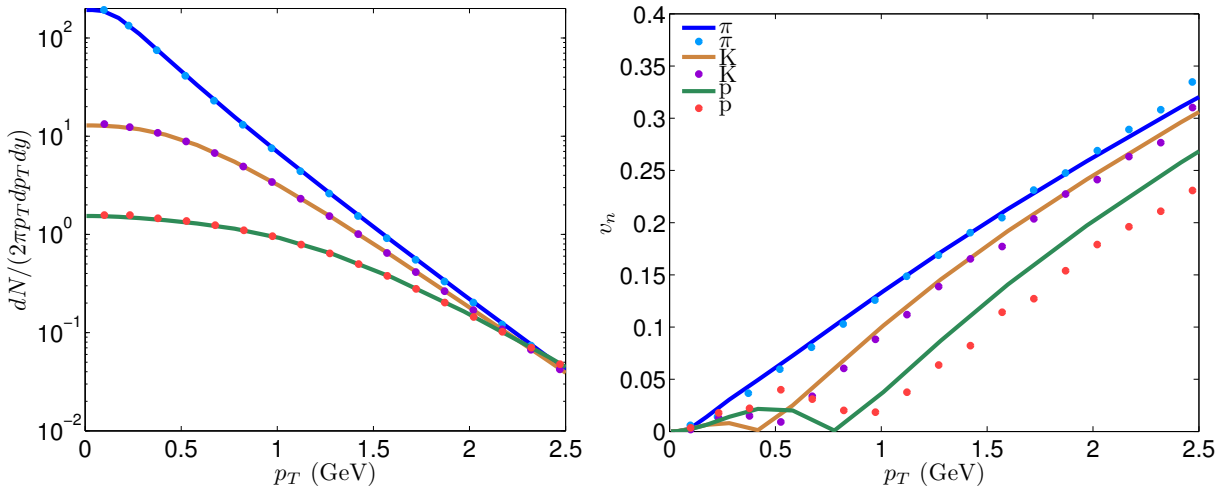


Figure 7.6: p_{\perp} -spectra (left) and differential elliptic flow (right) for thermal pions, kaons, and protons, calculated by integrating the emission function (solid curves) or from samples using the semi-analytic approach (dots). For other details, see the text.

Chapter 8: Miscellaneous topics

In this chapter, we discuss some topics addressing questions that occurred during my research. All sections in this chapter are independent from each other.

8.1 Comparison between eccentricities defined with r^2 and r^n weights

In this section we present a brief comparison between the r^2 -weighted eccentricity coefficients ε_n (Eq. (2.17)) and the r^n -weighted ε'_n (Eq. (2.17)), as well as their associated angles Φ_n and Φ'_n . Fig. 8.1 shows a scatter plot of ε'_n vs. ε_n for $n=3, 4, 5$. One observes approximate proportionality ($\varepsilon'_3 \approx 1.22 \varepsilon_3$, $\varepsilon'_4 \approx 1.48 \varepsilon_4$, $\varepsilon'_5 \approx 1.80 \varepsilon_5$) over most of the eccentricity range, with slopes that increase with n . So whereas Fig. 2.5 shows a decrease of ε_n with increasing n at large impact parameters, the same is not necessarily true for the ε'_n [10]. On the other hand, the linear relations between ε'_n vs. ε_n imply that the relations between v_n and ε'_n will look qualitatively the same as those between v_n and ε_n in Fig. 2.10, with appropriately rescaled horizontal axes.

At the same time, the participant plane angles associated with r^2 -weighted and r^n -weighted eccentricities are tightly correlated, as shown in Fig. 8.2. For given n , the angles Φ_n and Φ'_n fluctuate around each other, with a relative variance that increases with n , on account of the decreasing values of ε_n . From a practical point of view, both definitions are equivalent, and choosing between them is a matter of personal preference.

8.2 Robust viscous hydrodynamics

Viscous hydrodynamics is a theory perturbative around the ideal-fluid theory, where the energy-momentum tensor is expanded as:

$$T^{\mu\nu} = T_0^{\mu\nu} + \Pi^{\mu\nu} = e u^\mu u^\nu - (p + \Pi) \Delta^{\mu\nu} + \pi^{\mu\nu} + W^\mu u^\nu + W^\nu u^\mu.$$

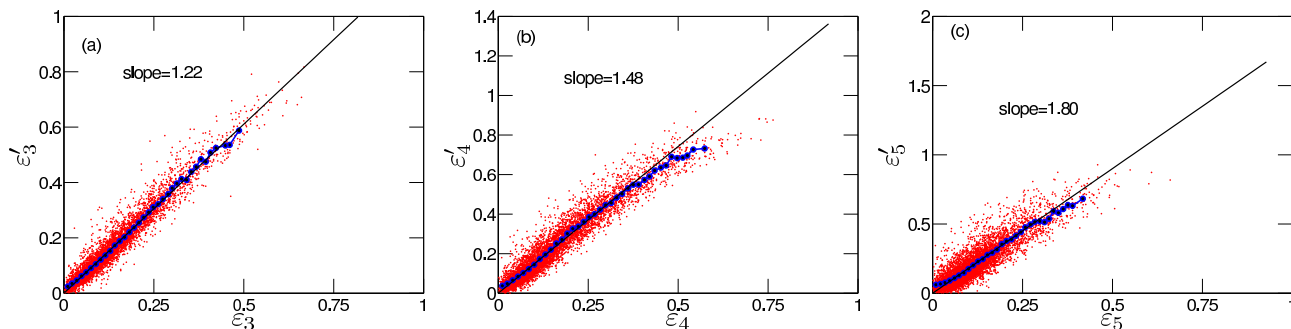


Figure 8.1: Correlation between ε_n and ε'_n , for $n=2, 3, 4$ (panels (a-c)). The blue dots are bin averages for bins that contain more than 10 events. The thick black lines are linear fits.

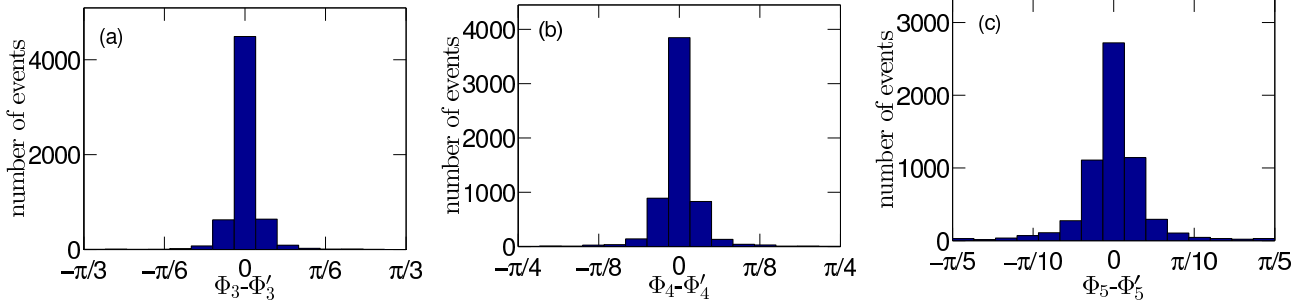


Figure 8.2: Event-by-event correlation between the participant plane angles associated with r^2 - and r^n -weighted eccentricities for harmonic orders $n = 3, 4$, and 5 (panels (a)-(c)). From [20].

Here e and p are the local energy density and pressure, u^μ is the flow 4-velocity, $T_0^{\mu\nu} = eu^\mu u^\nu - p\Delta^{\mu\nu}$ is the energy-momentum tensor assuming local equilibrium, and $\Delta^{\mu\nu} = g^{\mu\nu} - u^\mu u^\nu$ is the spatial projection operator in the local rest frame, $W^\mu = \frac{e+p}{n}V^\mu + q^\mu$ is the energy flow vector, with n the baryon density, V^μ the baryon flow vector, and q^μ the heat flow vector. Choosing the Landau frame and working in the case $W^\mu = q^\mu = 0$ and $\Pi = 0$, the only viscous effects come from the shear pressure tensor $\pi^{\mu\nu}$.

There are several criteria that $\pi^{\mu\nu}$ needs to satisfy.

1. Since viscous hydrodynamics is a perturbative theory, it is only reasonable as long as the $\pi^{\mu\nu}$ term is smaller than the $T_0^{\mu\nu}$ term. A component-wise comparison between them is not appropriate since this would be frame-dependent; $\pi^{\mu\nu}$ and $T^{\mu\nu}$ can only be compared after they are contracted into scalars. We choose:

$$\text{Tr}(\pi^2) = \pi^{\mu\nu}\pi_{\mu\nu} \text{ and } T_0^{\mu\nu}T_{0\mu\nu} = e^2 + 3p^2.$$

The positivity of the former can be checked easily in the local rest frame. Therefore from the perturbative nature of the theory we require:

$$\pi^{\mu\nu}\pi_{\mu\nu} \ll e^2 + 3p^2 \quad (8.1)$$

2. $\pi^{\mu\nu}$ should be traceless:

$$\pi^\mu{}_\mu = 0$$

3. $\pi^{\mu\nu}$ should be perpendicular to u^μ :

$$\pi^{\mu\nu}u_\nu = 0$$

In actual calculations, there are limits to the numerical accuracy so we choose a small number $\xi_0 \ll 1$ to be the “numerical zero” and conditions 2 and 3 become:

$$\pi^\mu{}_\mu \leq \xi_0 \sqrt{\pi^{\mu\nu}\pi_{\mu\nu}} \text{ and } \pi^{\mu\nu}u_\nu \leq \xi_0 \sqrt{\pi^{\mu\nu}\pi_{\mu\nu}}, \forall \nu \quad (8.2)$$

The vector $\pi^{\mu\nu}u_\nu$ should be component-wise zero (in any frame), therefore all its components should be compared to the “numerical zero”, multiplied by $\sqrt{\pi^{\mu\nu}\pi_{\mu\nu}}$. Here we use the scalar $\pi^{\mu\nu}\pi_{\mu\nu}$ as a measure for the magnitude of the $\pi^{\mu\nu}$ tensor that sets the scale (via the factor ξ_0) for how close the numerical result is to zero.

In practice, to ensure that eq. (8.1) is satisfied, we choose a number $\rho_{\max} \lesssim 1$ and require that³⁹:

$$\sqrt{\pi^{\mu\nu}\pi_{\mu\nu}} \leq \rho_{\max} \sqrt{e^2 + 3p^2}. \quad (8.3)$$

³⁹ $\rho_{\max} \ll 1$ corresponds to the required “ \ll ” condition in eq. (8.2); $\rho_{\max} = \infty$ corresponds to no constraint at all.

This, together with eq. (8.3), then implies

$$\begin{aligned}\pi^\mu_\mu &\leq \xi_0 \rho_{\max} \sqrt{\pi^{\mu\nu} \pi_{\mu\nu}}, \\ \pi^{\mu\nu} u_\nu &\leq \xi_0 \rho_{\max} \sqrt{\pi^{\mu\nu} \pi_{\mu\nu}}.\end{aligned}\tag{8.4}$$

These requirements may be violated during the hydrodynamic evolution for various reasons. For example, the $\pi^{\mu\nu}$ could be initialized to be unphysically large (we use the Navier-Stokes condition to initialize $\pi^{\mu\nu}$), so the relations would be violated at early time, or the initial profile could be not smooth enough, so the numerical derivative gives artificially large (and possibly wrong) numerical values that violate these conditions near discontinuities of the profile, etc. In principle, once the system is sufficiently close to thermal equilibrium, a properly generated $\pi^{\mu\nu}$, evolved on a super-fine lattice, should avoid such problems; in practice however, a super-fine lattice is computationally infeasible and (what is worse) the Isreal-Stewart equations are not causal on a super-fine lattice [122]. In practice, fluctuating initial conditions and early hydrodynamic starting times lead to patches in the numerical grid where one or several of the conditions 8.3 are violated. For our simulations, we found, however, that the region where these conditions are violated are mostly at the early stage and/or in the dilute regions outside the freeze-out surface. The violations in these regions do not have much influence on the dynamical behavior of the QGP in the physical region inside the freeze-out surface; however if they are left untreated, these violations lead to accumulating numerical errors that cause the evolution code to break down later. For these reasons, in the following we develop a systematic treatment that suppresses large viscous terms. This stabilizes the code at a low price to pay: we effectively change the evolution equations in the fireball region where we have very large viscous corrections to the ideal fluid $T_0^{\mu\nu}$.

We enforce a continuous systematic regulation on $\pi^{\mu\nu}$ in each time step on the whole lattice by replacing $\pi^{\mu\nu}$ by $\hat{\pi}^{\mu\nu}$:

$$\pi^{\mu\nu} \rightarrow \hat{\pi}^{\mu\nu} \equiv \pi^{\mu\nu} \frac{\tanh(\rho)}{\rho}\tag{8.5}$$

where ρ is the largest quantity at each lattice point among the following:

$$\frac{\sqrt{\pi^{\mu\nu} \pi_{\mu\nu}}}{\rho_{\max} \sqrt{e^2 + 3p^2}}, \frac{\pi^\mu_\mu}{\xi_0 \rho_{\max} \sqrt{\pi^{\mu\nu} \pi_{\mu\nu}}}, \text{ and } \frac{\pi^{\mu\nu} u_\nu}{\xi_0 \rho_{\max} \sqrt{\pi^{\mu\nu} \pi_{\mu\nu}}}, \forall \nu$$

It is easy to check that $\hat{\pi}^{\mu\nu}$ satisfies eq. (8.3), and that it is close to $\pi^{\mu\nu}$ when no modifications are needed; that is, when the left hand sides of the inequalities in eq. (8.3) are small compared to their right hand sides, the regulated quantity is close to its original value. Only those grid points where $\pi^{\mu\nu}$ violates or is close to violating the inequalities (8.3) will be strongly modified, in which case all components of $\pi^{\mu\nu}$ are suppressed by the same factor.

Because smoother flow velocity profiles give smaller $\pi^{\mu\nu}$, the systematic suppression of $\pi^{\mu\nu}$ can be understood as locally replacing sharp jumps in the flow profile by flatter pieces; the regulation process is therefore an implicit and automatic way of smoothing profiles. This treatment allows us to perform hydrodynamic calculations using very bumpy initial conditions, including those using disk-like nucleons that have density discontinuities. Without this regularization VISH2+1 breaks down for such initial conditions.

In our calculations, we take $\xi_0 = 0.001$, which is reasonable because the relative discretization error from solving transport equations is of the order of a few powers of the lattice spacing and our lattice spacing is chosen to be 0.1 fm. During our simulations we found that ρ_{\max} is best chosen to be a value between 1 – 10 in order to enable the simulation to finish, and to keep the momentum distribution generated from the QGP almost unmodified. By choosing ρ_{\max} of order unity or larger, we modify the effective evolution equations only in regions where the conditions of validity of the Isreal-Stewart equations are badly violated.

8.3 Time evolution of the event plane orientations

The orientations of the event planes are not fixed during the evolution of the fireball: one of the reasons for their changing is the mode-coupling effect, by which the orientation of an event plane of a particular harmonic order receives contributions from geometric deformations of the fireball of a different harmonic order. To demonstrate such effects visually, we take 3 randomly selected events, and divide their freeze-out surface into strips with time step 0.2 fm/c. Each strip of the freeze-out surface is then used to calculate the anisotropy flows formed by particles emitted only from this part of the freeze-out surface using the Cooper-Frye formula. The resulting anisotropic flow angles from different pieces are then studied; their evolution is interpreted as the time evolution of the anisotropic flow angles during the lifetime of the fireball. Typical results are shown in Fig. 8.3.

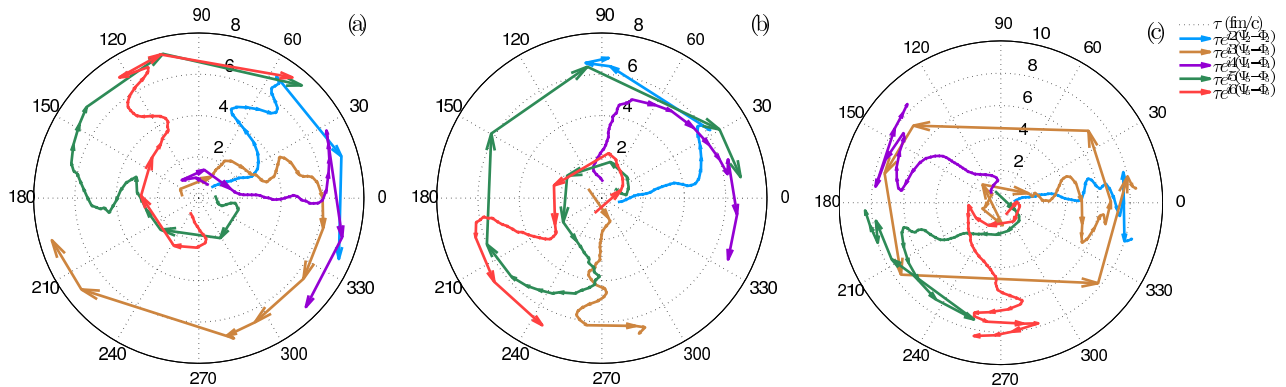


Figure 8.3: Time evolution of the anisotropic flow angles. See text for more explanation.

Here the anisotropy angles are the n th-order flow angles Ψ_n (see eq. (2.22)) calculated from the spectra emitted by the strips of the freeze-out surface, measured relative to the participant plane angles Φ_n . To make the time evolution manifest, we interpret $(\tau, n(\Psi_n - \Phi_n))$ as polar coordinates (r, θ) , i.e. we plot the complex quantities $\tau e^{in(\Psi_n - \Phi_n)}$ as trajectories (as a function of τ) in the complex plane. The arrows point to the positive τ direction along the trajectories.

An anisotropy angle is said to be “in-plane” if $\Psi_n - \Phi_n$ is close to 0° and “out-of-plane” if $\Psi_n - \Phi_n$ is close to 180° . The most dramatic rotation happens if the angle changes from one sector to the opposite sector that differs by 180° .

It is clear that the 3rd- through 6th-order anisotropy angles in the 1st event (Fig. 8.3 left), the 5th- and 6th- order anisotropy angles in the 2nd event (Fig. 8.3 middle), and the 3rd-order anisotropy angle in the 3rd event (Fig. 8.3 right) all have undergone dramatic rotations during the evolution of the fireball. The 2nd- and 3rd-order anisotropy angles are relatively stable during most of the early evolution, reflecting the relative smallness of the mode-coupling effects; the angles only rotate near the end of the evolution of the fireball where the remnant of the fireball becomes dilute and irregular and the orientation of all harmonics becomes somewhat random.

8.4 Best estimator for flows using eccentricities

The authors of [123] use regression methods to study the flow response from the eccentricity predictors, where they use a quantity similar to the coefficient of determination to find the “best estimator” and to study the second-order mode-coupling effects. Their calculations are based on simulations with NeXSPheRIO which uses ideal hydrodynamics, with flow calculated from Monte-Carlo sampled particles. Here we extend their work in three ways: 1) by including viscosity, 2) by using the continuous particle emission formalism, 3) and by including higher-order mixing terms. Including higher-order terms will always improve the fit, but the degree of improvement depends on whether the expansion is made with eccentricities defined using moments or cumulants [98].

We used the same pure event-by-event hydrodynamic simulation data tuned for Pb-Pb collision at 2.76 ATeV as reported in [84] (and Chap. 4), and plotted the “Quality value” [123] for various settings as functions of centrality in Fig. 8.4. The “Quality value” is so defined that it is between 0 and 1; the closer it is to 1, the better the approximation. When approximating v_n using only linear terms (equation (2) in [123])

$$v_n e^{in\Psi_n} = k\varepsilon_n e^{in\Phi_n} + \mathcal{E} \quad (8.6)$$

where \mathcal{E} is the “error”, the “Quality value” is defined to be (equation (3) in [123]):

$$Quality = k \frac{\sqrt{\langle \varepsilon_n^2 \rangle}}{\sqrt{\langle v_n^2 \rangle}} \quad (8.7)$$

using the best-fit parameter k from eq. (8.6). When approximating v_n including two terms (equation (5) in [123])

$$v_n e^{in\Psi_n} = k\varepsilon_n e^{in\Phi_n} + k'\varepsilon_{n'} e^{in\Phi_{n'}} + \mathcal{E} \quad (8.8)$$

the “Quality value” is defined to be (equation (6) in [123]):

$$Quality = \frac{\langle |k\varepsilon_n e^{in\Phi_n} + k'\varepsilon_{n'} e^{in\Phi_{n'}}|^2 \rangle}{\langle v_n^2 \rangle} \quad (8.9)$$

using the best-fit parameters k and k' from eq. (8.8). More terms can be included in the expansion and the “Quality value” is always defined to be the ratio between the fit and the actual value.

The differences from [123] include that we use continuous Cooper-Frye particle emission to calculate flows, and that we include viscosity, although the viscosity was found to play little role, so only the results using MC-KLN initial condition with $\eta/s = 0.2$ are shown here.

The elliptic and triangular flows are known to be well approximated as linear functions of the eccentricities of the same order, so we skip them here and only report on the results for the quadrangular and pentangular flows which receive large contributions from mode-coupling effects. More specifically, various studies including [123] show that the quartic flow v_4 mainly receives a contribution from ε_2^2 and the pentangular flow v_5 receives a contribution from $\varepsilon_2\varepsilon_3$, and it is shown in [123] that by including these two quadratic terms in the expansions the approximations are improved, but the approximations are still not good enough, especially in very peripheral collisions.

Here the four curves labeled as $\sqrt{\dots/\langle v_{4,5}^2 \rangle}$ are those “Quality values” calculated using expansions that contain only two terms: for v_4 , they are ε_4 and ε_2^2 , and for v_5 , they are ε_5 and $\varepsilon_2\varepsilon_3$ ⁴⁰; for the cumulant expansion, ε_n is replaced by C_n [98]. It is seen that when including two terms in the expansion, both the moment- and the cumulant-defined eccentricities give very similar results in terms of the goodness of the fit.

Next we allow more terms in the expansion to test the convergence. The terms we included in the linear combinations are summarized in the following. Here we use the complex eccentricity notation $\mathcal{E}_n = \varepsilon_n e^{in\Phi_n}$ (see Chap. 2), with \mathcal{E}_n replaced by C_n in the case for cumulants, and “*” for complex conjugate.

- v_4 using 5 moment-defined eccentricities: $\mathcal{E}_4, \mathcal{E}_2^2, \mathcal{E}_1\mathcal{E}_3, \mathcal{E}_3^2\mathcal{E}_2^*, \mathcal{E}_6\mathcal{E}_2^*$.
- v_5 using 12 moment-defined eccentricities: $\mathcal{E}_5, \mathcal{E}_2\mathcal{E}_3, \mathcal{E}_2^2\mathcal{E}_1, \mathcal{E}_1\mathcal{E}_4, \mathcal{E}_3^2\mathcal{E}_1^*, \mathcal{E}_2^3\mathcal{E}_1^*, \mathcal{E}_4^2\mathcal{E}_3^*, \mathcal{E}_2^4\mathcal{E}_3^*, \mathcal{E}_3^3\mathcal{E}_4^*, \mathcal{E}_7\mathcal{E}_2^*, \mathcal{E}_8\mathcal{E}_3^*, \mathcal{E}_9\mathcal{E}_4^*$.

⁴⁰In fact, it is the complex product of the complex eccentricity vectors that are used (see [123]).

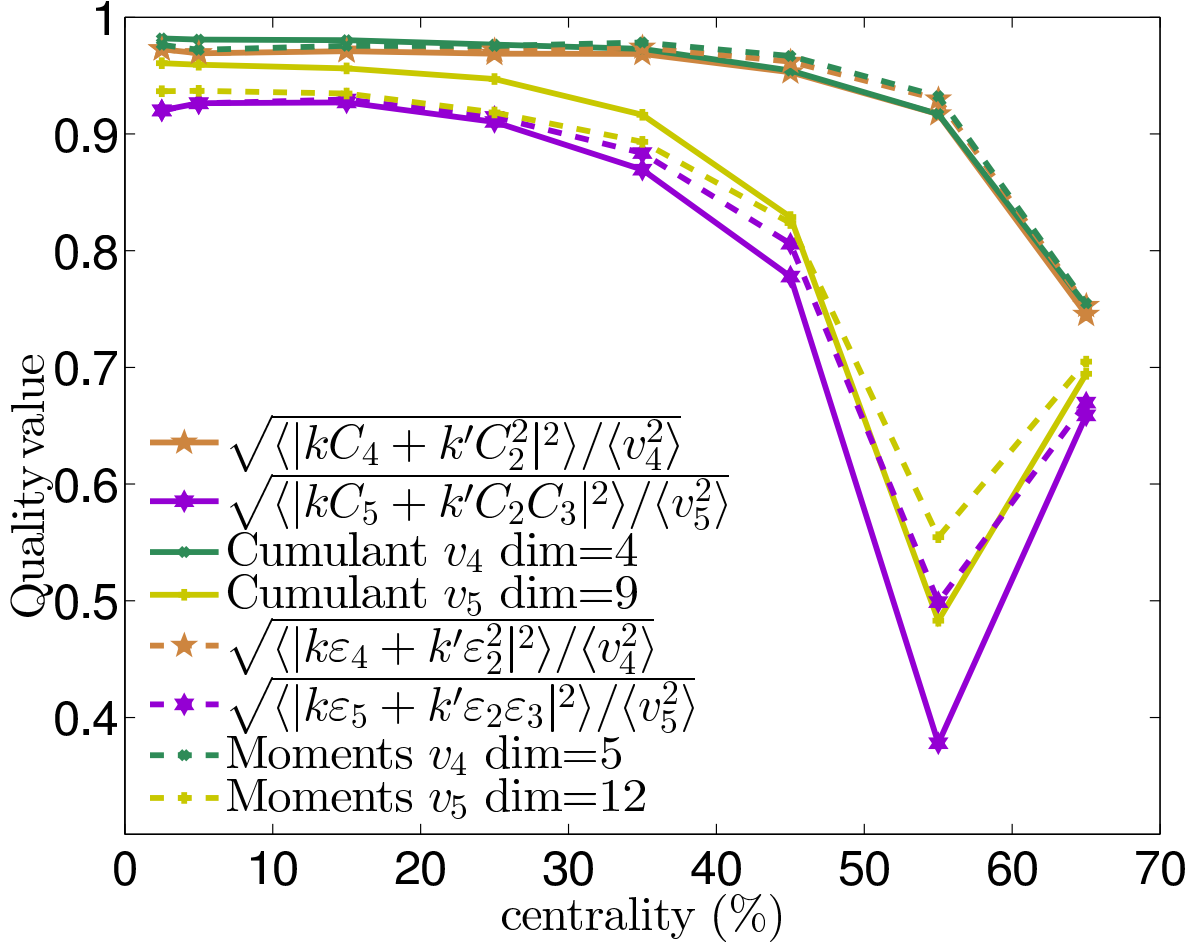


Figure 8.4: (Color online) The “Quality values” (equation 8.7, 8.9; see also [123]) giving the goodness of description of the flows in terms of a combination of eccentricities, as functions of centrality. The first 4 curves (solid) use the cumulant expansion and the last 4 curves (dashed) use the moment expansion. The curve labeled by “cumulant v_4 dim=4” means that the curve is the “Quality value” for v_4 using cumulant-defined eccentricities [98] which includes 4 terms in the expansion, etc. See the text for details.

- v_4 using 4 cumulant-defined eccentricities: $\mathcal{E}_4, \mathcal{E}_2^2, \mathcal{E}_1\mathcal{E}_3, \mathcal{E}_3^2\mathcal{E}_2^*$.
- v_5 using 9 cumulant-defined eccentricities: $\mathcal{E}_5, \mathcal{E}_2\mathcal{E}_3, \mathcal{E}_2^2\mathcal{E}_1, \mathcal{E}_1\mathcal{E}_4, \mathcal{E}_3^2\mathcal{E}_1^*, \mathcal{E}_2^3\mathcal{E}_1^*, \mathcal{E}_4^2\mathcal{E}_3^*, \mathcal{E}_2^4\mathcal{E}_3^*, \mathcal{E}_3^3\mathcal{E}_4^*$.

The curves labeled by “moment/cumulant $v_{4,5}$ dim=...” show the resulting “Quality values” by allowing more terms in the expansion listed above. It is seen that the cumulant-defined eccentricities give faster convergence (the “k values” for both expansion methods converge to 1 if an infinite number of terms are included) than moment-defined eccentricities, but neither is good enough to be used as a quantitative replacement of the hydrodynamics for v_5 (or higher flows), even when higher order couplings are taken into account. This suggests that, in terms of a quantitative study for higher-order flows, the role of hydrodynamics cannot be replaced by simply looking at the response of the flow to various eccentricities.

Chapter 9: Summary

In this thesis, I summarized my Ph.D. work on event-by-event hydrodynamic simulations for relativistic heavy-ion collisions and related fields.

In Chap. 2, we compared the previously dominating single-shot hydrodynamics with the current and future mainstream event-by-event hydrodynamic simulations. The event-by-event simulations are more realistic, but they are very time consuming; the single-shot simulation is economical, but then the question arises as to whether it can be used as a sufficiently precise replacement for the event-by-event simulations. The answer to this question depends on the observable studied. We showed that for the event average of the multiplicity and elliptic and triangular flow, the time consuming event-by-event hydrodynamic simulations can, to a good approximation, be replaced by the single-shot ones, when using properly constructed, participant-plane rotated and averaged initial conditions. For azimuthally averaged p_T spectra the single-shot simulation can still give results not very different from those given by event-by-event simulations, especially if the shear viscosity is not very small. For higher-order flows, such as $v_{4,5}$, the single-shot simulations are shown to be incapable of reproducing those from event-by-event simulations. The main reason for this failure are nonlinear mode-coupling effects that are very sensitive to initial-state density fluctuations. In this chapter, I also showed related quantities, such as the distributions of eccentricities and anisotropic flows from event-by-event calculations. These can be used as calibrations for future studies.

In Chap. 3, we showed that the elliptic and triangular flows can be studied using the much more economical single-shot hydrodynamic simulations to a good ($\sim 10\%$) approximation. We further showed that the eccentricity-normalized elliptic and triangular flows are “definition independent”: $v_2\{2\}/\varepsilon_2\{2\}$ is very close to $v_2\{4\}/\varepsilon_2\{4\}$, $\langle v_2 \rangle / \langle \varepsilon_2 \rangle$, and $\bar{v}_2 / \bar{\varepsilon}_2$; likewise, $v_3\{2\}/\varepsilon_3\{2\}$ is very close to $\langle v_3 \rangle / \langle \varepsilon_3 \rangle$ and $\bar{v}_3 / \bar{\varepsilon}_3$. The eccentricity normalized flows from single-shot hydrodynamic simulations can thus be used to study the experimental flow data when normalized by similarly constructed eccentricities. This is particularly important when comparing experimental results (which are always affected by event-by-event fluctuations) with results from single-shot hydrodynamics (which does not account for fluctuations). The eccentricity normalized flows can be used individually to extract the specific shear viscosity for a given initial condition model or, when combined, can be used to reduce the ambiguity introduced by different initial condition models with varying initial fluctuation spectra. We followed this strategy and showed that the elliptic and triangular flow data measured by the ALICE collaboration at the LHC prefer a small specific shear viscosity close to $\eta/s = 0.08$, when considering the MC-Glauber and MC-KLN models. In order to allow for a much larger η/s value, the initial condition model must feature triangularity values $\sim 50\%$ larger than the ones provided by the MC-Glauber and MC-KLN models. This was found to be the case in the IP-Glasma model [79].

Chap. 4 focused on correlations between event-plane angles. We showed that the event-plane angle correlation measurements by the ATLAS collaboration can be explained using results from the same set of hydrodynamic simulations tuned for spectra and flow observables. The same correlation patterns cannot be explained directly from the initial conditions, implying that they are generated dynamically during the evolution of the medium. Some of the strong correlation patterns, like the one between harmonic orders 2 and 4, and the one among orders 2, 3, and 5, are direct evidence for strong mode-coupling effects. The correlations serve as another set of observables, complementing the spectra and anisotropic flow coefficients v_n , and the success of their hydrodynamic explanation adds to the evidence that the medium created in heavy-ion collisions is fact hydrodynamical. We also note that the strong mode-coupling effects cannot be reproduced from a linear response treatment of hydrodynamics.

In Chap. 5, we showed that including only ~ 20 out of 319 carefully chosen resonances can already yield spectra and flow results within 1% relative error. Such a treatment can be used to shorten the currently lengthy (~ 3 hours) resonance decay calculations by a factor of ten — since these calculations are the current bottleneck for event-by-event hydrodynamic simulations — and consequently lower the cost of performing event-by-event simulations by the same factor. We provided a complete table listing the contribution of resonances to stable particles for all major stable particles.

Chap. 6 focused on various ways of calculating (theoretically) and measuring (experimentally) anisotropic flows, and their comparisons. We pointed out that the event-plane angle Ψ_n fluctuates from event to event, and that the differential event-plane angle $\Psi_n(p_T) - \Psi_n$ also fluctuates from event to event. We showed that traces of such angular fluctuations can be measured experimentally, and explained how such measurements allow the study of the fluctuation of the orientation of flows in addition to the fluctuation of the magnitude of flows. We showed that the effects are larger for heavy particles, in near-central collisions, and for small $p_T \lesssim m$. In particular, we proposed a precise measurement and comparison of $\langle v_n(p_\perp) \rangle$, $v_n\{\text{EP}\}(p_\perp)$, $v_n[2](p_\perp)$, and $v_n\{2\}(p_\perp)$ for identified pions, kaons and protons with transverse momenta $p_\perp < 2$ GeV to confirm the hydrodynamically predicted effects from flow angle fluctuations. We also pointed out the flow angle fluctuations are responsible for half of the factorization breaking effects, the other half being caused by fluctuations in the magnitudes $v_n(p_\perp)$ of the anisotropic flows.

In Chap. 7, we gave a thorough description of the general sampling methodology, and showed that it can be applied in an efficient way to sample particles whose emission is determined by the Cooper-Frye formula, using the simplification of longitudinal boost invariance. We explained several sampling algorithms and analyzed their strengths and weaknesses, focusing heavily on sampling efficiencies. This chapter serves as a study in sampling methodology as well as a technical document that explains the actual sampling implementation used in the iSpectraSampler program.

We also included discussions of a number of other miscellaneous topics in Chap. 8. We compared the r^2 - and r^n -weighted eccentricities. We described how we regulate unphysically large $\pi^{\mu\nu}$ values that can arise especially during the early stage or in the dilute tail of the density distribution of the fireball hydrodynamic evolution. In addition, we showed that the event plane angles determined using particles emitted at different proper times are not necessarily the same, and that their time evolution can be dramatic. Finally, we showed quantitatively that including non-linear combinations of eccentricities can improve the prediction of v_4 and v_5 as the corresponding responses.

Appendix A: Choice of parameters used in the simulations

This section contains tables for the choice of parameters used in our simulations. Unless for academic study (Chap. 2), all our simulations are tuned to explain experimental data, which requires a choice of parameters according to the following tables. These tables should be used for pure hydrodynamic simulations only, not for hybrid simulations (see Chap. 1).

Table A.1: Choice of parameters for Au+Au at 200 AGeV

Model	initial time	decoupling temp.	η/s	model parameter	norm.
MC-Glb	0.6 (fm/c)	120 MeV	0.08	$\alpha = 0.14$	28.66
MC-KLN	0.6 (fm/c)	120 MeV	0.2	$\lambda = 0.218$	7.42

Here the “initial time” is the initial proper time τ_0 when hydrodynamics starts. The “decoupling temp.” is the decoupling temperature under which hadrons cease to interact and fly into the detector via free streaming. The “model parameter” for the MC-Glauber model is the soft-hard ratio α (x in eq. (3.1), δ in eq. (20) in [6]), and for the MC-KLN model it is the λ parameter used when determining the saturation scale (Eq. (9) in [8]). Finally the “norm.” is the normalization factor that, when multiplied with the profile directly generated from the initial condition models, gives the initial entropy density profile that can be used in hydrodynamic simulations.⁴¹

Table A.2: Choice of parameters for Pb+Pb at 2760 AGeV

Model	initial time	decoupling temp.	η/s	model parameter	norm.
MC-Glb	0.6 (fm/c)	120 MeV	0.08	$\alpha = 0.118$	56.76
MC-KLN	0.6 (fm/c)	120 MeV	0.2	$\lambda = 0.138$	9.92

⁴¹For the MC-Glauber model, it is the κ parameter in eq. (3.1) or C in eq. (20) in [6]. For the MC-KLN model, we take $dN/dy = (\text{norm.})dN_g/dy$.

Appendix B: Table of parameters for cutting centralities

When using the optical Glauber model, the centrality class can be determined and cut in terms of ranges in impact parameter b ; Table B.1 lists the choice of impact parameters used in cutting centralities this way. A given centrality class includes events with impact parameters ranging from b_{\min} to b_{\max} ; the event-averaged impact parameter is \bar{b} and the averaged N_{part} is \bar{N}_{part} . This table was used in the study presented in Chap. 2.

In later studies, we use centrality classes determined by N_{part} ; such centrality class cuts are contained in tables B.2-B.8. For a given centrality bin, each table includes the $N_{\text{part},\min}$ and $N_{\text{part},\max}$ values which define the bin, the average $N_{\text{part},\text{avg}}$, the range in impact parameter b_{\min} to b_{\max} , and the average b_{avg} .

Table B.1: Centrality table for Au+Au at 200 A GeV [6].

centrality	b_{\min} (fm)	b_{\max} (fm)	b (fm)	N_{part}
0-5%	0.0	3.3	2.2	352.2
5-10%	3.3	4.7	4.04	294.7
10-15%	4.7	5.8	5.27	245.6
15-20%	5.8	6.7	6.26	204.2
20-30%	6.7	8.2	7.48	154.5
30-40%	8.2	9.4	8.81	103.8
40-50%	9.4	10.6	10.01	64.9
50-60%	10.6	11.6	11.11	36.6
60-70%	11.6	12.5	12.06	18.8
70-80%	12.5	13.4	12.96	7.5
80-90%	13.4	14.3	13.85	4.4

Table B.2: Centrality table for Au+Au at 63 AGeV (1,000,000 initial conditions)

centrality (%)	$N_{\text{part,min}}$	$N_{\text{part,max}}$	$N_{\text{part,avg}}$	b_{min} (fm)	b_{max} (fm)	b_{avg} (fm)
0- 5%	322.0	391.0	351.0	0.0	4.0	2.1
5-10%	273.0	322.0	296.7	2.2	5.3	3.8
10-15%	232.0	273.0	252.0	3.6	6.2	5.0
15-20%	197.0	232.0	214.2	4.7	7.1	5.9
20-25%	167.0	197.0	181.5	5.5	8.0	6.7
25-30%	140.0	167.0	153.1	6.2	8.6	7.4
30-35%	117.0	140.0	128.2	6.7	9.3	8.0
35-40%	96.0	117.0	106.3	7.3	10.0	8.6
40-45%	79.0	96.0	87.3	8.0	10.6	9.2
45-50%	63.0	79.0	70.8	8.4	11.3	9.7
50-55%	50.0	63.0	56.4	8.7	11.8	10.2
55-60%	39.0	50.0	44.1	9.2	12.4	10.7
60-65%	29.0	39.0	33.7	9.6	13.0	11.1
65-70%	21.0	29.0	25.0	9.8	13.5	11.6
70-75%	15.0	21.0	18.0	10.3	14.2	12.0
75-80%	10.0	15.0	12.5	10.4	14.7	12.4
80-85%	7.0	10.0	8.4	10.8	15.4	12.9
85-90%	4.0	7.0	5.3	10.9	16.2	13.3
90-95%	2.0	4.0	3.1	11.0	17.5	13.7

Table B.3: Centrality table for Au+Au at 200 AGeV (1,000,000 initial conditions)

centrality (%)	$N_{\text{part,min}}$	$N_{\text{part,max}}$	$N_{\text{part,avg}}$	b_{min} (fm)	b_{max} (fm)	b_{avg} (fm)
0- 5%	327.0	393.0	355.4	0.0	4.1	2.1
5-10%	278.0	327.0	302.0	2.5	5.3	3.9
10-15%	237.0	278.0	257.1	3.8	6.4	5.0
15-20%	202.0	237.0	218.8	4.7	7.2	5.9
20-25%	171.0	202.0	185.7	5.5	8.0	6.7
25-30%	144.0	171.0	156.8	6.3	8.7	7.4
30-35%	120.0	144.0	131.3	6.8	9.4	8.1
35-40%	99.0	120.0	109.1	7.3	10.3	8.7
40-45%	81.0	99.0	89.7	7.9	10.7	9.2
45-50%	65.0	81.0	72.7	8.3	11.2	9.8
50-55%	51.0	65.0	58.0	8.9	11.9	10.3
55-60%	40.0	51.0	45.5	9.2	12.4	10.8
60-65%	30.0	40.0	34.8	9.4	13.2	11.2
65-70%	22.0	30.0	25.9	9.9	14.2	11.7
70-75%	16.0	22.0	18.7	10.1	14.1	12.1
75-80%	11.0	16.0	13.0	10.5	14.8	12.5
80-85%	7.0	11.0	8.6	10.5	15.4	12.9
85-90%	4.0	7.0	5.4	11.1	16.2	13.4
90-95%	2.0	4.0	3.2	11.0	17.8	13.8

Table B.4: Centrality table for Cu+Cu at 63 AGeV (1,000,000 initial conditions)

centrality (%)	$N_{\text{part,min}}$	$N_{\text{part,max}}$	$N_{\text{part,avg}}$	b_{min} (fm)	b_{max} (fm)	b_{avg} (fm)
0- 5%	100.0	125.0	107.8	0.0	3.2	1.5
5-10%	86.0	100.0	92.5	0.8	4.2	2.6
10-15%	74.0	86.0	79.5	1.7	4.8	3.4
15-20%	63.0	74.0	68.2	2.9	5.6	4.1
20-25%	54.0	63.0	58.3	3.4	6.1	4.6
25-30%	46.0	54.0	49.6	3.8	6.8	5.1
30-35%	38.0	46.0	41.9	4.1	7.2	5.6
35-40%	32.0	38.0	35.2	4.5	7.9	6.0
40-45%	27.0	32.0	29.3	5.0	8.1	6.4
45-50%	22.0	27.0	24.2	5.0	8.8	6.7
50-55%	18.0	22.0	19.7	5.3	9.0	7.1
55-60%	14.0	18.0	15.9	5.6	9.8	7.4
60-65%	11.0	14.0	12.7	5.8	10.2	7.8
65-70%	9.0	11.0	9.9	5.9	10.7	8.1
70-75%	7.0	9.0	7.7	6.3	11.1	8.4
75-80%	5.0	7.0	5.8	6.3	11.9	8.7
80-85%	4.0	5.0	4.4	6.2	12.8	9.0
85-90%	3.0	4.0	3.2	6.1	13.1	9.3
90-95%	2.0	3.0	2.1	6.8	14.0	9.7

Table B.5: Centrality table for Cu+Cu at 200 AGeV (1,000,000 initial conditions)

centrality (%)	$N_{\text{part,min}}$	$N_{\text{part,max}}$	$N_{\text{part,avg}}$	b_{min} (fm)	b_{max} (fm)	b_{avg} (fm)
0- 5%	102.0	125.0	110.3	0.0	3.4	1.5
5-10%	88.0	102.0	95.1	0.9	4.2	2.7
10-15%	76.0	88.0	81.9	2.1	5.0	3.5
15-20%	65.0	76.0	70.4	2.8	5.5	4.1
20-25%	56.0	65.0	60.3	3.5	6.0	4.7
25-30%	47.0	56.0	51.3	3.6	6.9	5.2
30-35%	40.0	47.0	43.5	4.3	7.3	5.6
35-40%	33.0	40.0	36.6	4.6	7.8	6.1
40-45%	28.0	33.0	30.5	4.9	8.2	6.4
45-50%	23.0	28.0	25.1	5.3	9.0	6.8
50-55%	18.0	23.0	20.5	5.3	9.4	7.2
55-60%	15.0	18.0	16.5	5.7	10.0	7.5
60-65%	12.0	15.0	13.2	5.7	10.4	7.8
65-70%	9.0	12.0	10.3	5.9	10.8	8.2
70-75%	7.0	9.0	8.0	6.3	11.5	8.5
75-80%	5.0	7.0	6.0	6.3	11.6	8.8
80-85%	4.0	5.0	4.5	6.6	12.3	9.1
85-90%	3.0	4.0	3.3	6.7	13.0	9.4
90-95%	2.0	3.0	2.2	6.8	14.0	9.8

Table B.6: Centrality table for Pb+Pb at 2760 AGeV (10,000,000 initial conditions)

centrality (%)	$N_{\text{part,min}}$	$N_{\text{part,max}}$	$N_{\text{part,avg}}$	b_{min} (fm)	b_{max} (fm)	b_{avg} (fm)
0- 5%	357.0	416.0	384.4	0.0	4.4	2.2
5-10%	305.0	357.0	330.3	2.3	5.7	4.1
10-15%	261.0	305.0	282.6	3.8	6.8	5.3
15-20%	223.0	261.0	241.4	4.8	7.7	6.2
20-25%	189.0	223.0	205.4	5.6	8.7	7.1
25-30%	159.0	189.0	173.9	6.4	9.4	7.8
30-35%	133.0	159.0	146.1	7.2	10.1	8.5
35-40%	110.0	133.0	121.7	7.7	10.7	9.1
40-45%	90.0	110.0	100.2	8.3	11.4	9.7
45-50%	73.0	90.0	81.4	8.7	12.1	10.3
50-55%	58.0	73.0	65.0	9.3	12.9	10.8
55-60%	45.0	58.0	50.9	9.6	13.4	11.3
60-65%	34.0	45.0	39.0	10.1	14.1	11.8
65-70%	25.0	34.0	29.0	10.2	14.7	12.3
70-75%	17.0	25.0	20.9	10.4	15.2	12.7
75-80%	12.0	17.0	14.4	11.0	16.1	13.2
80-85%	7.0	12.0	9.5	11.3	16.4	13.6
85-90%	5.0	7.0	5.9	11.5	17.2	14.1
90-95%	2.0	5.0	3.4	11.8	18.5	14.5

Table B.7: Centrality table for Pb+Pb at 5500 AGeV (1,000,000 initial conditions)

centrality (%)	$N_{\text{part,min}}$	$N_{\text{part,max}}$	$N_{\text{part,avg}}$	b_{min} (fm)	b_{max} (fm)	b_{avg} (fm)
0- 5%	360.0	416.0	386.9	0.0	4.3	2.3
5-10%	309.0	360.0	333.6	2.5	6.1	4.1
10-15%	265.0	309.0	286.2	3.9	6.8	5.3
15-20%	226.0	265.0	244.9	4.9	7.9	6.3
20-25%	192.0	226.0	208.4	5.9	8.4	7.1
25-30%	162.0	192.0	176.5	6.6	9.3	7.9
30-35%	135.0	162.0	148.3	7.2	10.0	8.6
35-40%	112.0	135.0	123.5	8.0	10.8	9.2
40-45%	92.0	112.0	101.8	8.3	11.4	9.8
45-50%	74.0	92.0	82.7	9.0	11.9	10.3
50-55%	59.0	74.0	66.1	9.4	12.6	10.9
55-60%	45.0	59.0	51.8	9.8	13.1	11.4
60-65%	34.0	45.0	39.7	10.2	13.7	11.9
65-70%	25.0	34.0	29.6	10.6	14.2	12.4
70-75%	18.0	25.0	21.3	10.8	15.0	12.8
75-80%	12.0	18.0	14.7	11.4	15.4	13.3
80-85%	8.0	12.0	9.7	11.7	16.1	13.7
85-90%	5.0	8.0	6.0	11.8	17.5	14.1
90-95%	2.0	5.0	3.5	12.2	18.1	14.6

Table B.8: Centrality table for Pb+Pb at 2760 AGeV

centrality (%)	$N_{\text{part,min}}$	$N_{\text{part,max}}$	$N_{\text{part,avg}}$	b_{min} (fm)	b_{max} (fm)	b_{avg} (fm)
0- 1%	401.0	416.0	406.6	0.0	2.8	1.1
1- 2%	390.0	401.0	395.7	0.0	3.2	1.8
2- 3%	379.0	390.0	384.6	0.9	3.7	2.4
3- 4%	368.0	379.0	373.3	1.4	4.2	2.8
4- 5%	357.0	368.0	362.1	1.9	4.4	3.2
5- 6%	346.0	357.0	351.1	2.3	4.8	3.5
6- 7%	335.0	346.0	340.3	2.7	5.3	3.8
7- 8%	325.0	335.0	330.0	2.9	5.3	4.1
8- 9%	315.0	325.0	319.9	3.2	5.5	4.3
9-10%	305.0	315.0	310.1	3.5	5.7	4.6
10-11%	296.0	305.0	300.6	3.8	5.9	4.8
11-12%	287.0	296.0	291.4	4.0	6.2	5.1
12-13%	278.0	287.0	282.4	4.2	6.4	5.3
13-14%	269.0	278.0	273.7	4.4	6.7	5.5
14-15%	261.0	269.0	265.2	4.7	6.8	5.7
15-16%	253.0	261.0	256.9	4.8	7.1	5.9
16-17%	245.0	253.0	248.9	5.0	7.1	6.1
17-18%	237.0	245.0	241.2	5.2	7.3	6.2
18-19%	230.0	237.0	233.6	5.5	7.6	6.4
19-20%	223.0	230.0	226.3	5.7	7.7	6.6
20-21%	216.0	223.0	219.1	5.6	7.9	6.8
21-22%	209.0	216.0	212.1	5.8	8.1	6.9
22-23%	202.0	209.0	205.2	6.0	8.3	7.1
23-24%	195.0	202.0	198.6	6.3	8.4	7.2
24-25%	189.0	195.0	192.1	6.4	8.7	7.4
25-26%	183.0	189.0	185.9	6.4	8.8	7.5
26-27%	177.0	183.0	179.7	6.7	9.0	7.7
27-28%	171.0	177.0	173.7	6.7	9.0	7.8
28-29%	165.0	171.0	167.9	6.9	9.1	8.0
29-30%	159.0	165.0	162.3	6.8	9.4	8.1
30-31%	154.0	159.0	156.7	7.2	9.6	8.2
31-32%	149.0	154.0	151.3	7.3	9.6	8.4
32-33%	143.0	149.0	146.0	7.3	9.8	8.5
33-34%	138.0	143.0	140.8	7.5	9.9	8.6
34-35%	133.0	138.0	135.9	7.6	10.1	8.8
35-36%	129.0	133.0	131.0	7.7	10.2	8.9
36-37%	124.0	129.0	126.2	7.8	10.3	9.0
37-38%	119.0	124.0	121.6	8.0	10.4	9.1
38-39%	115.0	119.0	117.0	8.1	10.7	9.3
39-40%	110.0	115.0	112.6	8.2	10.7	9.4
40-41%	106.0	110.0	108.3	8.3	10.8	9.5
41-42%	102.0	106.0	104.1	8.4	11.1	9.6
42-43%	98.0	102.0	100.1	8.4	11.1	9.7

Continued on next page

Table B.8 – continued from previous page

centrality (%)	$N_{\text{part,min}}$	$N_{\text{part,max}}$	$N_{\text{part,avg}}$	b_{min} (fm)	b_{max} (fm)	b_{avg} (fm)
43-44%	94.0	98.0	96.1	8.6	11.2	9.8
44-45%	90.0	94.0	92.2	8.6	11.4	10.0
45-46%	87.0	90.0	88.5	8.7	11.5	10.1
46-47%	83.0	87.0	84.8	9.0	11.9	10.2
47-48%	80.0	83.0	81.3	8.9	11.8	10.3
48-49%	76.0	80.0	77.8	9.0	12.1	10.4
49-50%	73.0	76.0	74.4	9.1	12.0	10.5
50-51%	70.0	73.0	71.2	9.3	12.5	10.6
51-52%	66.0	70.0	68.0	9.3	12.3	10.7
52-53%	63.0	66.0	64.9	9.3	12.6	10.8
53-54%	60.0	63.0	61.9	9.5	12.4	10.9
54-55%	58.0	60.0	59.0	9.5	12.9	11.0
55-56%	55.0	58.0	56.2	9.6	12.7	11.1
56-57%	52.0	55.0	53.5	9.8	13.1	11.2
57-58%	50.0	52.0	50.9	9.8	13.0	11.3
58-59%	47.0	50.0	48.3	9.7	13.2	11.4
59-60%	45.0	47.0	45.9	9.9	13.4	11.5
60-61%	42.0	45.0	43.5	10.1	13.5	11.6
61-62%	40.0	42.0	41.1	10.2	13.6	11.7
62-63%	38.0	40.0	38.9	10.2	13.7	11.8
63-64%	36.0	38.0	36.8	10.3	14.1	11.9
64-65%	34.0	36.0	34.7	10.4	13.9	12.0
65-66%	32.0	34.0	32.7	10.2	14.0	12.1
66-67%	30.0	32.0	30.8	10.4	14.4	12.2
67-68%	28.0	30.0	28.9	10.7	14.2	12.3
68-69%	26.0	28.0	27.2	10.8	14.3	12.4
69-70%	25.0	26.0	25.5	10.6	14.7	12.5
70-71%	23.0	25.0	23.8	10.7	14.6	12.6
71-72%	22.0	23.0	22.4	10.4	14.9	12.6
72-73%	20.0	22.0	20.7	10.9	14.8	12.7
73-74%	19.0	20.0	19.4	10.8	15.2	12.8
74-75%	17.0	19.0	18.0	11.0	15.1	12.9
75-76%	16.0	17.0	16.7	11.1	15.2	13.0
76-77%	15.0	16.0	15.5	11.1	15.3	13.1
77-78%	14.0	15.0	14.4	11.0	15.5	13.2
78-79%	13.0	14.0	13.3	11.2	15.6	13.3
79-80%	12.0	13.0	12.2	11.1	16.1	13.4
80-81%	11.0	12.0	11.2	11.3	16.0	13.4
81-82%	10.0	11.0	10.3	11.5	16.0	13.5
82-83%	9.0	10.0	9.4	11.4	16.2	13.6
83-84%	8.0	9.0	8.7	11.6	16.2	13.7
84-85%	7.0	8.0	8.0	11.5	16.4	13.8
85-86%	7.0	7.0	7.0	11.6	16.5	13.9
86-87%	6.0	7.0	6.5	11.5	17.1	14.0

Continued on next page

Table B.8 – continued from previous page

centrality (%)	$N_{\text{part,min}}$	$N_{\text{part,max}}$	$N_{\text{part,avg}}$	b_{min} (fm)	b_{max} (fm)	b_{avg} (fm)
87-88%	6.0	6.0	6.0	11.8	16.9	14.0
88-89%	5.0	6.0	5.1	11.7	16.9	14.2
89-90%	5.0	5.0	5.0	11.5	17.2	14.2
90-91%	4.0	5.0	4.0	11.8	17.7	14.4
91-92%	4.0	4.0	4.0	11.8	17.7	14.4
92-93%	3.0	4.0	3.3	11.9	18.3	14.6
93-94%	3.0	3.0	3.0	12.1	18.4	14.6
94-95%	2.0	3.0	2.8	12.1	18.5	14.7
95-96%	2.0	2.0	2.0	12.2	19.2	14.9
96-97%	2.0	2.0	2.0	11.9	19.0	14.9
97-98%	2.0	2.0	2.0	11.9	18.9	14.9
98-99%	2.0	2.0	2.0	12.1	19.1	14.9

Appendix C: Feed down contribution tables for π , K , p , Λ , Σ^+ , and Ξ^- [100]

This section contains tables for the resonance decay contributions as explained in Chap. 5. For all the tables listed in this section, $T_{\text{conv}} = 120$ MeV.

Table C.1: Resonance contribution list for π^+

name	mass (GeV)	total contribution (%)	
ω	0.78259	15.398	
ρ^0	0.7758	11.179	
ρ^+	0.7758	11.098	
$K^{*+}(892)$	0.89166	5.54	
$\bar{K}^{*0}(892)$	0.8961	5.355	
η	0.54775	4.682	
$\bar{\Delta}^-(1232)$	1.232	2.613	
$\Delta^{++}(1232)$	1.232	2.606	
$b_1^+(1235)$	1.2295	2.498	60%
$\eta'(958)$	0.95778	2.069	
$a_0^+(980)$	0.9847	1.862	
$h_1(1170)$	1.17	1.26	
$a_1^+(1260)$	1.23	1.226	
$b_1^-(1235)$	1.2295	1.19	
$b_1^0(1235)$	1.2295	1.181	
$a_2^+(1320)$	1.3183	1.177	
$\Sigma^+(1385)$	1.3828	1.09	
$\bar{\Sigma}^-(1385)$	1.3872	1.057	
$f_1(1285)$	1.2818	0.994	
$\bar{K}_1^0(1270)$	1.273	0.963	
$K_1^+(1270)$	1.273	0.962	
$\bar{\Delta}^0(1232)$	1.232	0.857	
$\Delta^+(1232)$	1.232	0.856	
$a_1^0(1260)$	1.23	0.817	
$a_2^0(1320)$	1.3183	0.771	
$\phi(1020)$	1.0195	0.762	80%
$f_0(980)$	0.9741	0.613	
$K_1^0(1270)$	1.273	0.472	
$K_1^-(1270)$	1.273	0.472	

Continued on next page

Table C.1 – continued from previous page

name	mass (GeV)	total contribution (%)	
$f_2(1270)$	1.2754	0.45	
$a_1^-(1260)$	1.23	0.409	
$a_0^-(980)$	0.9847	0.402	
$a_0^0(980)$	0.9847	0.399	
$a_2^-(1320)$	1.3183	0.398	
$\pi_1^+(1400)$	1.376	0.373	
$K_2^{*+}(1430)$	1.4256	0.368	
$\Xi^0(1530)$	1.5318	0.357	
$\bar{\Delta}^-(1600)$	1.6	0.356	
$\Delta^{++}(1600)$	1.6	0.356	
$\bar{K}_2^{*0}(1430)$	1.4324	0.35	
$\bar{\Xi}^-(1530)$	1.535	0.347	
$\bar{K}_1^0(1400)$	1.402	0.341	
$K_1^+(1400)$	1.402	0.34	
$p(1520)$	1.52	0.305	
$\bar{n}(1520)$	1.52	0.305	
$\eta(1295)$	1.294	0.297	
$\bar{K}^{*-}(1410)$	1.414	0.294	
$K^{*+}(1410)$	1.414	0.294	
$\pi^+(1300)$	1.3	0.257	
$\bar{\Delta}^0(1600)$	1.6	0.249	
$\Delta^+(1600)$	1.6	0.249	
$\bar{n}(1440)$	1.44	0.241	
$p(1440)$	1.44	0.241	
$\omega(1420)$	1.419	0.205	
$a_0^+(1450)$	1.474	0.196	
$\Lambda(1405)$	1.4065	0.188	90%
$\Lambda(1405)$	1.4065	0.188	
$\eta_2(1645)$	1.617	0.185	
$f_1(1420)$	1.4263	0.174	
$K_1^0(1400)$	1.402	0.173	
$K_1^-(1400)$	1.402	0.173	
$a_0^0(1450)$	1.474	0.153	
$\bar{n}(1675)$	1.675	0.147	
$p(1675)$	1.675	0.147	
$\bar{\Delta}^-(1700)$	1.7	0.145	
$\Delta^{++}(1700)$	1.7	0.145	
$\omega_3(1670)$	1.667	0.144	
$\pi^0(1300)$	1.3	0.142	
$K^{*0}(1410)$	1.414	0.14	
$K^{*-}(1410)$	1.414	0.14	
$\Delta^0(1600)$	1.6	0.135	
$\bar{\Delta}^+(1600)$	1.6	0.134	
$\rho_3^+(1690)$	1.6888	0.123	

Continued on next page

Table C.1 – continued from previous page

name	mass (GeV)	total contribution (%)	
$p(1680)$	1.685	0.119	
$\bar{n}(1680)$	1.685	0.119	
$\bar{\Delta}^0(1700)$	1.7	0.117	
$\Delta^+(1700)$	1.7	0.117	
$K_2^{*-}(1430)$	1.4256	0.115	
$\bar{\Delta}^-(1620)$	1.63	0.113	
$\Delta^{++}(1620)$	1.63	0.113	
$\Lambda(1520)$	1.5195	0.112	
$\bar{\Lambda}(1520)$	1.5195	0.112	
$K_2^{*0}(1430)$	1.4324	0.109	
$\eta(1405)$	1.4103	0.104	
$\bar{n}(1535)$	1.535	0.103	
$p(1535)$	1.535	0.102	
$\bar{n}(1700)$	1.7	0.102	
$p(1700)$	1.7	0.102	
$\bar{n}(1720)$	1.72	0.098	
$p(1720)$	1.72	0.098	
$\rho_3^0(1690)$	1.6888	0.097	
$\pi^-(1300)$	1.3	0.093	
$a_0^-(1450)$	1.474	0.091	
$\bar{p}(1520)$	1.52	0.088	95%
$n(1520)$	1.52	0.088	
$\bar{\Delta}^0(1620)$	1.63	0.086	
$\Delta^+(1620)$	1.63	0.086	
$\pi_2^+(1670)$	1.6724	0.086	
$\rho^0(1450)$	1.465	0.082	
$\rho^+(1450)$	1.465	0.082	
$\pi_1^-(1400)$	1.376	0.08	
$\pi_1^0(1400)$	1.376	0.08	
$\bar{\Sigma}^-(1670)$	1.67	0.079	
$\Sigma^+(1670)$	1.67	0.079	
$\Sigma^+(1775)$	1.775	0.075	
$\bar{\Sigma}^-(1775)$	1.775	0.075	
$\rho^+(1700)$	1.72	0.072	
$n(1700)$	1.7	0.072	
$\bar{p}(1700)$	1.7	0.072	
$n(1440)$	1.44	0.072	
$\bar{p}(1440)$	1.44	0.072	
$\Delta^0(1700)$	1.7	0.07	
$\bar{\Delta}^+(1700)$	1.7	0.07	
$\Lambda(1690)$	1.69	0.069	
$\bar{\Lambda}(1690)$	1.69	0.069	
$\Sigma^0(1385)$	1.3837	0.069	
$\bar{\Sigma}^0(1385)$	1.3837	0.069	

Continued on next page

Table C.1 – continued from previous page

name	mass (GeV)	total contribution (%)	
$\omega(1650)$	1.67	0.067	
$n(1675)$	1.675	0.061	
$\bar{p}(1675)$	1.675	0.061	
$\pi_1^+(1600)$	1.653	0.06	
$\bar{K}_2^0(1770)$	1.773	0.056	
$K_2^+(1770)$	1.773	0.056	
$\Sigma^0(1670)$	1.67	0.05	
$\bar{\Sigma}^0(1670)$	1.67	0.05	
$\bar{\Delta}^-(1905)$	1.89	0.05	
$\Delta^{++}(1905)$	1.89	0.05	
$\rho^0(1700)$	1.72	0.049	
$\Delta^0(1620)$	1.63	0.048	
$\bar{\Delta}^+(1620)$	1.63	0.048	
$\pi_2^0(1670)$	1.6724	0.045	
$\bar{n}(1710)$	1.71	0.044	
$\bar{\Delta}^0(1905)$	1.89	0.044	
$K_0^{*+}(1430)$	1.412	0.044	
$\Delta^+(1905)$	1.89	0.044	
$p(1710)$	1.71	0.044	
$\bar{K}_0^{*0}(1430)$	1.412	0.044	
$\bar{\Sigma}^-(1660)$	1.66	0.043	
$\Sigma^+(1660)$	1.66	0.043	
$\bar{n}(1650)$	1.655	0.042	
$p(1650)$	1.655	0.042	
$f_0(1500)$	1.507	0.041	
$\eta(1475)$	1.476	0.04	98%
$\Delta^-(1950)$	1.93	0.04	
$\Delta^{++}(1950)$	1.93	0.04	
$\bar{\Delta}^-(1920)$	1.92	0.039	
$\Delta^{++}(1920)$	1.92	0.039	
$\Lambda(1830)$	1.83	0.037	
$\bar{\Lambda}(1830)$	1.83	0.037	
$\rho_3^-(1690)$	1.6888	0.037	
$\bar{K}_3^{*0}(1780)$	1.776	0.034	
$K_3^{*+}(1780)$	1.776	0.034	
$\rho^-(1700)$	1.72	0.034	
$n(1535)$	1.535	0.033	
$\bar{p}(1535)$	1.535	0.033	
$n(1720)$	1.72	0.033	
$\bar{p}(1720)$	1.72	0.033	
$\bar{p}(1680)$	1.685	0.032	
$n(1680)$	1.685	0.032	
$K_2^0(1770)$	1.773	0.032	
$\bar{K}_2^0(1820)$	1.816	0.032	

Continued on next page

Table C.1 – continued from previous page

name	mass (GeV)	total contribution (%)	
K_2^- (1770)	1.773	0.032	
K_2^+ (1820)	1.816	0.032	
π_2^- (1670)	1.6724	0.031	
Λ (1600)	1.6	0.03	
$\bar{\Lambda}$ (1600)	1.6	0.03	
f_0 (1370)	1.4	0.029	
Δ^0 (1905)	1.89	0.028	
$\bar{\Delta}^+$ (1905)	1.89	0.028	
n (1710)	1.71	0.027	
\bar{p} (1710)	1.71	0.027	
ϕ (1680)	1.68	0.026	
$\bar{\Delta}^0$ (1950)	1.93	0.024	
Δ^+ (1950)	1.93	0.024	99%
K^{*+} (1680)	1.717	0.024	
\bar{K}^{*0} (1680)	1.717	0.024	
π_1^- (1600)	1.653	0.024	
π_1^0 (1600)	1.653	0.024	
$\bar{\Sigma}^-$ (1915)	1.915	0.023	
Σ^+ (1915)	1.915	0.023	
$\bar{\Delta}^0$ (1920)	1.92	0.023	
Δ^+ (1920)	1.92	0.023	
Ξ^0 (1820)	1.823	0.023	
$\bar{\Xi}^-$ (1820)	1.823	0.023	
$\bar{\Sigma}^-$ (1940)	1.94	0.022	
Σ^+ (1940)	1.94	0.022	
Λ (1670)	1.67	0.021	
$\bar{\Lambda}$ (1670)	1.67	0.021	
$\bar{\Delta}^-$ (1910)	1.91	0.02	
Δ^{++} (1910)	1.91	0.02	
Σ^0 (1775)	1.775	0.02	
$\bar{\Sigma}^0$ (1775)	1.775	0.02	
K_2^0 (1820)	1.816	0.019	
K_2^- (1820)	1.816	0.019	
$\bar{\Delta}^-$ (1930)	1.96	0.017	
Δ^{++} (1930)	1.96	0.017	
f_2' (1525)	1.525	0.015	
Σ^0 (1660)	1.66	0.014	
$\bar{\Sigma}^0$ (1660)	1.66	0.014	
$\bar{\Sigma}^-$ (1750)	1.75	0.014	
Σ^+ (1750)	1.75	0.014	
Σ^0 (1750)	1.75	0.014	
$\bar{\Sigma}^0$ (1750)	1.75	0.014	
K_3^{*0} (1780)	1.776	0.014	
K_3^{*-} (1780)	1.776	0.014	

Continued on next page

Table C.1 – continued from previous page

name	mass (GeV)	total contribution (%)
$f_2(2010)$	2.011	0.012
$\Delta^-(1600)$	1.6	0.012
$\bar{\Delta}^{++}(1600)$	1.6	0.012
$\Lambda(1890)$	1.89	0.011
$\bar{\Lambda}(1890)$	1.89	0.011
$\Delta^0(1920)$	1.92	0.011
$\bar{\Delta}^+(1920)$	1.92	0.011
$\bar{\Delta}^0(1910)$	1.91	0.011
$\Delta^+(1910)$	1.91	0.011
$\Delta^0(1950)$	1.93	0.011
$\bar{\Delta}^+(1950)$	1.93	0.011
$\Lambda(1820)$	1.82	0.011
$\bar{\Lambda}(1820)$	1.82	0.011
$\pi^+(1800)$	1.812	0.01
$\Lambda(1800)$	1.8	0.01
$\bar{\Lambda}(1800)$	1.8	0.01
$\Sigma^0(1940)$	1.94	0.009
$\bar{\Sigma}^0(1940)$	1.94	0.009
$\Sigma^-(1750)$	1.75	0.009
$\bar{\Sigma}^+(1750)$	1.75	0.009
$\Sigma^0(1915)$	1.915	0.009
$\bar{\Sigma}^0(1915)$	1.915	0.009
$\Xi^0(1820)$	1.823	0.009
$\Xi^-(1820)$	1.823	0.009
$\Xi^0(1950)$	1.95	0.008
$\bar{\Xi}^-(1950)$	1.95	0.008
$\Lambda(1810)$	1.81	0.008
$\bar{\Lambda}(1810)$	1.81	0.008
$K^{*-}(1680)$	1.717	0.007
$K^{*0}(1680)$	1.717	0.007
$\bar{\Sigma}^+(1775)$	1.775	0.007
$\Sigma^-(1775)$	1.775	0.006
$\bar{\Delta}^0(1930)$	1.96	0.006
$\Delta^+(1930)$	1.96	0.006
$\Omega(2250)$	2.252	0.006
$\Delta^0(1910)$	1.91	0.005
$\bar{\Delta}^+(1910)$	1.91	0.005
$n(1650)$	1.655	0.005
$\bar{p}(1650)$	1.655	0.005
$\pi^-(1800)$	1.812	0.004
$\pi^0(1800)$	1.812	0.004
$\phi_3(1850)$	1.854	0.004
$f_2(1950)$	1.945	0.003
$\Delta^-(1920)$	1.92	0.003

Continued on next page

Table C.1 – continued from previous page

name	mass (GeV)	total contribution (%)	
$\Delta^{++}(1920)$	1.92	0.003	
$f_0(1710)$	1.715	0.002	
$\Delta^-(1910)$	1.91	0.002	
$\bar{\Delta}^{++}(1910)$	1.91	0.002	
$\Sigma^-(1940)$	1.94	0.001	
$\bar{\Sigma}^+(1940)$	1.94	0.001	
$\Sigma^-(1915)$	1.915	0	
$\bar{\Sigma}^+(1915)$	1.915	0	100%

Table C.2: Resonance contribution list for K^+

name	mass (GeV)	total contribution (%)	
$K^{*0}(892)$	0.8961	35.857	
$K^{*+}(892)$	0.89166	18.52	
$\phi(1020)$	1.0195	16.036	60%
$K_1^+(1270)$	1.273	3.631	
$K_1^0(1270)$	1.273	3.287	
$a_0^+(980)$	0.9847	1.807	
$f_1(1420)$	1.4263	1.754	80%
$K_2^{*0}(1430)$	1.4324	1.61	
$K_1^+(1400)$	1.402	1.446	
$K_2^{*+}(1430)$	1.4256	1.241	
$K^{*+}(1410)$	1.414	1.217	
$K_1^0(1400)$	1.402	1.127	
$K^{*0}(1410)$	1.414	1.033	
$a_0^0(980)$	0.9847	0.898	
$f_0(980)$	0.9741	0.869	90%
$\Lambda(1520)$	1.5195	0.798	
$f_2^'(1525)$	1.525	0.711	
$f_1(1285)$	1.2818	0.493	
$\bar{\Xi}^-(1690)$	1.69	0.462	
$\bar{\Sigma}^-(1775)$	1.775	0.431	
$\eta(1475)$	1.476	0.405	
$K_0^{*0}(1430)$	1.412	0.295	
$\bar{\Xi}^-(1820)$	1.823	0.288	
$a_2^+(1320)$	1.3183	0.274	
$\eta(1405)$	1.4103	0.265	
$\phi(1680)$	1.68	0.265	95%
$f_2(2010)$	2.011	0.259	
$\bar{\Sigma}^0(1775)$	1.775	0.237	
$\bar{\Xi}^0(1690)$	1.69	0.23	
$\bar{\Lambda}(1820)$	1.82	0.196	

Continued on next page

Table C.2 – continued from previous page

name	mass (GeV)	total contribution (%)	
$K_3^{*+}(1780)$	1.776	0.191	
$K_2^+(1770)$	1.773	0.189	
$\bar{\Sigma}^-(1670)$	1.67	0.177	
$\bar{\Sigma}^-(1750)$	1.75	0.171	
$K_2^0(1770)$	1.773	0.166	
$\bar{\Sigma}^-(1660)$	1.66	0.165	
$\bar{\Lambda}(1600)$	1.6	0.161	
$\eta(1295)$	1.294	0.157	
$K_0^{*+}(1430)$	1.412	0.148	
$K_2^+(1820)$	1.816	0.145	
$\bar{\Lambda}(1690)$	1.69	0.144	
$K_3^{*0}(1780)$	1.776	0.14	
$a_2^0(1320)$	1.3183	0.137	98%
$K^{*0}(1680)$	1.717	0.117	
$\phi_3(1850)$	1.854	0.114	
$f_2(1270)$	1.2754	0.099	
$\bar{\Lambda}(1810)$	1.81	0.091	
$\bar{\Sigma}^0(1670)$	1.67	0.089	
$\bar{\Lambda}(1890)$	1.89	0.087	
$\bar{\Sigma}^0(1750)$	1.75	0.085	
$\bar{\Sigma}^0(1660)$	1.66	0.082	
$K_2^0(1820)$	1.816	0.082	
$\bar{\Xi}^-(1950)$	1.95	0.082	
$\bar{\Lambda}(1670)$	1.67	0.082	99%
$K^{*+}(1680)$	1.717	0.078	
$\bar{\Lambda}(1800)$	1.8	0.076	
$p(1720)$	1.72	0.072	
$p(1710)$	1.71	0.068	
$\eta_2(1645)$	1.617	0.06	
$\bar{\Xi}^0(1820)$	1.823	0.052	
$a_0^+(1450)$	1.474	0.052	
$\bar{\Sigma}^+(1940)$	1.94	0.047	
$\bar{\Sigma}^0(1940)$	1.94	0.045	
$\bar{\Omega}(2250)$	2.252	0.044	
$\bar{\Sigma}^+(1775)$	1.775	0.043	
$\bar{\Sigma}^-(1940)$	1.94	0.043	
$\bar{\Sigma}^-(1915)$	1.915	0.036	
$p(1650)$	1.655	0.032	
$a_0^0(1450)$	1.474	0.026	
$f_0(1710)$	1.715	0.024	
$\rho_3^+(1690)$	1.6888	0.023	
$\bar{\Sigma}^0(1915)$	1.915	0.018	
$\bar{\Lambda}(1830)$	1.83	0.017	
$\rho_3^0(1690)$	1.6888	0.016	

Continued on next page

Table C.2 – continued from previous page

name	mass (GeV)	total contribution (%)	
$\pi_2^+(1670)$	1.6724	0.015	
$\pi_2^0(1670)$	1.6724	0.013	
$f_0(1500)$	1.507	0.012	
$\pi_2^-(1670)$	1.6724	0.01	
$f_0(1370)$	1.4	0.01	
$\rho_3^-(1690)$	1.6888	0.008	
$\Delta^{++}(1920)$	1.92	0.004	
$\Delta^+(1920)$	1.92	0.003	
$\Delta^{++}(1950)$	1.93	0.003	
$\Delta^+(1950)$	1.93	0.002	
$\bar{K}_1^0(1400)$	1.402	0.002	
$K_1^-(1400)$	1.402	0.002	
$\Delta^0(1920)$	1.92	0.001	
$f_2(1950)$	1.945	0.001	
$\Delta^0(1950)$	1.93	0.001	
$\bar{K}_2^0(1820)$	1.816	0	
$K_2^-(1820)$	1.816	0	100%

Table C.3: Resonance contribution list for p

name	mass (GeV)	total contribution (%)	
$\Delta^{++}(1232)$	1.232	29.842	
$\Delta^+(1232)$	1.232	19.816	
$\Delta^0(1232)$	1.232	9.813	
$\Delta^{++}(1600)$	1.6	2.787	60%
$n(1520)$	1.52	2.487	
$p(1520)$	1.52	2.169	
$\Delta^+(1600)$	1.6	2.049	
$p(1440)$	1.44	2.034	
$n(1440)$	1.44	1.943	
$p(1535)$	1.535	1.452	
$\Delta^{++}(1700)$	1.7	1.386	
$\Lambda(1520)$	1.5195	1.365	
$p(1675)$	1.675	1.347	
$\Delta^0(1600)$	1.6	1.314	
$p(1700)$	1.7	1.228	80%
$\Delta^{++}(1620)$	1.63	1.135	
$n(1680)$	1.685	1.003	
$\Delta^+(1700)$	1.7	0.987	
$n(1675)$	1.675	0.975	
$p(1680)$	1.685	0.917	
$n(1535)$	1.535	0.793	

Continued on next page

Table C.3 – continued from previous page

name	mass (GeV)	total contribution (%)	
$\Delta^+(1620)$	1.63	0.785	
$n(1720)$	1.72	0.752	
$\Sigma^+(1775)$	1.775	0.738	
$\Delta^-(1600)$	1.6	0.574	
$\Delta^0(1700)$	1.7	0.54	90%
$\Delta^{++}(1905)$	1.89	0.536	
$p(1720)$	1.72	0.487	
$p(1710)$	1.71	0.456	
$\Delta^0(1620)$	1.63	0.433	
$n(1650)$	1.655	0.429	
$\Delta^{++}(1950)$	1.93	0.411	
$\Sigma^0(1775)$	1.775	0.405	
$\Delta^+(1905)$	1.89	0.366	
$n(1700)$	1.7	0.342	
$\Lambda(1820)$	1.82	0.334	
$\Sigma^+(1670)$	1.67	0.302	
$p(1650)$	1.655	0.29	95%
$\Sigma^+(1750)$	1.75	0.289	
$\Sigma^+(1660)$	1.66	0.282	
$\Delta^+(1950)$	1.93	0.281	
$\Lambda(1600)$	1.6	0.275	
$\Lambda(1690)$	1.69	0.247	
$\Delta^{++}(1920)$	1.92	0.227	
$n(1710)$	1.71	0.203	
$\Delta^{++}(1930)$	1.96	0.196	
$\Delta^0(1905)$	1.89	0.189	
$\Delta^+(1920)$	1.92	0.182	
$\Lambda(1810)$	1.81	0.156	
$\Delta^0(1950)$	1.93	0.153	
$\Sigma^0(1670)$	1.67	0.151	
$\Lambda(1890)$	1.89	0.15	98%
$\Sigma^0(1750)$	1.75	0.145	
$\Sigma^0(1660)$	1.66	0.141	
$\Lambda(1670)$	1.67	0.139	
$\Sigma^+(1940)$	1.94	0.138	
$\Delta^0(1920)$	1.92	0.137	
$\Delta^-(1700)$	1.7	0.136	
$\Delta^+(1930)$	1.96	0.13	
$\Lambda(1800)$	1.8	0.13	99%
$\Delta^{++}(1910)$	1.91	0.121	
$\Delta^+(1910)$	1.91	0.096	
$\Delta^-(1920)$	1.92	0.092	
$\Delta^-(1620)$	1.63	0.081	
$\Sigma^0(1940)$	1.94	0.077	

Continued on next page

Table C.3 – continued from previous page

name	mass (GeV)	total contribution (%)	
$\Sigma^-(1775)$	1.775	0.074	
$\Delta^0(1910)$	1.91	0.071	
$\Delta^0(1930)$	1.96	0.065	
$\Sigma^+(1915)$	1.915	0.062	
$\Delta^-(1910)$	1.91	0.046	
$\Sigma^0(1915)$	1.915	0.031	
$\Lambda(1830)$	1.83	0.029	
$\Delta^-(1950)$	1.93	0.023	
$\Delta^-(1905)$	1.89	0.016	
$\Sigma^-(1940)$	1.94	0.015	100%

Table C.4: Resonance contribution list for Λ

name	mass (GeV)	total contribution (%)	
Σ^0	1.1926	24.775	
$\Sigma^+(1385)$	1.3828	17.893	
$\Sigma^-(1385)$	1.3872	17.346	60%
$\Sigma^0(1385)$	1.3837	16.555	
$\Lambda(1405)$	1.4065	3.103	
$\Lambda(1520)$	1.5195	2.18	80%
$\Sigma^-(1670)$	1.67	1.304	
$\Sigma^+(1670)$	1.67	1.297	
$\Lambda(1690)$	1.69	1.178	
$\Xi^-(1690)$	1.69	1.132	
$\Xi^0(1690)$	1.69	1.128	
$\Sigma^+(1775)$	1.775	0.771	
$\Sigma^-(1775)$	1.775	0.769	
$\Lambda(1830)$	1.83	0.754	90%
$\Sigma^0(1775)$	1.775	0.749	
$\Sigma^-(1660)$	1.66	0.708	
$\Sigma^+(1660)$	1.66	0.707	
$\Xi^0(1820)$	1.823	0.707	
$\Xi^-(1820)$	1.823	0.705	
$\Sigma^0(1750)$	1.75	0.619	
$\Lambda(1670)$	1.67	0.607	
$\Lambda(1600)$	1.6	0.486	95%
$\Sigma^0(1670)$	1.67	0.485	
$\Sigma^0(1660)$	1.66	0.471	
$\Sigma^-(1915)$	1.915	0.382	
$\Sigma^+(1915)$	1.915	0.381	
$\Sigma^0(1915)$	1.915	0.264	
$\Lambda(1820)$	1.82	0.216	

Continued on next page

Table C.4 – continued from previous page

name	mass (GeV)	total contribution (%)	
$\Xi^0(1950)$	1.95	0.202	98%
$\Xi^-(1950)$	1.95	0.201	
$\Sigma^-(1940)$	1.94	0.189	99%
$\Sigma^+(1940)$	1.94	0.188	
$n(1720)$	1.72	0.176	
$p(1720)$	1.72	0.176	
$\Lambda(1890)$	1.89	0.174	
$n(1710)$	1.71	0.167	
$p(1710)$	1.71	0.167	
$\Sigma^0(1940)$	1.94	0.155	100%
$\Lambda(1800)$	1.8	0.155	
$n(1650)$	1.655	0.078	
$p(1650)$	1.655	0.078	
$\Sigma^-(1750)$	1.75	0.076	
$\Sigma^+(1750)$	1.75	0.075	
$\Lambda(1810)$	1.81	0.05	
$\Delta^0(1920)$	1.92	0.007	
$\Delta^+(1920)$	1.92	0.007	
$\Delta^0(1950)$	1.93	0.004	
$\Delta^+(1950)$	1.93	0.004	

Table C.5: Resonance contribution list for Σ^+

name	mass (GeV)	total contribution (%)	
$\Lambda(1405)$	1.4065	25.159	60%
$\Lambda(1520)$	1.5195	10.121	
$\Sigma^+(1385)$	1.3828	9.288	
$\Sigma^0(1385)$	1.3837	9.179	
$\Sigma^0(1670)$	1.67	6.648	
$\Sigma^+(1670)$	1.67	6.618	80%
$\Xi^0(1690)$	1.69	4.578	
$\Sigma^+(1750)$	1.75	4.425	
$\Lambda(1600)$	1.6	3.969	
$\Lambda(1690)$	1.69	3.845	
$\Lambda(1830)$	1.83	2.243	90%
$\Lambda(1670)$	1.67	1.926	
$\Sigma^+(1660)$	1.66	1.916	
$\Sigma^0(1660)$	1.66	1.916	
$\Xi^0(1820)$	1.823	1.045	95%
$\Sigma^+(1915)$	1.915	0.974	
$\Sigma^0(1915)$	1.915	0.968	
$\Sigma^+(1775)$	1.775	0.859	

Continued on next page

Table C.5 – continued from previous page

name	mass (GeV)	total contribution (%)	
$\Sigma^0(1775)$	1.775	0.805	
$\Lambda(1820)$	1.82	0.791	
$\Sigma^-(1775)$	1.775	0.6	
$\Sigma^+(1940)$	1.94	0.405	98%
$\Lambda(1810)$	1.81	0.402	
$\Sigma^0(1940)$	1.94	0.387	99%
$\Lambda(1800)$	1.8	0.377	
$\Lambda(1890)$	1.89	0.231	
$\Sigma^-(1940)$	1.94	0.101	
$\Delta^{++}(1920)$	1.92	0.08	
$\Delta^{++}(1950)$	1.93	0.051	
$\Delta^+(1920)$	1.92	0.027	
$\Sigma^-(1750)$	1.75	0.02	
$\Sigma^0(1750)$	1.75	0.02	
$\Delta^+(1950)$	1.93	0.015	
$\Sigma^-(1915)$	1.915	0.007	100%

Table C.6: Resonance contribution list for Ξ^-

name	mass (GeV)	total contribution (%)	
$\Xi^0(1530)$	1.5318	62.049	60%
$\Xi^-(1530)$	1.535	30.103	90%
$\Xi^0(1820)$	1.823	2.42	
$\Xi^-(1820)$	1.823	2.334	95%
$\Xi^0(1950)$	1.95	1.427	98%
$\Omega(2250)$	2.252	0.957	99%
$\Xi^-(1950)$	1.95	0.71	100%

Appendix D: Compiling, running, and tuning iSS

D.1 Compiling

The iS and iSS⁴² codes are easily compiled using the provided *Zmake.sh* script files. These are not real makefiles, but are actually short bash scripts that compile the code in one line. Makefiles are convenient for compiling large scale programs whenever keeping the intermediate output binary files saves compiling time. For small scale programs, however, a cleaner direct compile is preferable. The script also tries to compile with Intel compilers when available, to generate faster executables.

D.2 Running

After compilation, executables with the name “iS.e” or “iSS.e” are generated. They can be executed either without supplying any command line parameters, or with specific parameter sets using the *variable=value* syntax. These programs read input data files from the *results* directory, and write output data files to the same directory; details for this are given in the following sections. The iSS program reads *parameters.dat* for all the parameter assignments, and overwrites them with any additional parameter assignments read from the command line arguments. The structure of the parameter file and explanations for parameters it contains are presented in the following sections.

The number of outputs can be modified by editing the *AMOUNT_OF_OUTPUT* macro in the *emissionfunction.cpp* file.

D.3 Input and output files

Currently⁴³ both programs read as input the freeze-out surface information data files *surface.dat* and *decdat2.dat*, and the chemical potential file *decdat_mu.dat* from the *results* directory, which are all output files from the VISH2+1 hydrodynamical simulation program. For the format of these files, refer to the corresponding documents.

Both programs also need equation of state (EOS) information and particle data information, which are given by files in the *EOS* directory: *EOS_particletable.dat*, *pdg.dat*, *resoweak.dat*. Another file *chosen_particles.dat* in the same directory is a one-column list of standard particle Monte-Carlo indices, and only particles whose Monte Carlo index is included in this file will be processed by the programs; others will be skipped. The Monte-Carlo indices can be looked up in the *pdg.dat* file, for example, π^0 is indexed as 211.

When the program finishes, depending on the operations that were performed, different sets of files will be generated in the *results* folder.

If spectra and flow calculations are enabled (optional in iSS, mandatory in iS), files with names like *thermal_XXXXX_vn.dat* and *thermal_XXXXX_integrated_vn.dat* will be generated. Here *XXXXX* refers to the standard Monte-Carlo particle index given by the particle data book (*pdg.dat*).

⁴²They can be found from the iEBE package at <https://bitbucket.org/qiu.24/iebe>.

⁴³By August 30, 2021, iSS has version 2.3.0.2 and iS has version 1.2.1.12.

The files *thermal_XXXXX_integrated_vn.dat* record p_{\perp} -integrated flow results. These files contain n rows of output, where n is the largest harmonic flow coefficient calculated, starting from 0. Each row has 6 columns: the first column is the order of the flow, the second and the third columns contain the real and imaginary part of the numerator on the right hand side of eq. (7.8)⁴⁴, and the fourth, fifth, and sixth columns contain the real and imaginary parts, and the magnitude of the complex flow vector $v_n e^{in\Psi_n}$.

The files *thermal_XXXXX_vn.dat* store differential flow results. These are block-shaped data files that store the $dN/(p_{\perp} dp_{\perp} d\phi)$ matrix for given p_{\perp} and ϕ indices. The row index corresponds to the p_{\perp} index and the column index to the ϕ index. For each p_{\perp} or ϕ index, the actual p_{\perp} or ϕ value can be looked up from the corresponding tables in the *tables* directory, which by default are the *pT_gauss.table.dat* or *phi_gauss.table.dat* files. The *tables* directory will be explained below.

If the sampling of particles is enabled (optional with iSS, not possible with iS), files with names like *samples_XXXXX.dat*, *samples_control_XXXXX.dat*, and *samples_format.dat* are generated, with *XXXXX* the Monte-Carlo particle indices.

The files *samples_control_XXXXX.dat* contain a one-column listing of the actual number of sampled particles from each of the given number of repeated samplings. The sum of all its elements gives the total number of sampled particles over the specified rapidity range whose average is given by the p_{\perp} -integrated Cooper-Frye formula.

The files *samples_XXXXX.dat* contain the information of the generated samples, with each line corresponding to one particle and containing all its spatial and momentum information. The meaning of elements in a particular column varies from version to version, so they are recorded in the *samples_format.dat* file to ease the reading process. The *samples_format.dat* file is written with “equal-sign assignment” syntax, which can be conveniently read back using the *ParameterReader* class (E.3). For example, the line *tau = 2* means that the τ information of the particles are written in the second column.

The iSS program also supports writing to OSCAR format⁴⁵, in which case the file *OSCAR_header.txt* is copied to as the header of the generated OSCAR file.

D.4 Parameter file

The *Parameters.dat* file is an “equal-sign assignment” file storing the major tunable parameters used by the iSS program. Such a file can be easily read using the *ParameterReader* class (§E.3).

All the parameters are accompanied by detailed explanations. The most important parameters are:

- *calculate_vn*: When set to 1, spectra and flows will be calculated.
- *MC_sampling*: When set to 0, no sampling will be done; setting it to 1 generates samples using the numerical sampling approach (§7.4.1); setting it to 2 generates samples using the semi-analytic approach (§7.4.2).
- *number_of_repeated_sampling*: How many repeated sampling should be performed.
- *dN_dy_sampling_model*: Used to switch between different models for generating the integer dN/dy from the averaged value, see 7.4.4.
- *use_dynamic_maximum*: Whether to turn on the “dynamic maximum” mentioned in §7.4.2.
- *grouping_particles* and *grouping_tolerance*: if *grouping_particles* is set to 1, particles with similar mass and chemical potentials will be grouped together for calculation, and the threshold for determining such similarity is controlled by the *grouping_tolerance* parameter, see §7.4.4.

Other parameters are explained by their comments in the file.

⁴⁴With an additional factor $1/2\pi$; therefore the second quantity in the first row is the total multiplicity. These two columns are mainly for debugging purposes.

⁴⁵<http://karman.physics.purdue.edu/OSCAR-old/>

D.5 Tables

Tables (§E.1) are used extensively throughout the iS and iSS programs. They are read from block-shaped data files located under the *tables* directory using *Table* or *TableFunction* class.

In particular, all the numerical integrals are performed by evaluating the sum:

$$\int_a^b f(x) = \sum_i f(x_i)w_i, x_i \in [a, b] \quad (\text{D.1})$$

with the location-weight pair (x_i, w_i) specified by some table. For example, it is set in the *main.cpp* file that the p_{\perp} integral should be done using the *pT_gauss_table.dat* file, which stores location and weight information for integration using Gauss quadrature. Other integration methods (e.g. Simpson's method etc.), can be conveniently substituted by simply switching the integration table file, without changing the source program. Similarly the file *phi_gauss_table.dat* and *eta_gauss_table_20_full.dat* are currently used to perform the ϕ and η_s integrals.

Files *p_integral_table_0.02.dat* and *m_integral_table_0.02.dat* are the pre-calculated tables used to evaluate the integral in eq. (7.15). The *lambertw_function.dat* and *z_exp_m_z.dat* files contain tables solving the transcendental equations (7.18).

There are other files for tables used during the binning process of the samples.

Appendix E: Introduction to iSS support classes

As mentioned in the introduction of Chap. 7, common tasks are encapsulated into classes for re-usability. In this section, such classes are introduced briefly; details can be found in the codes.

E.1 Table class and table-function classes

It is common to load a block of data of unknown size into memory to analyze. The *Table* class is made for such a purpose. It can be initialized from block-form data file or double array. It provides an interface to read and write elements in the table. The size of the table is dynamically allocated and it can change automatically once a write-action exceeds the current data boundary. It can perform interpolation between any two specified columns of data using nearest-neighbor, linear, or cubic methods, and it can perform bilinear interpolation using the whole block as a matrix as well. The *Table* class is used extensively throughout the iSS program to read in replaceable tables, like those used for integration or pre-tabulations.

The *TableFunction* class is oriented for 2-column tables that represent functions. It can be initialized from a file or directly, and it provides interpolation and inverse search interfaces. This class is intended to be used as the underlying class for representing numerical functions using tables.

E.2 Classes related to random variables

The sampling of random variables are implemented in the base class *RandomVariable*, which supports direct PDF sampling, sampling using the inverse CDF, and sampling with envelope distribution methods.

The PDF function and the inverse CDF function for the random variable being sampled and for the envelope random variables are implemented by default using a table through *TableFunction* class, which can conveniently return results using several methods of interpolation, and which can be initialized from file, double array, or generated directly. All these distribution functions are declared as virtual, meaning that, when the class is inherited, these functions can be overloaded and implemented in any desired way. For example, one implemented derived class *NBD* overloads the PDF function by an analytic expression, since the PDF depends on several parameters and it is more naturally expressed analytically, rather than in tabulated form.

Once the function required for one sampling method is loaded, the sampling of the random variable can be done by calling the corresponding sampling member function. The class also has a member function that can calculate the inverse CDF function from the PDF function, and a function that can automatically generate a stair-shaped envelope function (see §7.2.7) given the mode and standard deviation.

The *RandomVariable* class is meant to be the base class for the most general 1d random variable sampling. One derived class based on it is the *NBD* class which samples the negative binomial distribution (NBD) using an automatically constructed stair-shaped envelope function (see §7.2.7 and code). The PDF for the NBD is overloaded as an analytic function; for efficiency, the automatically generated envelope function is recalculated only when the parameters for NBD change.

There are several other simpler classes *RandomVariable1DArray*, *RandomVariable2DArray*, and *RandomVariableNDArray* that are designed for sampling discrete PDFs given as double arrays,

using the inverse CDF sampling method. They are less general compared to the *RandomVariable* class, but they are optimized for index sampling and they require less memory.

E.3 Parameter reader class

It is very common in scientific programming that results depend on many parameters. It would be convenient if they could be stored and loaded from files, which are then passed between functions via references instead of by values. The *ParameterReader* class is created for such a purpose. Parameters can be assigned using “equal-sign assignments” syntax throughout the file, from command line arguments, or by calling member functions directly. After initialization, the parameters are stored and can be extracted easily. With such a class, parameters can be passed between functions and classes using an instance of this class, instead of being passed directly, since this would be tedious to maintain, and prone to errors.

The most common usage of this class is to read parameters stored in a file, which can be done through a member function or simply through the constructor. In such cases, the file has to be written with “equal-sign assignment” syntax, meaning that each line of the file can contain an equal-sign assignment, a piece of comment beginning with the character “#”, or neither, or both. For example, the line:

MC_sampling = 2 # 0/1/2: whether to perform Monte-Carlo sampling

creates a variable with string name “MC_sampling” and assigns the initial value “2” to it, which can be conveniently extracted by the *getVal* member function. The part of the line after the “#” symbol is treated as a comment and is discarded during the reading process.

There is another member function that reads the command line arguments for parameter assignments. In this case, each argument needs to be an “equal-sign assignment”, without blanks or comments; for details, see the header file.

Parameters read later will overwrite any parameters with the same name read earlier; otherwise, new variables will be created. Parameters can also be assigned directly using a member function. For other functionalities and details, refer to the header file and comments directly following the implementation of each function.

Appendix F: The iEBE package

The iEBE package is a convenient package for automating event-by-event hybrid calculations. It divide calculations into “jobs”, where each job consists of multiple “ebe-calculations”. Each “ebe-calculation” is a complete hybrid calculation that in execution order performs: heavy-ion event generation (superMC), hydrodynamics simulation (VISHNew), particle emission sampling (iSS), hadron rescattering simulation (osc2u and urqmd), flow calculation (binUtilities), and finally, collection and storing of important results in databases (EbeCollector). Each “job” runs the given number of “ebe-calculations” sequentially, and “jobs” are run in parallel. The package has utility scripts that can combine the generated SQLite database files from different jobs into one, which can be analyzed later.

The main programs are contained in the subfolder “EBE-Node”, which is used to perform one job, and which will be duplicated when multiple jobs are run. The package needs two locations to perform multi-job calculations: one folder is used to store duplications of “EBE-Node” and intermediate results generated during the calculation (refer to as “working folder” in the following), and another folder is used to store final results (refer to as “result folder” in the following). By default, the working folder is named “PlayGround” and the result folder is named “RESULTS”, both in the root directory of the package.

F.1 How to use the package to perform multi-job calculations

This section explains how to use the highest-level scripts provided by the package to perform event-by-event hybrid calculations. Any one using the package should read this section thoroughly, even those who are not interested in modifying the package.

VERY IMPORTANT: Make sure you have Python 2.7+ (or Python 3) installed before proceeding.

In the following, all paths are relative to the root directory of the package.

Step 1 Generate jobs using the `./generateJobs.py` script.

To generate jobs, use the `generateJobs.py` script in the root directory. Most of the runnable scripts in this package provide the feature that if you run them without additional arguments, they will print the usage echo, for example:

```
$ ./generateJobs.py
```

And you should see the output:

```
Usage: generateJobs.py number_of_jobs number_of_events_per_job  
[working_folder=“./PlayGround”] [results_folder=“./RESULTS”]  
[walltime=“03:00:00” (per event)] [compress_results_folder=“yes”]
```

The echo says that the 1st argument for the script should specify the number of jobs you want to generate; the 2nd argument specifies the number of ebe-calculations for each job; the 3rd argument points to the result folder; the 4th argument specifies the “wall time” (used in torque system, explained later); the 5th argument points to the working folder; and the 6th argument is for whether to compress final results. Except for the first two, all other arguments have default values. The simplest way to generate jobs is just to accept the default values. As an example, to generate 2 jobs, each performing 5 ebe-calculations, simply do the following:

```
$ ./generateJobs.py 2 5
```

This script will first check required libraries, compile any programs not existing already, and generate the actual folders for jobs.

After you see the echo “Jobs generated.”, you should see the working folder “PlayGround” and the result folder “RESULTS” in the root directory.

Step 2 Submit jobs.

The way to submit jobs depends on the system. For a cluster that has the “Torque” scheduling system (therefore the “qsub” command is available), submit jobs using the submitJobs_qsub.py script; for a local computation, use the submitJobs_local.py script. The difference is that the local computation is only paralleled for the local CPUs and calculation on the cluster, via the torque system, will be distributed (trivially) to multiple nodes. To submit a local calculation, simply type (the script knows how to get the location of the working folder automatically):

```
$ ./submitJobs_local.py
```

You should see some feedbacks listing the jobs that have been submitted.

Step 3 Checking progress.

Progress for all jobs can be checked by the progressReport.py script in the root directory:

```
$ ./progressReport.py
```

It will list the current progress for all jobs.

Step 4 Combining databases.

Once all calculations are finished, the generated database files from all events will be combined automatically, and a single file “collected.db” will be generated in the results folder.

F.2 How to analyze generated data

The “collected.db” generated from previous steps is the SQLite database file that can be analyzed by any desired means. The recommended way is to use the uhg.py script in the utilities folder. This script not only reads the database, but also performs additional analyses, like interpolation along p_T , calculation of the mean, etc. It can either be run from the command line to evaluate a single expression or interactively from a shell. To evaluate a single expression, run the uhg.py script in the utilities folder:

```
$ ./uhg.py database_filename “expression to evaluate”
```

A more convenient way to evaluate multiple expressions as well as perform additional analyses is to run the uhg.py script interactively. For example:

```
$ python -ic “from uhg import *”
```

The interactive mode will also print out a simple help showing recognizable symbols that can be included in the expression.

Another way is to use the databaseQuery.py script to evaluate a single piece of SQL query from the command line:

```
# ./databaseQuery.py database_filename “SQL_query”
```

A third way is to use unpackDatabase.py under /EBE-Node/EbeCollector/ to dump the whole database into separated space-separated text files, each for individual tables. For example, running the following under /RESULTS/:

```
$ ../EBE-Node/EbeCollector/unpackDatabase.py ./collected.db .
```

will generate several “.dat” files, each containing data for the corresponding type. Each file has a one-line header to indicate what data each column records, and the rest are data separated by spaces.

For more details about the structure of the database and the uhg.py script, see /EBE-Node/EbeCollector/E

F.3 How to tune parameters

After you have familiarized yourself with how to perform multi-job hybrid calculations, you are finally ready to tune parameters for the simulations. The most commonly tuned parameters are in the ParameterDict.py file in the directory, which should be the only file used to direct the simulations. This file will be copied to the result folder for record-keeping purposes when generating jobs.

Bibliography

- [1] Gred Graumann, *Mathematica for theoretical physics: electrodynamics, quantum mechanics, general relativity, and fractals* Springer, ISBN 0387219331 (2005).
- [2] K. Yagi, T. Hatsuda and Y. Miake, *Quark-gluon plasma: from big bang to little bang*, Cambridge Univ. Press, 2005.
- [3] U. Heinz, *Concepts of heavy ion physics*, hep-ph/0407360.
- [4] U. Heinz, *Towards the little bang standard model*, arXiv:1304.3634 [nucl-th].
- [5] M. L. Miller, K. Reygers, S. J. Sanders and P. Steinberg, *Glauber modeling in high energy nuclear collisions*, Ann. Rev. Nucl. Part. Sci. **57**, 205 (2007).
- [6] T. Hirano and Y. Nara, *Eccentricity fluctuation effects on elliptic flow in relativistic heavy ion collisions*, Phys. Rev. C **79**, 064904 (2009).
- [7] D. Kharzeev, M. Nardi, *Hadron production in nuclear collisions at RHIC and high density QCD*, Phys. Lett. **B507**, 121 (2001). D. Kharzeev, E. Levin, *Manifestations of high density QCD in the first RHIC data*, Phys. Lett. **B523**, 79 (2001).
- [8] H. J. Drescher and Y. Nara, *Effects of fluctuations on the initial eccentricity from the color glass condensate in heavy ion collisions*, Phys. Rev. C **75**, 034905 (2007).
- [9] T. Hirano, P. Huovinen and Y. Nara, Phys. Rev. C **83**, 021902 (2011) [arXiv:1010.6222 [nucl-th]].
- [10] G.-Y. Qin, H. Petersen, S. A. Bass, and B. Müller, *Translation of collision geometry fluctuations into momentum anisotropies in relativistic heavy-ion collisions*, Phys. Rev. C **82**, 064903 (2010).
- [11] P. Huovinen, P. Petreczky, *QCD Equation of state and hadron resonance gas*, Nucl. Phys. **A837**, 26 (2010).
- [12] C. Shen, U. Heinz, P. Huovinen and H. Song, *Systematic parameter study of hadron spectra and elliptic flow from viscous hydrodynamic simulations of Au+Au collisions at $\sqrt{s_{NN}} = 200$ GeV*, Phys. Rev. C **82**, 054904 (2010).
- [13] J. L. Albacete, A. Dumitru and C. Marquet, *The initial state of heavy-ion collisions*, Int. J. Mod. Phys. **A28**, 1340010 (2013).
- [14] U. Heinz, H. Song and A. K. Chaudhuri, *Dissipative hydrodynamics for viscous relativistic fluids*, Phys. Rev. C **73**, 034904 (2006).
- [15] H. Song and U. Heinz, *Causal viscous hydrodynamics in 2+1 dimensions for relativistic heavy-ion collisions*, Phys. Rev. C **77**, 064901 (2008).

- [16] A. Bazavov, T. Bhattacharya, M. Cheng, N. H. Christ, C. DeTar, S. Ejiri, S. Gottlieb and R. Gupta *et al.*, *Equation of state and QCD transition at finite temperature*, Phys. Rev. D **80**, 014504 (2009).
- [17] P. Petreczky, *Review of recent highlights in lattice calculations at finite temperature and finite density*, PoS ConfinementX 2012, 028 (2012).
- [18] S. A. Bass, M. Belkacem, M. Bleicher, M. Brandstetter, L. Bravina, C. Ernst, L. Gerland and M. Hofmann *et al.*, *Microscopic models for ultra-relativistic heavy ion collisions*, Prog. Part. Nucl. Phys. **41**, 255 (1998).
- [19] H. Song, *VISHNU hybrid model for viscous QCD matter at RHIC and LHC energies*, Central Eur. J. Phys. **10**, 1242 (2012).
- [20] Z. Qiu and U. Heinz, *Event-by-event shape and flow fluctuations of relativistic heavy-ion collision fireballs*, Phys. Rev. C **84**, 024911 (2011).
- [21] B. Alver and G. Roland, *Collision geometry fluctuations and triangular flow in heavy-ion collisions*, Phys. Rev. C **81**, 054905 (2010).
- [22] B. H. Alver, C. Gombeaud, M. Luzum, and J. Y. Ollitrault, *Triangular flow in hydrodynamics and transport theory*, Phys. Rev. C **82**, 034913 (2010).
- [23] P. F. Kolb and U. W. Heinz, *Hydrodynamic description of ultrarelativistic heavy ion collisions*, In *Hwa, R.C. (ed.) et al.: Quark gluon plasma* 634-714 [nucl-th/0305084].
- [24] B. Alver *et al.*, *Importance of correlations and Fluctuations on the Initial Source Eccentricity in High-Energy Nucleus-Nucleus Collisions*, Phys. Rev. C **77**, 014906 (2008).
- [25] J. Y. Ollitrault, A. M. Poskanzer and S. A. Voloshin, *Effect of flow fluctuations and nonflow on elliptic flow methods*, Phys. Rev. C **80**, 014904 (2009).
- [26] J. Jia and S. Mohapatra, *Disentangling flow and non-flow correlations via Bayesian unfolding of the event-by-event distributions of harmonic coefficients in ultra-relativistic heavy-ion collisions*, arXiv:1304.1471 [nucl-ex].
- [27] R. S. Bhalerao, J. -Y. Ollitrault, *Eccentricity fluctuations and elliptic flow at RHIC*, Phys. Lett. **B641**, 260 (2006).
- [28] S. A. Voloshin, A. M. Poskanzer, A. Tang, and G. Wang, *Elliptic flow in the Gaussian model of eccentricity fluctuations*, Phys. Lett. **B659**, 537 (2008).
- [29] S. Voloshin and Y. Zhang, *Flow study in relativistic nuclear collisions by Fourier expansion of azimuthal particle distributions*, Z. Phys. **C70**, 665 (1996).
- [30] H. Song, S. A. Bass, U. Heinz, T. Hirano and C. Shen, *200 A GeV Au+Au collisions serve a nearly perfect quark-gluon liquid*, Phys. Rev. Lett. **106**, 192301 (2011).
- [31] H. Song, S. A. Bass, U. Heinz, T. Hirano and C. Shen, *Hadron spectra and elliptic flow for 200 A GeV Au+Au collisions from viscous hydrodynamics coupled to a Boltzmann cascade*, Phys. Rev. C **83**, 054910 (2011).
- [32] F. Cooper and G. Frye, *Comment on the single particle distribution in the hydrodynamic and statistical thermodynamic models of multi-particle production*, Phys. Rev. D **10**, 186 (1974).

- [33] Y. Bai, Ph.D. Thesis, Nikhef and Utrecht University, The Netherlands (2007). B. I. Abelev *et al.* (STAR Collaboration), *Centrality dependence of charged hadron and strange hadron elliptic flow from $\sqrt{s_{NN}} = 200$ GeV Au+Au collisions*, Phys. Rev. C **77**, 054901 (2008).
- [34] K. Aamodt *et al.* (ALICE Collaboration), *Elliptic flow of charged particles in Pb-Pb collisions at 2.76 TeV*, Phys. Rev. Lett. **105**, 252302 (2011).
- [35] K. Aamodt *et al.* (ALICE Collaboration), *Higher harmonic anisotropic flow measurements of charged particles in Pb-Pb collisions at $\sqrt{s_{NN}}=2.76$ TeV*, Phys. Rev. Lett. **107**, 032301 (2011).
- [36] H. Song, S. A. Bass and U. Heinz, *Elliptic flow in 200 A GeV Au+Au collisions and 2.76 A TeV Pb+Pb collisions: insights from viscous hydrodynamics + hadron cascade hybrid model*, Phys. Rev. C **83**, 054912 (2011).
- [37] R. A. Lacey, R. Wei, J. Jia, N. N. Ajitanand, J. M. Alexander, and A. Taranenko, *Initial eccentricity fluctuations and their relation to higher-order flow harmonics*, Phys. Rev. C **83**, 044902 (2011).
- [38] H. Holopainen, H. Niemi, and K. J. Eskola, *Event-by-event hydrodynamics and elliptic flow from fluctuating initial state*, Phys. Rev. C **83**, 034901 (2011).
- [39] M. Luzum, C. Gombeaud, and J.-Y. Ollitrault, *v_4 in ideal and viscous hydrodynamic simulations of nuclear collisions at the BNL Relativistic Heavy Ion Collider (RHIC) and the CERN Large Hadron Collider (LHC)*, Phys. Rev. C **81**, 054910 (2010).
- [40] D. Teaney and L. Yan, *Triangularity and Dipole Asymmetry in Heavy Ion Collisions*, Phys. Rev. C **83**, 064904 (2011).
- [41] R. Chatterjee, H. Holopainen, T. Renk, and K. J. Eskola, *Enhancement of thermal photon production in event-by-event hydrodynamics*, Phys. Rev. C **83**, 054908 (2011).
- [42] R. Andrade, F. Grassi, Y. Hama, T. Kodama and O. Socolowski, *On the necessity to include event-by-event fluctuations in experimental evaluation of elliptical flow*, Phys. Rev. Lett. **97**, 202302 (2006).
- [43] B. Schenke, S. Jeon, C. Gale, *Elliptic and triangular flow in event-by-event (3+1)D viscous hydrodynamics*, Phys. Rev. Lett. **106**, 042301 (2011).
- [44] Z. Qiu, C. Shen and U. Heinz, *Hydrodynamic elliptic and triangular flow in Pb-Pb collisions at $\sqrt{s}=2.76$ ATeV*, Phys. Lett. **B707**, 151 (2012).
- [45] Z. Qiu and U. Heinz, *Event-by-event hydrodynamics for heavy-ion collisions*, AIP Conf. Proc. **1441**, 774 (2012).
- [46] D. Teaney, *The Effects of viscosity on spectra, elliptic flow, and HBT radii*, Phys. Rev. C **68**, 034913 (2003).
- [47] R. A. Lacey and A. Taranenko, *What do elliptic flow measurements tell us about the matter created in the little bang at RHIC?*, PoS CFRNC2006, 021 (2006).
- [48] P. Romatschke and U. Romatschke, *Viscosity information from relativistic nuclear collisions: how perfect is the fluid observed at RHIC?*, Phys. Rev. Lett. **99**, 172301 (2007).
- [49] M. Luzum and P. Romatschke, *Conformal relativistic viscous hydrodynamics: applications to RHIC results at $s(NN)^{1/2} = 200$ GeV*, Phys. Rev. C **78**, 034915 (2008).

- [50] M. Luzum and P. Romatschke, *Viscous hydrodynamic predictions for nuclear collisions at the LHC*, Phys. Rev. Lett. **103**, 262302 (2009).
- [51] M. Luzum, *Elliptic flow at energies available at the CERN Large Hadron Collider: Comparing heavy-ion data to viscous hydrodynamic predictions*, Phys. Rev. C **83**, 044911 (2011).
- [52] R. A. Lacey, A. Taranenko, N. N. Ajitanand and J. M. Alexander, *Initial indications for the production of a strongly coupled plasma in Pb+Pb collisions at $\sqrt{s_{NN}} = 2.76$ TeV*, Phys. Rev. C **83**, 031901 (2011).
- [53] P. Bozek, M. Chojnacki, W. Florkowski and B. Tomasik, *Hydrodynamic predictions for Pb+Pb collisions at $\sqrt{s_{NN}} = 2.76$ TeV*, Phys. Lett. **B694**, 238 (2010).
- [54] B. Schenke, S. Jeon and C. Gale, *Anisotropic flow in $\sqrt{s}=2.76$ TeV Pb+Pb collisions at the LHC*, Phys. Lett. **B702**, 59 (2011).
- [55] T. Hirano, U. Heinz, D. Kharzeev, R. A. Lacey, and Y. Nara, *Hadronic dissipative effects on elliptic flow in ultra-relativistic heavy-ion collisions*, Phys. Lett. **B636**, 299 (2006).
- [56] A. Adil, H. J. Drescher, A. Dumitru, A. Hayashigaki and Y. Nara, *The eccentricity in heavy-ion collisions from color glass condensate initial conditions*, Phys. Rev. C **74**, 044905 (2006).
- [57] U. Heinz, J. S. Moreland and H. Song, *Viscosity from elliptic flow: the path to precision*, Phys. Rev. C **80**, 061901 (2009).
- [58] A. Adare *et al.* (PHENIX Collaboration), *Measurements of higher-order flow harmonics in Au+Au collisions at $\sqrt{s_{NN}} = 200$ GeV*, Phys. Rev. Lett. **107**, 252301 (2011).
- [59] P. Sorensen *et al.* (STAR Collaboration), *Higher flow harmonics in heavy-ion collisions from STAR*, J. Phys. **G38**, 124029 (2011)
- [60] K. Aamodt *et al.* (ALICE Collaboration), *Higher harmonic anisotropic flow measurements of charged particles in Pb-Pb collisions at 2.76 TeV*, Phys. Rev. Lett. **107**, 032301 (2011).
- [61] Chatrchyan S, *et al.* (CMS Collaboration), *Measurement of higher-order harmonic flow in Pb+Pb collisions at center-of-mass energy = 2.76 TeV*, CMS-PAS-HIN-11-005.
- [62] P. Steinberg, *Recent heavy-ion results with the ATLAS detector at the LHC*, J. Phys. **G38**, 124004 (2011).
- [63] H. Petersen, G.-Y. Qin, S. A. Bass and B. Müller, *Triangular flow in event-by-event ideal hydrodynamics in Au+Au collisions at $\sqrt{s_{NN}} = 200$ GeV*, Phys. Rev. C **82**, 041901 (2010).
- [64] M. Luzum, *Collective flow and long-range correlations in relativistic heavy ion collisions*, Phys. Lett. **B696**, 499-504 (2011).
- [65] J. Xu and C. M. Ko, *Triangular flow in heavy ion collisions in a multiphase transport model*, Phys. Rev. C **84**, 014903 (2011).
- [66] M. Luzum, *Flow fluctuations and long-range correlations: elliptic flow and beyond*, J. Phys. **G38**, 124026 (2011).
- [67] A. K. Chaudhuri, *Fluctuating initial conditions and fluctuations in elliptic and triangular flow*, Phys. Lett. **B710**, 339 (2012).
- [68] B. Schenke, S. Jeon and C. Gale, *Higher flow harmonics from (3+1)D event-by-event viscous hydrodynamics*, Phys. Rev. C **85**, 024901 (2012).

- [69] C. Shen, S. A. Bass, T. Hirano, P. Huovinen, Z. Qiu, H. Song and U. Heinz, *The QGP shear viscosity: elusive goal or just around the corner?*, J. Phys. **G38**, 124045 (2011).
- [70] K. Aamodt *et al.* (ALICE Collaboration), *Suppression of charged particle production at large transverse momentum in central Pb-Pb collisions at $\sqrt{s_{NN}} = 2.76$ TeV*, Phys. Lett. **B696**, 30 (2011).
- [71] C. Shen, U. Heinz, P. Huovinen and H. Song, *Radial and elliptic flow in Pb+Pb collisions at the Large Hadron Collider from viscous hydrodynamic*, Phys. Rev. C **84**, 044903 (2011).
- [72] K. Aamodt *et al.* (ALICE Collaboration), *Charged particle multiplicity density at mid-rapidity in central Pb-Pb collisions at $\sqrt{s_{NN}} = 2.76$ TeV*, Phys. Rev. Lett. **105**, 252301 (2010).
- [73] K. Aamodt *et al.* (ALICE Collaboration), *Centrality dependence of the charged particle multiplicity density at mid-rapidity in Pb-Pb collisions at $\sqrt{s_{NN}} = 2.76$ TeV*, Phys. Rev. Lett. **106**, 032301 (2011).
- [74] U. Heinz, C. Shen, and H. Song, *The viscosity of quark-gluon plasma at RHIC and the LHC*, AIP Conf. Proc. **1441**, 766 (2012).
- [75] E. Shuryak, *The Cone, the ridge and the fate of the initial state fluctuations in heavy-ion Collisions*, Phys. Rev. C **80**, 054908 (2009).
- [76] T. Hirano and K. Tsuda, *Collective flow and two pion correlations from a relativistic hydrodynamic model with early chemical freezeout*, Phys. Rev. C **66**, 054905 (2002).
- [77] H. Song and U. Heinz, *Multiplicity scaling in ideal and viscous hydrodynamics*, Phys. Rev. C **78**, 024902 (2008).
- [78] M. Miller and R. Snellings, *Eccentricity fluctuations and its possible effect on elliptic flow measurements*, nucl-ex/0312008.
- [79] B. Schenke, P. Tribedy and R. Venugopalan, *Fluctuating Glasma initial conditions and flow in heavy ion collisions*, Phys. Rev. Lett. **108**, (2012) 252301.
- [80] C. Gale, S. Jeon, B. Schenke, P. Tribedy and R. Venugopalan, *Initial state fluctuations and higher harmonic flow in heavy-ion collisions*, Nucl. Phys. **A904** (2013).
- [81] U. Heinz and R. Snellings, *Collective flow and viscosity in relativistic heavy-ion collisions*, Annu. Rev. Nucl. Part. Sci. 2013. 63:125-51 arXiv:1301.2826 [nucl-th].
- [82] Wei Li *Quark Matter 2012 Poster*.
- [83] B. Schenke, P. Tribedy and R. Venugopalan, *Event-by-event gluon multiplicity, energy density, and eccentricities in ultra-relativistic heavy-ion collisions*, Phys. Rev. C **86**, 034908 (2012).
- [84] Z. Qiu and U. Heinz, *Hydrodynamic event-plane correlations in Pb+Pb collisions at $\sqrt{s}=2.76$ ATeV*, Phys. Lett. **B717**, 261 (2012).
- [85] S. A. Voloshin, A. M. Poskanzer and R. Snellings, *Collective phenomena in non-central nuclear collisions*, in *Relativistic Heavy Ion Physics*, Landolt-Börnstein New Series, Vol. I/23, edited by R. Stock (Springer Verlag, New York, 2010).
- [86] A. P. Mishra, R. K. Mohapatra, P. S. Saumia and A. M. Srivastava, *Super-horizon fluctuations and acoustic oscillations in relativistic heavy-ion collisions*, Phys. Rev. C **77**, (2008) 064902.

- [87] A. Mocsy and P. Sorensen, *Analyzing the power spectrum of the little bangs*, Nucl. Phys. **A855**, (2011) 241-244.
- [88] P. Staig and E. Shuryak, *The Fate of the initial state fluctuations in heavy-ion collisions. II The Fluctuations and sounds*, Phys. Rev. C **84**, (2011) 034908.
- [89] J. L. Nagle and M. P. McCumber, *Heavy-ion initial conditions and correlations between higher moments in the spatial anisotropy*, Phys. Rev. C **83**, 044908 (2011).
- [90] R. S. Bhalerao, M. Luzum and J. -Y. Ollitrault, *Determining initial-state fluctuations from flow measurements in heavy-ion collisions*, Phys. Rev. C **84** (2011) 034910.
- [91] G.-Y. Qin and B. Müller, *Counting hot/cold spots in quark-gluon plasma*, Phys. Rev. C **85** (2012) 061901.
- [92] J. Jia and S. Mohapatra, *A method for studying initial geometry fluctuations via event plane correlations in heavy ion collisions*, arXiv:1203.5095 [nucl-th].
- [93] J. Jia *et al.* (ATLAS Collaboration), *Measurement of event plane correlations in Pb-Pb collisions at $\sqrt{s_{NN}}=2.76$ TeV with the ATLAS detector*, arXiv:1208.1427 [nucl-ex].
- [94] R. S. Bhalerao, J. -Y. Ollitrault and S. Pal, *Event-plane correlators*, arXiv:1307.0980 [nucl-th].
- [95] P. F. Kolb and U. Heinz, N. Borghini and J.-Y. Ollitrault, *Momentum spectra, anisotropic flow, and ideal fluids*, Phys. Lett. **B642**, 227 (2006).
- [96] Z. -W. Lin, C. M. Ko, B. -A. Li, B. Zhang and S. Pal, *A Multi-phase transport model for relativistic heavy ion collisions*, Phys. Rev. C **72**, 064901 (2005).
- [97] P. Staig and E. Shuryak, *The Fate of the initial state fluctuations in heavy-ion collisions. III The Second act of hydrodynamics*, Phys. Rev. C **84** (2011) 044912.
- [98] D. Teaney and L. Yan, *Non linearities in the harmonic spectrum of heavy ion collisions with ideal and viscous hydrodynamics*, Phys. Rev. C **86**, 044908 (2012).
- [99] L. Yan, talk presented at *Quark Matter 2012*, Washington, D.C., August 12-18, 2012.
- [100] Z. Qiu, C. Shen and U. Heinz, *Resonance decay contributions to higher-order anisotropic flow coefficients*, Phys. Rev. C **86**, 064906 (2012).
- [101] H. Song, S. A. Bass and U. Heinz, *Viscous QCD matter in a hybrid hydrodynamic+Boltzmann approach*, Phys. Rev. C **83**, 024912 (2011).
- [102] J. Adams *et al.* (STAR Collaboration), *Identified particle distributions in pp and Au+Au collisions at $s(NN)^{1/2} = 200$ GeV*, Phys. Rev. Lett. **92**, 112301 (2004).
- [103] S. S. Adler *et al.* (PHENIX Collaboration), *Identified charged particle spectra and yields in Au+Au collisions at $S(NN)^{1/2} = 200$ GeV*, Phys. Rev. C **69**, 034909 (2004).
- [104] J. Sollfrank, P. Koch and U. Heinz, *The influence of resonance decays on the $P(t)$ spectra from heavy ion collisions*, Phys. Lett. **B252**, 256 (1990).
- [105] P. Braun-Munzinger, K. Redlich and J. Stachel, *Particle production in heavy ion collisions, Quark-Gluon Plasma 3*, R. C. Hwa and X.-N. Wang, eds. (World Scientific, Singapore, 2004), pp. 491-599.

- [106] W. Israel, J. M. Stewart, *Transient relativistic hydrodynamics and transport theory*, Ann. Phys. **118**, 349 (1979).
- [107] R. Baier, P. Romatschke and U. A. Wiedemann, *Dissipative hydrodynamics and heavy ion collisions*, Phys. Rev. C **73**, 064903 (2006).
- [108] U. Heinz, Z. Qiu and C. Shen, *Fluctuating flow angles and anisotropic flow measurements*, Phys. Rev. C **87**, 034913 (2013).
- [109] F. G. Gardim, F. Grassi, M. Luzum and J.-Y. Ollitrault, *Mapping the hydrodynamic response to the initial geometry in heavy-ion collisions*, Phys. Rev. C **85**, 024908 (2012).
- [110] J. -Y. Ollitrault and F. G. Gardim, *Hydro overview*, Nucl. Phys. A904-905 2013, 75c (2013).
- [111] F. G. Gardim, F. Grassi, M. Luzum and J. -Y. Ollitrault, *Breaking of factorization of two-particle correlations in hydrodynamics*, Phys. Rev. C **87**, 031901.
- [112] B. Alver *et al.* (PHOBOS Collaboration), *Non-flow correlations and elliptic flow fluctuations in gold-gold collisions at $\sqrt{s_{NN}} = 200$ GeV*, Phys. Rev. C **81**, 034915 (2010).
- [113] K. Aamodt *et al.* (ALICE Collaboration), *Harmonic decomposition of two-particle angular correlations in Pb-Pb collisions at $\sqrt{s_{NN}} = 2.76$ TeV*, Phys. Lett. **B708**, 249 (2012).
- [114] S. Chatrchyan *et al.* (CMS Collaboration), *Centrality dependence of dihadron correlations and azimuthal anisotropy harmonics in Pb-Pb collisions at $\sqrt{s[NN]} = 2.76$ TeV*, Eur. Phys. J. **C72**, 2012 (2012).
- [115] G. Aad *et al.* (ATLAS Collaboration), *Measurement of the azimuthal anisotropy for charged particle production in $\sqrt{s_{NN}} = 2.76$ TeV lead-lead collisions with the ATLAS detector*, Phys. Rev. C **86**, 014907 (2012).
- [116] E. Retinskaya, M. Luzum and J. -Y. Ollitrault, *Directed flow at mid-rapidity in $\sqrt{s_{NN}} = 2.76$ TeV Pb+Pb collisions*, Phys. Rev. Lett. **108**, 252302 (2012).
- [117] N. Borghini, P. M. Dinh and J.-Y. Ollitrault, *A New method for measuring azimuthal distributions in nucleus-nucleus collisions*, Phys. Rev. C **63**, 054906 (2001).
- [118] N. Borghini, P. M. Dinh and J.-Y. Ollitrault, *Flow analysis from multiparticle azimuthal correlations*, Phys. Rev. C **64**, 054901 (2001).
- [119] A. Bilandzic, R. Snellings and S. Voloshin, *Flow analysis with cumulants: Direct calculations*, Phys. Rev. C **83**, 044913 (2011).
- [120] A. M. Poskanzer and S. A. Voloshin, *Methods for analyzing anisotropic flow in relativistic nuclear collisions*, Phys. Rev. C **58**, 1671 (1998).
- [121] M. Luzum and J. -Y. Ollitrault, *The event-plane method is obsolete*, Phys. Rev. C **87**, 044907 (2013).
- [122] P. Romatschke, *New developments in relativistic viscous hydrodynamics*, Int. J. Mod. Phys. **E19**, 1 (2010).
- [123] F. G. Gardim, F. Grassi, M. Luzum and J. -Y. Ollitrault, *Characterizing the hydrodynamic response to the initial conditions*, Nucl. Phys. **A904**, (2013).
- [124] K. Dusling, F. Gelis and R. Venugopalan, *The initial spectrum of fluctuations in the little bang*, Nucl. Phys. **A872**, (2011) 161-195.

- [125] C. Flensburg, *Correlations and fluctuations in the initial state of high energy heavy-ion collisions*, arXiv:1108.4862 [nucl-th].
- [126] H. Petersen, R. La Placa and S. A. Bass, *A systematic study of the sensitivity of triangular flow to the initial state fluctuations in relativistic heavy-ion collisions*, J. Phys. **G39**, 055102 (2012).
- [127] P. Bozek and W. Broniowski, *Transverse-momentum fluctuations in relativistic heavy-ion collisions from event-by-event viscous hydrodynamics*, Phys. Rev. C **85**, 044910 (2012).
- [128] P. Mota and T. Kodama, *Flow and eccentricity correlation in fluctuating initial conditions*, Prog. Theor. Phys. Suppl. **193**, 315 (2012).
- [129] R. Chatterjee, H. Holopainen, T. Renk and K. J. Eskola, *Collision centrality and τ_0 dependence of the emission of thermal photons from fluctuating initial state in ideal hydrodynamic calculation*, Phys. Rev. C **85**, 064910 (2012).
- [130] L. Pang, Q. Wang and X. -N. Wang, *Effects of initial flow velocity fluctuation in event-by-event (3+1)D hydrodynamics*, Phys. Rev. C **86**, 024911 (2012).
- [131] P. Bozek, *Event-by-event viscous hydrodynamics for Cu-Au collisions at 200 GeV*, Phys. Lett. **B717**, 287 (2012).
- [132] F. Cooper and G. Frye, *Single-particle distribution in the hydrodynamic and statistical thermodynamic models of multiparticle production*, Phys. Rev. D **10**, 186 (1974).